

MML-00-3

**Durability and Damage Tolerance of High
Temperature Advanced Titanium Metal Matrix
Composites**

**Final Report
August 2000**

by

Hamouda Ghonem

**Department of Mechanical Engineering
University of Rhode Island
Kingston, RI 02881-0805**

Prepared for

**Department of Air Force
Air Force Office of Scientific Research**

Grant AFOSR - F49620-95-1-0348

DISTRIBUTION STATEMENT A
Approved for Public Release
Distribution Unlimited

20001016 006

DTIC QUALITY INSPECTED 4

REPORT DOCUMENTATION PAGE

AFRL-SR-BL-TR-00-

8

ng and
ion, including
is Highways,
a collection of

0508

Public reporting burden for this collection of information is estimated to average 1 hour per response, including the time for reviewing the data needed, and completing and reviewing this collection of information. Send comments regarding this burden estimate or any other aspect of this collection of information, including suggestions for reducing this burden to Department of Defense, Washington Headquarters Services, Directorate for Information Operations and Reports, 1215 Jefferson Davis Highway, Suite 1204, Arlington, VA 22202-4302. Respondents should be aware that notwithstanding any other provision of law, no person shall be held liable for any damages resulting from any collection of information that does not display a currently valid OMB control number. PLEASE DO NOT RETURN YOUR FORM.

1. REPORT DATE (DD-MM-YYYY) August 2000		2. REPORT TYPE Final		3. DATES COVERED (From - To) May 1996 - May 1999	
4. TITLE AND SUBTITLE Durability and Damage Tolerance of High Temperature Advanced Titanium Metal Matrix Composites				5a. CONTRACT NUMBER	
				5b. GRANT NUMBER AFOSR - F49620-95-1-0348	
				5c. PROGRAM ELEMENT NUMBER	
				5d. PROJECT NUMBER	
6. AUTHOR(S) Hamouda Ghonem				5e. TASK NUMBER	
				5f. WORK UNIT NUMBER	
				8. PERFORMING ORGANIZATION REPORT NUMBER URI-MML-00-3	
7. PERFORMING ORGANIZATION NAME(S) AND ADDRESS(ES) Department of Mechanical Engineering University of Rhode Island Kingston, Ri 02881				10. SPONSOR/MONITOR'S ACRONYM(S) Dr. Ozden Ochoa	
9. SPONSORING / MONITORING AGENCY NAME(S) AND ADDRESS(ES) USAF Office of Scientific Research 801 N. Randolph St., Rm 947 Arlington, VA 22203				11. SPONSOR/MONITOR'S REPORT NUMBER(S)	
12. DISTRIBUTION / AVAILABILITY STATEMENT Approved for Public release Distribution is unlimited					
13. SUPPLEMENTARY NOTES					
14. ABSTRACT The bridging fatigue crack growth damage mechanisms in a unidirectional SiC/Ti MMC include matrix cracking, fiber/matrix interface debonding and sliding along bridging fibers and fracture of these fibers. The basic components of these mechanisms are examined in this program. The evolution features of residual stresses indicated that stress relaxation occurred in the Ti matrix phase of the composite following post-fabrication cool down to 600 °C. Parametric study of the SiC fiber coating materials showed that the effective residual stress component has an inverse relationship with the thickness of the fiber reaction zone. The debonding shear strength of the composite is determined by the localized shear stress distribution along the fiber/matrix interface at the onset of debonding. An interphase debonding model, which combine fracture mechanics with FE results on interphase shear stress and bridging fiber traction range, is proposed to establish a distribution of debonding lengths along a fiber-bridged matrix crack length as a function of temperature. The driving force for the interface debond crack, however, has an inverse relationship with the test temperature. The concurrent damage events of fiber stress evolution and continuous fiber strength degradation were postulated into a fiber fracture criterion to describe the fracture process of a bridging fiber. Furthermore, the fiber crack density has been correlated with the density of crack initiation sites observed in the interphase region along the reinforcing fibers in a SCS-6/Ti-21S composite.					
15. SUBJECT TERMS Titanium Metal Matrix Composites, Silicon Carbide Fibers, Fatigue Crack Bridging, Residual stresses, Interphase, Debonding					
16. SECURITY CLASSIFICATION OF:			17. LIMITATION OF ABSTRACT UL	18. NUMBER OF PAGES 294	19a. NAME OF RESPONSIBLE PERSON Hamouda Ghonem
a. REPORT Unclassified	b. ABSTRACT Unclassified	c. THIS PAGE Unclassified			19b. TELEPHONE NUMBER (include area code) 401-874-2909

Abstract

The bridging fatigue crack growth damage mechanisms in a unidirectional SiC/Ti MMC include matrix cracking, fiber/matrix interface debonding and sliding along bridging fibers and fracture of these fibers. The basic components of these mechanisms are examined in this program. The evolution characteristics of residual stresses indicated that extensive stress relaxation occurred in the Ti matrix phase of the composite following post-fabrication cool down to 600 °C. Parametric study on the SiC fiber coating materials showed that the effective residual stress component has an inverse relationship with the thickness of the composite reaction zone. The debonding shear strength of the composite is determined based on localized shear stress distribution along the fiber/matrix interface at the onset of debonding. The resulting shear strength is found to decrease from 221 MPa at ambient temperature to 139 MPa at 650 °C. An interphase debonding model, which combine fracture mechanics equations with finite element results on interphase shear stress and bridging fiber traction range, is proposed to establish a distribution of debonding lengths along a fiber-bridged matrix crack length. The longest debonding lengths in a SiC/Ti MMC was predicted along the first intact fiber at the crack mouth and the lengths decrease for fibers located closer to the crack tip. In addition, the debonding crack length increases with increasing temperature. The driving force for the interface debond crack, however, has an inverse relationship with the test temperature. The concurrent damage events of fiber stress evolution and continuous fiber strength degradation were postulated into a fiber fracture criterion to describe the fracture process of a bridging fiber. Although the strength properties of SCS-6 fibers are found to be unaffected by test temperature of 650 °C and below, temperature influenced the fracture process of these fibers through the density of cracks in the outermost carbon-rich fiber coating. This fiber crack density has been correlated with the density of crack initiation sites observed in the interphase region along the reinforcing fibers in a SCS-6/Ti-21S composite.

ACKNOWLEDGEMENT

This research is supported by USAF Office of Scientific Research under grant F49620-95-1-0348. Dr. Ozden Ochoa is the program manager.

PREFACE

This report consists of six chapters in the form of the manuscripts which have been submitted for publication in peer reviewed scientific journals as a result of the work carried out in this program. The paper titles, original authors and publishing journal are included in footnotes at the beginning of each chapter. Chapters 1 and 2 are the expanded version of the cited paper while chapters 3-6 have been inserted into the dissertation without modification to the manuscripts as submitted for publication. This leads to some redundancy in this dissertation in regard to the figures and tables. The author felt that this would make the document easier for the reader to manipulate. Individual abstracts have been retained from the manuscripts to introduce each chapter.

A literature review of the bridging fatigue crack growth process in a unidirectional metal matrix composite highlighting the components of the damage mechanism is added in Appendix A. Appendix B contains a complete description of the fiber and composite materials along with experimental procedures developed for fiber testing. Scanning electron microscopy of fractured surfaces is also covered in this appendix. Finite element analysis procedures incorporated in the study is described in Appendix C. Appendix D presents a summary and general discussion of the results of the program along with suggestion for future work related to this study.

TABLE OF CONTENTS

Abstract	ii
Acknowledgement	iii
Preface	iv
Table of Contents	v
List of Tables	viii
List of Figures	ix
CHAPTER 1 Micromechanical Modeling of Time-Dependent Behavior of Continuous-Fiber-Reinforced Metal Matrix Composites	1
Abstract	1
1.1 Introduction	2
1.2 Concepts of the Micromechanical Approach	5
1.3 Formulations	9
1.3.1 Elastic-Plastic Analysis	13
1.3.2 Creep Analysis	18
1.4 Solution Procedures	25
1.5 Summary and Conclusions	29
1.6 References	31
CHAPTER 2 Parametric Study of the Time-Dependent Behavior of Continuous-Fiber Reinforced Metal Matrix Composites Based on Micromechanical Model	41
Abstract	41
2.1 Introduction	42
2.2 Parametric Study	44
2.2.1 Thickness of the Equivalent Composite Media	46
2.2.2 Fiber Coating Material and Thickness of the Interfacial Region	48
2.2.3 Role of Creep Deformation in the Evolution of Thermal Stresses	50
2.2.4 Evolution of Thermal Stresses During Thermal Cycling	52
2.3 Conclusion	54
2.4 References	55
CHAPTER 3 Debonding Shear Strength of Titanium Metal Matrix Composites	79
Abstract	79
3.1 Introduction	80
3.2 Material and Experimental Procedures	83
3.3 Residual Stress Analysis	86
3.4 Stress Analysis for Fiber Pushout Test	89

3.5	Interphase Shear Strength	91
3.6	Discussion	93
3.7	Summary	97
3.8	References	98
CHAPTER 4	Interface Debonding in Titanium Metal Matrix Composites	115
	Abstract	115
4.1	Introduction	116
4.2	Interface Debonding Criterion	120
4.3	Crack Bridging Model	123
4.4	Driving Force for Interface Crack	126
4.5	Results and Discussion	129
4.6	Summary	135
4.7	References	136
4.8	Appendix	144
	4.8.1 Crack Bridging Model	144
	4.8.2 Finite Element Model	145
CHAPTER 5	Evolution of Bridging Fiber Stress in Titanium Metal Matrix Composites at Elevated Temperature	159
	Abstract	159
5.1	Introduction	160
5.2	Material and Experimental Procedures	162
5.3	The Crack Growth Process	164
5.4	Stress Distribution in Bridging Fibers	165
5.5	Stress Evolution in Bridging Fibers	168
5.6	Fatigue Strength of Bridging Fibers	171
5.7	Conclusions	172
5.8	References	174
CHAPTER 6	Fiber Damage Mechanisms in Titanium Metal Matrix Composites	191
	Abstract	191
6.1	Introduction	192
6.2	Material and Experimental Procedures	195
6.3	Results	197
	6.3.1 Fiber Residual Strength	198
	6.3.2 Fiber Cracks	200
6.4	Bridging Fiber Damage Mechanism	204
6.5	Conclusions	206
6.6	References	208
6.7	Appendix	218

APPENDIX A	Introduction to the Study	237
A.1	Damage Mechanisms in Metal Matrix Composites	237
A.2	Bridging Fatigue Crack Growth Process	242
A.3	Factors Influencing Crack Bridging Process	248
A.3.1	Crack Opening Displacement	249
A.3.2	Bridging Fiber Stress	251
A.3.3	Fiber/Matrix Frictional Shear Stress	253
A.3.4	Fiber/Matrix Interface Debonding Length	255
A.3.5	Bridging/Acceleration Fatigue Crack Growth Transition	259
A.4	Thesis Objectives	260
APPENDIX B	Materials and Experimental Methods	277
B.1	Tensile and Fatigue Testing on Fibers	277
B.1.1	Fiber Materials	278
B.1.2	Specimen Preparation	278
B.1.3	Tensile Testing Procedures	279
B.1.4	Fatigue Testing Procedures	282
B.2	Fatigue Testing on Metal Matrix Composites	283
B.2.1	Composite Materials	283
B.2.2	Specimen Preparation	286
B.2.3	Fatigue Testing Procedures	286
B.2.4	Acoustic Emission Monitoring	287
B.3	Scanning Electron Microscopy	290
B.3.1	Surface Cracks on Fiber Coatings	290
B.3.2	Microcrack Initiation Sites Along the Fibers	293

LIST OF TABLES

Table 3.1	Test matrix for fiber pushout tests of SCS-6/Timetal-21S composites.	106
Table 3.2	Process-related interphase properties of SCS-6/Timetal-21S Composites.	106
Table 5.1	Test parameters for the cases used in the finite element calculations.	170
Table 6.1	Properties of amorphous carbon and SiC SCS-6 fiber.	215
Table 6.2	Test matrix for fatigue testing of SCS-6 fibers.	216
Table 6.3	Test parameters and fatigue properties of bridging fibers.	217
Table B.1	Chemical composition of titanium alloy Timetal-21S.	284
Table B.2	System parameters used for AE damage monitoring in MMCs.	288

LIST OF FIGURES

Figure 1.1(a)	Selected Configuration of a unit cell with surrounding composite material.	35
Figure 1.1(b)	Cut-out section of the four-phase model.	36
Figure 1.2	Discretization of the cooling/heating path (no externally applied mechanical load).	37
Figure 1.3	(a) Reference state at consolidation. (b) Constraint-free thermal deformation. (c) Equilibrium conditions due to boundary constraints. (d) Constraint-free creep deformation. (e) Equilibrium conditions due to boundary constraints. (f) Final equilibrium conditions at the end of the first temperature-time step loading (sum of conditios at (c) and (e)).	38
Figure 1.4	Flow charts for elastic-plastic-creep algorithm.	39
Figure 1.5	Strain history predictionfor the firsttwo load steps from strain hardening method.	40
Figure 2.1(a)	Physical properties of the constituents: CTE	59
Figure 2.1(b)	Physical properties of the constituents: Young's modulus.	60
Figure 2.1(c)	Physical properties of the constituents: Yield strength of Timetal 21S.	61
Figure 2.2(a)	Variation of stress field in the matrix layer with size of the equivalent composite: Radial Component. $\underline{v_f = 35\%}$, $\underline{\underline{v_f = 20\%}}$	62
Figure 2.2(b)	Variation of stress field in the matrix layer with size of the equivalent composite: Hoop component. $\underline{v_f = 35\%}$, $\underline{\underline{v_f = 20\%}}$	63
Figure 2.2(c)	Variation of stress field in the matrix layer with size of the equivalent composite: Axial component. $\underline{v_f = 35\%}$, $\underline{\underline{v_f = 20\%}}$	64
Figure 2.3	Frequency distribution of center-to-center spacings between fibers in Ti-15-3 composite with 35% fiber volume fraction.	65
Figure 2-4	Idealized array of fibers in MMC with 35 % fiber volume fraction.	66
Figure 2.5(a)	Variation of radial stress field in the matrix with thickness of fiber coating for different coating materials: $\underline{\underline{TiB_2}}$, \underline{Nb} , \underline{C} , \underline{Cu}	67
Figure 2.5(b)	Variation of hoop stress field in the matrix with thickness of fiber coating for different coating materials: $\underline{\underline{TiB_2}}$, \underline{Nb} , \underline{C} , \underline{Cu}	68
Figure 2.-5(c)	Variation of axial stress field in the matrix with thickness of fiber coating for different coating materials: $\underline{\underline{TiB_2}}$, \underline{Nb} , \underline{C} , \underline{Cu}	69
Figure 2.5(d)	Variation of radial stress field in the interfacial region with thickness of fiber coating for different coating materials:	

	—TiB ₂ — —Nb— —C— —Cu	70
Figure 2.5(e)	Variation of hoop stress field in the interfacial region with thickness of fiber coating for different coating materials:	
	—TiB ₂ — —Nb— —C— —Cu	71
Figure 2.5(f)	Variation of axial stress field in the interfacial region with thickness of fiber coating for different coating materials:	
	—TiB ₂ — —Nb— —C— —Cu	72
Figure 2.6(a)	Physical properties of the composite constituents at room temperature: CTE.	73
Figure 2.-6(b)	Physical properties of the composite constituents at room temperature: Young's modulus.	74
Figure 2.-7	Evolution of axial thermal stress in the matrix during initial cool-down at 0.5 °C/sec.: —elastic-plastic-creep, —elastic-plastic, —elastic. $\sigma_y^{(2)}$ is the matrix yield strength.	75
Figure 2.8	Amount of stress reduction due to creep in the matrix at various cooling rates.	76
Figure 2.9	Evolution of axial thermal stress during initial cool-down at 0.5 °C/sec.: —experiment [Ghon93], —present result.	77
Figure 2.10	Evolution of axial thermal stress in the matrix during initial cool-down and thermal cycle between 100 - 550 °C at 0.5 °C/sec.	78
Figure 3.1	Polished and etched cross section of a SCS-6/Timetal-21S composite showing a staggered array architecture of fiber distribution.	107
Figure 3.2	(a) Load-displacement curve of a fiber pushout test for a SCS-6/Timetal-21S composite at ambient temperature, 500 and 650 °C. The specimen thickness, H=1.4 mm. (b) Load-effective displacement curve corrected for compliance for test at 650 °C.	108
Figure 3.3	(a) A representative unit cell of the composite consisting of a fiber embedded in the matrix phase. (b) Finite element mesh employed in modeling the evolution characteristics of residual stress in the composite during initial cooldown. (c) Refine finite element mesh use in modeling fiber pushout test.	109
Figure 3.4	Evolution of residual stresses in the matrix phase of a SCS-6/Timetal-21S composite during initial cool down at 0.03 °C/sec from stress-free to ambient temperature. The matrix stress is taken in the region adjacent to the fiber/matrix interface.	110
Figure 3.5	Variations of residual radial and shear stress components along the fiber/matrix interface in a thin-slice composite specimen at 25 °C. The sample thickness, H = 0.50 mm.	111
Figure 3.6	Shear stress distribution along the interface due to applied load	

	at the onset of interface debonding in a fiber pushout test performed at 25 °C. The specimen thickness, $H = 0.5$ mm.	112
Figure 3.7	(a) Superposition of shear stress distributions due to effect of thermal residual stress and stress field due to pushout load at the onset of interface debonding in a fiber pushout test performed at 25 °C. (b) Resultant interface shear stress distributions for various test conditions. The specimen thickness, $H=0.50$ mm for 25°C and $H=1.4$ mm for 500 and 650 °C. The concept of stress localization in determining the interphase shear strength, τ_d , is illustrated for the case of 25°C.	113
Figure 3.8	Influence of temperature on interphase shear strength, τ_d , and frictional shear stress, τ_s . The dashed line represents the average shear strength values, τ_{d-ave} , determined using the assumption of uniformly distributed shear force along the pushout fiber.	114
Figure 4.1	Concept for fiber/matrix interface debonding criterion.	147
Figure 4.2	Variation of interphase debonding shear strength, τ_d , and frictional shear stress, τ_s , with test temperature.	148
Figure 4.3	Procedures for establishing the initial debonding length, L_i , along a bridging fiber through incremental debonding and force equilibrium considerations.	149
Figure 4.4	Schematic of a crack bridging scenario in a unidirectional MMC.	150
Figure 4.5	Growth behavior of a fiber-bridged crack in a SCS-6/Timetal-21S composite at 25 °C.	151
Figure 4.6	Influence of test temperature on initial debonding length of a SCS-6/Timetal-21S composite subjected to $\Delta\sigma = 270$ Mpa, $R = 1$. Also shown are experimental measurements for several SiC/Ti MMCs.	152
Figure 4.7	Distribution of interface debonding lengths along a fiber-bridged matrix crack.	153
Figure 4.8	Correlation between closure pressure, Δp , and interface debonding lengths, L_d , at 25 °C.	154
Figure 4.9	Interface crack opening displacement profile for different debond crack lengths at 25 °C.	155
Figure 4.10	Interface Crack tip driving force for various debond crack length and temperature levels.	156
Figure 4.A-1	Flow diagram for crack bridging model to establish debonding lengths and closure pressure profile along a fiber-bridged crack.	157
Figure 4.A-2	(a) Unit cell model for fiber bridging. (b) Finite element mesh and boundary conditions for unit cell model of fiber bridging.	158
Figure 5.1	A Polished and etched cross section of the as-received SM1240/Timetal-21S composite showing (a) the distribution of fibers, and (b) the region of fine matrix grains around the fiber.	180

Figure 5.2	Fatigue crack growth rate, da/dN , versus the applied stress intensity factor, ΔK_a , during the initial crack growth deceleration and acceleration stages.	181
Figure 5.3	Finite element mesh employed in modelling the response of bridging fiber under cyclic loading.	182
Figure 5.4	Young's modulus, E , yield strength, σ_y , and coefficient of thermal expansion, α_m , for Timetal-21S matrix alloy, and coefficient of thermal expansion, α_f , for SM1240 fiber. The properties are normalized by their respective values at 24 °C: $E_{RT} = 94$ GPa, $\sigma_{y,RT} = 1040$ MPa, $\alpha_{m,RT} = 8.41 \times 10^{-6} / ^\circ\text{C}$, and $\alpha_{f,RT} = 4.72 \times 10^{-6} / ^\circ\text{C}$	183
Figure 5.5	Cross section of the axisymmetric model showing the debonded length, L_d , radius of fiber, r_f and radius of matrix cylinder, r_m . z and r are the axial and radial coordinate axes, respectively.	184
Figure 5.6	Variation of axial stress along the bridging fiber at different loading cycles. Curve A represents the stress variation after 1 load cycle while curve B is the variation at the end of 500 load cycles. The debonded length, $L_d = 1200 \mu\text{m}$	185
Figure 5.7	Fracture sites of bridging fibers for test condition 2B, (see Table 5.1), marked with white arrows, above and below the matrix crack plane. The dark areas are the fiber phase.	186
Figure 5.8	Variation of radial stress along the fiber/matrix interface at the peak of the first applied load cycle. The temperature is 650 °C and the debonded length, $L_d = 1200 \mu\text{m}$	187
Figure 5.9	Variation of shear stress along the fiber/matrix interface. The frictional shear stress, τ_f , acts along the slip length, $L_s = 950 \mu\text{m}$, with the coefficient of friction, $\nu = 0.05$ at test temperature 650 °C. The debonded length, $L_d = 1200 \mu\text{m}$	188
Figure 5.10	Evolution of axial stress in the bridging fiber at the loading frequencies of (A) 0.1 Hz and (B) 10 Hz. - - - - - without process induced residual stress and with uniform large matrix grain size, ——— with residual stress and duplex microstructure of the matrix phase, — — — — with residual stress and uniform large matrix grain size. The filled diamond symbols on curves b and e represent the fatigue strength, S_f of the bridging fibers.	189
Figure 5.11	The influence of temperature and loading frequency on the fatigue strength of bridging fiber in SM1240/Timetal-21S composite.	190
Figure 6.1	Surface morphology of a SiC SCS-6 fiber.	220
Figure 6.2	Weibul distribution of tensile strengths of SCS-6 fibers.	221
Figure 6.3	Residual fatigue strength of SCS-6 fibers at 500 and 650 °C for various maximum applied stress (stress ratio, $R = 0.1$).	222

Figure 6.4	Fatigue strength-life (S-N) curve for SCS-6 fibers.	223
Figure 6.5	(a) Calculated axial strain distribution in the vicinity of a carbon-rich coating crack along a SiC. (b) Variation of minimum coating crack spacing with temperature under monotonic tensile loading.	224
Figure 6.6	Typical surface morphology of SCS-6 fibers fatigued at 650 °C showing distribution of circular coating cracks.	225
Fig 6.7	(a) Statistical distribution of 785 measurements of spacing between adjacent cracks along SCS-6 fibers fatigued at 650 °C for 24.8 (10 ⁶) cycles, σ_{max} = 1500 MPa, R = 0.1. (b) Statistical distribution of 78 % of the measurements which fall within a 40- μ m spacing.	226
Figure 6.8	Variation of surface cracks density on fatigued fibers at fracture with maximum applied stress and temperature.	227
Figure 6.9	Spalling of the carbon-rich coating layer from SCS-6 fiber due to abrasion by the molybdenum weave during fatigue test at 650 °C.	228
Figure 6.10	Acoustic emission signal in terms of: (a) amplitude and (b) energy count from a fatigue test on SCS-6/Timetal-21S composite at 650 °C during a representative period of 10 seconds.	229
Figure 6.1	Extensive matrix cracking in a fatigued SCS-6/Timetal-21S composite at 650 °C. (Magnification 600X).	230
Figure 6.12	Statistical distribution of measurements of spacing between adjacent crack initiation sites in a fatigued SCS-6/Timetal-21S composite at 500 and 650 °C.	231
Figure 6.13	Correlation between density of cracks on isolated SCS-6 fiber with density of crack initiation sites along the interphase in a SCS-6/Timetal-21S composite.	232
Figure 6.14	(a) Concept for bridging fiber fracture criterion. (b) Illustration of the fracture process for a bridging fiber.	233
Figure 6.15	(a) unit cell model for crack bridging condition. (b) Finite element mesh and boundary conditions of a radial section of the model.	234
Figure 6.16	Evolution of bridging fiber stresses at various loading conditions.	235
Figure 6.A.1	A twophase cylinder model of a SiC SCS-6 fiber.	236
Figure A.1	Fatigue crack growth rate of SCS-6/Ti-15-3 composite using SEN specimen in three-point bending tests [Cott93].	265
Figure A.2	Fatigue crack growth of SM1240/Timetal-21S composite at room temperature, 500 and 650 °C for loading frequencies of 10 Hz using center-notch specimens.	266
Figure A.3	Micrograph of different fracture processes encountered in each of the crack growth stages, namely; bridging,	

	transition and acceleration.	267
Figure A.4	Example of a debonded carbon layer at a plane located immediately under the fracture surface of a room temperature test.	268
Figure A.5	Example of an unstable fracture zone with matrix deformation surrounding the pulled-out fibers.	269
Figure A.6	Room temperature crack growth rates for specimens in as-received condition and aged for 42 hours at 650 °C.	270
Figure A.7	Crack opening displacement, COD, at positions along different bridged crack lengths in a SM1240/Timetal21S composite tested at three different temperatures; 24, 500 and 650°C.	271
Figure A.8	Relationship between crack tip opening displacement, Δu_T , and crack length, a , for the different test temperatures.	272
Figure A.9	Fiber pressure distribution as function of crack length and temperature 24, 500 and 650°C.	273
Figure A.10	Evolution of ΔS_f calculated at the crack mouth as a function of the crack length and at different temperatures.	274
Fig. A.11	Fiber/matrix interface debonding lengths, slip lengths and pullout lengths at various temperatures. The line represents calculated trends of initial debonding lengths, L_i for SCS-6/Timetal-21S composite.	275
Figure A.12	Basic components of fatigue crack bridging process illustrated in relation to the overall propagation of a fiber-bridged crack.	276
Figure B.1	A typical tensile test result of a SiC SCS-6 fiber-mat specimen.	280
Figure B.2	A Weibull distribution of tensile strengths of SiC SCS-6 fibers.	281
Figure B.3	Cross-section of a SCS-6/Timetal-21S composite showing a staggered array distribution of fibers.	285
Figure B.4	Acoustic emission (AE) data from a fatigue test on SCS-6/Timetal-21S composite specimen at 650 °C.	289
Figure B.5	Distribution of surface cracks on fatigued SCS-6 fibers. The test was performed at 650 °C with a maximum load of 1500 Mpa, $R = 0.1$. The accumulated load cycles is 247.6×10^3	291
Figure B.6	(a) Distribution of crack spacing measurements along SCS-6 fibers fatigued at 650 °C for a total of 247.6×10^3 cycles. Maximum applied stress is 1500 MPa, $R = 0.1$. (b) Statistical distribution of 77 % of the measurements which fall within a 20- μm range.	292
Figure B.7	Statistical distribution of crack initiation sites along fibers in a composite fatigued at 500 and 650 °C.	294

CHAPTER 1. Mechanical Modeling of Time-Dependent Behavior of Continuous-Fiber-Reinforced Metal Matrix Composites¹

Abstract

A new time-dependent model has been developed in order to predict the response of metal matrix composites subjected to thermal loadings. In this model, elastic, plastic and creep behavior have been considered. The model consists of a fiber and an interphase zone which behave elastically while the matrix and the surrounding composite media exhibit creep deformation. The cooling/heating path is discretized into load steps where elastic-plastic behavior is assumed to occur spontaneously over a temperature increment while creep behavior occurred over the following time increment. The plastic characteristics follows the deformation theory of plasticity. In the transient and steady-state stages of creep, the constraint-free creep deformation of the matrix and the composite media are calculated using the Bailey-Norton law with an Arrhenius-type expression for

¹Based on: "Time-Dependent Behavior of Continuous-Fiber-Reinforced Metal Matrix Composites: Modeling and Applications." M. N. Tamin, D. Zheng and H. Ghonem, *Journal of Composites Technology & Research*, JCTRER, Vol.16, No. 4, October 1994. pp. 314-322.

time-dependent creep coefficient. The "stiffness" method with a modified load vector is employed in calculating the constrained deformation in the composite. The accumulated creep strain history is predicted using the "strain hardening" formulation. The model can be easily extended to include external loading and employed to study the evolution of the stress and strain states in the constituents of the composite during isothermal and thermo-mechanical loadings.

1.1 Introduction

In Titanium-based metal matrix composites, the metallic matrix properties of ductility and toughness are combined with reinforcement properties of high strength and high modulus to yield increased strength-to-weight ratio and higher stiffness materials. These metal matrix composites (MMCs) are being developed as high performance materials capable of withstanding high temperatures and operating loads typical for advanced aerospace applications.

Continuous-fiber-reinforced MMCs are consolidated at high temperature which induce high thermal residual stresses during post-fabrication cool down. This is a consequence of mismatches of the coefficients of thermal expansions (CTEs) of the matrix and the fibers. These thermal residual stresses may initiate fiber/matrix debonding and radial cracking in the matrix and hence, dictate the subsequent behavior of the composites when subjected to thermo-mechanical loading. It was found that post-fabrication

procedures such as thermal cycling can alter the residual stress states in titanium composites [Saig92]. Consequently, determination of thermal residual stress and strain fields in a continuous-fiber-reinforced MMC is an essential step in characterizing the performance of the composite system.

Various analytical models have been developed and applied to study the thermal stress behavior of continuous-fiber-reinforced composites. Besides the plane-stress lamina model (e.g. [Min81, Min82]), the concentric cylinder model has been well studied (e.g. [Heck70, Uemu79, Mika85, Jaya92]). Uemura [Uemu79] developed a two-phase model which consists of inner and outer cylinder to simulate the fiber and the matrix phase, respectively. In this model, the fiber-matrix interface has been treated as a perfect mathematical surface. Experimental work, however, indicated that the interphase formation accompanying the development of reaction zones in metal matrix composites is inevitable (e.g. [Yang89, Gund91]). Incorporation of interphase behavior into the micromechanical analyses of composite systems is therefore critical in realistic modeling of the mechanical behavior of the composites [Jaya92, Theo85]. Based on this consideration, several researchers have proposed the three-phase model (fiber/interphase/matrix) to account for interphase effects (e.g. [Jaya92, Theo85, Nair85, Jans92]). In reality, the "matrix cylinder" is surrounded by the composite media instead of a free surface, thus it is reasonable to impose a layer of homogeneous material with the composite properties surrounding the matrix layer in order to retain realistic boundary conditions (e.g. [Hash64, Chri79]). Following these ideas, Mikata [Mika85] proposed a four-phase cylinder model (fiber / interphase (coating) / matrix / surrounding composite

media) for elastic analysis of stress field in the composites.

As mentioned above, Titanium-based metal matrix composites are primarily developed for high temperature applications. At such extreme thermal and mechanical service conditions, the composite will experience time dependent deformation. Accurate representation of this nonlinear material behavior is essential in realistic determination of the stress and strain response of the composite. Experimental creep study on SCS-6/Ti-6Al-4V composite indicated that titanium-based composite exhibits creep behavior similar to that of the monolithic matrix (even though the longitudinal creep has been suppressed considerably by fiber reinforcement). This fact implies that creep behavior of the matrix alloy and the corresponding composite must be incorporated into the model formulation. However, fewer work has been done to model the creep behavior of fiber-reinforced metal matrix composites. Min [Min82] developed a plane-stress continuum model to analyze the primary creep deformation of a unidirectional metal matrix composite. Gayda [Gayd90] employed a cylindrical two-phase model to study the time-dependent behavior of TMCs in which the creep behavior of the matrix was considered by a relaxation curve obtained from an empirical fit of stress relaxation data for the matrix alloy. Since the composite media and the reaction zone were not included in these models, the models could not consider influences of the existence of these two phases on the overall creep behavior of the composite.

The objective of this section is to develop a micromechanical approach to analyze the elastic-plastic and creep behavior of a unidirectional continuous-fiber-reinforced metal matrix composite. This approach emphasizes the time-dependent stress analysis which is

critical to high temperature applications. The four-phase cylinder model adopted in the present approach makes it possible to trace the evolution of the stress states for each constituent in the composite during cyclic thermal loadings. The concept of the model including mathematical formulations of the elastic, plastic and creep analyses are presented in the next section of the paper. This is followed by narration of a typical elastic-plastic-creep calculation routine. The last part of the paper includes conclusions and summary.

1.2 Concepts of the Micromechanical Approach

The four-phase configuration adopted in this approach is illustrated in Fig. 1-1(a) where the fibers in the composite are assumed to be arranged in a hexagonal array. A hexagonal unit is substituted for the concentric fiber, reaction zone and matrix cylinders with radii r_1 , r_2 , and r_3 , respectively, while the equivalent composite media is represented by the outermost cylinder with radius r_1 , as shown in Fig. 1-1(b). The fiber and the reaction zone are assumed to behave elastically at all loading conditions while the matrix and the surrounding equivalent composite media may undergo any combination of elastic, plastic and creep deformation depending on the nature of the applied load. All the constituent phases are assumed to be isotropic. In addition, the model is subjected to axisymmetric thermal loading with a uniform temperature distribution across all layers.

During post-fabrication cool down and subsequent thermal cycling, the cooling/heating path is piecewise discretized into load steps, each of which consists of a

temperature increment, ΔT , followed by a time increment, Δt , as shown in Fig. 1-2. For a particular load step, the elastic-plastic and creep response is a summation of the elastic-plastic response due to ΔT and the creep response over the range of Δt .

In order to illustrate the fundamental concepts of the approach proposed here, a one-dimensional four-bar model is utilized as schematically detailed in Fig. 1-3. The assumed stress-free state of the composite at consolidation temperature, T_c , is shown in Fig. 1-3(a) while Fig. 1-3(b) represents the relative amount of thermal strain increments (shrinkage), $\Delta \epsilon_1^{(I),th}$, in each layer if subjected to a uniform finite temperature drop, $-\Delta T_1$ corresponding to the first load step. Superscript $I = 1, 2, 3, 4$ denotes the outermost composite media, the matrix, the reaction zone and the fiber, respectively. Assuming that all layers are perfectly bonded at interfaces, the deformation compatibility requires that an isostrain condition exists in all layers giving rise to elastic stress increments, $\Delta \sigma_1^{(I),e}$ as illustrated in Fig. 1-3(c). These uniaxial stresses are compressive in the fiber and reaction zone thus making the layers as if compressed from their initial strain-free position to the common level A-A. However, the matrix layer and the composite media are elongated from their initial strain-free position to the same level A-A resulting in tensile stresses. The magnitude of the stresses depend on the values of CTE and elastic modulus of each layer. The difference between the strain level due to free thermal contraction for each layer and the strain at the constrained level A-A is termed the mechanical strain. The mechanical strain increments corresponding to each of the model layers, $\Delta \epsilon_1^{(I),me}$ are represented as shaded areas in Fig. 1-3(b) with positive values lying below and negative values above the level A-A.

If the effective stress in the matrix exceeded the yield limit of the matrix material at a particular temperature level, plastic deformation in the matrix is calculated using the deformation theory of plasticity [Heck69]. Stresses in all layers are redistributed such that equilibrium and compatibility conditions are satisfied. The new stress and strain increments in all layers due to matrix plasticity are denoted as $\Delta\sigma^{(l),mp}$ and $\Delta\epsilon^{(l),mp}$, respectively.

The important feature of the present model is the incorporation of the creep behavior of the matrix and the surrounding equivalent composite media into the stress analysis. This concept can also be explained by the four-bar representation shown in Fig. 1-3. The stresses induced in the matrix and the composite media due to temperature change, ΔT_1 will produce a relative constraint-free creep strain increment, $\Delta\epsilon_1^{(l),cr}$ in the respective layer over the proceeding time duration, Δt_1 (see Fig. 1-3(d)). The existence of non-creeping phases (the reaction zone and the fiber) and perfect bonding at layer interfaces will restrain the creep deformation in both the matrix and the equivalent composite media, resulting in stress redistribution in all layers. These creep-related stress increments are denoted as $\sigma_1^{(l),mc}$ (see Fig. 1-3(e)). The net stress developed for the first load step is taken as the summation of the stress increments, $\Delta\sigma^{(l),c}$ or $\Delta\sigma^{(l),mp}$, generated by restriction imposed on free thermal contraction of each layer, and the stress increments, $\Delta\sigma^{(l),mc}$, induced by constrained creep deformation of the matrix and the equivalent composite media. Since the creep stress increments in the matrix and equivalent composite media are compressive, the net stress increments in these layers are always less than that calculated for the elastic-plastic case.

The concepts discussed above are identical for subsequent load steps. For the k^{th} load step, elastic calculation is first performed to obtain the elastic stress increments, $\Delta\sigma_k^{(i),e}$ corresponding to the current temperature change, ΔT_k . The elastic stress increments are then added to the total stress level in the matrix up to the last load step and the value is compared with the yield limit at the current temperature. If the yield criterion is satisfied, the plasticity analysis is executed and the stresses in all phases are redistributed resulting in the stress increments, $\Delta\sigma_k^{(i),mp}$. The total stresses acting in the matrix and the equivalent composite media may cause constraint-free creep deformation during the time duration, Δt_k . However, restriction imposed on the creep deformation by the elastic reaction zone and fiber, and perfect bonding at layer interfaces result in stress increments, $\Delta\sigma_k^{(i),mc}$ in all layers. At the end of the k^{th} load step, the total stress is the sum of the accumulated stresses from all previous load steps, stress increment due to temperature change and stress increment due to creep flow restriction imposed in the current load step, i.e.

$$\sigma_k^{(i)} = \sigma_{k-1}^{(i)} + \Delta\sigma_k^{(i),mp} + \Delta\sigma_k^{(i),mc} \quad (1.1)$$

The simultaneous evolution of the corresponding radial and hoop stress components in the complex stress state of MMC are analogous to the axial component described above. However, the relative magnitudes of these transverse stresses are also influenced by the Poisson's ratio effects in all the phases.

1.3 Formulations

A cylindrical coordinate system with the radial, hoop, and axial coordinates denoted as r , θ , and z , respectively is shown in Fig. 1-1(a). Due to the axisymmetry of the model, the shear stress and shear strain components are zero. Neglecting body forces, the equilibrium equations for the i^{th} layer can be written as:

$$\frac{\partial \sigma_{rr}^{(i)}}{\partial r} + \frac{\sigma_{rr}^{(i)} - \sigma_{\theta\theta}^{(i)}}{r} = 0, \quad \frac{\partial \sigma_{zz}^{(i)}}{\partial z} = 0 \quad (1.2)$$

It is assumed that the total strain in i^{th} layer can be decomposed into elastic, $\epsilon^{(i),e}$, thermal, $\epsilon^{(i),th}$, plastic, $\epsilon^{(i),p}$, and creep, $\epsilon^{(i),cr}$, components such that:

$$\begin{aligned} \epsilon_{rr}^{(i)} &= \epsilon_{rr}^{(i),e} + \epsilon_{rr}^{(i),th} + \epsilon_{rr}^{(i),p} + \epsilon_{rr}^{(i),cr} \\ \epsilon_{\theta\theta}^{(i)} &= \epsilon_{\theta\theta}^{(i),e} + \epsilon_{\theta\theta}^{(i),th} + \epsilon_{\theta\theta}^{(i),p} + \epsilon_{\theta\theta}^{(i),cr} \\ \epsilon_{zz}^{(i)} &= \epsilon_{zz}^{(i),e} + \epsilon_{zz}^{(i),th} + \epsilon_{zz}^{(i),p} + \epsilon_{zz}^{(i),cr} \end{aligned} \quad (1.3)$$

The constitutive relations for isotropic material behavior in generalized plane strain conditions can be written as:

$$\sigma_{rr}^{(i)} = K^{(i)} \left[(1 - \nu^{(i)}) (\epsilon_{rr}^{(i)} - \epsilon_{rr}^{(i),p} - \epsilon_{rr}^{(i),cr}) + \nu^{(i)} (\epsilon_{\theta\theta}^{(i)} - \epsilon_{\theta\theta}^{(i),p} - \epsilon_{\theta\theta}^{(i),cr}) \right. \\ \left. + \nu^{(i)} (\epsilon_{zz}^{(i)} - \epsilon_{zz}^{(i),p} - \epsilon_{zz}^{(i),cr}) - (1 + \nu^{(i)}) \epsilon^{(i),th} \right]$$

$$\sigma_{\theta\theta}^{(i)} = K^{(i)} \left[(1 - \nu^{(i)}) (\epsilon_{\theta\theta}^{(i)} - \epsilon_{\theta\theta}^{(i),p} - \epsilon_{\theta\theta}^{(i),cr}) + \nu^{(i)} (\epsilon_{zz}^{(i)} - \epsilon_{zz}^{(i),p} - \epsilon_{zz}^{(i),cr}) \right. \\ \left. + \nu^{(i)} (\epsilon_{rr}^{(i)} - \epsilon_{rr}^{(i),p} - \epsilon_{rr}^{(i),cr}) - (1 + \nu^{(i)}) \epsilon^{(i),th} \right] \quad (1.4)$$

$$\sigma_{zz}^{(i)} = K^{(i)} \left[(1 - \nu^{(i)}) (\epsilon_{zz}^{(i)} - \epsilon_{zz}^{(i),p} - \epsilon_{zz}^{(i),cr}) + \nu^{(i)} (\epsilon_{rr}^{(i)} - \epsilon_{rr}^{(i),p} - \epsilon_{rr}^{(i),cr}) \right. \\ \left. + \nu^{(i)} (\epsilon_{\theta\theta}^{(i)} - \epsilon_{\theta\theta}^{(i),p} - \epsilon_{\theta\theta}^{(i),cr}) - (1 + \nu^{(i)}) \epsilon^{(i),th} \right]$$

where the constant $K^{(i)}$ is defined as:

$$K^{(i)} = \frac{E^{(i)}}{(1 + \nu^{(i)})(1 - 2\nu^{(i)})} \quad (1.5)$$

and $E^{(i)}$ is the elastic modulus, $\nu^{(i)}$ is the Poisson's ratio, $\epsilon_{rr}^{(i),p}$, $\epsilon_{\theta\theta}^{(i),p}$ and $\epsilon_{zz}^{(i),p}$ are the radial, hoop and axial components, respectively of the plastic strain, while $\epsilon_{rr}^{(i),cr}$, $\epsilon_{\theta\theta}^{(i),cr}$ and $\epsilon_{zz}^{(i),cr}$ are the radial, hoop and axial components, respectively of the creep strain of the constituent phases. The thermal strain, $\epsilon^{(i),th}$, is defined as:

$$\epsilon^{(i),th} = \int_{T_0}^T \alpha^{(i)} dT \quad (1.6)$$

where $\alpha^{(i)}$ is the CTE of Ψ layer, T_0 is the reference temperature and T is the current temperature.

Due to the axial symmetry of the model configuration, the radial and axial displacements in each layer can be expressed as functions of r and z , respectively while the hoop displacement component is zero, i.e.:

$$u_r^{(i)} = u^{(i)}(r) \quad , \quad u_\theta^{(i)} = 0 \quad , \quad u_z^{(i)} = w^{(i)}(z) \quad (1.7)$$

The non-zero strain-displacement relations could then be obtained using the displacement field which, when used in the constitutive relations, eqs. (1.4), would result in the governing equations for elastic-plastic-creep behavior of MMC as follows:

$$r^2 \frac{d^2 u^{(i)}}{dr^2} + r \frac{du^{(i)}}{dr} - u^{(i)} = \Phi^{(i)}(r) \quad , \quad \frac{d^2 w^{(i)}}{dz^2} = 0 \quad (1.8)$$

where $\Phi^{(i)}(r)$ is defined as:

$$\begin{aligned} \Phi^{(i)}(r) = r \left(\frac{1 - 2\nu^{(i)}}{1 - \nu^{(i)}} (\epsilon_{rr}^{(i),p} + \epsilon_{rr}^{(i),cr}) + r \frac{d}{dr} (\epsilon_{rr}^{(i),p} + \epsilon_{rr}^{(i),cr}) - \frac{1 - 2\nu^{(i)}}{1 - \nu^{(i)}} (\epsilon_{\theta\theta}^{(i),p} + \epsilon_{\theta\theta}^{(i),cr}) \right. \\ \left. + r \frac{\nu^{(i)}}{1 - \nu^{(i)}} \frac{d}{dr} (\epsilon_{\theta\theta}^{(i),p} + \epsilon_{\theta\theta}^{(i),cr}) + r \frac{\nu^{(i)}}{1 - \nu^{(i)}} \frac{d}{dr} (\epsilon_{zz}^{(i),p} + \epsilon_{zz}^{(i),cr}) \right) \end{aligned} \quad (1.9)$$

It is noted that $\Phi^{(i)}(r)$ consists of plastic strain terms pertaining to the matrix and creep strain terms pertaining to both the matrix and the outermost composite media. Consequently, for a purely elastic loading, the function, $\Phi^{(i)}(r)$ is reduced to zero. The form of $\Phi^{(i)}(r)$ used in this analysis will be discussed in detail in the creep analysis part of this section.

The boundary conditions for the present study under the assumption that no external applied loading exist, are specified as follows:

- (a) The continuity requires that both radial displacements and stresses at all layer interfaces be continuous.
- (b) Since there is no external radial load at the outermost surface, therefore:

$$\text{at } r = r_1, \sigma_{rr}^{(1)} = 0 \quad (1.10)$$

- (c) In the absence of external axial load, the axial forces in each layer due to thermal loading are equilibrated in the average sense, i.e.:

$$\int_0^{r_4} \sigma_{zz}^{(4)} r dr + \int_{r_4}^{r_3} \sigma_{zz}^{(3)} r dr + \int_{r_3}^{r_2} \sigma_{zz}^{(2)} r dr + \int_{r_2}^{r_1} \sigma_{zz}^{(1)} r dr = 0 \quad (1.11)$$

In addition, under the assumption of perfect bonding at layer interfaces, the isostrain condition is applied to the total strains for all layers.

1.3.1 Elastic-Plastic Analysis

As discussed above, the cooling and heating paths are discretized into load steps each of which consists of a temperature increment, ΔT followed by a time increment, Δt . The analysis begins with a purely elastic formulation due to the temperature increment, so that the function $\Phi^{(i)}(r)$ diminishes and eq. (1.8) is reduced to:

$$r^2 \frac{d^2 u^{(i)}}{dr^2} + r \frac{du^{(i)}}{dr} - u^{(i)} = 0 \quad , \quad \frac{d^2 w^{(i)}}{dz^2} = 0 \quad (1.12)$$

The above homogeneous equations have the following general solutions for the radial and axial displacement, respectively:

$$u^{(i)} = A_i r + \frac{B_i}{r} \quad , \quad w^{(i)} = L_i z + P_i \quad (1.13)$$

where A_i , B_i , L_i and P_i are unknown constants.

Since the displacement is finite at the center of the fiber, where $r = 0$, i.e. $|u^{(4)}(0)| < \infty$, thus $B_4 = 0$. It is also noted that P_i in the above equations account for rigid body motion in axial direction, thus P_i can be set to zero without loss of generality. In addition, application of the boundary conditions for axial displacement components results in:

$$L_1 = L_2 = L_3 = L_4 = L \quad (1.14)$$

The elastic strain field can now be expressed as:

$$\epsilon_{rr}^{(i),e} = A_i - \frac{B_i}{r^2}, \quad \epsilon_{\theta\theta}^{(i),e} = A_i + \frac{B_i}{r^2}, \quad \epsilon_{zz}^{(i),e} = L \quad (1.15)$$

and the corresponding stress field for the elastic case are given as:

$$\begin{aligned} \sigma_{rr}^{(i),e} &= K^{(i)} \left[A_i - (1 - 2\nu^{(i)}) \frac{B_i}{r^2} + \nu^{(i)} L - (1 + \nu^{(i)}) \epsilon^{(i),th} \right] \\ \sigma_{\theta\theta}^{(i),e} &= K^{(i)} \left[A_i + (1 - 2\nu^{(i)}) \frac{B_i}{r^2} + \nu^{(i)} L - (1 + \nu^{(i)}) \epsilon^{(i),th} \right] \\ \sigma_{zz}^{(i),e} &= K^{(i)} \left[2\nu^{(i)} A_i + (1 - \nu^{(i)}) L - (1 + \nu^{(i)}) \epsilon^{(i),th} \right] \end{aligned} \quad (1.16)$$

The unknown constants in eqs. (1.13) ~ (1.16) are determined by the boundary conditions. Applying these conditions to eqs. (1.13) and (1.16) results in a set of eight simultaneous equations which should be solved for the determination of the constants $A_1 \sim A_4$, $B_1 \sim B_3$ and L . These equations can be arranged in the following matrix form:

$$\mathbf{A} \mathbf{c} = \mathbf{b} \quad (1.17)$$

where \mathbf{A} is an 8×8 matrix termed the stiffness matrix consisting of model geometry and mechanical properties of all constituents of the composite, \mathbf{b} is the thermal loading vector

and \mathbf{c} is the vector of unknown constants. Once the unknown vector \mathbf{c} is solved from eq. (1.17), the elastic stress and strain states in the composite are then established.

The thermal stresses developed in the matrix during cool down may be high enough to initiate plastic yielding in the monolithic matrix material. Matrix plasticity is assumed to be a time-independent process and its effect can be treated separately from the time-dependent creep response of the matrix material. The governing equation for the elastic-plastic deformation of the composite is then given by eqs. (1.8) but without the creep strain terms in the loading function, $\Phi^{(i)}(\mathbf{r})$ given by eq. (1.9). One solution approach requires the knowledge of plastic strain distribution across the matrix layer. The assumption on this distribution will dictate the form and order of the displacement field in each layer due to the occurrence of matrix plasticity. This approach results in a similar stiffness equation, eq. (1.17) but with a new load vector, \mathbf{f} , for thermal and matrix plasticity effects.

An alternate solution approach which modifies the stiffness matrix instead of the load vector of eq. (1.17), to account for strain hardening of the matrix material is employed in the present analysis. This approach utilizes the deformation theory of plasticity in conjunction with the von Mises yield criterion and the isotropic hardening rule. Matrix yielding commences when the effective stress, $\bar{\sigma}$ is equal to the temperature-dependent yield limit of the matrix material, $\sigma_{ys}(T)$. Here, $\bar{\sigma}$ is defined as:

$$\bar{\sigma} = \frac{1}{\sqrt{2}} \left[(\sigma_{rr} - \sigma_{\theta\theta})^2 + (\sigma_{\theta\theta} - \sigma_{zz})^2 + (\sigma_{zz} - \sigma_{rr})^2 \right]^{\frac{1}{2}} \quad (1.18)$$

The constitutive relations for total strain increment (elastic plus plastic) are employed based on the work of Hecker [Heck69, Heck70], and are given as:

$$\begin{aligned} d\epsilon_{rr} &= \frac{1}{H(T)} [d\sigma_{rr} - \eta(d\sigma_{\theta\theta} + d\sigma_{zz})] \\ d\epsilon_{\theta\theta} &= \frac{1}{H(T)} [d\sigma_{\theta\theta} - \eta(d\sigma_{rr} + d\sigma_{zz})] \end{aligned} \quad (1.19)$$

$$d\epsilon_{zz} = \frac{1}{H(T)} [d\sigma_{zz} - \eta(d\sigma_{rr} + d\sigma_{\theta\theta})]$$

where $H(T)$ is the plastic modulus of the uniaxial tensile stress-strain curve of the matrix and η is the effective Poisson's ratio which is defined for a small increment of effective total strain, $d\bar{\epsilon}$, as:

$$\eta = 0.5 - (0.5 - \nu) \frac{H(T)}{E(T)} \quad (1.20)$$

The effective total strain increment is defined as:

$$d\bar{\epsilon} = \frac{\sqrt{2}}{2(1+\eta)} \left[(d\epsilon_{rr} - d\epsilon_{\theta\theta})^2 + (d\epsilon_{\theta\theta} - d\epsilon_{zz})^2 + (d\epsilon_{zz} - d\epsilon_{rr})^2 \right]^{\frac{1}{2}} \quad (1.21)$$

It is assumed that the effective stress-strain curve of the matrix material in the region the yield limit can be represented by:

$$\bar{\sigma} = k(T) \bar{\epsilon}^{\frac{1}{n(T)}} \quad (1.22)$$

where $k(T)$ and $n(T)$ are material parameters varying with temperature T . The slope of the curve represented by this equation is equal to the plastic modulus, $H(T)$, i.e.:

$$\frac{d\bar{\sigma}}{d\bar{\epsilon}} = \frac{\bar{\sigma}}{n(T)\bar{\epsilon}} = H(T) \quad (1.23)$$

If plastic deformation occurs in the matrix, the stresses in all the four layers must be redistributed such that equilibrium and compatibility conditions are always satisfied. The stiffness matrix in eq. (1.19) is modified by substituting the plastic modulus, $H(T)$ and the effective Poisson's ratio, η for the elastic modulus, $E(T)$ and Poisson's ratio, ν , respectively. Consequently, the stiffness equation which accounts for matrix plasticity can be written as:

$$\mathbf{M} \mathbf{c} = \mathbf{b} \quad (1.24)$$

It is noted that in elastic region $H(T)$ is equivalent to $E(T)$ and η reduces to ν , so that eq. (1.19) resembles the Hooke's law. Since the equilibrium equations, the compatibility equations and the boundary conditions are independent of the state of the material, therefore, the plasticity formulation is identical to the elastic case with the modified

stiffness matrix, \mathbf{M} in eq. (1.24). The resulting stress components, $\Delta\sigma_{ij}^{(i).mp}$ and strain components, $\Delta\epsilon_{ij}^{(i).mp}$ due to matrix yielding are given by eqs. (1.16) and (1.15), respectively.

1.3.2 Creep Analysis

The effect of creep deformation in both the monolithic matrix and the surrounding effective composite media on the residual stress and strain fields in the composite is now considered. It is assumed that the creep behavior of both layers in the primary and secondary stages of creep can be represented by the Bailey-Norton law as:

$$\epsilon^{cr} = B \sigma^m t^n \quad (1.25)$$

where ϵ^{cr} is the creep strain occurring in the material under uniaxial stress, σ , over a time duration t . The superscript i is omitted in the following derivation for convenience. Parameters B , m and n are material parameters. Based on the fit of experimental data, parameters B and m are generally taken to be functions of temperature while n is viewed as temperature-independent (e.g. [Krau90, Lema90]). Here, B is assumed to follow a general expression of Arrhenius-type:

$$B = b_0 \exp\left(-\frac{Q}{RT}\right) \quad (1.26)$$

where b_0 is a constant. Q is the activation energy for creep. R is the gas constant and T is temperature in Kelvin scale. Extension of uniaxial case to multiaxial case is made by introducing effective quantities such that:

$$\bar{\epsilon}^{cr} = B \bar{\sigma}^{m(T)} t^n \quad (1.27)$$

where $\bar{\sigma}$ is the effective stress defined in eq. (1.18).

The path-dependent creep process is incorporated into the model through the use of the flow rate which describes the creep strain components, ϵ_{ij}^{cr} , in terms of the stress deviator tensor, S_{ij} , i.e.:

$$\dot{\epsilon}_{ij}^{cr} = \lambda S_{ij} \quad (1.28)$$

The use of the deviatoric stress components, S_{ij} in the above equation ensures that creep deformation is independent of the hydrostatic state of stress as have been observed experimentally. In this equation, the proportionality factor, λ , is defined as:

$$\lambda = \frac{3}{2 \bar{\sigma}} \frac{d \bar{\epsilon}^{cr}}{dt} = n B \bar{\sigma}^{m(T)} t^{n-1} \quad (1.29)$$

The strain history prediction in this analysis follows the "strain hardening" formulation in which the creep strain rate in a variable stress situation depends on the stress, strain and temperature. Eliminating time from eq.(1.29) with the aid of eq.(1.25), the flow rule can

be rewritten as:

$$\dot{\epsilon}_{ij}^{cr} = \frac{3}{2} n B \frac{1}{n} \frac{m}{\bar{\sigma}} \left(\bar{\epsilon}^{cr} \right)^{\frac{n-1}{n}} \frac{S_{ij}}{\bar{\sigma}} = \frac{3 F}{2 \bar{\sigma}} S_{ij} \quad (1.30)$$

where F is a scalar defined as:

$$F = n B \frac{1}{n} \frac{m}{\bar{\sigma}} \left(\bar{\epsilon}^{cr} \right)^{\frac{n-1}{n}} \quad (1.31)$$

It can be shown using eqs. (1.27) and (1.29) that:

$$\bar{\epsilon}^{cr} = \left(\frac{2}{3} \dot{\epsilon}_{ij}^{cr} \dot{\epsilon}_{ij}^{cr} \right)^{\frac{1}{2}} = F \quad (1.32)$$

thus, the flow rule can now be expressed in differential form as:

$$d \epsilon_{ij}^{cr} = \frac{3}{2} \frac{d \bar{\epsilon}^{cr}}{\bar{\sigma}} S_{ij} \quad (1.33)$$

This equation can be written explicitly for the three components of the constraint-free creep strain increments as:

$$\Delta \epsilon_{rr}^{cr} = \frac{\Delta \bar{\epsilon}^{cr}}{2 \bar{\sigma}} (2 \sigma_{rr} - \sigma_{\theta\theta} - \sigma_{zz})$$

$$\Delta \epsilon_{\theta\theta}^{cr} = \frac{\Delta \bar{\epsilon}^{cr}}{2 \bar{\sigma}} (2 \sigma_{\theta\theta} - \sigma_{rr} - \sigma_{zz}) \quad (1.34)$$

$$\Delta \epsilon_{zz}^{cr} = \frac{\Delta \bar{\epsilon}^{cr}}{2 \bar{\sigma}} (2 \sigma_{zz} - \sigma_{rr} - \sigma_{\theta\theta})$$

where the effective creep strain increment, $\Delta \bar{\epsilon}^{cr}$, occurring over the time increment, Δt is approximated from uniaxial creep behavior given by eq. (1.27) as:

$$\Delta \bar{\epsilon}^{cr} = B \bar{\sigma}^{m(T)} \Delta t^n \quad (1.35)$$

The axisymmetric creep strain components are represented by the effective value defined as:

$$\bar{\epsilon}^{cr} = \frac{\sqrt{2}}{3} \left[\left(\epsilon_{rr}^{cr} - \epsilon_{\theta\theta}^{cr} \right)^2 + \left(\epsilon_{\theta\theta}^{cr} - \epsilon_{zz}^{cr} \right)^2 + \left(\epsilon_{zz}^{cr} - \epsilon_{rr}^{cr} \right)^2 \right]^{\frac{1}{2}} \quad (1.36)$$

Constraint-free creep deformation in the matrix and the composite media, as described above, is coupled with the existence of perfect bonding at layer interfaces and the relative inextensibility of the reaction zone and the fiber. Consideration of creep behavior of the composite, therefore, results in inhomogeneous Euler equation as described by eq. (1.8) but without the plastic strain terms in the loading function, $\Phi^{(i)}(r)$ of eq. (1.9). The solution for the displacement field is obtained by assuming that the radial variation of the constraint-free creep strain increments in the matrix and the outermost equivalent composite media can each be represented as a third order polynomial as follows:

$$\begin{aligned}\Delta \epsilon_{rr}^{(i),cr} &= a_1^{(i)} + a_2^{(i)} r + a_3^{(i)} r^2 + a_4^{(i)} r^3 \\ \Delta \epsilon_{\theta\theta}^{(i),cr} &= b_1^{(i)} + b_2^{(i)} r + b_3^{(i)} r^2 + b_4^{(i)} r^3 \\ \Delta \epsilon_{zz}^{(i),cr} &= c_1^{(i)} + c_2^{(i)} r + c_3^{(i)} r^2 + c_4^{(i)} r^3\end{aligned}\tag{1.37}$$

where the coefficients $a_1^{(i)} \sim a_4^{(i)}$, $b_1^{(i)} \sim b_4^{(i)}$, and $c_1^{(i)} \sim c_4^{(i)}$ ($i = 1, 2$) are obtained from least-squared curve fit procedures. This assumption dictates the form and order of the particular solution for the displacement field in the creeping layers. Upon substitution of eqs. (1.37) into eq. (1.9), the governing differential equations for the deformation of the composite in the case of elastic-plastic-creep can be written as:

$$r^2 \frac{d^2 u^{(i)}}{dr^2} + r \frac{du^{(i)}}{dr} - u^{(i)} = \phi_1^{(i)} r - \phi_2^{(i)} r^2 + \phi_3^{(i)} r^3 + \phi_4^{(i)} r^4, \quad \frac{dw^{(i)}}{dz} = 0 \quad (1.38)$$

where the coefficients, $\phi_1^{(i)} \sim \phi_4^{(i)}$ consists of material constants for the i^{th} layer. For the elastic fiber and interphase zone, these coefficients are zero. The solution of the above equations which corresponds to the displacement field with creep deformation in the matrix and the equivalent composite media are obtained as:

$$u^{(i),mc} = A_i r + \frac{B_i}{r} + \frac{\phi_1^{(i)}}{2} \ln r + \frac{\phi_2^{(i)}}{3} r^2 + \frac{\phi_3^{(i)}}{8} r^3 + \frac{\phi_4^{(i)}}{15} r^4, \quad w^{(i)} = L z \quad (1.39)$$

The stress field in the composite for the elastic-plastic-creep case accumulate incrementally throughout the cooling process. The expressions for this stress field are obtained with the aid of the strain-displacement relations and the above displacement field as follows:

$$\begin{aligned} \sigma_{rr}^{(i),mc} = K^{(i)} & \left[A_i - (1 - 2\nu^{(i)}) \frac{B_i}{r^2} + \nu^{(i)} L - (1 + \nu^{(i)}) \epsilon^{(i),th} \right. \\ & + (1 - \nu^{(i)}) \frac{\phi_1^{(i)}}{2} + \frac{\phi_1^{(i)}}{2} \ln r + (2 - \nu^{(i)}) \frac{\phi_2^{(i)}}{3} r + (3 - 2\nu^{(i)}) \frac{\phi_3^{(i)}}{8} r^2 \\ & \left. + (4 - 3\nu^{(i)}) \frac{\phi_4^{(i)}}{15} r^3 - (1 - \nu^{(i)}) \epsilon_{rr}^{(i),mc} - \nu^{(i)} \epsilon_{\theta\theta}^{(i),mc} - \nu^{(i)} \epsilon_{zz}^{(i),mc} \right] \end{aligned}$$

$$\begin{aligned}
\sigma_{\theta\theta}^{(i),mc} = K^{(i)} & \left[A_i + (1 - 2\nu^{(i)}) \frac{B_1}{r^2} + \nu^{(i)} L - (1 + \nu^{(i)}) \epsilon^{(i),th} \right. \\
& + \nu^{(i)} \frac{\phi_1^{(i)}}{r} + \frac{\phi_1^{(i)}}{2} \ln r + (1 + \nu^{(i)}) \frac{\phi_2^{(i)}}{3} r + (1 + 2\nu^{(i)}) \frac{\phi_3^{(i)}}{8} r^2 \\
& \left. + (1 + 3\nu^{(i)}) \frac{\phi_4^{(i)}}{15} r^3 - (1 - \nu^{(i)}) \epsilon_{\theta\theta}^{(i),mc} - \nu^{(i)} \epsilon_{rr}^{(i),mc} - \nu^{(i)} \epsilon_{zz}^{(i),mc} \right]
\end{aligned} \tag{1.40}$$

$$\begin{aligned}
\sigma_{zz}^{(i),mc} = K^{(i)} & \left[2\nu^{(i)} A_i + (1 - \nu^{(i)}) L - (1 + \nu^{(i)}) \epsilon^{(i),th} + \nu^{(i)} \frac{\phi_1^{(i)}}{2} + \nu^{(i)} \phi_1^{(i)} \ln r + \nu^{(i)} \phi_2^{(i)} r \right. \\
& \left. + \nu^{(i)} \frac{\phi_3^{(i)}}{2} r^2 + \nu^{(i)} \frac{\phi_4^{(i)}}{3} r^3 - (1 - \nu^{(i)}) \epsilon_{zz}^{(i),mc} - \nu^{(i)} \epsilon_{rr}^{(i),mc} - \nu^{(i)} \epsilon_{\theta\theta}^{(i),mc} \right]
\end{aligned}$$

Applying the same boundary conditions specified earlier results in a similar set of eight simultaneous equations as arranged in eq. (1.17), but with additional terms in the load vector, **d** resulting from creep contributions, i.e.:

$$\mathbf{A} \mathbf{c} = \mathbf{d} \tag{1.41}$$

This equation should be solved for the unknown constants, $A_1 \sim A_4$, $B_1 \sim B_4$ and L appearing in the vector c .

1.4 Solution Procedures

The algorithm for the determination of thermal stresses in MMC is shown in Fig. 1.4. It initially reads the model geometry, cooling rate and temperature dependent material data from a tabular input file. Starting with an initial stress and strain free states at consolidation temperature, the first load step is initiated which consists of a negative temperature increment followed by a time step. The stiffness equation, eq. (1.17) is solved for elastic stress increments induced over the temperature drop. A yield limit is determined for the present temperature and compared with the effective stress in the matrix. If the effective stress is less than the yield limit, the procedure proceeds to calculate creep strain increments for the matrix and the outermost equivalent composite media. Otherwise, plasticity calculations are executed in which the plastic modulus, $H(T)$, and the effective Poisson's ratio, η , are determined using the current values of the effective stress and strain in eq. (1.23) and eq. (1.20), respectively. They are substituted for the elastic modulus, $E(T)$, and the Poisson's ratio, ν , respectively in the stiffness matrix of eq. (1.17). These equations are then solved for the new stress and strain increments in all layers due to matrix plasticity and the latter is compared with the previous value. If the difference is less than a prescribed value, plasticity calculations are

completed. Otherwise, new values for $H(T)$ and η are established and plasticity calculations are repeated until convergence of the incremental effective strain is achieved.

The procedure then performs the creep analysis of the composite over the proceeding time increment. During the first Δt step, the constraint-free creep strain increments for the matrix and the composite media are initially calculated using eqs. (1.34) with the previously calculated stress acting in the respective layers. The distribution of each component of the creep strain increment across the matrix layer and the equivalent composite media are fitted to polynomials as described by eqs. (1.37). The creep effect is accommodated in the load vector, \mathbf{d} of eq. (1.41) and the resulting stiffness equation. is solved for the constrained deformation of all layers due to creep. Since temperature decreases and time proceeds simultaneously during the consolidation stage of the composite, employing the average of the stress increments from elastic-plastic calculation and the creep calculation should provide a better estimate of the constrained creep deformation. This is utilized in the second estimation of the creep strain increments, and the resulting stress increments due to constrained creep deformation in the matrix and the equivalent composite media are used in the next iteration. Convergence of the iterative process is achieved when the difference between the incremental creep strain in the matrix from the last two successive iterations are within a small prescribed value.

The stress and strain increments from both the elastic-plastic and the creep calculations are then summed to represent the total thermal stress and strain at the beginning of the next load step.

For any subsequent load step, the elastic stress increments occurring over the

current temperature increment is summed with the previously accumulated thermal stress until the last load step. This (effective) stress is then used to determine the occurrence of plastic flow in the matrix at the current temperature. The sum of the stress increments from the elastic-plastic calculations and the previously accumulated thermal stress is used to provide the first estimate of the constraint-free creep strain increment in the matrix and the equivalent composite media. Equation (1.41) is again solved to provide the constrained creep deformation in these layers and the resulting stress increments in all layers due to creep. The average of the resulting stress increments due to creep and the stress increments from elastic-plastic calculations are summed with the previously accumulated stress for the next estimate of the constraint-free creep strain. The iteration process continues until convergence is achieved.

The accumulated stress and strain values at the current temperature are written to output files. The next load step is then incremented and the process continues until room temperature is reached.

The history of the accumulated creep strain in both the matrix and the equivalent composite media, as mentioned before is based on the strain hardening creep formulation in which the creep strain rate is assumed to be a function of stress, strain and temperature. This history is schematically illustrated in Fig. 1.5 in terms of effective stress and strain values for the first two load steps. During the initial load step from consolidation temperature, constraint-free creep strain increment, $\Delta \bar{\epsilon}_1^{\text{cf}}$, occurring over time increment Δt_1 , is estimated using eqs. (1.33) - (1.35) and indicated as open circle (point 1) on the creep curve corresponding to load condition $(\bar{\sigma}_1, T_1)$. Physical constraints imposed by the

existence of perfectly bonded interfaces and non-creeping phases modify the magnitude of $\Delta\bar{\epsilon}_1^{cr}$ to a lower value $\Delta\bar{\epsilon}_1^c$ (point 2). This latter strain must fall on the creep curve corresponding to current stress and temperature levels. This would then lead to the determination of point 3. In the second load step, as the stress increases to $\bar{\sigma}_2$, the end response of the load step, following the strain hardening concept, is shifted horizontally to point 4 which marks the onset of the creep flow of the unconstrained matrix and equivalent composite material along the creep curve corresponding to load condition $(\bar{\sigma}_2, T_2)$. Tracing this curve for the duration Δt_2 would define point 5. Again, this point under constrained deformation condition would be modified to point 7 along the path 5-6-7. The strain magnitude generated between the points 4 and 7 thus represents the actual $\Delta\bar{\epsilon}_2^{mc}$ occurring during the second load step. This path 4-7 must be shifted horizontally to have its starting position initiating at point 3. This would then generate the curve 3-8 for which point 8 marks the starting position for the third load step. The total creep strain accumulated in the matrix at the end of the second load step, $\bar{\epsilon}_2^{mc}$, is then the sum of $\Delta\bar{\epsilon}_1^{mc}$ and $\Delta\bar{\epsilon}_2^{mc}$. This procedure is repeated for all load steps between consolidation temperature and end temperature level.

The composite may be subjected to thermal fatigue in order to reduce the magnitude of the thermal residual stress induced during post-fabrication cool down. Throughout these processes, creep deformation is expected to progress.

1.5 Summary and Conclusions

In this section, a new micromechanical stress analysis approach has been proposed which considers time-dependent behavior of a continuous-fiber-reinforced MMC during post-fabrication cool down and subsequent thermal fatigue. A four-phase concentric cylinder model consisting of an embedded fiber and an interphase zone which behave elastically, while the matrix and the equivalent composite media may experience plasticity and creep was employed in the formulation. All the constituent phases of the composite model are assumed to be isotropic. The conceptual uniaxial four-bar model has illustrated that the deformation behavior of the composite can be isolated into time-independent and time-dependent deformation and treated separately for mathematical convenience. The former considers elastic-plastic deformation occurring over discrete temperature change, while the latter emphasizes creep response of the matrix and the equivalent composite media over the corresponding duration of time. Both effects are then combined at the end of each discrete load step. The tensile thermal stress induced in the matrix due to mismatches of the CTEs of the matrix and other constituents of the composite is lowered through the evolution of the compressive stress set-up in the matrix due to constrained creep deformation at elevated temperature. The occurrence of matrix plasticity is treated using the deformation theory of plasticity with total strain increment (elastic plus plastic) in conjunction with the von Mises yield criterion. Strain hardening characteristics of the matrix material are represented by the tangent modulus of the stress-strain curve beyond the initial yield point and the corresponding effective Poisson's ratio. Constraint-free

creep deformation of the matrix and the equivalent composite media is estimated using the Bailey-Norton law in the transient and steady-state stages of creep. An Arrhenius-type expression is used for the time-dependent creep coefficient of the creep law. Constrained creep deformation in the composite is calculated using the "stiffness" method with modified load vector resulting in stress redistribution in all layers due to creep. The creep strain history prediction followed the strain hardening formulation which assumed the creep strain rate to be dependent on stress, strain and temperature. The model has been used in a parametric study and the results will be discussed in the next section.

The present micromechanical analysis can be extended to predict the variation of stress and strain states in the fiber, the interphase zone and the matrix when subjected to thermo-mechanical loadings. External radial pressure and axial stress can be accommodated through the boundary conditions in eqs. (1.10) and (1.11), respectively. In addition, non-uniform temperature distribution across a layer can be specified by the temperature gradient through the right-hand side of the governing equation (1.8). This will result in additional terms in the load vector, **b** and **d** of eq. (1.17) and (1.41), respectively. Extension of the model to n-layers can be made with additional boundary conditions on the continuity of the radial displacements and radial stresses specified at each new interface. An additional pair of unknown constants and hence additional two new equations in the stiffness equation, eq. (1.41) are associated with each new layer.

1.6 References

- [Chri79] Christensen, R. M. and Lo, K. H., 1979. "Solutions for Effective Shear Properties in Three-Phase Sphere and Cylinder Models". J. The Mechanics and Physics of Solids, 27:315-330.
- [Gayd90] Gayda, J., Gabb, T. P. and Freed, A. D., 1990, "The Isothermal Fatigue Behavior of a Unidirectional SiC/Ti Composite and the Ti Alloy Matrix." in Fundamental Relationships Between Microstructure and Properties of Metal Matrix Composites, ed. by Liaw, P.K. and Gungor, M.N., The Mineral, Metal and Materials Society, Warrendale, PA:497-513.
- [Gund91] Gundel, D. B. and Wawner, F. E., 1991 "Interfacial Reaction Kinetics of Coated SiC Fibers with Various Titanium Alloys," Scripta Metallurgica et Materialia, 25:437-441.
- [Hash64] Hashin, Z. and Rosen, B. W., 1964, "The Elastic Moduli of Fiber-Reinforced Materials," J. Applied Mechanics, 31:223-232.
- [Heck69] Hecker, S. S., Hamilton, C. H. and Ebert, L. J., 1969, "Elastic-Plastic Analysis: A Simplified Approach," Metallurgica, 3:793-798.

- [Heck70] Hecker. S. S., Hamilton. C. H. and Ebert. L. J., 1970. "Elastoplastic Analysis of Residual Stresses and Axial Loadings in Composite Cylinders." J. Materials, JMLSA. 5.No.4:868-900.
- [Jans92] Jansson. S. and Leckie. F. A., 1992. "Reduction of Thermal Stresses in Continuous Fiber Reinforced Metal Matrix Composites With Interface Layers." J. Composite Materials, 26:1474-1486.
- [Jaya92] Jayaraman. K. and Reifsnider, K. L., 1992. "Residual Stresses in a Composite with Continuously Varying Young's Modulus in the Fiber/Matrix Interphase." J. Composite Materials, 26.No.6:771-791.
- [Krau80] Kraus. H., 1980. Creep Analysis, John Wiley and Sons, Inc., NY.
- [Lema90] Lemaitre. J. and Chaboche. L., 1990. Mechanics of Solid Materials (English Translation), Cambridge University Press, NY.
- [Mika85] Mikata. Y. and Taya. M., 1985, "Stress Field in a Coated Continuous Fiber Composite Subjected to Thermo-Mechanical Loadings." J. Composite Materials, 19:554-578.

- [Min81] Min. B. K., 1981, "A Plane Stress Formulation for Elastic-Plastic Deformation of Unidirectional Composites." J. The Mechanics and Physics of Solids, 29:327-352.
- [Min82] Min. B. K. and Crossman, F. W., 1982, "History-Dependent Thermo-mechanical Properties of Graphite/Aluminum Unidirectional Composites." in Composite Materials: Testing and Design (Sixth Conf), ASTM STP 787, ed. by Daniel, I. M., Am Soc for Testing and Materials, :371-392.
- [Min82] Min. B. K. and Crossman, F. W., 1982, "Analysis of Creep for Metal Matrix Composites." J. Composite Materials, 16:188-203.
- [Nair85] Nairn, J. A., 1985. Polymer Composites, 6:123-130.
- [Saig92] Saigal, A., Kupperman, D. S. and Majumdar, 1992, "Residual Strain in Titanium Matrix High-Temperature Composites," Mat. Sc. Engng., :59-66.
- [Theo85] Theocaris, P., 1985, "The Mesophase and its Influence on the Mechanical Behavior of Composites." Advances in Polymers Science, ed. by Kausch, H. H. and Zachmann, H. G., Springer-Verlag, Berlin, 66:149-187.

- [Uemu79] Uemura, M., Iyama, H. and Yamaguchi, Y., 1979, "Thermal Residual Stresses in Filament-Wound Carbon-Fiber-Reinforced Composites." J. Thermal Stresses, 2:393-412.
- [Yang89] Yang, J. M. and Jeng, S. M., 1989, "Interfacial Reactions in Titanium-Matrix Composites." J. Metals, Nov.:56-59.

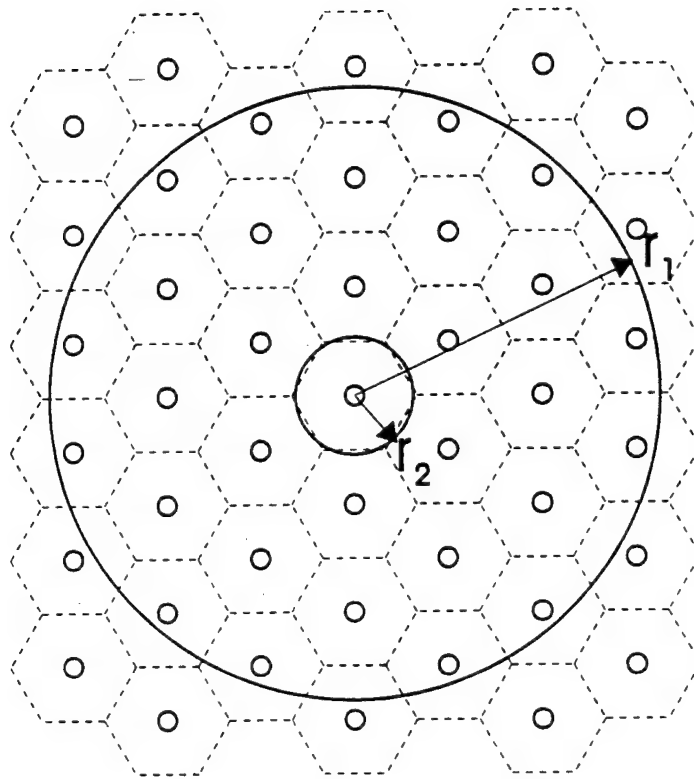


Fig. 1.1(a) Selected configuration of a unit cell with surrounding composite material.

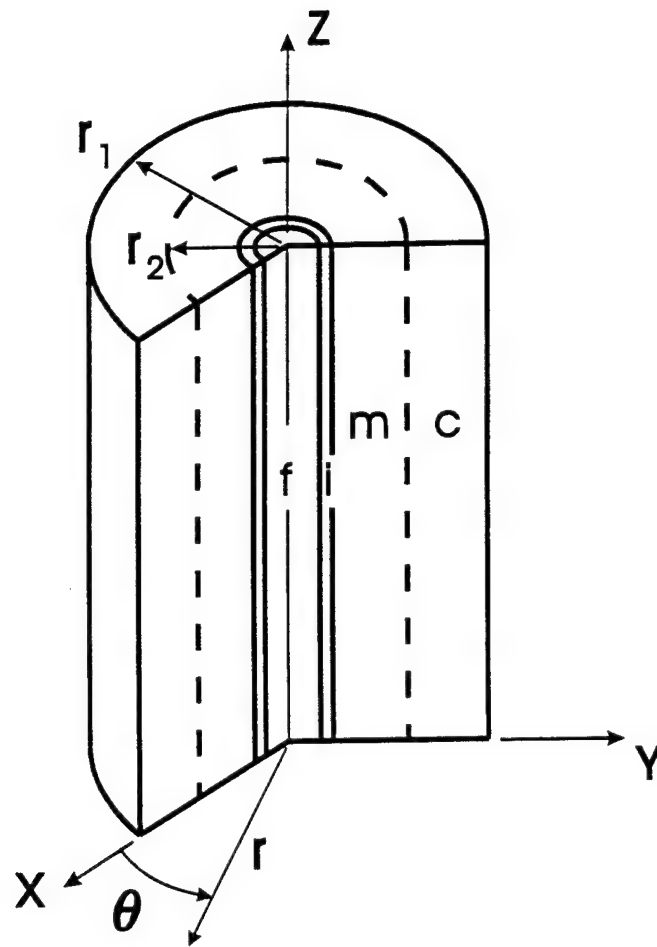


Fig. 1.1(b) Cut-out section of the four-phase model.

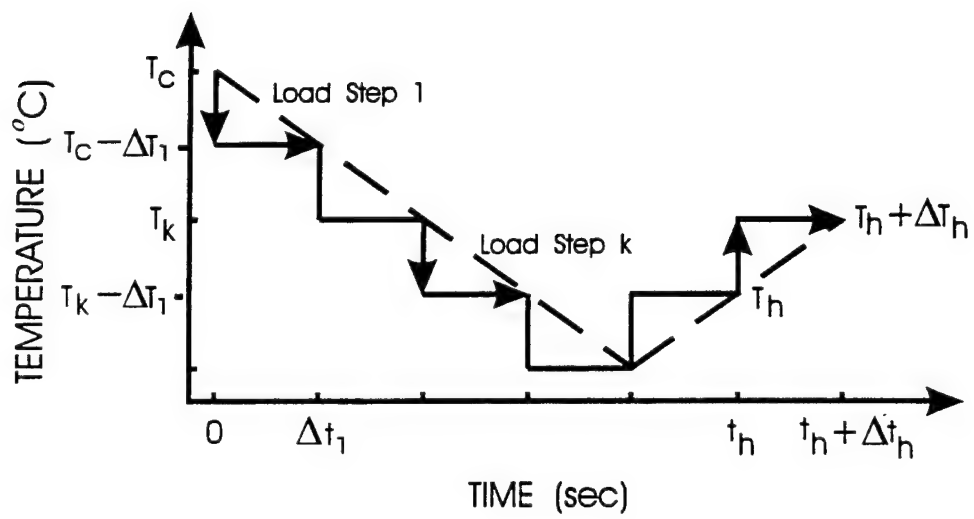


Fig. 1.2 Discretization of the cooling/heating path (no externally applied mechanical load).

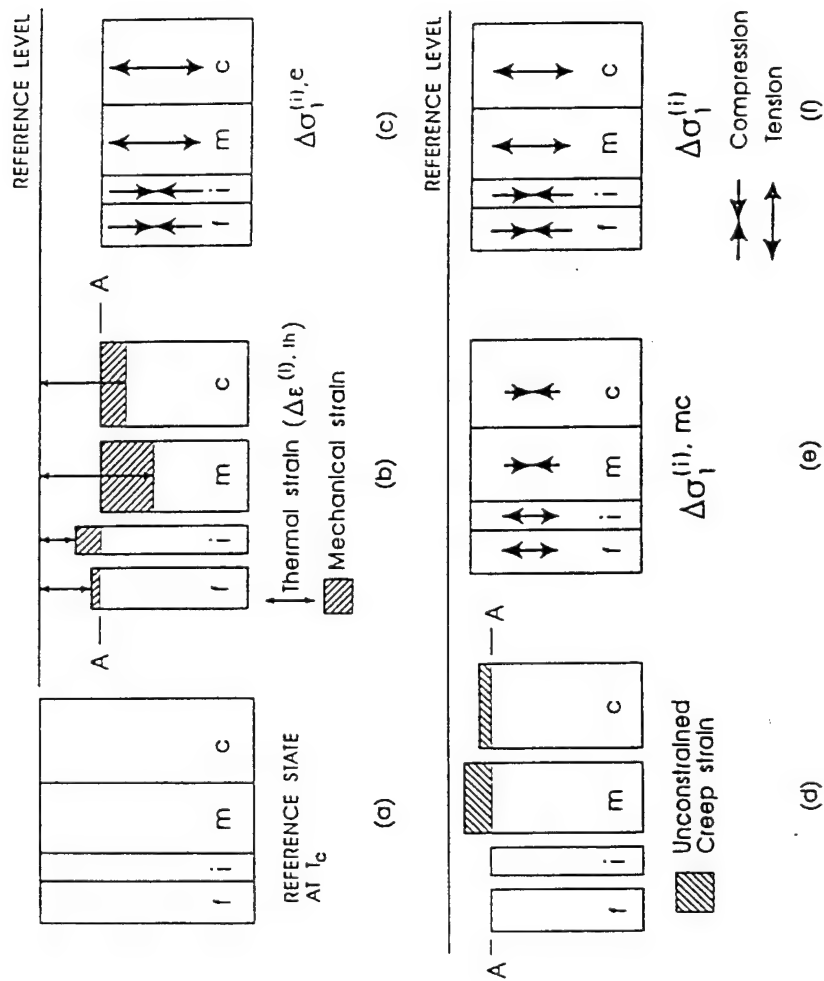


Fig. 1.3 (a) Reference state at consolidation. (b) Constraint-free thermal deformation. (c) Equilibrium conditions due to boundary constraints. (d) Constraint-free creep deformation. (e) Equilibrium conditions due to boundary constraints. (f) Final equilibrium conditions at the end of the first temperature-time step loading (sum of conditions at (c) and (e)).

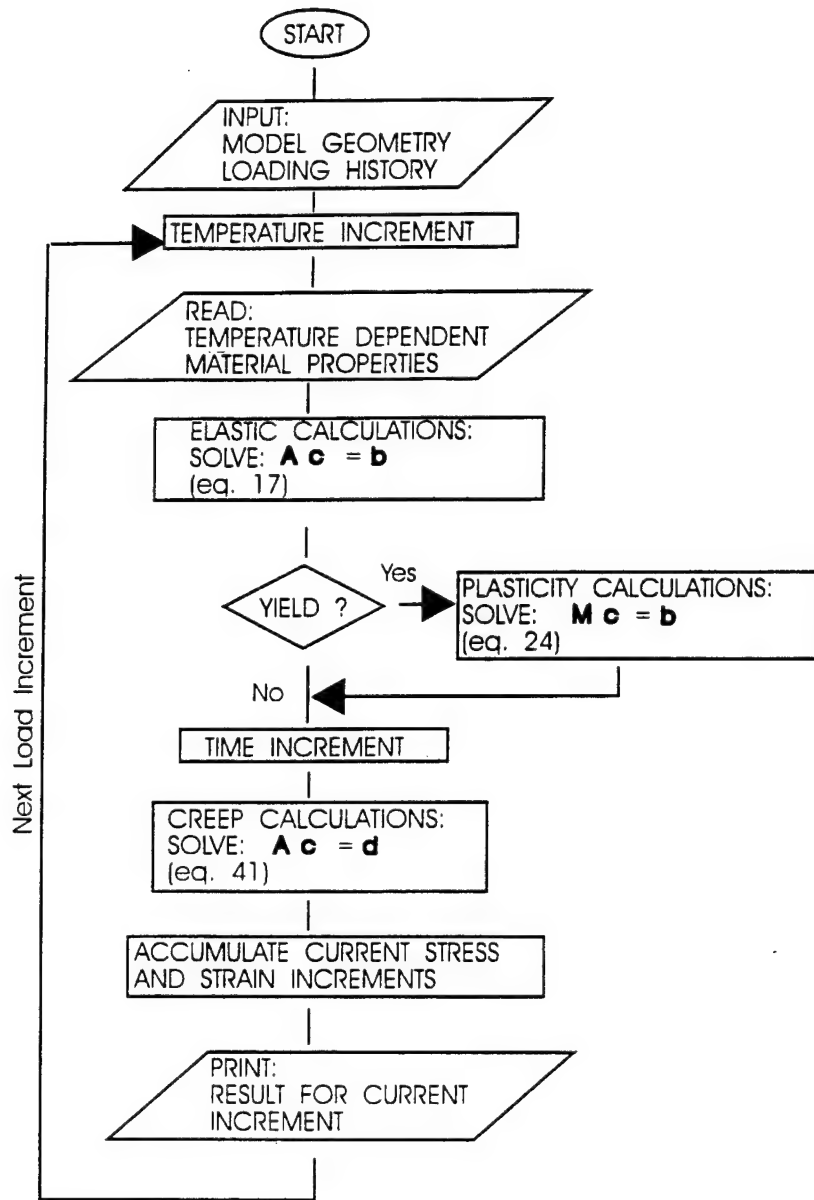


Fig. 1.4 Flow charts for elastic-plastic-creep algorithm.

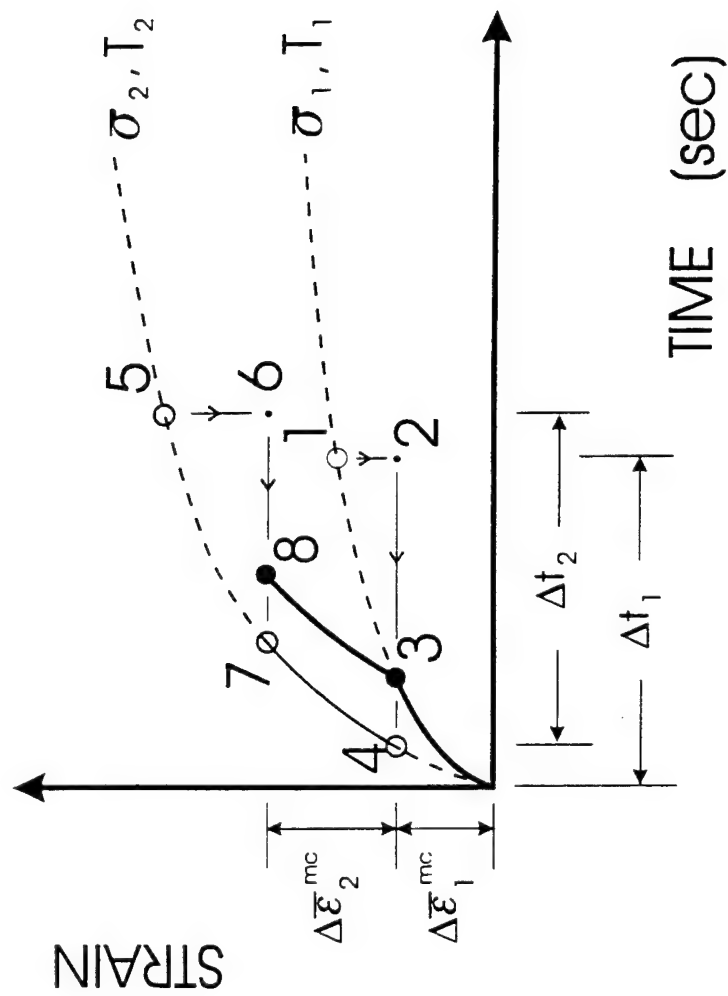


Fig. 1.5 Strain history prediction for the first two load steps from strain hardening method.

CHAPTER 2. Parametric Study of the Time-dependent Behavior of Continuous-fiber Reinforced Metal Matrix Composites Based on Micromechanical Model ²

Abstract

The micromechanical model developed in Chapter 1 for the evaluation of the time-dependent stress-strain response of continuous-fiber-reinforced MMCs is applied to the SCS-6/Timetal 21S composite system. The influence of several parameters were examined; they include the thickness of the equivalent composite media, the type of fiber coating material, the thickness of the reaction zone, cooling rate from the consolidation temperature and the kinetics of the creep process during thermal cyclic loading. Results of this application show that the optimum ratio of the radii of composite media to that of the matrix layer should be larger than seven. At this ratio, sufficient fiber interactions is provided by the equivalent composite media. The analysis also indicates that the process-induced thermal stresses in

² Based on: "Time-Dependent Behavior of Continuous-Fiber-Reinforced Metal Matrix Composites: Modeling and Applications," M. N. Tamin, D. Zheng and H. Ghonem, *Journal of Composites Technology & Research*, JCTRER, Vol. 16, No. 4, October 1994, pp. 314-322.

the matrix can be relaxed due to creep during initial cool-down from fabrication. This stress reduction is enhanced at a slower cooling rate. Furthermore, the study of the role of different fiber coating materials shows that Copper coating is most effective in lowering the tensile stress components in the matrix when compared to Niobium, porous TiB_2 and Amorphous Carbon. The effectiveness increases with increasing thickness of the interfacial region. TiB_2 and Niobium coatings are favorable because they induce compressive radial stress in the brittle interfacial region and the matrix. The effect of thermal cycles subsequent to initial cool-down has been analyzed. It is found that the matrix thermal activation energy, Q , is history dependent and can be correlated with the level of the accumulated creep strain in the matrix layer. Furthermore, the residual thermal stresses in the matrix due to cool-down from consolidation can be fully relaxed by the thermal fatigue process.

2.1 Introduction

A micromechanical approach which takes into account the influence of time dependent effects on the evolution of thermal stresses in continuous fiber-reinforced metal matrix composites (MMCs) was developed in Chapter 1. This approach which adopts the four-phase concentric cylinder model is able to provide information on the stress and strain states as well as their evolution in each constituent of the composite during the loading history.

A critical aspect of this approach is the inclusion of the creep deformation developed in the matrix and the effective composite media due to thermal variations. This inelastic deformation is described through the use of the Bailey-Norton's equation which accounts for the primary and secondary creep stages. A numerical scheme based on the "strain-hardening" creep formulation is employed to predict the accumulation of creep strain during the simultaneous variation of both stress and temperature in the composite.

In this section, the model is applied to SCS-6/Timetal 21S composite system under the thermal loading conditions which include cooling from processing temperature and subsequent thermal cycling. Through this application, an attempt has been made to identify the key parameters in the model and their physical significance. The minimum size of the equivalent composite media necessary to account for the effect of fibers interaction in the composite is investigated. MMCs with different fiber coating materials and various thickness are modelled to study their effects on the thermal stress level in the constituents of the composite. The significant influence of time-dependent behavior of MMCs during initial cool-down and subsequent thermal fatigue are also studied. In addition, effects of different cooling rates during consolidation on the residual thermal stress level in the composite are considered. The characteristics of the stress state in the fiber, the reaction zone and the matrix during consolidation and subsequent thermal cycles are presented. Finally, certain interesting features of the thermal stresses in the composites revealed from the application of the model to thermal fatigue conditions are discussed.

2.2 Parametric Study

The composite employed for the model here is the Titanium-based SCS-6/Timetal 21S composite system. The Silicon Carbide fiber reinforcement, SCS-6 is assumed to behave elastically for all loading conditions with temperature-independent elastic modulus and Poisson's ratio. The coefficient of thermal expansion (CTE) is taken as temperature-dependent [Schw92, Dica86, Saig92, Arno92]. The reaction zone formed between the fiber and the matrix with a thickness of 3 μm is assumed to have mechanical and thermal properties similar to those of the fiber coating material used. The elastic modulus, CTE, and yield limit of the metastable Timetal-21S monolithic matrix alloy were also considered to be temperature-dependent [Khob91]. The properties of the equivalent composite media were obtained using the rule of mixture for fiber volume fraction of 35%. The volume fractions of the fiber, v_f , the reaction zone, v_{re} , and the matrix, v_m , are expressed as:

$$v_f = \left(\frac{r_4}{r_2} \right)^2, \quad v_{re} = \frac{r_3^2 - r_4^2}{r_2^2}, \quad v_m = 1 - \left(\frac{r_3}{r_2} \right)^2 \quad (2.1)$$

where r_1 , r_2 , r_3 and r_4 are the radii of the equivalent composite media, the matrix, the reaction zone and the fiber, respectively. The mechanical properties of all the constituents of the composite are shown in Fig. 2.1(a)~(c).

Both the monolithic matrix and the composite exhibit creep behavior during consolidation. The creep properties of Timetal 21S monolithic matrix and the composite

material are based on limited experimental data given in reference [Khob91, Mart92]. It is assumed that the creep curves can be represented by the Bailey-Norton's equation in the transient and the steady state stages of creep as:

$$\bar{\epsilon}^{cr} = B \bar{\sigma}^{m(T)} t^n \quad (2.2)$$

where $\bar{\epsilon}^{cr}$ and $\bar{\sigma}$ are the effective creep strain and the effective stress, respectively. The parameters B , $m(T)$ and n are obtained from correlations with the experimental data. The coefficient, B can be expressed by an Arrhenius-type expression:

$$B = b_0 \exp\left(-\frac{Q}{RT}\right) \quad (2.3)$$

where b_0 is a constant, R is the gas constant, Q is the thermal activation energy and T is temperature in degrees Kelvin. The stress exponent, $m(T)$, which is treated as a function of temperature is described as a polynomial function in the form [Lema90]:

$$m(T) = A_1 + A_2 T + A_3 T^2 + A_4 T^3 \quad (2.4)$$

where A_i , ($i=1,2,3,4$) are material constants.

Due to lack of creep data for the SCS-6/Timetal-21S composite, the creep response of the equivalent composite media under thermal loading conditions is estimated from the matrix creep data by accounting for the effect of fiber reinforcement in the following manner:

$$\epsilon_{rr}^{(1),cr} = (1 - v_f) \epsilon_{rr}^{(2),cr} \quad , \quad \epsilon_{\theta\theta}^{(1),cr} = (1 - v_f) \epsilon_{\theta\theta}^{(2),cr} \quad , \quad \epsilon_{zz}^{(1),cr} = (1 - v_f) \epsilon_{zz}^{(2),cr} \quad (2.5)$$

where $\epsilon_{rr}^{(1),cr}$, $\epsilon_{\theta\theta}^{(1),cr}$ and $\epsilon_{zz}^{(1),cr}$ are the radial, hoop and axial component, respectively, of the unconstrained creep strain for the composite while $\epsilon_{rr}^{(2),cr}$, $\epsilon_{\theta\theta}^{(2),cr}$ and $\epsilon_{zz}^{(2),cr}$ are the corresponding creep strain components for the matrix.

The first part of this section will deal with the thickness of the equivalent composite media surrounding the matrix, the reaction zone and the embedded fiber. The effect of the reaction zone thickness and different types of fiber coating materials on the stress states in the matrix and the reaction zone will be examined next. This will be followed by analysis related to the role of creep deformation and the response of the matrix activation energy to thermal loadings. In this section, the stress fields in the matrix and the reaction zone are calculated in the vicinity of the matrix/reaction zone interface.

2.2.1 Thickness of the Equivalent Composite Media

As described in the last section, the geometry of the model adopted in the present approach consists of a fiber surrounded by a reaction zone and the matrix layer, and embedded in an unbounded homogeneous media that has the properties of the composite. This model is the counterpart for multi-phase media of the self-consistent method for single phase media [Chri79]. Theoretically, the equivalent composite media surrounding the matrix

cylinder should be infinitely large, and generally the numerical techniques take this size fairly large to meet infinite requirement. The choice of a large equivalent composite media leads to a stable stress field solution at the expense of longer computational time and larger required computer memory. Fig. 2.2(a)~(c) show the relationship between the stress fields in the matrix layer and the size of the equivalent composite media in terms of the ratio of the radii of the matrix to the surrounding equivalent composite media. The stresses are normalized by $\sigma_0 = E^{(2)} \alpha^{(2)} \Delta T$, where $E^{(2)}$ and $\alpha^{(2)}$ are the Young's modulus and CTE, respectively of the matrix at room temperature, and ΔT is 840 °C. It indicates that the stress fields of the phases are stable until the ratio is less than seven, and this trend is not affected by the fiber volume fraction. The significance of this ratio of seven could be explained in terms of the minimum number of fibers that should be contained in the optimum thickness of the composite media for the model. In the real composite, the fibers are not regularly align in the matrix. The distribution of the center-to-center fiber spacing for a typical SCS-6/Ti-15-3 composite with 35% fiber volume fraction can be obtained using the method of quantitative stereology [Unde69] as illustrated in Fig. 2.3. The mean center-to-center fiber spacing for this composite is 230 μm . Assuming that the fiber arrangement follows the hexagonal array with the fiber, the reaction zone and the matrix cylinders at the center of the arrangement, then other fibers are arranged in series of concentric hexagonal arrays about this center as depicted in Fig. 2.4. The minimum diameter of the equivalent composite media is also illustrated in the figure. It can be shown that for the hexagonal array architecture, the minimum size of the equivalent composite media consists of 40 fibers surrounding the embedded fiber which is being modelled (see Fig. 2.4). This provides

sufficient effects of interaction of fibers in the composite.

2.2.2 Fiber Coating Material and Thickness of the Interfacial Region

Previous work showed that the reaction zone in the composites is a susceptible site for generating cracks after fabrication [Arno92, Arno90, Sohi91]. Microscopic radial cracks after fabrication are frequently observed in several titanium metal matrix composites. These cracks are caused by the high level of tensile hoop stress component induced in the reaction zone during consolidation [Bues92]. The popular criteria for selecting coating material are currently based on the enhancement of wetting behavior of fiber and matrix and the minimization of interface reactions by reducing the rate of diffusion [Maru91]. Besides being an effective diffusion barrier against chemical reaction leading to the formation of a brittle layer, a promising coating material should also minimize the local tensile residual thermal stresses in the composite especially at the interfacial region. In view of either preventing premature damage caused by residual thermal stresses in the composite, or load transfer mechanism provided by these stresses, the stress state in the reaction zone and the matrix as influenced by the thickness of the reaction zone and the mechanical properties of the fiber coating material have been investigated. Typical SiC fiber coating materials: Cu, Nb, Amorphous Carbon and TiB_2 with 50% porosity are employed here.

Fig. 2.5(a)~(f) show the variation of the radial, hoop and axial stress components induced in the matrix and the reaction zone during post fabrication cool-down with various

thickness of the interfacial region for different fiber coating materials. The results do not reveal any general trend for the relationship between the thickness of the reaction zone, its mechanical properties and the thermal stress states in the constituents of the composite for all coating materials considered. The magnitude of the transverse (radial and hoop) stress components in the matrix decreases as the thickness of the interfacial region increases. While Cu-coating also decreases the axial thermal stress in the matrix, other coating materials considered cause an increase in the axial stress component with increasing thickness of the interfacial region. The radial stress component is compressive in the interfacial regions for all fiber coating materials considered. However TiB_2 - and Cu-coating induce highly tensile hoop and axial stresses in the interfacial region. Since this region is usually brittle in nature and is sensitive to tensile loading, thus reducing the magnitude of the tensile stress components in this layer is of prime importance. This tensile hoop stress is responsible for generating radial cracks in the composite. The result indicates that Cu-coating induces the highest tensile hoop and axial stress level in the reaction zone which would facilitate the nucleation and propagation of radial cracks in this layer. On the other hand, a small compressive hoop and axial stress components result from the use of C-coated fibers, which potentially increase the ability of the layer to resist cracking. From the load transfer point of view, both fiber coating materials, TiB_2 and Nb, are favorable because they induce high compressive radial stress components in the reaction zone and the matrix. The relative magnitudes of the CTEs and Young's moduli of the different coating materials considered, the SCS-6 fiber, and the Timetal-21S matrix are shown in Fig. 2.6(a)~(b). It is noted that C-coating with both CTE and Young modulus values much smaller than for the

matrix generates lower level of residual thermal stress in the interfacial region. Although the radial stress component decreases substantially with increasing thickness of the interfacial layer, the thickness has small effect on other components of thermal stress in the layer (see Fig. 2.5(d)~(f)). The radial stress component which is beneficial based on the load transfer mechanism is preserved in the reaction zone and the matrix when employing fiber coating materials (Nb or TiB_2) with both CTE and Young's modulus values close to the values for the matrix.

Throughout consolidation, a compressive stress state is induced in the fiber because both the reaction zone and the matrix with higher CTEs but lower Young's moduli than the fiber shrink rapidly around the fiber.

The results of this study indicate that the selection of a suitable fiber coating material should be based on the application requirement of the composite.

2.2.3 Role of Creep Deformation in the Evolution of Thermal Stresses

During post-fabrication cool-down of the composite from consolidation temperature, the thermal stresses induced in the matrix may cause creep deformation at relatively high temperature. The deformation however, is constrained by the relative inextensibility of the elastic fiber and the reaction zone, and the bonding between each constituents of the composite. In the present study, the significant influence of time-dependent deformation behavior on the evolution of thermal stresses in MMCs during initial cool-down has been

investigated. Fig. 2.7 shows the evolution of thermal stresses in the matrix throughout consolidation for purely elastic, elastic-plastic and elastic-plastic-creep cases. The elastic-plastic-creep calculations predicted that at high temperature following consolidation, the thermal stresses were relaxed extensively by creep. Consequently, no plasticity occurred in the composite since the effective stress level is always lower than the yield stress of the matrix throughout the initial cool-down. However, elastic-plastic calculations predicted that the matrix yielded at 720 °C and the stress is brought down to the yield value of the matrix. The final locked-in residual thermal stresses at room temperature are considerably lowered due to creep deformation.

The time-dependent characteristics have been studied through the effect of cooling rate during consolidation on the creep behavior and the residual thermal stress state of the composite. Several cooling rates ranging from 5×10^{-3} to 1.0 °C/sec are utilized in the model and the results are presented in terms of the reduction in effective stress accounted for creep effect in relation to elastic case as shown in Fig. 2.8. The amount of reduction in the effective stress increases exponentially as the cooling rate is lowered. A stress reduction of 9.97% was calculated for cooling rate of 0.5 °C/sec while an additional 10.72% occurred for a slower cooling rate of 0.005 °C/sec. At a slower cooling rate, the composite is exposed to high temperature creep for a longer duration of time, which enhance the accumulation of creep strain resulting in extensive stress relaxation in the matrix. This result indicates that the final locked-in residual thermal stress can be tailored by controlling the cooling rate during consolidation of the composite.

For a particular cooling rate, the maximum reduction in thermal stress always occurs in the vicinity of the matrix/reaction zone interface where the elastic stress is maximum due to the largest difference in CTEs of adjacent layers. The magnitude of the stress relaxation in the matrix due to creep decreases non-linearly from 10% at the interface to 5.3% at the outer layer of the matrix. The results indicate that the matrix creep deformation has a significant effect on the evolution of the thermal stresses and the stress relaxation mechanism in MMCs.

2.2.4 Evolution of Thermal Stresses During Thermal Cycling

As discussed above, the time-dependent deformation plays a significant role in generating thermal stresses in MMCs. The determination of the key parameters which yield the correct stress state in the composite is of prime importance in the current mathematical modelling. During initial cool-down from consolidation temperature, the matrix experiences creep deformation which is governed by eq. (2.2) and (2.3). The matrix thermal activation energy, Q in eq. (2.3) can be treated as a constant for the evolution of thermal stresses in the matrix throughout this process, as indicated by a good agreement between the calculated and the experimental results, see Fig. 2.9. Previous experimental work by Ghonem and Zheng [Ghon93] showed that for loading conditions consisting of the initial cool-down followed by thermal cycling between 100 - 550 °C, the axial thermal stress in the matrix has been reduced to zero at the upper temperature level after the application of only five cycles, as

shown in Fig. 3-10. This reduction in thermal stresses has been attributed to the influence of the creep deformation developed in the matrix material during thermal cycling. However, the attempt to predict the stress history during a loading process similar to that of [Ghon93] using the present model with Q being kept as a constant, has resulted in a stress cycle pattern with a negligible amount of stress reduction at the upper limit of the thermal cycle. The parameter Q , was then linked to the variation in temperature to obtain the best curve fitting to experimental data. The resulting Q was further correlated to the induced matrix stress and strain during the thermal cyclic process. This correlation could be expressed in terms of the inelastic strain energy density, W_{pc} , as:

$$Q = Q_0 - f(W_{pc}) \quad (2.6)$$

where Q_0 is the value of Q prior to thermal cycling and $f(W_{pc})$ is a monotonic increasing function of W_{pc} , in which W_{pc} is defined as:

$$W_{pc} = \int_{\bar{\epsilon}_0^{cr}}^{\bar{\epsilon}^{cr}} \bar{\sigma} d\bar{\epsilon}^{cr} \quad (2.7)$$

$\bar{\sigma}$, $\bar{\epsilon}^{cr}$ are the effective stress and the creep strain, respectively, and $\bar{\epsilon}_0^{cr}$ is the initial creep strain.

This result indicates that the level of thermal activation energy, Q , in the matrix is affected by the simultaneous variation of stress, strain and temperature experienced by the

composite throughout consolidation and thermal cycling. This observation, in fact, supports similar conclusion made by Ghonem and Zheng [Ghon91] in their experimental work on Alloy 718 at 650 °C and by Freed et al. [Free92], on the basis of thermodynamics analysis conducted on Copper and LiF-22mol percent CaF hypereutectic salt.

2.3 Conclusions

The model developed in the last section was employed in a parametric study using SCS-6/Timetal 21S composite system. The following conclusions are derived through the analysis of the results:

- 1- The geometry of the four-phase model requires that the radius of the surrounding composite media to be at least seven times larger than the radius of the matrix to ensures its role in providing realistic geometrical constraints through the surrounding fiber interactions with the model unit.
- 2- The residual thermal stress induced in the composite during consolidation can be reduced considerably by the creep deformation occurring in the matrix. A slow cooling rate allows longer duration of time for the composite to be exposed to high-temperature creep effects resulting in extensive stress relaxation. The matrix layer experiences significant creep effects at the matrix/reaction zone interface where the residual stress level is high.

- 3- Subjecting a composite system to reversing thermal cycles indicate that the matrix thermal activation energy, Q , should be correlated with the creep behavior through the level of accumulated creep strain in the matrix layer.
- 4- The properties and thickness of the reaction zone formed in MMCs influence the thermal stress behavior in the matrix layer. The effective residual stress decreases as the thickness of the reaction zone increases.
- 5- The choice of a fiber coating material that inhibit fiber/matrix reaction and reduce the residual thermal stress level in the composite, and a particular cooling rate following fabrication provide a potential mean of optimizing the mechanical performance of the composite system.

2.4 References

- [Arno90] Arnold, S. M., Arya, V. K. and Melis, M. E., 1990, "Elastic/Plastic Analysis of Advanced Composites Investigating the Use of the Compliant Layer Concept in Reducing Residual Stresses Resulting From Processing," NASA TM103204.

- [Arno92] Arnold, S. M. and Wilt, T. E., 1992. "Influence of Engineered Interfaces on Residual Stresses and Mechanical Response in Metal Matrix Composites." NASA TM 105438.
- [Bues92] Buesking, K. W., Young, J. L. and Reynolds, G. H., 1992. "Status of Advanced Filament Development for Titanium Alloy and Titanium Intermetallic Matrix Composites. Part 2. Computed Residual Stresses in Gamma TiAl/Advances Filament Composites." Titanium Matrix Components, Workshop Proceedings, ed. by Smith, P. R. and Revelos, W. C., WL-TR-92-4035, :42-64.
- [Chri79] Christensen, R. M. and Lo, K. H., 1979. "Solution for Effective Shear Properties in Three Phase Sphere and Cylinder Model." J. The Mechanics and Physics of Solids, 27:315-330.
- [Dica86] Dicarlo, J. A., 1986. "Creep of Chemically Vapor Deposited SiC Fibers." J. Material Science, 21:217-224.
- [Free92] Freed, A. D., Raj, S. V. and Walker, K. P., 1992. "Stress Versus Temperature Dependence of Activation Energies for Creep." J. Engng. Mat. and Tech., 114:46-50.2

- [Ghon91] Ghonem. H. and Zheng. D.. 1991. "Oxidation-Assisted Fatigue Crack Growth Behavior in Alloy 718 - Part I. Quantitative Modeling. Part II. Applications." Fatigue & Fracture of Engineering Materials and Structures. 14:749-760.
- [Ghon93] Ghonem. H. and Zheng. D.. 1993. Mat. Sc. Engng. (in press).
- [Khob91] Khobaib. M. and Ashbaugh. N.. 1991. Unpublished work.
- [Lema90] Lemaitre. J. and Chabache. L.. 1990. Mechanics of Solids (English Translation). Cambridge University Press. NY.
- [Mart92] Martin. P.L., Bingel. W. H. and Mahoney. M.W.. 1992. "SiC-Reinforced β -21S Creep Properties." Titanium Matrix Components. Workshop Proceedings, ed. by Smith. P. R. and Revelos. W.C.. WL-TR-92-4035. :277-291.
- [Maru91] Maruyama. G. Barrera.E. and Rabenberg. L.. 1991. Characterization and Modification of Composite Interfaces. Metal Matrix Composites: Processing and Interfaces, ed. by Everett. R. K. and Arsenault. R. L.. Academic Press. Inc.. NY. :181-216.

- [Saig92] Saigal, A., Kupperman, D. S. and Majumdar, S., 1992. "Residual Strains in Titanium Matrix High-Temperature Composites." Mat. Sc. Engng., :59-66.
- [Schw92] Schwenker, S. W., Evans, D. J. and Eylon, D., 1992. "Interface Reaction Kinetics of Ti_3Al /SCS-6 Metal Matrix Composites." in Longitudinal Creep Behavior and Damage in SCS-6/Ti-6Al-4V Metal Matrix Composites, Seventh World Conference on Titanium, San Diego, CA.
- [Sohi91] Sohi, M., Adams, J. and Mahapatra, R., 1991. "Transverse Constitutive Response of Titanium-Aluminum Metal-Matrix Composites." Constitutive Laws of Engineering Materials, ed. by Desai, C. D., Krempl, E., Frantziskonis, G. and Saadatmanesh, H., ASME Press NY, :617-626
- [Unde69] Underwood, E. E., 1969. Quantitative Stereology, Addison-Wesley, Reading, Man.

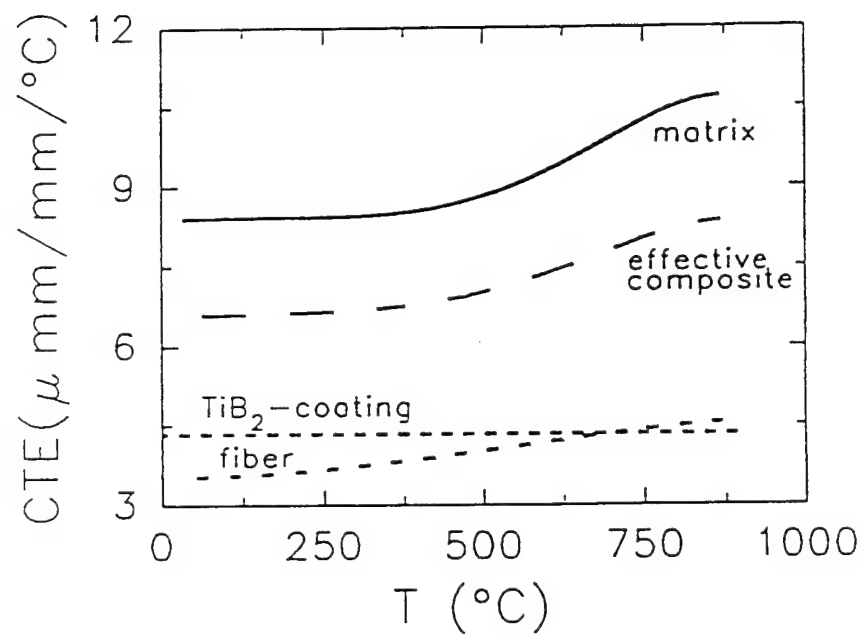


Fig. 2.1 (a) Physical properties of the constituents: CTE.

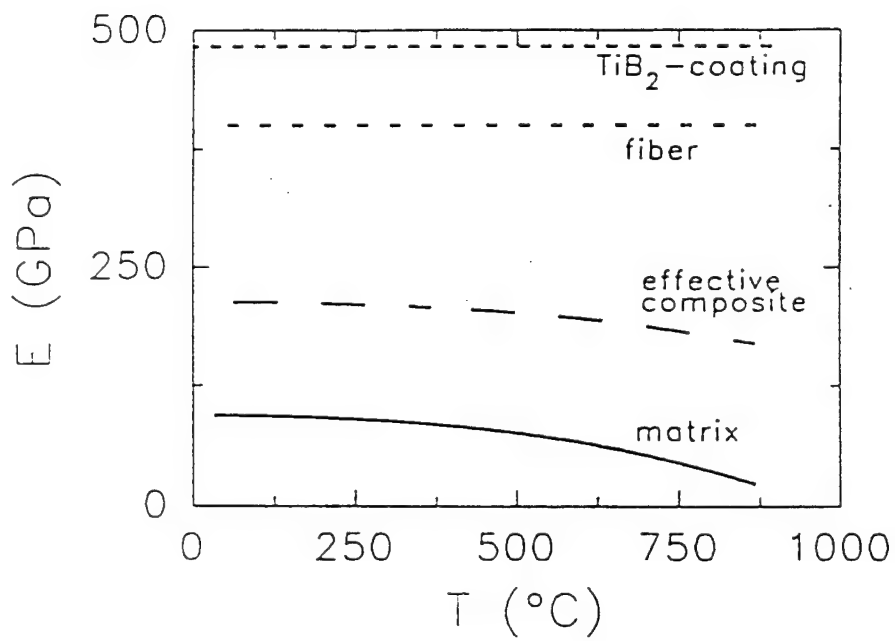


Fig. 2.1 (b) Physical properties of the constituents: Young's modulus.

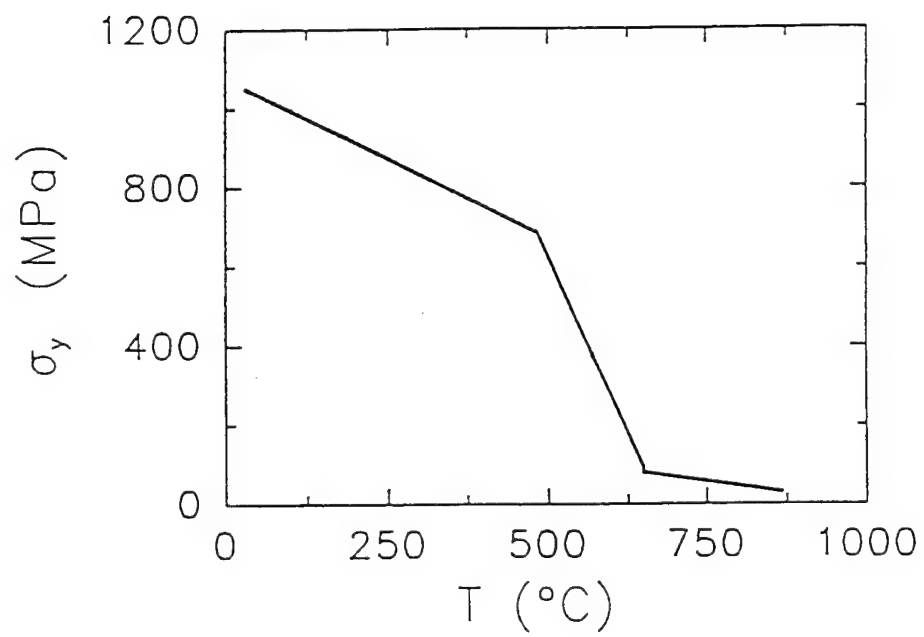


Fig. 2.1 (c) Physical properties of the constituents: Yield strength of Timetal 21S.

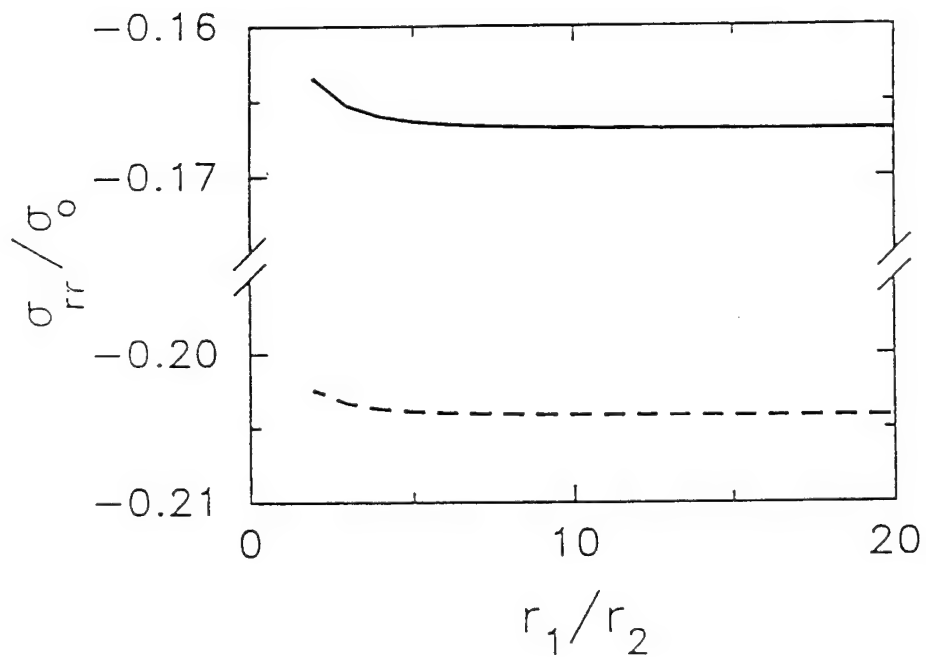


Fig. 2.2(a) Variation of stress field in the matrix layer with size of the equivalent composite: Radial Component. — $v_f = 35\%$, - - - $v_f = 20\%$.

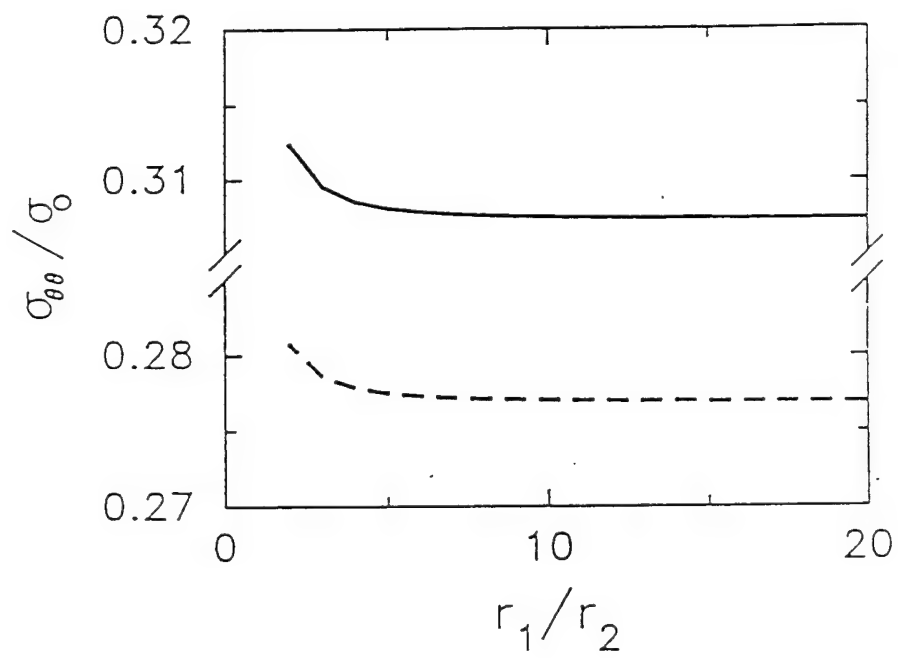


Fig. 2.2(b) Variation of stress field in the matrix layer with size of the equivalent composite: Hoop component. — $v_f = 35\%$, - - - $v_f = 20\%$.

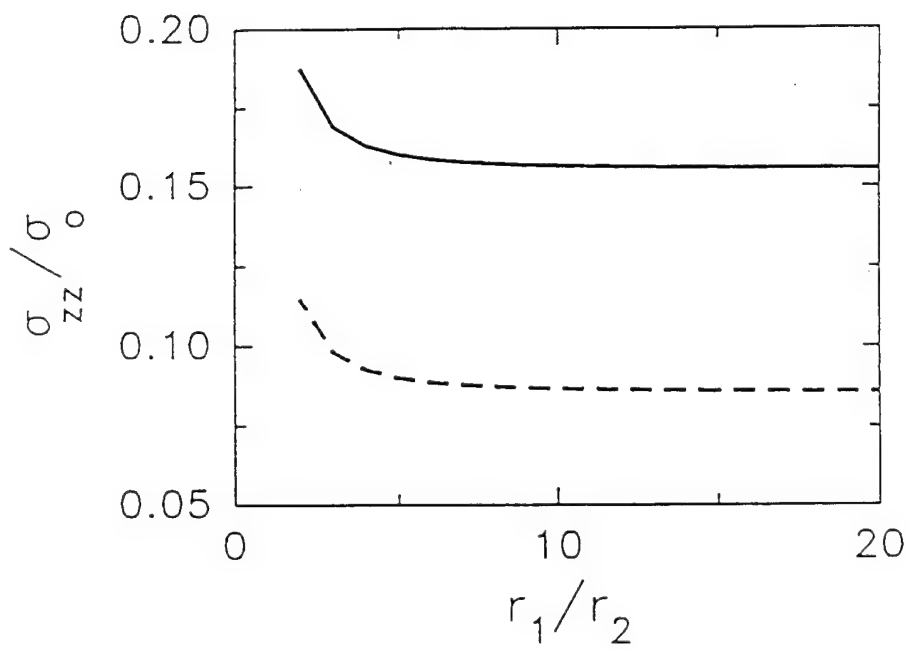


Fig. 2.2(c) Variation of stress field in the matrix layer with size of the equivalent composite: Axial component. — $v_f = 35\%$, - - - $v_f = 20\%$.

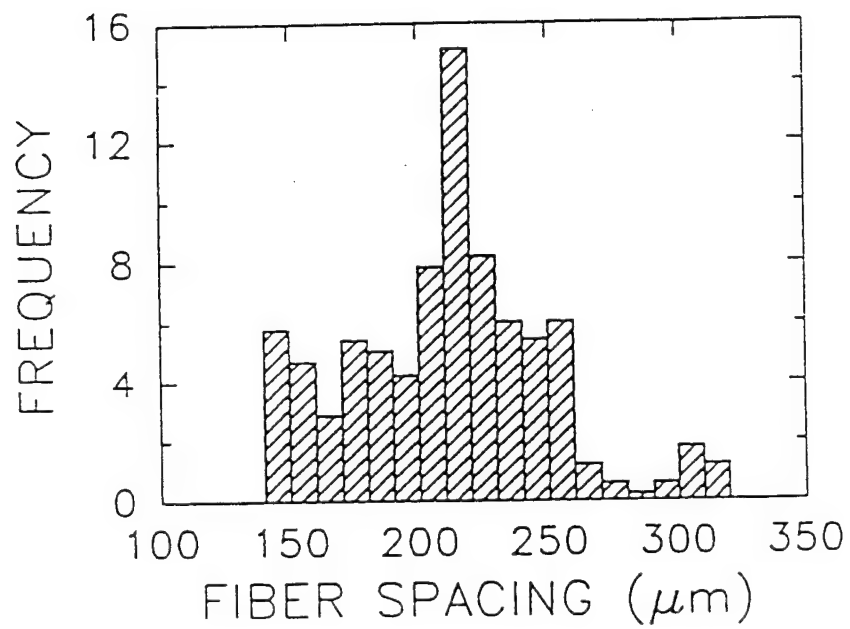


Fig. 2.3 Frequency distribution of center-to-center spacings between fibers in Ti-15-3 composite with 35% fiber volume fraction.

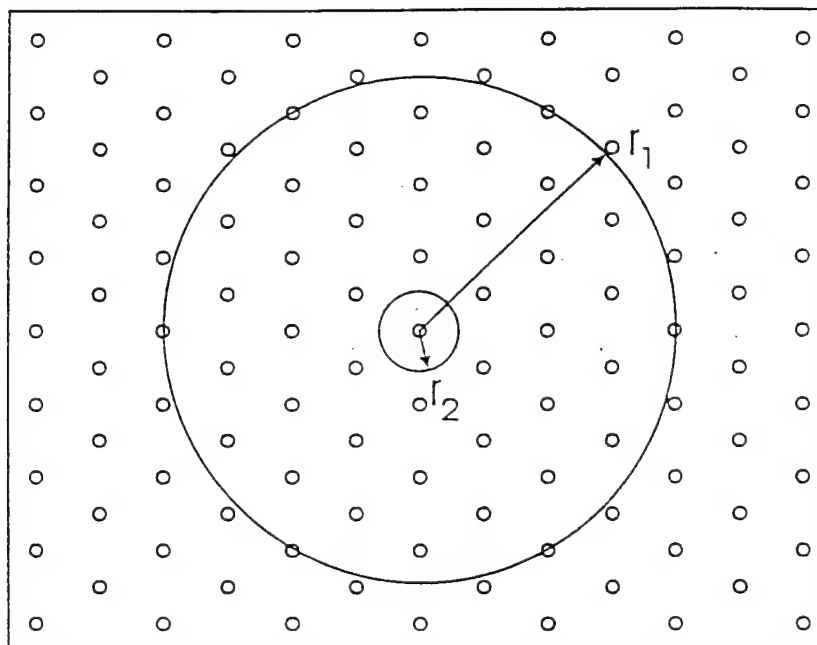


Fig. 2-4 Idealized array of fibers in MMC with 35 % fiber volume fraction.

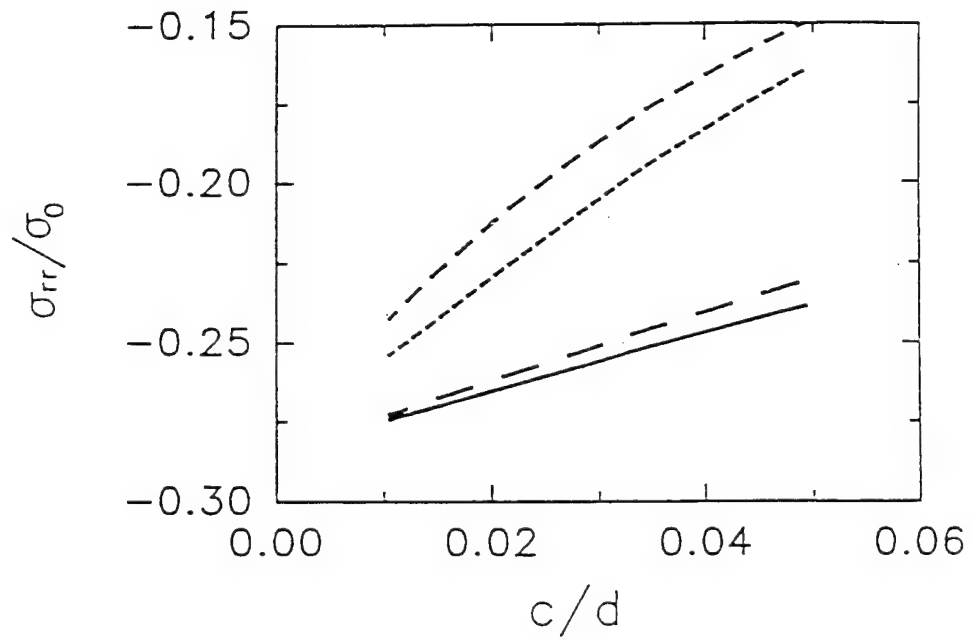


Fig. 2.5(a) Variation of radial stress field in the matrix with thickness of fiber coating for different coating materials: ——— TiB₂, — — — Nb, - - - - C, Cu

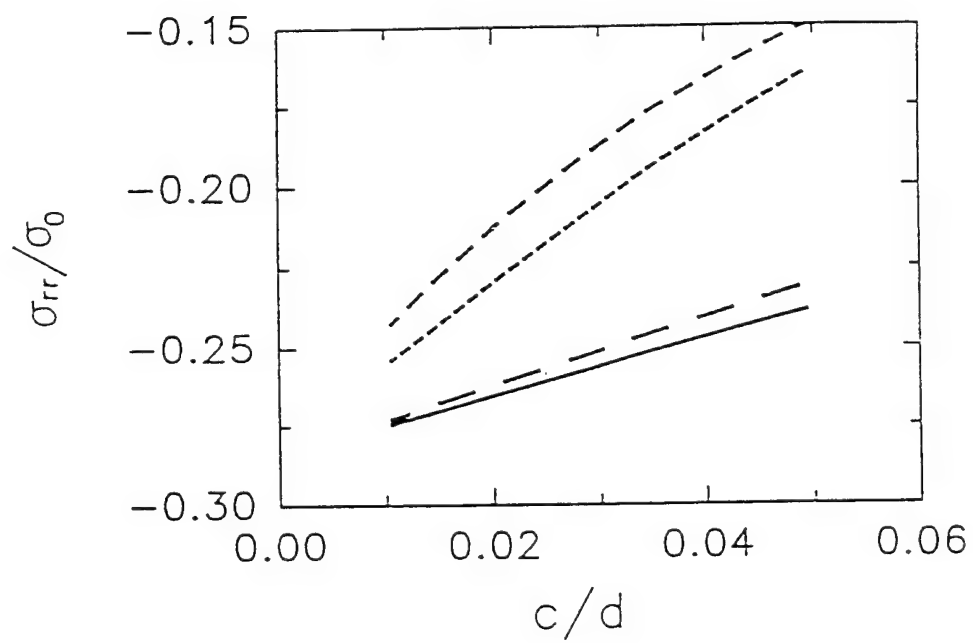


Fig. 2.5(a) Variation of radial stress field in the matrix with thickness of fiber coating for different coating materials: ——— TiB₂, — — — Nb, - - - - C, Cu

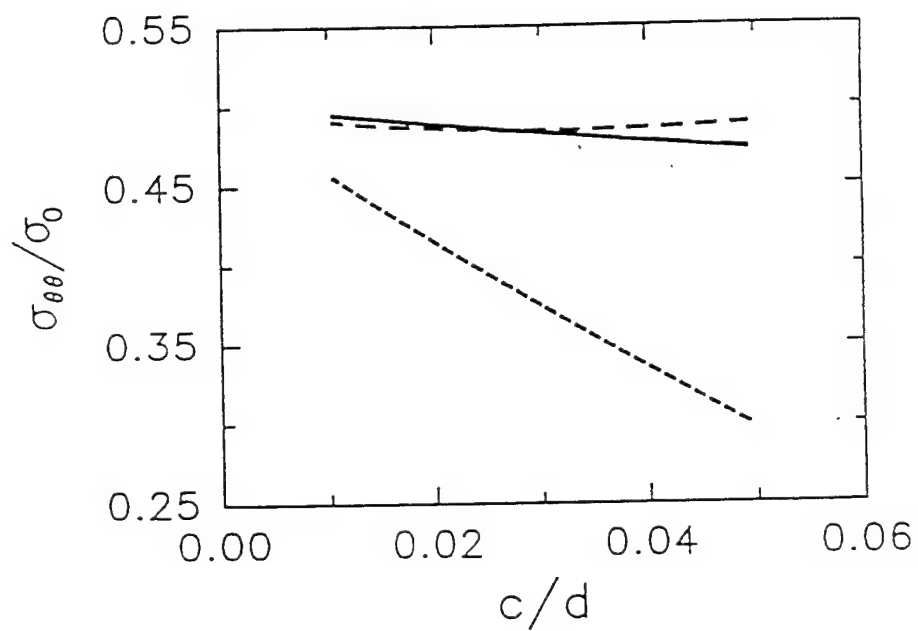


Fig. 2.5(b) Variation of hoop stress field in the matrix with thickness of fiber coating for different coating materials ——— TiB₂, — — — Nb, - - - - C, Cu.

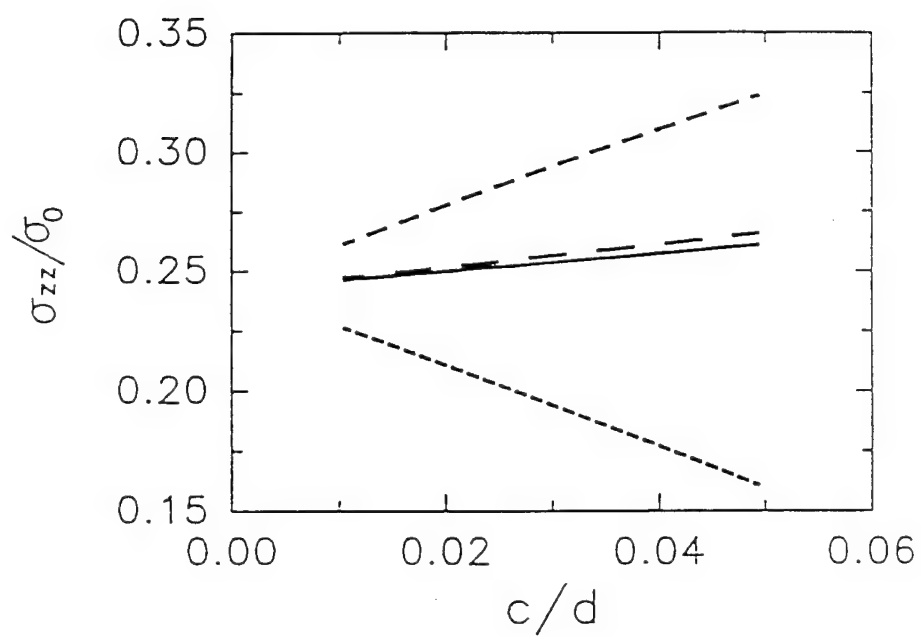


Fig. 2.-5(c) Variation of axial stress field in the matrix with thickness of fiber coating for different coating materials: ——— TiB₂, — — — Nb, - - - - C, Cu.

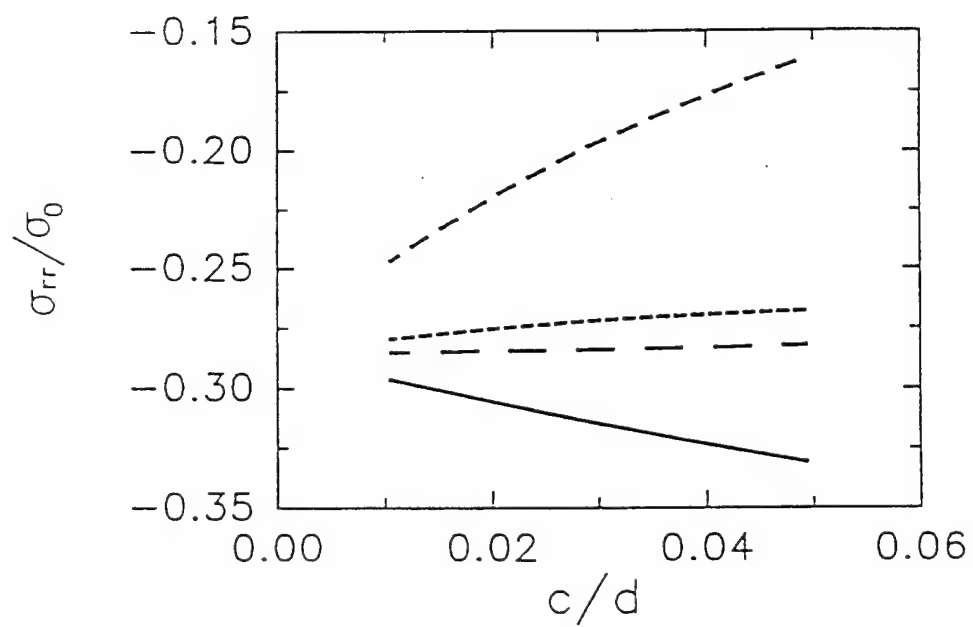


Fig. 2.5(d) Variation of radial stress field in the interfacial region with thickness of fiber coating for different coating materials: ——— TiB₂, - - - Nb, C, Cu.

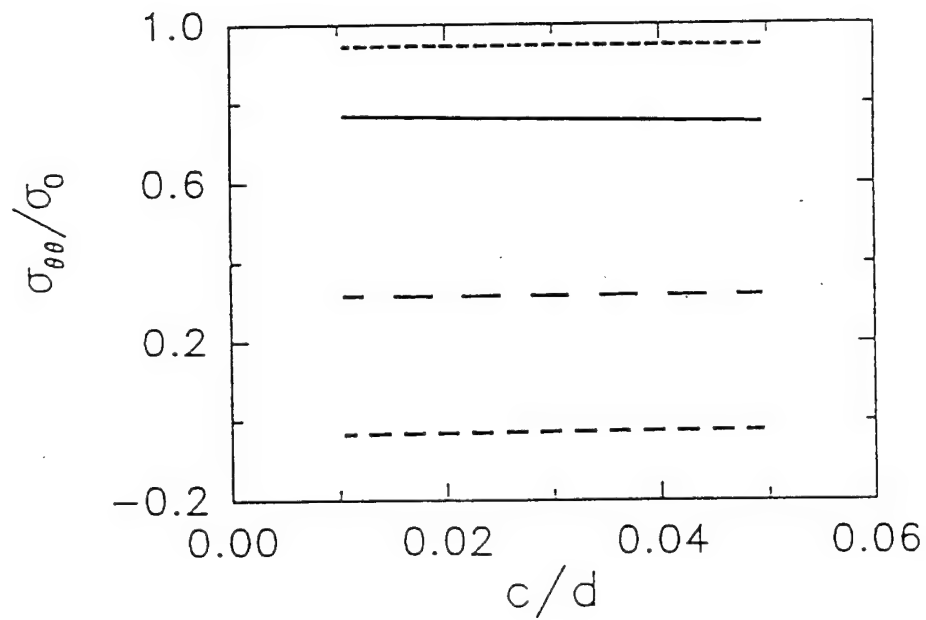


Fig. 2.5(e) Variation of hoop stress field in the interfacial region with thickness of fiber coating for different coating materials: ——— TiB₂, - - - Nb, - - - C, Cu.

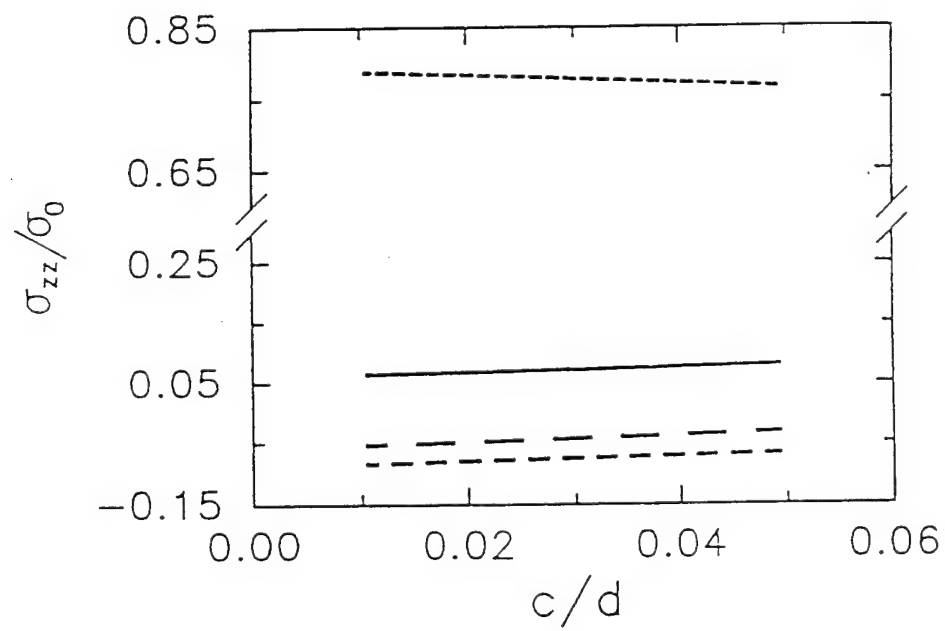


Fig. 2.5(f) Variation of axial stress field in the interfacial region with thickness of fiber coating for different coating materials: ——— TiB₂, - - - Nb, C, - · - · - Cu.

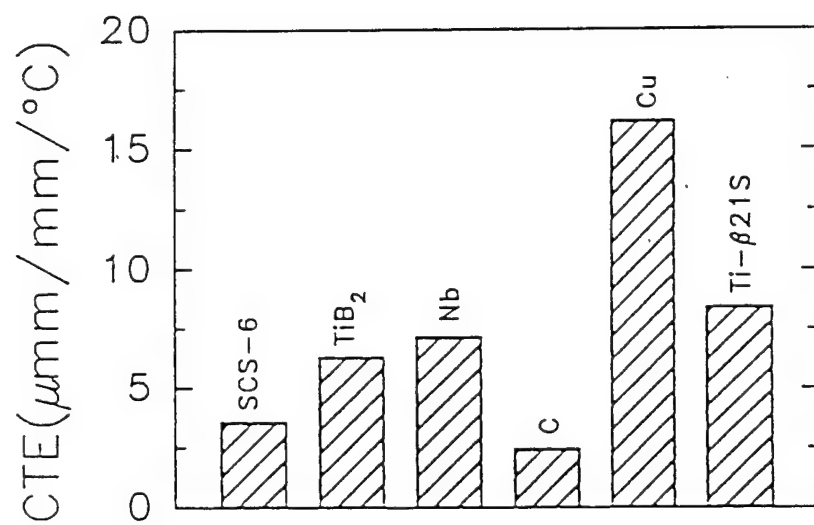


Fig. 2.6(a) Physical properties of the composite constituents at room temperature: CTE.

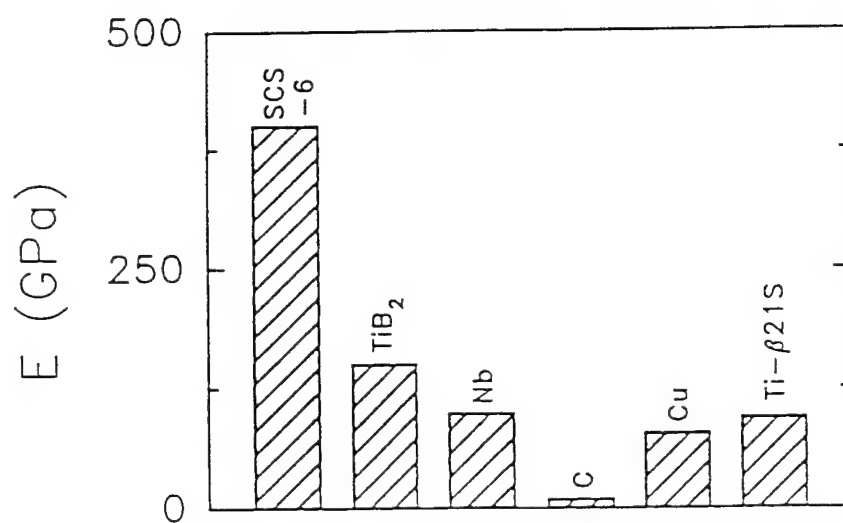


Fig. 2.6(b) Physical properties of the composite constituents at room temperature: Young's modulus.

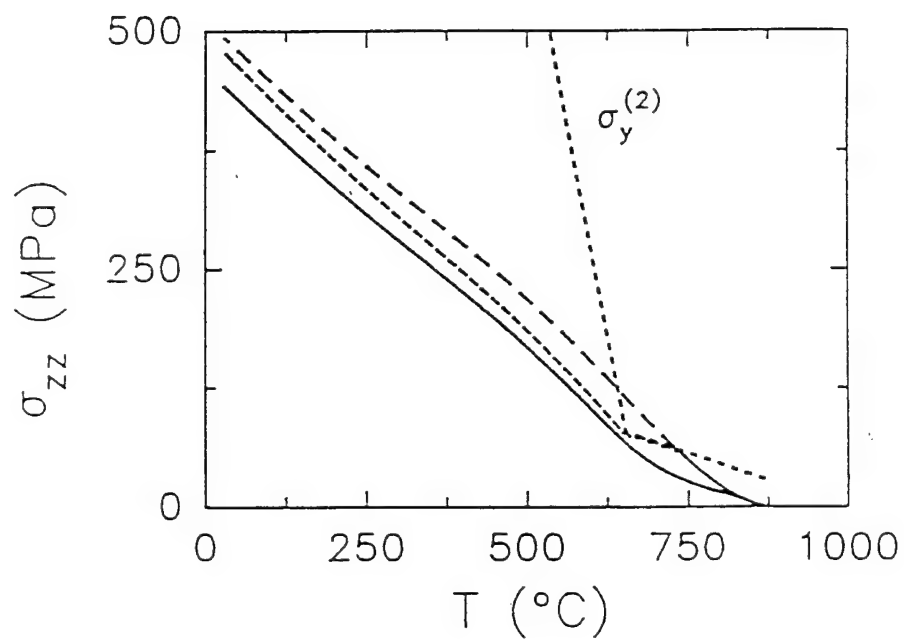


Fig. 2.-7 Evolution of axial thermal stress in the matrix during initial cool-down at 0.5 °C/sec.: — elastic-plastic-creep. - - - elastic-plastic, — — — elastic. $\sigma_y^{(2)}$ is the matrix yield strength.

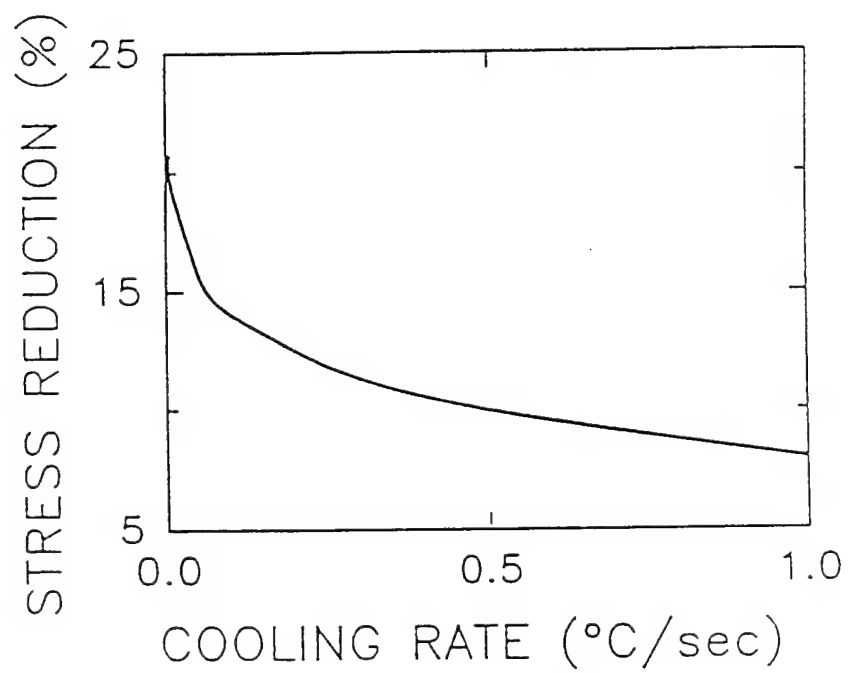


Fig. 2.8 Amount of stress reduction due to creep in the matrix at various cooling rates.

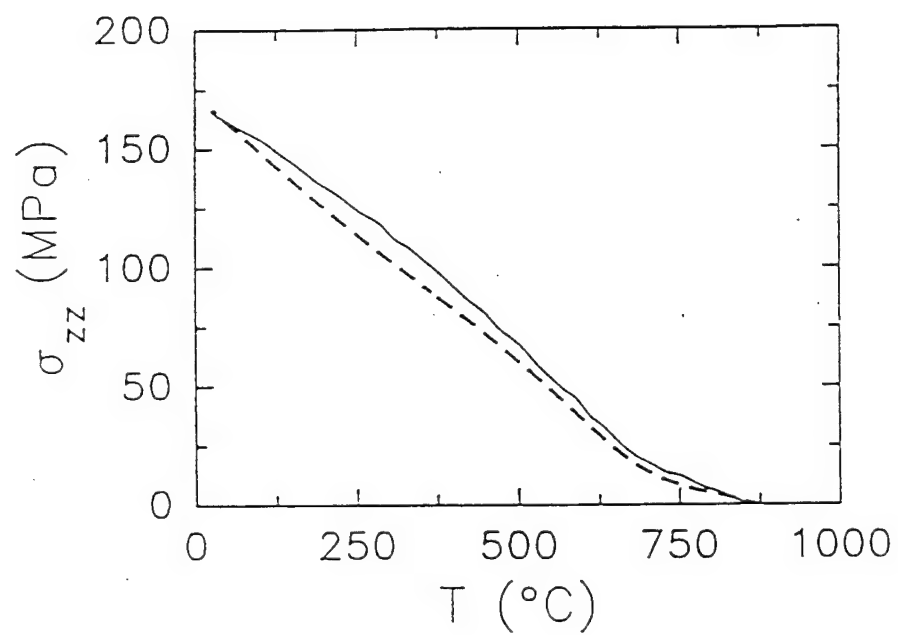


Fig. 2.9 Evolution of axial thermal stress during initial cool-down at 0.5 °C/sec.:
 — experiment [Ghon93], - - - - - present result.

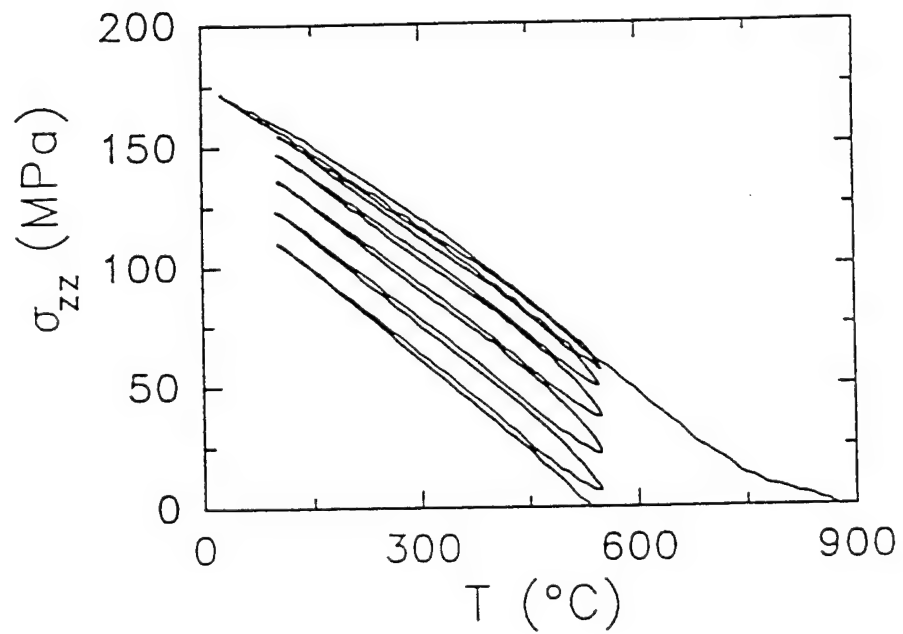


Fig. 2.10 Evolution of axial thermal stress in the matrix during initial cool-down and thermal cycle between 100 - 550 °C at 0.5 °C/sec.

CHAPTER 3. Interphase Debonding Strength of Titanium Metal Matrix Composites³

Abstract

An experimental/numerical procedure to assess the fiber/matrix interphase shear strength in a unidirectional fiber reinforced titanium metal matrix composite is proposed in this paper. The procedure relies on a series of fiber pushout tests carried out on samples of a composite to determine the load values at the onset of interface debonding. Finite element calculations employing an axisymmetric cylinder model of a fiber embedded in the matrix phase are then utilized to establish the interphase stress distribution along the fiber. A region of stress localization along the interface due to geometrical constraints of the fiber pushout test configuration is simulated. The interphase shear strength is defined as the peak of the shear stress localization along the pushout fiber where initial debonding would occur. The calculated strength considers the contribution provided by the process-induced residual stress field as modified by geometrical constraints of fiber pushout test configuration. Results of

³ Submitted for publication: M. N. Tamin and H. Ghonem, "Interphase Debonding Strength of Titanium Metal Matrix Composites", *Materials Science and Engineering*, in review, March 1997.

the study showed that the interphase shear strength in a SCS-6/Timetal-21S composite has an inverse relationship with test temperature. The calculated shear strength at 650 °C was found to be four times larger than that calculated assuming a uniform distributed shear stress along the pushout fiber. Furthermore, the contribution of the locked-in residual stress to the interphase shear strength, as calculated in this paper, was assessed as 35 % at room temperature and 15 % at 650 °C.

3.1 Introduction

Fiber/matrix interface debonding in a titanium metal matrix composite, MMC, has been shown to be influenced by the interphase strength which dictates the extent of interface failure (McCa87, Sens90, McMe90). The carbon-rich coating of SiC-type fibers used in SiC/Ti MMCs acts as a reaction barrier against the reactive titanium alloy matrix. Consequently, the chemical bonding in this type of Ti-MMC systems is considered insignificant (Phil74, Prew80, Davi92, Yang91, Eldr94, Zhen95). The strength of the fiber/matrix interphase region is, therefore, assumed to be generated by the mechanical clamping on the fiber due to the process-induced residual stress. The residual stress states in each constituent of the composite are the result of fabrication method and post-processing heat treatment procedures. The interphase strength could then be viewed as a processing by-product parameter which can be tailored to optimize the resistance of the composite to fatigue failure. In addition, the strength is influenced by the growth kinetics and thermal

aging characteristics of the interphase region (Osbo97).

While direct measurement of the interphase strength is difficult to obtain, information leading to the determination of the strength values could be extracted from results of fiber pullout, fiber push-through, fiber fragmentation or fiber pushout test of the composite samples (Yang91, Eldr94, Wats92, Warr92, Kera91, Osbo95). In a fiber pushout test, the onset of interface debonding is identified by the first departure from linearity in the pushout load-displacement curve. The initial debonding event is controlled by the amount of allowable relative displacement across the fiber/matrix interface and/or the debonding strength of the interphase region. As the applied load is increased, the initial debond crack extends to a critical length where a sudden load drop occurs as the entire fiber length is debonded and starts to slide. The fiber pushout process should be viewed as the propagation of an interface debond crack along the pushout fiber. The progressive damage of the interface along the pushout fiber relies on the stresses as well as the strength properties and toughness of the interphase region.

Much of the previous work on extracting the shear strength of the interphase region from results of fiber pushout test consider the shear stress at the interphase to be uniform along the pushout fiber (Eldr94, Wats92). This assumption provides a simple determination of interphase shear strength defined by the debonding pushout load divided by the fiber/matrix contact area. An accurate assessment of the interphase shear strength should account for the effect of traction-free specimen surface and geometrical constraints of the pushout test on the stress field along the interface. Finite element calculations showed that the interphase shear stress varies significantly along the interface with shear stress

localization near the free surface (Kera91, Anan95, Ghos94, Tami95, Kall92).

Successful modeling of fatigue crack bridging process relies on accurate measurement of interphase strength properties and frictional shear characteristics of debonded interfaces (McCa87, McMe90, Zhen95, Aves71, Budi86, Mars85, Tele93, Nguy94). An accurate determination of the interphase shear properties of titanium MMCs, therefore, is critical both in predicting the crack growth behavior and in designing a composite system for a specific damage mechanism. In particular, the influence of temperature and its consequent modification of the damage mechanism in a SiC/Ti MMC has received little attention.

The objective of this work is to propose a new methodology to determine the interphase shear strength in unidirectional SiC/Ti MMCs. The procedures combine experimental method of fiber pushout with numerical calculations of stress distribution along the pushout fiber at the onset of debonding. The interphase shear strength is viewed in this work as the equivalent interphase shear stress at a critical location along the pushout fiber at initial debonding event. The determination of the strength, therefore, requires the knowledge of the shear stress distribution along the fiber at the onset of interface debonding. This objective can be achieved by a procedure which combine results of pushout tests on thin-slice composite specimens with finite element calculations of the stress field in the corresponding specimens. The pushout tests determine the load level required to initiate interface debonding along the pushout fiber. Finite element calculations are then performed on a representative volume element of the composite subjected to the load at initial debonding. The results are utilized in determining the location of debonding along the fiber

based on localized stress distribution arising from geometrical constraints of the fiber pushout test. The contributions of process-induced residual stress and geometry-induced modification of the stress field due to pushout test configuration on the shear strength are evaluated. The effect of elevated temperature on interphase strength of a SiC/Ti MMC is examined in this work. The resulting shear strength is compared to that calculated using the assumption of a uniform shear stress distribution.

The first section of the paper describes the material used in the study as well as experimental procedure and related results. This is followed by a description of a finite element cylinder model employed to calculate the evolution of residual stress field in the composite as well as in a finite thickness composite specimens intended for fiber pushout tests. The calculated stress field corresponding to the debond load level in each of the pushout specimen is then presented and the interphase shear strength based on the localization of shear stress is defined. The last section of the paper discusses the implication of the calculated interphase shear strength on damage modes encountered in metal matrix composites.

3.2 Material And Experimental Procedures

The material used in this study is a unidirectional SCS-6/Timetal-21S metal matrix composite. The metastable β titanium matrix phase, Timetal-21S, is alloyed with (in wt. %) 0.1 Fe, 16.0 Mo, 3.06 Al, 2.9 Nb, 0.2 Si, 0.22 C, 0.12 O and 0.005 N. The SCS-6 reinforcing

fiber is a chemically vapor deposited SiC on a 33- μm diameter carbon core with a final layer of a 3- μm thickness dual carbon-rich coatings. The final diameter of the SCS-6 fiber is 142 μm . The $[0^\circ]_6$ composite has been fabricated using Foil/Fiber/Foil layups technique and consolidated by vacuum hot pressing with a resulting nominal fiber volume fraction of 0.35. The post-fabrication cooling rate from consolidation to 650 $^\circ\text{C}$ is 0.03 $^\circ\text{C}/\text{sec}$ and below 650 $^\circ\text{C}$ the composite is cooled in the vacuum chamber with the heat being turned off. The cross section of the composite exhibited a staggered array distribution of fibers with full consolidation taking place around the fiber and at the foil/foil interfaces as shown in Fig. 3.1.

A series of fiber pushout tests were performed on thin-slice composite specimens to determine loads corresponding to the initiation of interface debonding, full debonding and frictional sliding. The thickness of a thin-slice specimen is governed by two requirements essential for a valid fiber pushout test. Minimum thickness must be sufficient to ensure that the residual stress field in the composite is preserved and the onset of interface debonding is occurring in shear. The minimum thickness to satisfy this requirement, at each test temperature, has been calculated using the finite element method (Osbo97). Maximum thickness is limited by the pushout load that can be sustained by the punch. According to these limits, the composites are cut perpendicular to the fiber direction using a diamond saw for thicknesses ranging from 0.5 to 1.4 mm. Each specimen is then ground using progressively finer grids of SiC-paper from 320 to 600 grid, followed by polishing consecutively with 9, 3 and 1- μm diamond spray on nylon cloth. The polished specimen is then mounted in a pushout testing machine and heated to the test temperature in vacuum (10^{-6} torr). At each test temperature, between 8 to 12 fibers which were aligned over 250- μm

width grooves in the specimen holder were pushed out in a displacement-control testing mode. A load-motor displacement curve for each fiber pushout test is recorded for analysis.

Pushout load-motor displacement curves obtained from a fiber pushout tests at ambient temperature, 500 and 650 °C are shown in Fig. 3.2(a). The initial linear response of the motor displacement to increasingly applied load terminates with a noticeable decrease in the slope of the curve (illustrated as point A for pushout test at 650 °C). The initial linear portion of the curve (line 0-M) represents the compliance of the load train. The compliance is eliminated from the data by subtracting the displacement corresponding to pushout load along line 0-M. The resulting load-effective displacement curve for fiber pushout at 650 °C is shown in Fig. 3.2(b). The departure from linearity at point A marks the onset of interface debonding. The combination of specimen thickness, width of groove in the specimen holder, diameter of fiber, pushout load magnitude at initial debonding and test temperature renders insignificant effects due to specimen bending. Therefore, Point A is associated with shear debonding either at the top- or bottom-face of the specimen. Additional load is required to propagate the initial debond crack to a critical length (point B) where the remaining bonded length of the interface fractured catastrophically causing a sudden load drop. The magnitude of the load drop (B to C) due to frictional sliding of the fiber is reflective of the toughness of the interphase while the load level corresponding to the end of the drop (point C) is representative of the frictional shear characteristics of the debonded interfaces. The pushout test matrix is shown in Table 3.1 where P_A , P_{max} and P_s denote the load levels corresponding to point A, point B and point C, respectively.

3.3 Residual Stress Analysis

Significant level of thermal residual stresses are induced in the composite due to mismatches in the coefficients of thermal expansion of the constituent phases. The evolution characteristics of the residual stress field is investigated using the finite element method. In this analysis, the fiber distribution, as shown in Fig. 3.1, is idealized as a hexagonal array and a representative unit cell of a fiber embedded in the matrix phase is isolated for analysis as illustrated in Fig. 3.3(a). A radial plane of this axisymmetric cylinder model with a radius of $(R_f / \sqrt{V_f})$, where R_f and V_f are the radius of the fiber and the fiber volume fraction, respectively, is then discretized into finite elements with a mesh as illustrated in Fig. 3.3(b). The analysis assumes a generalized plane strain condition throughout the initial cool down of the composite. Boundary conditions of axial symmetry and plane symmetry about the $z = 0$ axis are imposed on the model. In an infinitely long composite where the free surface effect is negligible, and perfect bonding is assumed to exist between the fiber and the matrix, the shear stress component diminishes and the mechanical bonding is provided by the compressive radial stress only. This cylinder model is applied to a SCS-6/Timetal-21S metal matrix composite. The mechanical and physical properties of the SiC SCS-6 fiber and the titanium alloy Timetal-21S are obtained from several publications (LePe88, Mart92, Ghon93). While the fiber is assumed to behave elastically throughout the applied loading, the matrix inelastic strain response is described using a unified viscoplastic theory (Bodn75, Neu95). Since interface debonding in a SiC/Ti MMC have been observed to occur along the carbon-rich coating which is a thin layer in relation to the fiber or matrix dimension, the

interface can therefore be represented by a mathematical plane with zero thickness. This interface plane, therefore, accommodates only radial and shear stress components.

The process-induced residual stress field is established in the composite by a procedure involving cooling down from a stress-free temperature to room temperature and reheating to the test temperature at a rate of 0.03 °C/sec. The fiber and matrix phase are subjected to compressive and tensile residual axial stresses, respectively, during cool down because the coefficient of thermal expansion, CTE, of the SiC fiber (4.0×10^{-6} /°C at 25 °C) is less than of the titanium alloy matrix (9.8×10^{-6} /°C). The interphase region is a highly stressed region in the composite since it experiences the effect of both thermal strain due to CTE mismatches and mechanical strain due to differences in poisson ratios between the fiber and the matrix phase. The calculated evolution curves for the residual stresses in the matrix phase adjacent to the fiber/matrix interface is shown in Fig. 3.4. The axial component of residual stress predicted at 25 °C is 166 MPa. By comparison, an interactive experimental/mathematical technique, determined the axial component of residual stress in a SCS-6/Timetal-21S composite to be 160 and 174 MPa at 25 °C following a simulated cooling rate of 0.05 and 0.5 °C/sec, respectively (Ghon94). In the same study, a residual stress level of 198 MPa was achieved in a SCS-6/Ti-15-3 composite for a cooling rate of 0.5 °C/sec. Experimental measurement using X-ray diffraction technique on a SCS-6/Ti-15-3 composite showed a locked-in residual stress of 130 ± 30 MPa following an expected lower natural cooling rate (Cox90). These results indicate that the simulation as carried out in this study generate reasonable values for the internal stress field in the composite. In addition, the equivalent or von Mises stress, as shown in Fig. 3.4, is always lower than the yield

strength of the Timetal-21S matrix laminates (Ghon93. Rose84). The result of this study indicates that while the elastic portion of the evolution curve is controlled by the mismatches in the coefficients of thermal expansion between the fiber and the matrix, the stress magnitude is set by the degree of inelastic flow permitted in the viscoplastic affected range, from consolidation to about 600 °C.

The thickness requirement for a thin-slice composite specimen for fiber pushout test necessitates the influence of traction-free surface of the specimen on the residual stress field to be examined. A new finite element mesh for the cylinder model with finite thickness, H , is employed for this purpose as illustrated in Fig. 3.3(c). Smaller element size in the vicinity of the interphase region close to the surface enable the expected stress localization due to the traction-free surface to be accurately predicted. Additional constraint of a constant radial displacement is imposed on the outer surface of the modeled cylinder to acknowledge the interaction of surrounding fibers to the modeled fiber. Process-induced residual stress field at the test temperature is initially established using the procedure as described above. The traction-free surface is then simulated by relaxing the isostrain condition on both surfaces of the cylinder model. These boundary conditions allows the tensile and compressive axial residual stress components in the matrix and fiber, respectively, to diminish on the traction-free surface of the sample causing strain mismatch across the interface. Consequently, continuum shear stress develops in the interphase region along the fiber with greatest magnitude being located immediately below the traction-free surface and diminishes to zero at a distance of about three fiber radius beneath the surface. In addition, the axial displacement of the matrix surface produces a tensile radial stress component in the

immediate region below the surface. These variations of both radial and shear components of residual stresses along the interface in a thin-slice specimen at room temperature are shown in Fig. 3.5. The sample thickness is sufficient to retain the residual stress field of a thick composite specimen as indicated by a region of zero shear in the middle section of the sample. The calculated shear stress field has the same magnitude but opposite sign at the top and bottom side of the sample to satisfy the force equilibrium condition along the interface. Combination of tensile radial and continuum shear stress components could synergistically cause interface debonding at the traction-free surface of the sample. In this work, however, interface debonding is assumed to be a shear-dominated event for sufficiently thick samples. thus, the proposed methodology for shear strength determination is based on shear stress field at initial debonding.

3.4 Stress Analysis For Fiber Pushout Test

The stress field in a thin-slice composite sample following a pushout test is established using finite element method employing identical mesh as shown in Fig. 3.3(c). The pushout configuration is simulated by constraining the axial displacement of the matrix on one side (bottom) and pushing the fiber from the other (top). These displacement boundary conditions which exclude the effect of bending is adequate for describing initial debonding event during a fiber pushout test on sufficiently thick samples. At the test temperature, the applied load is increased from zero to the level, P_i , corresponding to initial

debonding as obtained from fiber pushout curve (Point A in Fig. 3.2). Perfect bonding of the interface is assumed throughout this loading. The calculated shear stress distribution in the interphase region along the pushout fiber due to P_i for the test temperature of 25 °C is illustrated in Fig. 3.6. The distribution indicates that the greatest magnitude of interphase shear stress due to pushout load occurs just beneath the bottom surface of the thin-slice specimen. The large shear stress magnitude indicates a large relative fiber/matrix displacement along the interface at this location. A shear stress localization of lesser magnitude is also predicted near the top surface of the specimen.

In a fiber pushout test, the thin-slice specimen is experiencing both the residual shear stress distribution as modified by the traction-free surface effect and the distribution of shear stress due to applied debond load. Both calculated stress fields, therefore, should be combined to yield a resultant shear stress distribution in the interphase region along the pushout fiber, as illustrated in Fig. 3.7(a) for the test condition at 25 °C. The superposition of both stress contributions from residual and pushout load at initial debonding resulted in an intense interphase shear stress localization at the bottom side of the specimen. On the other hand, the residual stress and pushout load contributions to the shear stress near the top surface result in a reduced shear stress localization. It is noted that the shear stress distribution diminishes to zero in a region along the interface away from the surface indicating that the residual shear stress field in this region is unaffected by geometrical constraints of the pushout test at the onset of interface debonding. The resulting interphase shear stress distributions along the pushout fiber at the onset of debonding are shown in Fig. 3.7(b) for the three temperatures considered in this work: 25, 500 and 650 °C. The large

magnitude of shear stress at the bottom surface of the specimen, coupled with a tensile radial component of residual stress suggested that interface debonding initiates from this location. At the onset of shear debonding, the shear stress magnitude should have reached the strength of the interphase region. The shear strength of the interphase, therefore, could be determined from this distribution.

3.5 Interphase Shear Strength

The interphase shear strength, τ_d , in the present work, is equivalent to the shear stress at which initial interface debonding occurs. The radial stress component, σ_{rr} , acting across the interface is prominent in dealing with the transverse strength of the interphase region. In a pushout test, the radial stress component contributes to frictional shear during progressive debonding of the interface debond crack. At the onset of debonding, the calculated shear stress in its limit, is infinite at the surface due to singularity arising from the traction-free surface boundary condition. The stress singularity is resolved by invoking an initial debond crack which could have initiated from the face of the specimen during cutting and sample preparation. In this work, a finite interface crack length of one fiber radius, fully controlled by a shear debonding process, is assumed to exist prior to performing a fiber pushout test. Therefore, the strength of the interphase region is determined by the resultant shear stress magnitude along the interface at a distance of one fiber radius from the bottom surface of the specimen. This procedure of determining the debonding shear strength of the

interphase region by considering the localization of shear stress along the interphase is illustrated in Fig. 3.7(b) for test temperature of 25 °C. Identical procedures are then repeated for different fiber pushout test conditions.

The experimental/numerical procedure proposed in this study to determine the interphase shear strength of a unidirectional MMC examines the contributions of both process-induced residual stress along the interface in a thin-slice specimen and that of the geometry-induced constraint of fiber pushout test configuration to the shear stress distribution. The resulting contributions of the residual shear stress component, τ_{res} , and of the shear stress induced by the effect of pushout load, τ_p , are quantified as listed in Table 3.2. At the onset of debonding, the residual stress contributes about 35 percent to the continuum shear of the interphase at room temperature while at 500 and 650 °C, the contribution is significantly less. The interphase shear strength of a SCS-6/Timetal-21S composite determined using the concept of stress localization is shown in Fig. 3.8 as a function of test temperature. The result indicates that the shear strength, τ_d , decreases with an increase in test temperature as larger magnitude of residual stress are relieved at higher temperature.

The average shear strength, τ_{d-ave} , calculated assuming a uniform interface shear is also shown in Fig. 3.8 as a dashed line. The strength is computed based on the peak pushout load prior to sliding of the fiber after fully debonded. The differences in results obtained by these two approaches indicate that the assumption of uniform interface shear stress along a pushout fiber underestimate the shear strength of the interphase region.

3.6 Discussion

The pushout load at initial debonding is determined through a fiber pushout test. The corresponding stress field along the pushout fiber is then computed using finite element method. The location of initial debonding is inferred by examining the peak of the stress localization along the pushout fiber. The shear stress magnitude at this location, therefore, is equivalent to the debonding shear strength of the interphase region. The shear strength values for a SCS-6/Timetal-21S composite determined using this approach ranges from 221 MPa at 25 °C to 138 MPa at 650° C. The result is consistent with the notion that in the absence of chemical bonding at the interface, the strength is derived from mechanical clamping due to process-induced residual stress which decreases with increasing temperature. Similar trends of decreasing interphase shear strength with test temperatures were also observed in a SCS-6/Ti-24-11 and a SCS-6/Ti-15-3 composites (Eldr94).

The selection of the initial debonding crack length, L_i , which forms during thin-slice specimen preparation is arbitrary. A better estimate of the initial crack length could have been obtained by recalculating the stress field along the fiber/matrix interface and employing an interface debonding criterion to establish L_i (Tami95). An assumed frictional behavior of debonded interface required in these calculations, however, contribute to a new uncertainty in the result. Therefore, this procedures is viewed by the authors as a refinement of the current work.

Specimen bending effects on the stress field during a fiber pushout test depends on combination of sample thickness, fiber diameter, width of groove in specimen holder, load

magnitude and test temperature. Specimen bending becomes significant at a loading condition for a large ratio of pushout load over specimen thickness. In this study, the application of pushout load is simulated up to the level at which a debond crack is initiated. The bending effect on load-displacement results of a fiber-pushout test performed on SCS-6/Timetal-21S and SM1240/Timetal-21S composites has been investigated (Osbo97). The study showed that the thicknesses of SCS-6/Timetal-21S composite specimen, as listed in Table 3.1, do not initiate an opening (mode I) crack at the traction-free surface prior to the onset of interface debonding. Consequently, the assumption of a shear-controlled debond crack initiation, as employed in this study, is adequate. Another factor which could modify the stress field along the interface is the growth of the interphase layer due to prolonged thermal exposure at elevated temperature. The growth kinetic study of a heat-treated SCS-6/Timetal-21S composite, however, indicated that thermal aging contributes insignificant variation in the interphase thickness at 650 and 900 °C for duration of up to 200 and 100 hours, respectively (Osbo95). As a result, the growth of this interphase has not been modeled in the simulation procedure used in this study.

Several analyses of fiber pushout test results assume a uniform interfacial shear stress distribution along the pushed out fiber at the initiation of debonding. The debond load, in such studies, is usually taken to be the maximum pushout load level prior to the load drop due to fiber sliding as indicated in a pushout load-displacement plot. This assumption of uniform shear implies that the debonding event occurs instantaneously along the interface followed by fiber sliding. In fiber pushout tests performed on a SCS-6/Timetal-21S and a SM1240/Timetal-21S composite specimen, particularly at elevated temperatures of 500 °C

and above, however, the reduction in the initial slope of the load-displacement curve is prominent. This change in slope indicates an initiation event of a debond crack, either at top- or bottom-face of the specimen, followed by the propagation of the debond crack and a possible inelastic matrix deformation. The average shear strength of the interphase, τ_{d-ave} , determined using the uniform shear stress assumption is also shown in Fig. 3.8. The plot indicates that this assumption underestimates the shear strength at all temperatures. In fact, the shear strength at 600 °C, determined by considering the localized shear stress field is four times larger than that calculated by assuming a uniformly distributed field. The discrepancy, however, is smaller at lower temperature as indicated in Fig. 3.7. The extension of a matrix crack at the fiber location during crack bridging creates a similar geometrical constraints, both in the traction-free matrix crack surface and in inducing additional clamping on the fiber, as observed in a thin-slice pushout specimen near the traction-free surface. A better comparison of these boundary conditions is achieved when considering a fiber pullout test setup. In view of the similarity in geometry between the fiber pushout test and that of crack bridging at the initial debond location, the interphase shear strength values, determined in the present work, can be treated as 'corrected' shear strength in modeling fatigue crack bridging in titanium MMCs.

The frictional shear stress associated with the load drop following fiber sliding can be determined from the force balance on the fiber at the end of the load drop. These interphase shear properties are related to the fracture toughness of the interphase. In Ref. (Lian93), the interphase toughness, G_i , is expressed to be proportional to the squared of the difference between the debond shear strength, τ_d , and the frictional shear stress, τ_s , i.e., $(\tau_d -$

τ_c). The resulting variations of the shear properties of the interphase with test temperature, as shown in Fig. 3.8, indicate that the assumption of a uniform stress distribution, which underestimates the shear strength of the interphase region, also leads to a lower value of interphase toughness, G_I . The calculated values of the interphase toughness as determined using τ_d obtained in the present work increases with increasing temperature. The values of the toughness for temperatures of 25, 500 and 650 °C are compared in Table 3.2.

Since the interphase region is the key in defining the damage process in a MMC, the knowledge of interphase toughness, in relation to the applied stress, would be critical in predicting the operating mode of fracture. The failure mode between interface delamination and fiber fracture can be predicted from the ratio of τ_d / σ_f , where σ_f is the fracture strength of the fiber (He89, Chan93). An underestimated value of the interphase shear strength employed in tailoring a composite properties would result in a failure dominated by fiber fracture. Since the interphase shear strength governs the length of interface debonding, which in turn, controls the extent of fiber/matrix interface debonding, it also controls the amount of crack tip shielding in the crack bridging process. In addition, the frictional shear stress on debonded interfaces has been identified as a significant parameter in understanding the mechanics of fiber/matrix interface region (Chan93, Ghos92, Baku93, Thou89). An accurate determination of the strength properties and frictional characteristic of debonded interfaces, therefore, is essential in successfully modeling the various damage modes operating during bridging fatigue crack growth in unidirectional Ti-MMCs.

3.7 Summary

The interphase shear strength of a SCS-6/Timetal-21S composite have been determined utilizing the concept of shear stress localization along the fiber in a fiber pushout test. The results can be summarized as follows:

1. An accurate assessment of the interphase shear strength through a fiber pushout test requires the load values at initial debonding and the distribution of stress field along the pushout fiber at this load. The assumption of a uniform shear stress distribution along the pushout fiber underestimates the shear strength of the interphase region.
2. The interphase shear strength consists of contributions from the effect of thermal residual stress field as modified by traction-free surfaces of thin-slice specimen geometry and the stress field due to pushout load at the onset interface debonding. The residual stress contributes about 35 % to the debonding interphase shear stress at room temperature while the contribution at 650 °C is about 15 %.
3. The interphase shear strength decreases with the increase in test temperature while the toughness of the interphase region increases with temperature.

3.8 References

- [Anan95] Ananth. C. R. and Chandra. N.. "Numerical Modeling of Fiber Push-out Test in Metallic and Intermetallic Matrix Composites - Mechanics of the Failure Process". Journal of Composite Materials. Vol. 29, No. 11, 1995, pp. 1488-1514.
- [Aves71] Aveston. J., Cooper. G. A. and Kelly. A.. "Single and Multiple Fracture." in The Properties of Fiber Composites. Conference Proceedings, National Physical Laboratory, Guildford, U.K., IPC Science and Technology Press Ltd., Surrey, England, 1971, pp. 15-26.
- [Baku93] Bakuckas. J. G. and Johnson. W. S.. "Application of Fiber Bridging Model in Fatigue Crack Growth in Unidirectional Titanium Matrix Composites". Journal of Composites Technology and Research. Vol. 15, No. 3, 1993, pp. 242-255.
- [Bodn75] Bodner. S. R. and Partom. Y.. "Constitutive Equations for Elastic Viscoplastic Strain Hardening Materials". Journal of Applied Mechanics. Vol. 42, 1975, pp. 385-389.

- [Budi86] Budiansky, B., Hutchinson, J. W. and Evans, A. G., "Matrix Fracture in Fiber-Reinforced Ceramics", Journal of the Mechanics and Physics of Solids, Vol. 34, No. 2, 1986, pp. 167-189.
- [Chan93] Chan, K. S., "Effects of Interface Degradation on Fiber Bridging of Composite Fatigue Cracks", Acta Metall. Mater., Vol. 41, No. 3, 1993, pp. 761-768.
- [Cox90] Cox, B. N., Dadkhah, M. S., James, M. R., Marshall, D. B., Moris, W. L. And Shaw, M., "On Determining Temperature Dependent Interfacial Shear Properties and Bulk Residual Stresses in Fibrous Composites", Acta Metall Mater., Vol. 38, No. 12, 1990, pp. 2425.
- [Davi92] Davidson, D. L., "The Micromechanics of Fatigue Crack Growth at 25 °C in Ti-6Al-4V Reinforced With SCS-6 Fibers", Metallurgical Transaction A, Vol. 23A, 1992, pp. 865-879.
- [Eldr94] Eldridge, J. I. and Ebihara, B. T., "Fiber Push-out Testing Apparatus for Elevated Temperatures", Journal of Materials Research, Vol. 9, No. 4, 1994, pp. 1035-1042.

- [Ghon93] Ghonem. H., Wen. Y., Zheng. D., Thompson. M. and Linsey. G., "Effect of Temperature and Frequency on Fatigue Crack Growth in Ti- β -21S Monolithic Laminate", Materials Science and Engineering, Vol. 161, 1993, pp. 45-53.
- [Ghon94] Ghonem. H., Wen. Y. and Zheng. D., "An Interactive Simulation Technique to Determine the Internal Stress States in Fiber Reinforced Metal Matrix Composites", Material Science and Engineering, Vol. A177, 1994, pp. 125-134.
- [Ghos92] Ghosn. L. J., Kantzos. P. and Telesman. J., "Modeling of Crack Bridging in a Unidirectional Metal Matrix Composite", International Journal of Fracture, Vol. 54, 1992, pp. 345-357.
- [Ghos94] Ghosn. L. J., Eldridge. J. I. and Kantzos. P., "Analytical Modeling of the Interfacial Stress State During Pushout Testing of SCS-6/Ti-Based Composites", Acta metall. mater., Vol. 42, No. 11, 1994, pp. 3895-3908.
- [He89] He. M. Y. and Hutchinson. J. W., International Journal of Solids and Structure, Vol. 25, 1989, pp. 1053-1068.

- [Kall92] Kallas. M. N., Koss. D. A., Hahn. H. T. And Hellmann. J. R., "On the Interfacial Stress State Present in a 'Thin-slice' Fiber Push-out Test." Journal of Materials Science. Vol. 27, 1992, pp. 3821-3826.
- [Kera91] Kerans. R. J. and Parthasarathy, T. A., "Theoretical Analysis of Fiber Pullout and Push Out Tests", Journal of the American Ceramic Society, Vol. 7, 1991, pp. 1585-1596.
- [Lian93] Liang. C. and Hutchinson. J. W., "Mechanics of Fiber Pushout Test". Mechanics of Materials, Vol. 14, 1993, pp. 207-221.
- [Mars85] Marshall. D. B., Cox. B. N. and Evans. A. G., "The Mechanics of Matrix Cracking in Brittle-Matrix Fiber Composites", Acta Metallurgica, Vol. 33, 1985, pp. 2013-2021.
- [Mart92] Martin. P. L., Bingel. W. H. and Mahoney. M., "SiC-Reinforced β -21S Creep Properties". Workshop Proceedings for Titanium Matrix Components, P. R. Smith and W. C. Revelos. eds., Wright-Patterson AFB, Ohio, WL-TR-92-4035, 1992, pp. 277-291.

- [McCa87] McCartney, L. N., "Mechanics of Matrix Cracking in Brittle-Matrix Fiber-Reinforced Composites", Proceedings of The Royal Society London, Vol. 409A, 1987, pp. 329-350.
- [McMe90] McMeeking, R. M. and Evans, A. G., "Matrix Fatigue Cracking in Fiber Composites", Mechanics of Materials, Vol. 9, 1990, pp. 217-227.
- [Neu95] Neu, R. W. and Bodner, S. R., "Determination of the Material Constants of Timetal-21S for a Constitutive Model", Contributive Research and Development, Vol. 6, Prepared for Wright-Patterson AFB, Ohio, Sept 1995.
- [Nguy94] Nguyen, T. -H. B. and Yang, J. -M., "Elastic Bridging for Modeling Fatigue Crack Propagation in a Fiber-Reinforced Titanium Matrix Composite", Fatigue Fract. Engng Mater. Struct., Vol. 17, No. 2, 1994, pp. 119-131.
- [Osbo95] Osborne, D. and Ghonem, H., "High Temperature Interphase Behavior of SiC Fiber-Reinforced Titanium Matrix Composites", Mechanics of Materials Laboratory, University of Rhode Island, Report: MML-95-1, 1995.
- [Osbo97] Osborne, D. and Ghonem, H., "Elevated Temperature Interfacial Properties of Continuous Fiber Reinforced Titanium Metal Matrix Composites", to be submitted to Materials Science and Engineering, 1997.

- [LePe88] Le Petitcorps, Y., Lahaye, M., Pailler, R. and Naslain, R., "Modern Boron and SiC CVD Filaments: A Comparative Study", Composites Science and Technology, Vol. 32, 1988, pp. 31-55.
- [Phil74] Phillips, D. C., "Interfacial Bonding and Toughness of Carbon Whisker Reinforced Glass-Ceramics", Journal of Material Science, Vol. 9, No. 11, 1974, pp. 1847-1854.
- [Prew80] Prew, K. M. and Brennan, J. B., "High-Strength Silicon Carbide Fiber-Reinforced Glass-Matrix Composites", Journal of Material Science, Vol. 15, No. 2, 1980, pp. 463-468.
- [Rose84] Rosenberg, H. W., "Ti-15-3- Property Data", in Beta Titanium Alloys in the 80's, R. R. Boyer and H. W. Rosenberg, eds., The Metallurgical Society of AIME, Warrendale, PA, 1984, pp. 409-432.
- [Sens90] Sensmier, M. D. and Wright, P. K., "The Effect of Fiber Bridging on Fatigue Crack Growth in Titanium Matrix Composites", Fundamental Relationships Between Microstructure and Mechanical Properties of Metal Matrix Composites, M. N. Gungor and P. K. Liaw, eds., The Mineral, Metal and Materials Society, Warrendale, PA, 1990, pp. 441-457.

- [Tami95] Tamin, M. N., Osborne, D. and Ghonem, H., "Influence of Interfacial Properties on Fiber Debonding in Titanium Metal Matrix Composites". Fatigue and Fracture at Elevated Temperature, A. Nagar and S. Mall, eds., The American Society of Mechanical Engineers, New York, NY, AD-Vol. 50, 1995, pp. 121-134.
- [Tele93] Telesman, J., Ghosn, L. J. and Kantzos, P., "Methodology for Prediction of Fiber Bridging Effects in Composites". Journal of Composites Technology and Research, Vol. 15, No. 3, 1993, pp. 234-241.
- [Thou89] Thouless, M. D., Sbaizro, O., Sigl, L. S. and Evans, A. G., "Effect of Interface Mechanical Properties on Pullout in a SiC Fiber-Reinforced Lithium Aluminum Silicate Glass-Ceramic". Journal of The American Ceramics Society, Vol. 72, 1989, pp. 525-532.
- [Warr92] Warren, P. D., Mackin, T. J. and Evans, A. G., "Design, Analysis and Application of an Improved Push-through Test for the Measurement of Interface Properties in Composites". Acta Metall Mater., Vol. 40, 1992, pp. 1243-1249.

- [Wats92] Watson, M. C. and Clyne, T. W., "The Use of Single Fiber Pushout Testing to Explore Interfacial Mechanics in SiC Monofilament-Reinforced Ti - II. Application of the Tests to Composite Material", Acta Metall Mater., Vol. 40, 1992, pp. 141-148.
- [Yang91] Yang, J. M., Jeng, S. M. and Yang, C. J., "Fracture Mechanisms of Fiber-Reinforced Titanium Alloy Matrix Composites. Part I: Interfacial Behavior", Material Science and Engineering, Vol. A138, 1991, pp. 155-167.
- [Zhen95] Zheng, D. and Ghonem, H., "Fatigue Crack Growth of SM1240/Timetal-21S Metal Matrix Composites at Elevated Temperatures", Metallurgical and Materials Transactions A, Vol. 26A, 1995, pp. 2469-2478.

Table 3.1 Test matrix for fiber pushout tests of SCS-6/Timetal-21S composites.

ID	T (°C)	H (mm)	P _i (N)	P _s (N)	P _{max} (N)	τ_{d-ave} (MPa)
1	25	0.50	46	37.5	46.0*	209.2
2	163	0.52	31	23.9	33.4	146.0
3	250	0.91	50	40	53.2	133.0
4	350	1.10	44	28	54.3	112.3
5	500	1.40	23	25.5	32.5	52.8
6	650	1.40	20.5	17.9	27.0	43.8
7	735	0.95	12	2.5	16.0	38.3

* Load corresponding to the first load drop which is less than the peak value

Table 3.2 Process-related interphase properties of SCS6/Timetal-21S composites

T (°C)	τ_d (MPa)	τ_{res} (MPa)	τ_p (MPa)	τ_s (MPa)	G _i (Jm ⁻²)
25	221.2	76	145.24	149.2	45.9
500	160.5	23	137.5	41.2	1039
650	138.6	8.75	130	20.6	1034

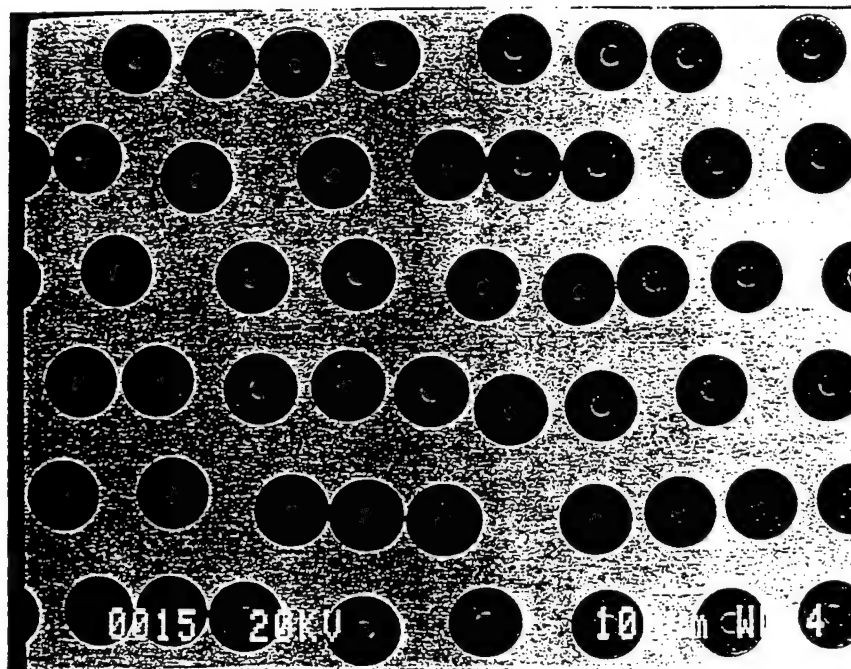
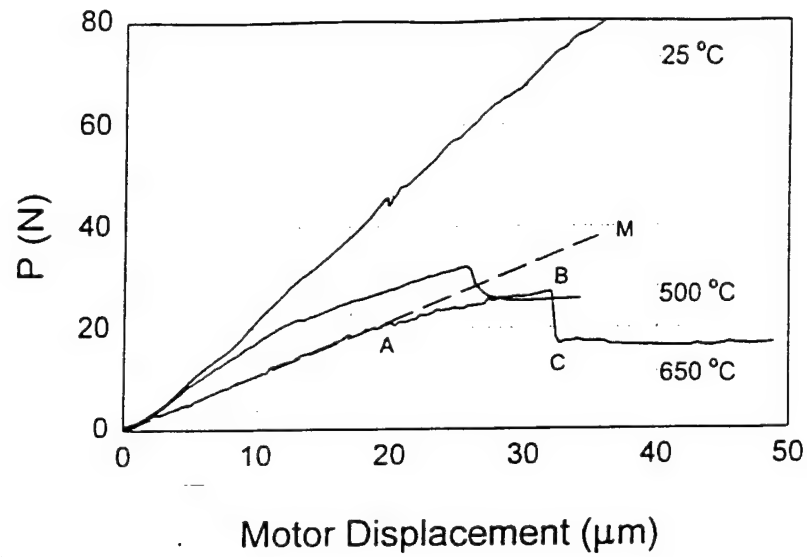
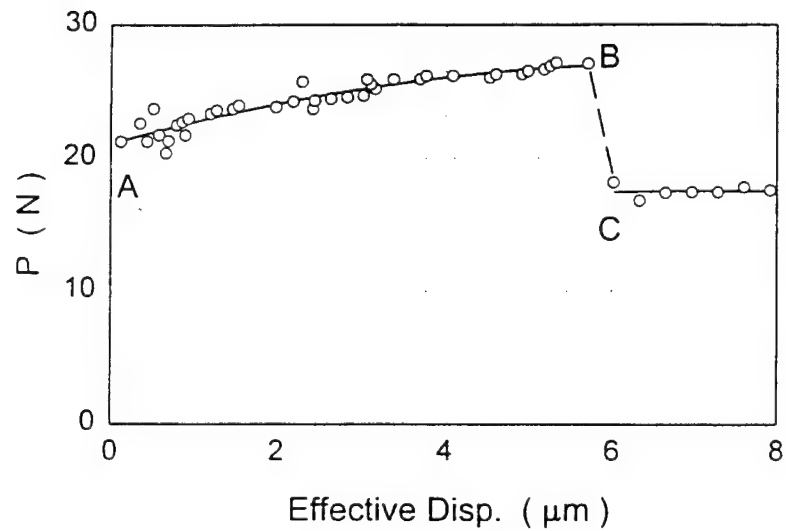


Fig. 3.1 Polished and etched cross section of a SCS-6/Timetal-21S composite showing a staggered array architecture of fiber distribution.



(a)



(b)

Fig. 3.2 (a) Load-displacement curves for fiber pushout tests of a SCS-6/Timetal-21S composite at ambient temperature, 500 and 650 °C. The specimen thickness, $H=1.4$ mm. (b) Load-effective displacement curve corrected for compliance for test at 650 °C.

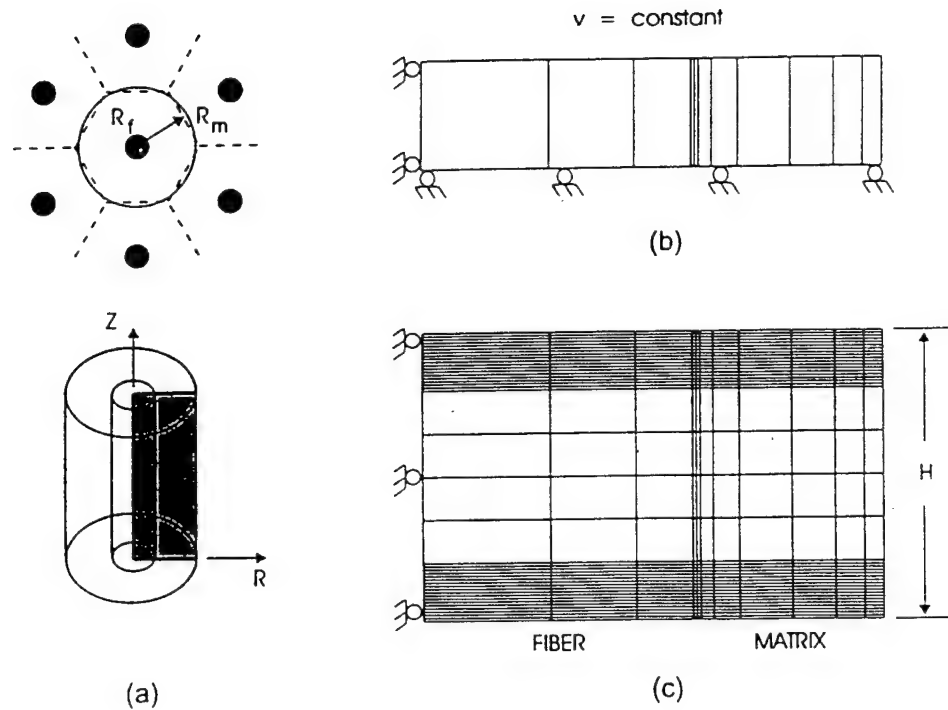


Fig. 3.3

(a) A representative unit cell of the composite consisting of a fiber embedded in the matrix phase. (b) Finite element mesh employed in modeling the evolution characteristics of residual stress in the composite during initial cooldown. (c) Refined finite element mesh use in modeling fiber pushout test.

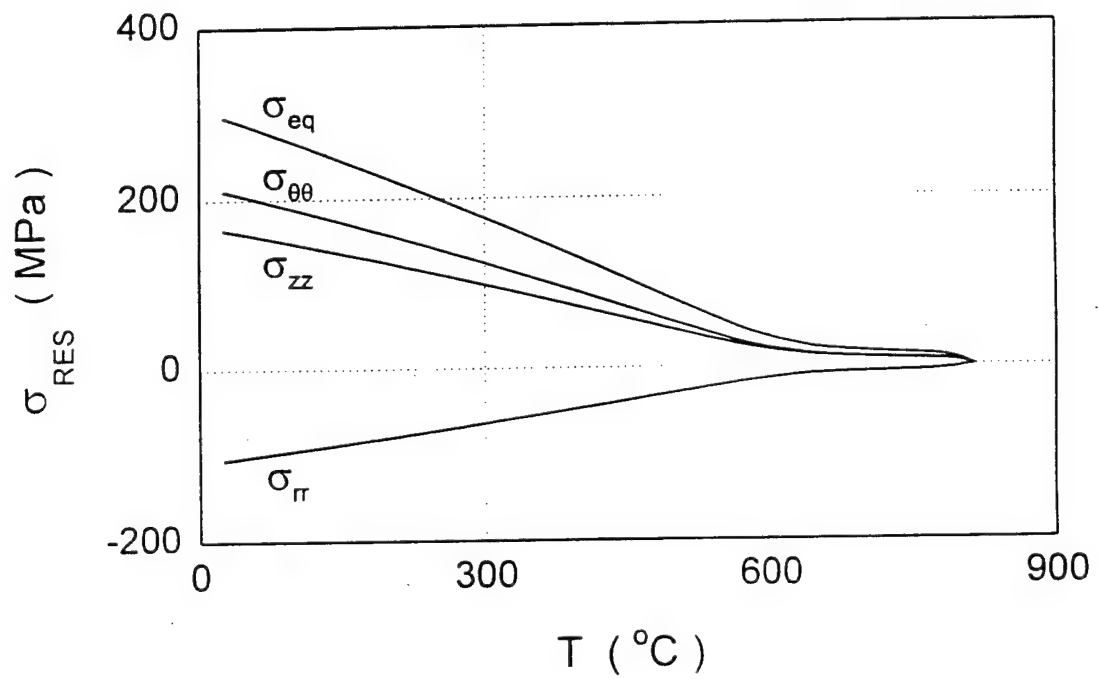


Fig. 3.4

Evolution of residual stresses in the matrix phase of a SCS-6/Timetal-21S composite during initial cool down at 0.03 °C/sec from stress-free to ambient temperature. The matrix stress is taken in the region adjacent to the fiber/matrix interface.

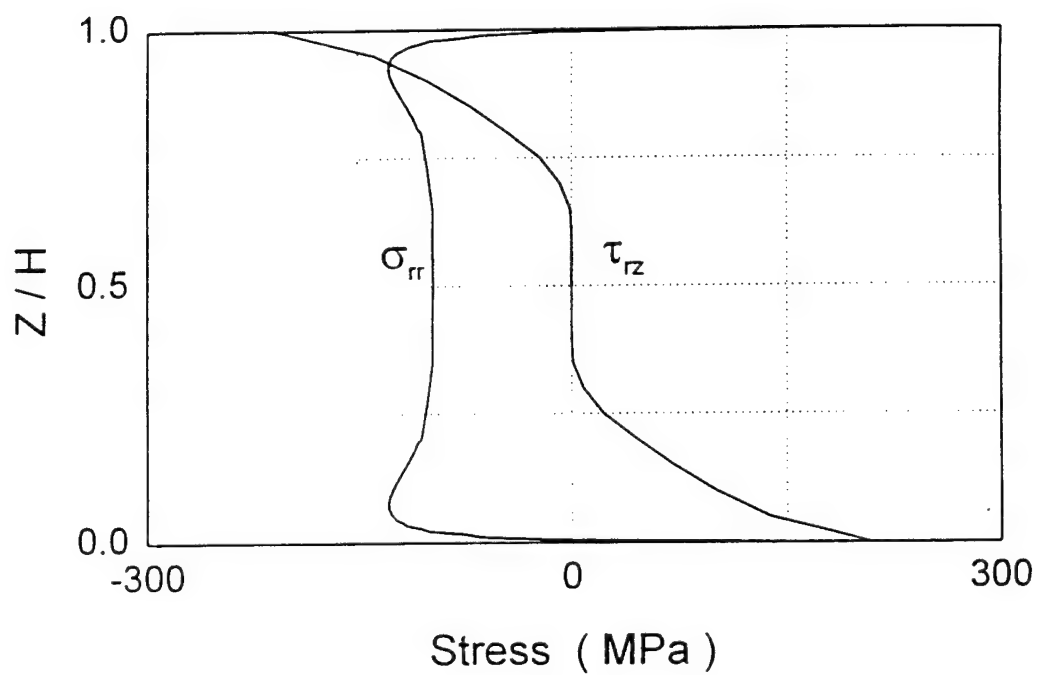


Fig. 3.5 Variations of residual radial and shear stress components along the fiber/matrix interface in a thin-slice composite specimen at 25 °C. The sample thickness, $H = 0.50$ mm.

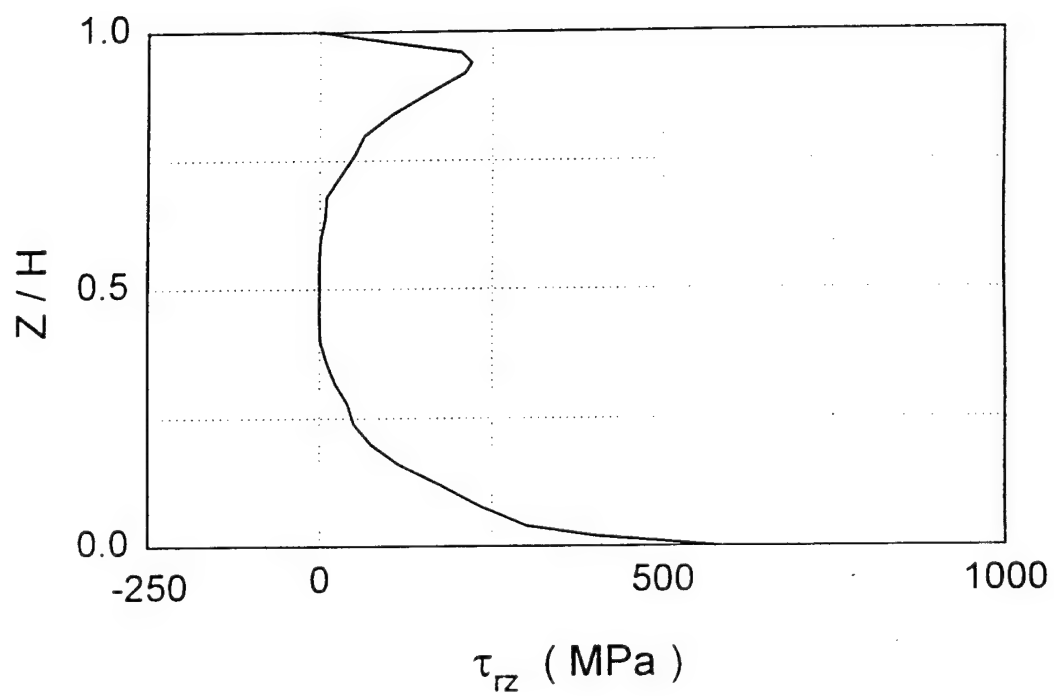
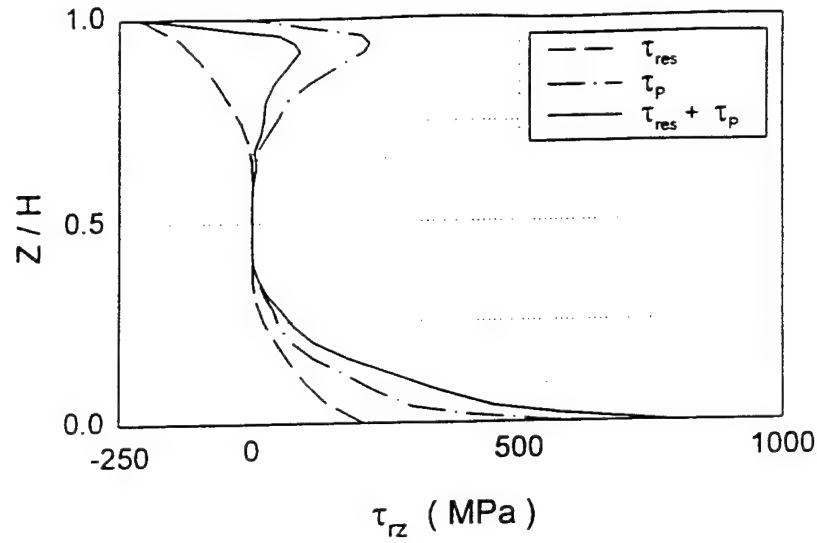
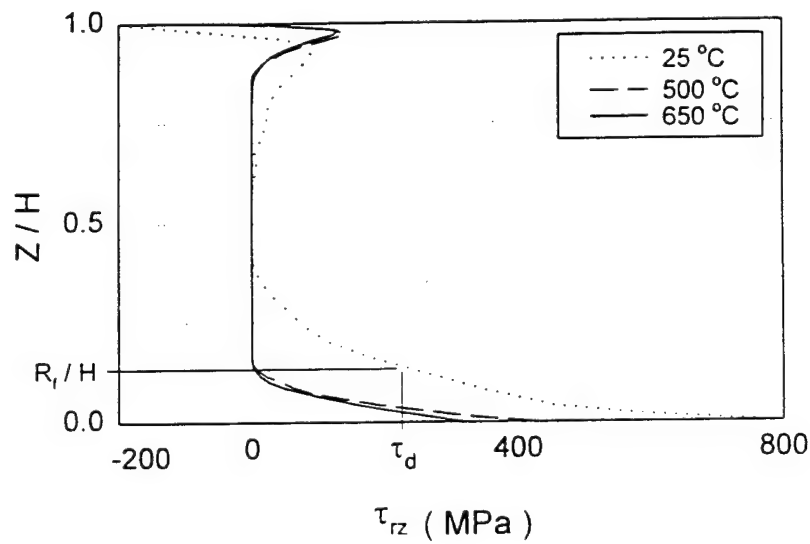


Fig. 3.6 Shear stress distribution along the interface due to applied load at the onset of interface debonding in a fiber pushout test performed at 25 °C. The specimen thickness, $H = 0.5$ mm.



(a)



(b)

Fig. 3.7

(a) Superposition of shear stress distributions due to effect of thermal residual stress and stress field due to pushout load at the onset of interface debonding in a fiber pushout test performed at 25 °C. (b) Resultant interface shear stress distributions for various test conditions. The specimen thickness, $H=0.50$ mm for 25°C and $H=1.4$ mm for 500 and 650 °C. The concept of stress localization in determining the interphase shear strength, τ_d , is illustrated for the case of 25°C

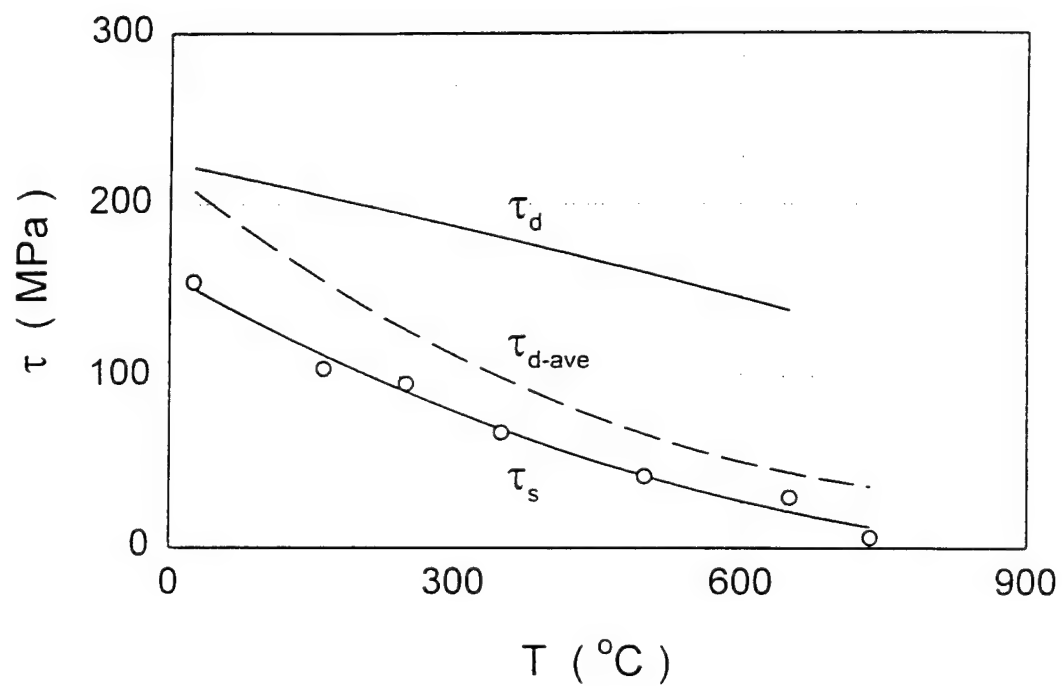


Fig. 3.8 Influence of temperature on interphase shear strength, τ_d , and frictional shear stress, τ_s . The dashed line represents the average shear strength values, τ_{d-ave} , determined using the assumption of uniformly distributed shear force along the pushout fiber.

CHAPTER 4. Interface Debonding in Titanium Metal Matrix Composites⁴

Abstract

A crack bridging model is proposed based on the notion that the fiber/matrix interface debonding length along a bridging fiber has a direct relationship with the traction provided by the fiber. An interface debonding criterion which compares the localized shear stress field due to a traction-free matrix crack surface with the debonding shear strength of the interphase region is introduced and incorporated into the model. The model is examined by establishing a correlation between debonding lengths and closure pressure distribution along a fiber-bridged crack surface in a SCS-6/Timetal-21S composite. Once the initial debonding length along a bridging fiber has been established, the interface mode II crack tip driving force is determined using an analysis which employ the knowledge of the interface debond crack opening displacement along the fiber. Results of this study showed that the debonding length of a bridging fiber increases with increasing test temperature level. The mode II

⁴ To be submitted for publication: M. N. Tamin and H. Ghonem, "Interface Debonding in Titanium Metal Matrix Composites." *Fatigue and Fracture of Engineering Materials and Structures*, March 1997.

debond crack tip driving force increases with an increase in debond crack length but has an inversely relationship with test temperature.

4.1 Introduction

The crack bridging process in a unidirectional SiC/Ti metal matrix composite, Ti-MMC, involves matrix cracking accompanied by interface debonding along bridging fibers. The localized stress field associated with matrix crack surfaces initiates a debond crack at the fiber matrix interface. The initial debonding length will depend on the stress field and the strength properties of the interphase region. The stress field at the interface along a bridging fiber has been previously examined [McCa87, Tami95]. The debonding shear strength of the interphase region has been determined experimentally [Eldr94, Wats92] or through a combined experimental/numerical procedure [Tami97]. Several approaches for interphase strength characterization include fiber pushout, fiber pullout, fiber push-through and fiber fragmentation tests [Eldr94, Wats92, Yang91, Warr92, Kera91, Osbo95]. The growth of the debond crack during subsequent loading cycles, however, is dictated by the crack-tip driving force and fracture toughness of the interphase material. The tip of a fiber-matrix interface crack may also experience a combination of opening and shearing modes of failure, therefore, more than one stress intensity factor are expected to coexist [Chan89]. Since the interphase region in a Ti-MMC is a reaction product of the fiber material, the carbon-rich fiber coating and the titanium alloy matrix, assessment of its

fracture properties is a challenging task. The interphase toughness of B/Ti and SiC/Ti MMCs at room temperature have been estimated [Chan89].

The extension of the matrix crack tip during bridging fatigue crack growth is resisted by intact fibers in the wake of the crack. These fibers provide traction which acts in opposing direction to the applied load. The discrete fiber traction along a bridged crack length, therefore, provides the shielding force for the matrix crack tip [McMe90, Mars85, McCa87, Zhen95]. This traction on a bridging fiber can be visualized through a force-balance on an isolated fiber with the fiber traction resisted by applied load, shear force in the bonded region ahead of the debond crack tip, and frictional force on debonded interfaces. The length of interface debonding, therefore, has a direct relationship with the bridging fiber traction. The magnitude of the bridging fiber traction is further influenced by the load transfer process from the matrix to the fiber resulting from time-dependent inelastic deformation of the matrix phase, particularly at elevated temperature.

The bridging fiber traction, expressed as a closure pressure distribution on the bridged portion of the crack surfaces, however, could not be measured directly. Several approaches which have been attempted to quantify the closure pressure include the force-based formulation [Mars85] and the energy balance calculations [McCa87], both applied to a shear lag model, as well as a strength of material approach to stress calculations on beams [Hoag72, Ghos92]. The shear lag model relies on crack opening displacement (COD) measurements along the crack length as well as the frictional shear stress along the debonded interfaces. The COD profile for a bridged crack in a unidirectional SiC/Ti MMC is obtained by measuring the displacements at several positions along a propagating crack [Zhen95,

John93]. The resulting closure pressure is then utilized in a fracture mechanics equation for the crack tip driving force by superimposing the solution of a crack subjected to a far field applied stress range and a crack subjected to a change in the pressure [Tada85]. It is noted that the frictional shear stress, τ_s , which is an important parameter in deriving these models, is assumed as a constant. The degradation of τ_s with time, temperature and fatigue reversals, however, appear to be an important consideration as dictated by the wide and different values reported by many authors [Osbo97, Eldr94, Wats92]. This variation in τ_s , however, is difficult to implement in these models. As a result, a wide range of the frictional shear stress values was obtained from various shear-lag type analyses which suggest that these models lack predictive capability [Baku93, Tele93, Hutc90, Cox91].

A recent analysis of fatigue crack growth in a SiC/Ti MMC to correlate the crack tip shielding and the interface debonding length has been performed by some authors aiming at estimating the effective crack tip driving force. Nguyen and Yang [Nguy94] proposed a crack bridging model based upon elastic extension of the fiber out of the matrix with and without sliding friction resisting the deformation. The model, which utilizes experimentally measured COD profile, identified the debonding length as a defining variable for the bridging fiber traction, and hence, the crack tip shielding force. Results of a modified shear lag model developed by Ghonem [Ghon96] supported this conclusion. The fiber/matrix interface debonding length along a bridging fiber, L_d , can be viewed to consist of an initial debonding length, L_i , and the debond crack increment, ΔL , due to subsequent fatigue cycles. The initial debonding length is caused by crack deflection in a localized stress field of a matrix crack tip approaching the fiber while its increment is a result of interface crack

propagation along the fiber.

The objective of this study is to establish a closure pressure distribution along a fiber-bridged crack length with the notion that the fiber traction, thus, the crack tip shielding force is directly related to the interface debonding length. The mechanics of fiber/matrix interface debonding in a titanium matrix composite is described through a proposed stress-based criterion for debond crack initiation. The criterion, which is incorporated into a crack bridging model, is examined by establishing an initial debonding length along a bridging fiber in a SiC/Ti MMC. The model was executed by combining fracture mechanics equations with the results of a two-phase cylinder finite element model simulating a bridging fiber embedded in the matrix phase. Once the debonding lengths of bridging fibers along the crack length have been established, the corresponding fiber traction is evaluated through force-balance analysis on each bridging fiber. A correlation between debonding lengths and bridging fiber closure pressure is then established. The influence of test temperature on the length of interface debonding is also investigated. The interface crack tip driving force is estimated using the calculated interface mode II COD along the debond crack length.

The stress-based debonding criterion, which establishes an initial debonding length along a bridging fiber, is described in the next section along with the requirements for its implementation. The criterion is then incorporated into a crack bridging model which attempts to establish the profile of debonding lengths along bridging fibers in a bridged crack region. The concept of the model is described in the following section. The procedures are outlined in the appendix along with the description of a finite element model employed for crack bridging simulation. The results on interface debonding lengths, their correlation with

the closure pressure, and the interface crack tip driving force for a SiC/Ti MMC are presented and discussed.

4.2 Interface Debonding Criterion

In a bridging crack growth process, interface debonding initiates in the stress field of a matrix crack tip approaching a fiber. The traction-free matrix crack surface relieves the longitudinal stress component on the surface with a corresponding crack opening displacement. The associated strain mismatches across the fiber/matrix interface, then, induces a continuum shear stress distribution in the interphase region along the fiber which peaks at the section coinciding with the matrix crack plane and diminishes completely in the far-field region along the interface. The crack opening displacement also presents a geometrical constraint which causes a tensile radial stress to act in the immediate region beneath the traction-free crack surface.

Based on the localized stress field at the interface, the concept of fiber/matrix debond crack initiation is presented, as illustrated in Fig. 4.1. Interface debonding is assumed to occur instantaneously along the fiber for a length where the shear stress magnitude, $|\tau_{rz}|$, exceeds the debonding shear strength of the interphase region, τ_d . This stress-based debonding criterion can be expressed mathematically as

$$|\tau_{rz}| \geq \tau_d = L_1 \quad (4.1)$$

where L_1 is the initial debonding length along the bridging fiber. Upon initial debonding, frictional shear stress acts between the debonded interfaces under the compressive radial stress component acting across the interfaces. In the absence of chemical bonding at the interface, the frictional behavior of the debonded interfaces is assumed to be adequately represented by Coulombs law in which the frictional shear stress, τ_s , can be written as

$$\tau_s = -\eta p \quad (4.2)$$

where η is the coefficient of friction between the debonded interfaces and p is the pressure acting across the fiber/matrix interface. The relative displacement between the fiber and the matrix along the debonding length lowers the peak of the shear stress distribution to the shear strength value at tip of the debond crack.

The debonding criterion, as described above, requires the knowledge of the stress field at the fiber/matrix interface and the interfacial properties, namely, the debonding shear strength and the coefficient of friction for debonded interfaces. In this study, the shear stress variation along a bridging fiber is simulated using finite element analysis performed on a unit cell model of a bridging fiber embedded in the cracked matrix phase. Details of the mesh and boundary conditions of the model are described in the appendix of this paper. Previous work have shown that different initial cooling rates in the range of 0.03 to 0.1 °C/sec and heat

treatment for duration of 8 hours at 650 °C did not alter significantly the residual stress level in the SCS-6/Timetal-21S composite [Tami97], therefore, the heat treatment procedure is not being model in simulating the evolution of residual stresses in this composite. In addition, the fiber/matrix interface is assumed to be perfectly bonded throughout the cooldown process.

The modification of the stress state along the interface region due to a matrix crack is simulated by allowing the matrix boundary along the r-axis to displace longitudinally, thus creating a traction-free crack surface. The applied loading to the cylinder model mimics that which was used in the experimental study on bridging fatigue crack growth of a SCS-6/Timetal-21S composite. The tests were performed using center-hole specimens at room temperature, 500 and 650 °C and a loading frequency of 10 Hz. In these tests, the applied stress range, $\Delta\sigma_a = 270$ MPa with the ratio of minimum to maximum applied stress ratio, $R = 0.1$ was employed.

The debonding shear strength of the interphase region have been determined in a separate study [Tami97]. In the study, pushout load values at initial fiber/matrix interface debonding in a thin-slice composite specimen are used to generate the variation in the stress field along the pushout fiber in the corresponding specimen. The debonding shear strength is then defined as equivalent to the peak of the shear stress localization at the onset of debonding. The resulting debonding shear strength as a function of temperature is shown in Fig. 4.2. In the absence of chemical bonding, the strength is provided by process-induced residual stress through mechanical clamping on the fiber, therefore, the strength decreases with temperature as the residual stress is relieved at higher temperature. The influence of

surface roughness of debonded interfaces on the initial debonding length and the associated bridging fiber traction have been examined [Osbo97, Tami95]. In the present study, however, a single value of the coefficient of friction $\eta = 0.15$, is used in eq. (4.2) in order to minimize scatter of results due to many parameters involved in the proposed crack bridging model.

The initial debonding length along a bridging fiber is established through a series of discrete calculations of force equilibrium on the cylinder model with increasing debond crack length. This concept in establishing the initial debonding length is schematically illustrated in Fig. 4.3 for test temperature of 25 °C. A finite debond crack is first introduced along the interface which lowers the peak shear stress distribution. The peak of the shear stress variation always occurs at the tip of the debond crack due to sudden change in interface geometry from debonded to perfectly bonded region ahead of the crack tip. Additional increments of crack length are introduced and the equilibrium stress field in the composite are re-established until the peak shear stress is lowered to the shear strength value of the interphase region. The procedure is then repeated for different test conditions.

4.3 Crack Bridging Model

The distribution of interface debonding lengths along bridging fibers over a bridged matrix crack length is established through the concept of local effective stress range. The model is applied to a specimen geometry with a center-crack of length $2a$, as illustrated in

Fig. 4.4. A stress range, $\Delta\sigma_a$, is remotely applied to the composite specimen in the direction parallel to the fiber orientation. The effective crack tip driving force for this bridging crack is given by the applied stress intensity factor range less the shielding effect [Tada85], i.e.

$$\Delta K_{tip} = Y \Delta\sigma_a \sqrt{\pi a} - 2 Y \sqrt{\frac{a}{\pi} \int_{a_0}^a \frac{\Delta p(x)}{\sqrt{a^2 - x^2}} dx} \quad (4.3)$$

The distance, x , in the above equation is measured from the center of the crack of length $2a$ while the parameter Y is a geometric factor for finite specimen width correction [Broe74]. The profile, $\Delta p(x)$ is the distribution of bridging fiber pressure over the bridged region of the crack ($a - a_0$), where a is the crack length and a_0 is the non-bridged initial crack length (see Fig. 4.4). The model aims at describing the closure pressure profile, $\Delta p(x)$, and its correlation with the debonding lengths along bridging fibers in the bridged crack region.

In this study, the matrix crack is assumed to extend in a discrete manner with each crack extension encompassing one bridging fiber. Consequently, the debonding length along the first bridging fiber, which is the one farthest away from the crack tip, is determined by considering a length of matrix crack bridged by a fiber and is subjected to the far-field applied stress range. The debonding length along the bridging fiber, L_d , is established through the interface debonding criterion, as described in the previous section. The corresponding fiber traction range, $\Delta S(x)$, is converted into the bridging fiber pressure, $\Delta p(x) = \Delta S(x) * V_f$, where V_f is the fiber volume fraction of the composite, and employed in the shielding term of eq. (4.3) to calculate the effective matrix crack tip stress intensity factor

range, ΔK_{up} , for this crack length. This driving force can be viewed as being provided by an effective stress range, $\Delta\sigma_e$, acting on a homogenized composite specimen with a center crack of total length encompassing two bridging fibers, one on each side. Thus one can write

$$\Delta K_{up} = Y \Delta\sigma_e \sqrt{\pi a} \quad (4.4)$$

The extension of the matrix crack over the second bridging fiber, adjacent to it, depends on the magnitude of this driving force and the toughness of the matrix phase. In this model, the interface debonding length along the second bridging fiber is determined by considering the existing crack which is bridged by a fiber and has propagated past the second bridging fiber. In order to employ the cylinder model on the second bridging fiber, the existence of the first bridging fiber need to be considered. This is achieved by calculating the local stress range acting on the cylinder model representing the second bridging fiber. An initial estimate of this stress range, denoted as $\Delta\sigma_e^*$, could be obtained by assuming that the crack tip stress intensity factor range, ΔK_{up} , as calculated in eq. (4.4) provides the driving force for the new crack of a length which span past two bridging fibers. The resulting traction provided by this bridging fiber is combined with the traction on the first fiber to yield the closure pressure distribution, $\Delta p(x)$, along the current bridged crack length. The updated stress intensity factor range for this crack, which include two bridging fibers, can be calculated using eq. (4.3). The corresponding effective stress range acting on an equivalent homogenized composite specimen containing this crack is determined from eq.

(4.4). This newly determined stress range is compared with the initial estimate and the calculations are repeated until a converged value of $\Delta\sigma_c$ acting on the cylinder model is achieved. The crack is then extended past the next bridging fiber and the procedure for establishing the interface debonding length along the fiber is repeated. These steps are outlined in the appendix of this paper.

The crack bridging model is applied to a SCS-6/Timetal-21S composite with nominal fiber volume fraction, $V_f = 0.35$. Crack bridging condition is induced in this composite by performing a fatigue test at room temperature on a center-hole specimen with an initial pre-crack length of $2a_0 = 2.13$ mm. The test was conducted at a loading frequency of 10 Hz with an applied stress range of 270 MPa and load ratio, $R = 0.1$. The crack geometry and bridging crack growth behavior of the composite at 25 °C is shown in Fig. 5, where the crack was arrested beyond 1.5×10^6 fatigue cycles with a final crack length of 8.63 mm. The distribution of debonding lengths along bridging fibers when the crack reached a length of $2a = 5.92$ mm ($N = 7.15 \times 10^5$ cycles) will be established in this analysis. The simulations were performed for an estimated 7 bridging fibers (per fiber layer in the composite) along half crack length, a .

4.4 Driving Force for Interface Crack

Fiber/matrix interface debonding is viewed in this study as a sequence of an initial debonding event followed by propagation of the debond crack length during subsequent

loading cycles. The debond crack along the fiber/matrix interface may experience a combined opening (mode I) and shearing (mode II) types of failure. The complex crack-extension driving force has been examined, based on elastic COD, for a crack along a bimaterial interface [Chan89]. The propagation of a fiber/matrix interface crack, however, is assumed in this study to be dominated by a shear-type (mode II) fracture in the presence of compressive residual stress acting across the interface. Based on the model in Ref. [Chan89], the stress intensity factor range for the interface crack, ΔK_{II} , therefore, can be written as follows

$$\Delta K_{II} = \sqrt{\frac{\pi}{2}} \frac{\lambda_1 D}{C (\lambda_1^2 - \lambda_2^2)} \quad (4.5)$$

where the parameters λ_1 and λ_2 for matrix and fiber, respectively, are defined as

$$\begin{Bmatrix} \lambda_1 \\ \lambda_2 \end{Bmatrix} = \frac{1}{\cosh \pi \epsilon} \begin{Bmatrix} \cos \epsilon \ln \left(\frac{r}{2L_d} \right) \\ \sin \epsilon \ln \left(\frac{r}{2L_d} \right) \end{Bmatrix} \quad (4.6)$$

In the above equation, r is a distance along the interface crack measured from the crack tip.

and L_d is the length of the interface crack. The two phases, namely, matrix and fiber are described by the bimaterial elastic constant for plane strain condition, ϵ [Hut87]. The value of ϵ for a SCS-6/Timetal-21S composite is 0.035. For a monolithic matrix material, the constant ϵ is reduced to zero. The material constant, C , in eq. (4.5) is defined as

$$C = \frac{1 - \nu_1}{\mu_1} + \frac{1 - \nu_2}{\mu_2} \quad (4.7)$$

where ν_1 and μ_1 are poisson ratio and shear modulus for the matrix phase while ν_2 and μ_2 are the respective values for the fiber. The constant D is related to the shear crack opening displacement or the relative tangential displacement between the fiber and the matrix, which is defined as the slope of mode II COD versus \sqrt{r} plot.

The propagation of the interface crack along a bridging fiber is described in this work in terms of the available mode II crack tip stress intensity factor range, ΔK_{II} , for various debond crack lengths. This is achieved by calculating the relative tangential displacement between fiber and matrix along the debonded interfaces as influenced by the stress and strain field in the interphase region. This interface crack tip driving force also define the shielding effect on a fiber-bridged crack tip.

4.5 Results and discussion

The initial debonding lengths along the first bridging fiber is shown in Fig. 4.6 as a function of temperature. The length, which increases with increasing test temperature, ranges from 0.75 mm at 25 °C to 1.45 mm at 650° C. The length of the fiber-matrix debonded interface along the bridged matrix crack in several SiC/Ti MMC systems have been previously studied [e.g. Zhen95, Baku93, Hutc90, Cox91, Davi92]. Davidson [Davi92] showed that the slip length, which include the entire interface damage process zone in a SCS-6/Ti-6-4 composite, measured from the crack plane, could reach up to 1 mm at 25 °C. Bakuckas and Johnson [Baku93] estimated the debonded length in a SCS-6/Ti-15-3 composite at room temperature to be 1500 μm at the first intact fiber closest to the crack mouth of a fiber-bridged crack length, $a = 4.28$ mm. Zheng and Ghonem [Zhen95] measured the fiber pull-out length along the fracture surfaces of a SM1240/Timetal-21S composite specimens. This length, which was assumed to be proportional to the debonded length of the corresponding fiber, was found to be temperature dependent with an average ranging from 120 μm at 24 °C to 215 μm at 650 °C. These values are plotted in Fig. 4.6 for comparison.

The trend of longer debonding lengths at higher temperature is attributed to the dependency of residual stress field in the interphase region on temperature. Since fiber/matrix interface bonding is provided by mechanical clamping on the fiber through the compressive radial stress component acting along the interface, weaker bond is expected at elevated temperature when this residual stress field relaxes. This is supported by the

observed lower debond shear strength of the interphase at higher temperature, as shown in Fig. 4.2. In addition, elevated temperature of 650 °C have shown to leave a smooth debonded interfaces within the carbon-rich coating layers of SiC SM1240 fibers [Zhen95]. This smooth surfaces indicate that interface debonding is enhanced at elevated temperature. The surface roughness of the interface, which influence the debonding process, depends on the debonding location and coating characteristics of the SiC fibers. Zheng and Ghonem [Zhen95], in their work on a SM1240/Timetal-21S composite, found that debonding occurs within the carbon coating layer or between the carbon and the TiB_2 layers. For the same composite, Marshall et al. [Mars92] examined the surface of pulled out fibers and concluded that sliding occurs between carbon and TiB_2 fiber coating layers in both as-fabricated and heat treated specimens. On the other hand, in a SCS-6/Ti-6-4 composite, cyclic loading causes debonding to occur between the carbon-rich coating and the SiC part of the fiber, as well as between the different layers of the carbon coating [Davi92]. Yang et al. [Yang91] and, Eldridge and Ebihara [Eldr94]) in separate studies, reached similar conclusion regarding the locations of interfacial debonding in a SCS-6/Ti-15-3 composite. They observed that debonding occurs at locations between the fiber and its multiple carbon coatings, within the carbon layers, and occasionally between the coating and the reaction zone. SEM observation of fiber surface of a SCS-6/Ti-24-11 composite, however, reveals that interface debonding always occurs between the carbon coating and the reaction zone of the composite [Eldr94]. From these studies it is apparent that, for the same temperature level, interfacial debonding in SiC/Ti-MMCs occurs at different locations along the fiber/interphase/matrix region. These observations contributes to the large scatter in the measured

debonding lengths in SiC/Ti MMCs. A range of coefficient of friction values, η , therefore, is required to describe the different surface roughness of the fractured interfaces [Li94, Tami95].

The calculated distribution of debonding lengths obtained in this study varies from 550 μm at the first bridging fiber closest to the crack mouth to 300 μm at 1.6 mm away from this bridging fiber, as illustrated in Fig. 4.7. Similar conclusion on the profile of debonding lengths over the bridged crack region was obtained for a SCS-6/Ti-15-3 composite at room temperature [Baku93]. The debonding length was estimated to range from 1500 μm at the first intact fiber closest to the crack mouth to 100 μm at 1.2 mm away from this fiber (crack length, $a = 4.28$ mm). Since measurements of debonding lengths for a fiber-bridged crack in a SCS-6/Timetal-21S composite is unavailable, the calculated results will be discussed in relation to that obtained for a SCS-6/Ti-15-3 composite [Baku93]. Several aspects, however, should be considered. Although both matrix phases, Timetal-21S and Ti-15-3 alloys, are metastable beta titanium alloys, the different inelastic response to temperature during initial cool down of the composite yielded different levels of locked-in residual stresses. Finite element simulation of the residual stress evolution in a SCS-6/Timetal-21S performed in this study showed that the axial component of the matrix residual stress in the vicinity of the interface is 170 MPa at room temperature while a high value of 300 MPa was predicted by Bahei-El-Din and Dvorak [Bahe95] for a SCS-6/Ti-15-3 composite. The residual clamping stress, however, is of comparable magnitude at room temperature. This high magnitude of residual axial stress coupled with a tensile applied stress to the composite, when relieved due to the extension of the matrix crack, would results in larger localized

magnitude of continuum shear stress at the interface. In addition, the debond shear strength for the SCS-6/Timetal-21S, $\tau_d = 221.2$ MPa [Osbo97, Tami97], is higher than that reported for the SCS-6/Ti-15-3 composite ($\tau_d = 112.4$ MPa) [Yang90]. Consequently, the debonding criterion would predict a longer debonding length for the SCS-6/Ti-15-3 composite than for the SCS-6/Timetal-21S composite, for a given crack geometry and loading conditions. Furthermore, a longer fiber-bridged crack length as reported for the SCS-6/Ti-15-3 composite would yield a longer interface debond crack. The comparison of these results indicated that the procedures for the debonding model give comparable results on the basis of stress field in a SiC/Ti MMC.

Since the traction exerted by each bridging fiber is directly related to the debonding length along the corresponding fiber through force-balance requirement on the fiber, the closure pressure profile also follows similar trends as the distribution of the debonding lengths. The resulting closure pressure is correlated to the debonding lengths, as illustrated in Fig. 4.8 for a particular matrix crack geometry and loading condition. The pressure peaks at the crack mouth and decreases to a finite value towards the crack tip. Similar correlation is expected to remain at elevated temperature because both Δp and L_d increase with increasing temperature due to load transfer from the matrix to the fiber and the relaxation of residual stresses at the interface, respectively. The work of Zheng and Ghonem [Zhen95] which is based on measured values of crack opening displacements at different loading conditions, showed a similar trend on the variation of the bridging fiber traction along the crack length for a SM1240/Timetal-21S composite. In addition, the closure pressure increases with increasing temperature or crack length and, in general, dependent upon the

properties of the fiber/matrix interface as well as residual stresses [Mars85]. Once the closure pressure function, $\Delta p(x)$, is known, the shielding component can be evaluated and the effective crack tip driving force be determined.

The simplified model of Chan and Davidson [Chan89] for estimating the interface crack tip driving force, as described above, requires an experimentally determined interface mode II crack opening displacement, COD in the wake of the debond crack. Experimental measurement of the COD profile for a ZE41A magnesium/alumina composite with 45° alumina fibers have been determined [Chan89]. For unidirectional SiC/Ti MMCs, however, such experimental data is unavailable. In this work, the interface COD data is generated numerically through finite element analysis on the cylinder model. The mode II COD is the relative tangential displacement between the fiber and the matrix along the debonded interfaces for a particular debond crack length and applied loading conditions. The requirement for equilibrium of forces on the cylinder model dictates the COD profile along the debond crack as a function of frictional characteristics and compressive radial stress along the debond crack. The calculated profile of the interface COD for various debond crack length at 25 °C is shown in Fig. 4.9. Increasing interface COD values are predicted at a particular location along the debond crack length as the crack extends.

The driving force for the interface mode II debond crack, however, is assumed to be represented by a power law function. The mode II stress intensity factor range defined in eq. (4.5) relies on the crack opening displacement profile along a debond crack length as well as the properties of the fiber and matrix phases. This profile which is defined as the relative tangential displacement between the fiber and the matrix is dependent on the stress field

acting along the crack length and in the vicinity of the crack tip. The interface crack-tip driving force is calculated at a distance of 1 μm behind the crack tip. The single-valued slope of the interface COD versus \sqrt{r} plot, required in eq. (4.5), is determined as an average value by curve-fitting the COD curve from the debond crack mouth to a distance of $\sqrt{(1 \text{ mm})}$ from the crack tip. The calculated variation of the interface crack-tip driving force, ΔK_{II} , as a function of the debond crack length, L_d , is shown in Fig. 4.10 for the test temperatures of 25, 500 and 650 $^{\circ}\text{C}$. The result indicates that, for a particular debond crack length, the available crack-tip driving force is larger at a lower temperature levels. It is noted that the interface crack tip driving force, ΔK_{II} , is an increasing function of the debond crack length, which could be described by a power law function in the following form

$$\Delta K_{II} = A (\Delta \sigma_a) L_d^n \quad (4.8)$$

where A and n are the material coefficient and exponent, respectively, which could be temperature-dependent. It is, however, important to recognize that the propagation rate of a debond crack along a bridging fiber is a function of the effective mode I stress intensity factor range for the fiber-bridged crack. The crack growth rate data for the interface debond crack in a SiC/Ti MMC required to correlate with the calculated driving force is not available to date. The magnitude of the driving force as calculated in this study, however, could be compared with the toughness of the interphase region to indicate the potential of a debond crack extension beyond the current length. The interphase toughness for various SiC SCS-

6.Ti MMC ranges from 1.45 to 4.46 Jm⁻² with the value determined for a SCS-6 Ti-15-3 composite to be 1.45 Jm⁻² [Chan93]. Although the calculated values using the model proposed in this study (see Fig. 4.9) are comparable in magnitude to the interface toughness reported in literature, thus, reflect on the suitability of the model, experimental validation of the model using debond crack growth data is required. The effort in generating the crack growth rate data for interface debond crack in SiC/Ti MMCs is being performed by the authors.

4.6 Summary

A crack bridging model is proposed in this study based on the notion that the fiber/matrix interface debonding lengths along bridging fibers are related to the closure pressure distribution over the bridged crack region. The model is examined on a unidirectional SCS-6/Timetal-21S MMC. The study is summarized as follows:

1. A criterion for the onset of fiber/matrix interface debonding is proposed. The criterion is based on the continuum shear stress localization along the interface due to a traction-free matrix crack surface and the debonding shear strength of the interphase region.

2. The initial fiber/matrix interface debonding length along a bridging fiber in a SiC/Ti MMC increases with an increase in test temperature.
3. The debonding lengths along bridging fibers have been correlated with the closure pressure over the bridged crack region. Finite bridging fiber traction is predicted near the crack tip.
4. The interface mode II crack tip driving force is determined using a simplified crack propagation model based on elastic crack opening displacement. The calculated driving force for interface crack is proportional to the debond crack length but has an inverse relationship with test temperature.

4.7 References

- [Bahe95] Bahei-El-Din, Y. A. and Dvorak, G. J., "Mechanics of Hot Isostatic Pressing of a Densified Unidirectional SiC/Ti Composite," Acta metall. Mater., Vol. 43, No. 7, 1995, pp. 2531-2539.
- [Yang90] Yang, J. M., Jeng, S. M. and Yang, C. J., "Interfacial Properties Measurements for SiC Fiber-Reinforced Titanium Alloy Composites," Scripta Metallurgica, Vol. 24, 1990, pp. 469-474.

- [Osbo97] Osborne, D. and Ghonem, H., "Elevated Temperature Interfacial Properties of Continuous Fiber Reinforced Titanium Metal Matrix Composites", to be submitted to Materials Science and Engineering, 1997.
- [Baku93] Bakuckas, J. G. and Johnson, W. S., "Application of Fiber Bridging Model in Fatigue Crack Growth in Unidirectional Titanium Matrix Composites", Journal of Composites Technology and Research, Vol. 15, No. 3, 1993, pp. 242-255.
- [Bodn75] Bodner, S. R. and Partom, Y., "Constitutive Equations for Elastic Viscoplastic Strain Hardening Materials." Journal of Applied Mechanics, Vol. 42, 1975, pp. 385-389.
- [Broe74] Broek, D., Elementary Engineering Fracture Mechanics, Kluwer Academic Publishers, Norwell, MA, 1974
- [Chan89] Chan, K. S. and Davidson, D. L., "Driving Forces for Composite Interface Fatigue Cracks", Engineering Fracture Mechanics, Vol. 33, No. 3, 1989, pp. 451-466.

- [Chan93] Chan, K. S.. "Effects of Interface Degradation on Fiber Bridging of Composite Fatigue Cracks." Acta Metall. Mater., Vol. 41, No. 3, 1993, pp 761-768.
- [Cox91] Cox, B. N. and Marshall, D. B.. "Crack Bridging in the Fatigue of Fibrous Composites". Fatigue and Fracture of Engineering Materials and Structures. Vol. 14, No. 8, 1991, pp. 847-861.
- [Davi92] Davidson, D. L.. "The Micromechanics of Fatigue Crack Growth at 25 °C in Ti-6Al-4V Reinforced with SCS-6 Fibers". Metallurgical Transaction, Vol. 23A, 1992, pp. 865-879.
- [Eldr94] Eldridge, J. I. and Ebihara, B. T.. "Fiber Push-out Testing Apparatus for Elevated Temperatures." Journal of Material Research, Vol. 9, No. 4, 1994, pp. 1035-1042.
- [Ghon93] Ghonem, H., Wen, Y., Zheng, D., Thompson, M. and Linsey, G.. "Effect of Temperature and Frequency on Fatigue Crack Growth in Ti- β -21S Monolithic Laminate." Materials Science and Engineering, Vol. 161, 1993, pp. 45-53.

- [Ghon96] Ghonem. H. 1996
- [Ghos92] Ghosn. L. J., Kanaizos. P. and Telesman. J., "Modeling of Crack Bridging in a Unidirectional Metal Matrix Composites." International Journal of Fracture. Vol. 54. 1992. pp. 345-357.
- [Hoag72] Hoagland. R. G., Rosenfield. A. R. and Hahn. G. T., "Mechanisms of Fast Fracture and Arrest in Steels." Metallurgical Transactions. Vol. 3. Jan. 1972. pp. 123-136.
- [Hutc87] Hutchinson. J. W., Mear. M. E. and Rice. J. R., "Crack Paralleling an Interface Between Dissimilar Materials". Journal of Applied Mechanics. Vol. 54. Dec. 1987. pp. 828-832.
- [Hutc90] Hutchinson. J. W. and Jensen. H. M., "Models for Fiber Debonding and Pullout in Brittle Composites with Friction". Mechanics of Material, Vol. 9. 1990. pp. 139-163.
- [John93] John. R., Kaldon. S. G. and Ashbaugh. N. E., "Applicability of Fiber Bridging Models to Describe Crack Growth in Unidirectional Titanium

Matrix Composites." in Workshop Proceedings on Titanium Matrix Components. P. R. Smith and W. C. Revelos, eds.. Wright-Patterson AFB, Ohio. WL-TR-93-4105. 1993. pp. 270-290.

- [Kera91] Kerans, R. J. and Parthasarathy, T. A., "Theoretical Analysis of Fiber Pullout and Push Out Tests", Journal of the American Ceramic Society, Vol. 7. 1991. pp. 1585-1596.
- [LePe88] Le Petitcorps, Y., Lahaye, M., Pailler, R. and Naslain, R., "Modern Boron and SiC CVD Filaments: A Comparative Study." Composites Science and Technology, Vol. 32. 1988. pp. 31-55.
- [Li94] Li, D. S. and Wisnom, M. R., "Unidirectional Tensile Stress-Strain Response of BP-SiC Fibre Reinforced Ti-6Al-4V. Journal of Composites Technology and Research, Vol. 16, No. 3. July 1994. pp. 225-233.
- [Mars85] Marshall, D. B., Cox, B. N. and Evans, A. G., "The Mechanics of Matrix Cracking in Brittle-Matrix Fiber Composites." Acta Metallurgica, Vol. 33. 1985. pp. 2013-2021.

- [Mars92] Marshall, D. B., Shaw, M. C., Morris, W. L. and Graves, J., "Interfacial Properties and Residual Stresses in Titanium and Titanium Aluminide Matrix Composites." in Workshop Proceedings on Titanium Matrix Components. P. R. Smith and W. C. Revelos, eds., WL-TR-92-4035. Wright-Patterson AFB, Ohio, April 1992, pp. 329-347.
- [Mart92] Martin, P. L., Bingel, W. H. and Mahoney, M., "SiC-Reinforced β -21S Creep Properties." in Workshop Proceedings for Titanium Matrix Components. P. R. Smith and W. C. Revelos, eds., Wright-Patterson AFB, Ohio, WL-TR-4035, 1992, pp. 277-291.
- [McCa87] McCartney, L. N., "Mechanics of Matrix Cracking in Brittle-Matrix Fiber-Reinforced Composites." Proceedings of The Royal Society London, Vol. 409A, 1987, pp. 329-350.
- [McMe90] McMeeking, R. M. and Evans, A. G., "Matrix Fatigue Cracking in Fiber Composites". Mechanics of Materials, Vol. 9, 1990, pp. 217-227.
- [Neu95] Neu, R. W. and Bodner, S. R., "Determination of the Material Constants for Timetal-21S for a Constitutive Model." Contributive Research and Development, Vol. 6, Prepared for Wright-Patterson AFB, Ohio, Sept. 1995.

- [Nguy94] Nguyen, T. -H. B. and Yang, J. -M.. "Elastic Bridging for Modeling Fatigue Crack Propagation in a Fiber-Reinforced Titanium Matrix Composite". Fatigue and Fracture of Engineering Materials and Structures, Vol. 17, No. 2, 1994, pp. 119-131.
- [Osbo95] Osborne, D. and Ghonem, H.. "High Temperature Interphase Behavior of SiC Fiber-Reinforced Titanium Matrix Composites". Mechanics of Materials Laboratory, University of Rhode Island. Report: MML-95-1, 1995.
- [Tada85] Tada, H., Paris, P. and Irwin, G. R.. The Stress Analysis of Cracks Handbook. Del Research Corporation, St. Louis, MO, 1985.
- [Tami95] Tamin, M. N., Osborne, D. and Ghonem, H.. "Influence of Interfacial Properties on Fiber Debonding in Titanium Metal Matrix Composites". Fatigue and Fracture at Elevated Temperature, A. Nagar and S. Mall, eds., The American Society of Mechanical Engineers, New York, NY, AD-Vol. 50, 1995, pp. 121-134.
- [Tami95] Tamin, M. N. and Ghonem, H.. "Evolution of Bridging Fiber Stress in Titanium Metal Matrix Composites at Elevated Temperature." Advances in

- Fatigue Lifetime Predictive Techniques, 3rd Volume. ASTM STP 1292. M. R. Mitchell and R. W. Landgraf. eds.. American Society for Testing and Materials. Philadelphia, PA. 1995. pp. 24-38.
- [Tami97] Tamin, M. N. and Ghonem, H., "Interphase Debonding Strength of Titanium Metal Matrix Composite", submitted to Materials Science and Engineering. In review. 1997.
- [Tele93] Telesman, J., Ghosn, L. J. and Kantzos, P., "Methodology for Prediction of Fiber Bridging Effects in Composites", Journal of Composites Technology and Research. Vol. 15. No. 3. 1993, pp. 234-241.
- [Warr92] Warren, P. D., Mackin, T. J. and Evans, A. G., "Design, Analysis and Application of an Improved Push-through Test for the Measurement of Interface Properties in Composites", Acta Metall Mater. Vol. 40. 1992. pp. 1243-1249.
- [Wats92] Watson, M. C. and Clyne, T. W., "The Use of Single Fiber Pushout Testing to Explore Interfacial Mechanics in SiC Monofilament-Reinforced Ti - II. Application of the Tests to Composite Material." Acta Metall. Mater., Vol. 40. 1992. pp. 141-148.

- [Yang91] Yang, J. M., Jeng, S. M. and Yang, C. J., "Fracture Mechanisms of Fiber-Reinforced Titanium Alloy Matrix Composites. Part I: Interfacial Behavior." Material Science and Engineering, Vol. A138, 1991, pp. 155-167.
- [Zhen95] Zheng, D. and Ghonem, H., "Fatigue Crack Growth of SM1240/Timetal-21S Metal Matrix Composite at Elevated Temperature". Metallurgical and Material Transactions, Vol. 26A, 1995, pp. 2469-2478.

4.8 Appendix

4.8.1 Crack Bridging Model

The procedures for establishing debonding lengths along bridging fibers in the bridged region of the matrix crack is summarized in Fig. 4.A-1. The variables are defined as follows:

- a_0 Non-bridged half crack length
- a_i current crack length encompassing i fibers
- ϵ Convergence tolerance
- i counter for fiber ($i=1$ for first bridging fiber)
- L_d interface debonding length

n_p	Number of bridging fibers
ΔK_{irr}	Crack-tip stress intensity factor range. eq. (4.3)
$\Delta p(x)$	Closure pressure distribution
$\Delta \sigma_a$	Applied stress range
$(\Delta \sigma_a)_i$	Applied stress range to the cylinder model for i-th fiber
$(\Delta \sigma_e)_i$	Effective applied stress range. eq. (4.4)
T	Temperature

4.8.2 Finite Element Model

The unit cell model for a bridging fiber embedded in the cracked matrix phase is illustrated in Fig. 4.A-2(a). The cylinder has an outer radius defined by (R_f / V_f) where R_f and V_f are the radius of the fiber and the fiber volume fraction in the composite, respectively. A radial section of the model with a length of $140 R_f$ is then discretized into finite elements. Such length is sufficient to isolate the effect of stress localization due to the matrix and interface debond crack on the far-field stress state. The mesh and boundary conditions applied to the model is shown in Fig. 4.A-2(b). Smaller element size is employed in the vicinity of the crack to capture the high stress gradient associated with the crack tip.

The cylinder model is applied to a SCS-6/Timetal-21S composite with a nominal fiber volume fraction, $V_f = 0.35$. The SCS-6 fiber is assumed to behave elastically throughout the applied loading cycles with the temperature-dependent mechanical and

physical properties obtained from literature [LePe88] . The elastic viscoplastic response of the matrix phase, Timetal-21S, is modeled using a unified inelastic strain theory [Neu95, Bodn75]. The properties of the titanium alloy matrix laminate, required for the constitutive model of the matrix phase, is obtained from published data [Neu95, Ghon93, Mart92]. Since interface debonding occurs within the carbon-rich coating layer which is thin compared to the fiber or matrix dimension, the fiber/matrix interface is modeled as a plane which accommodate radial and shear stress components only. Imperfect bonding between the fiber and the matrix is assumed to be adequately described by Coulomb frictional law which allows sliding and strain discontinuity across the interface.

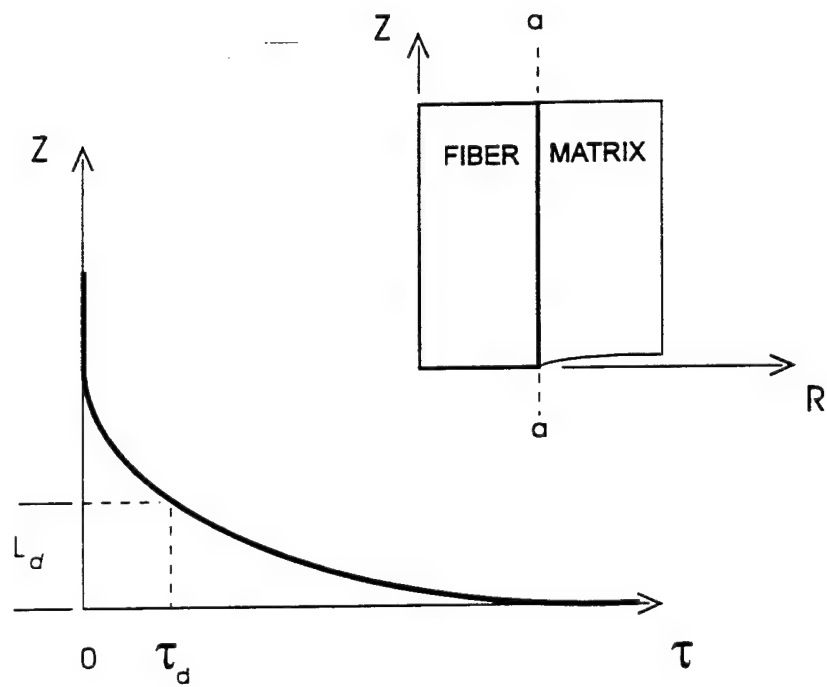


Fig. 4.1 Concept for fiber/matrix interface debonding criterion.

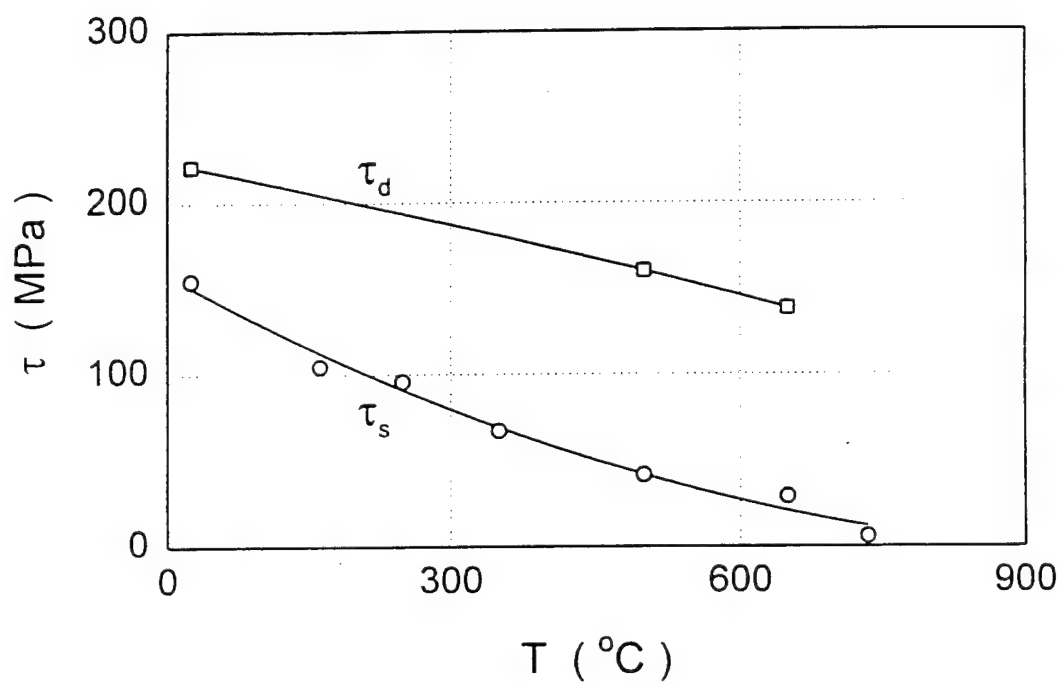


Fig. 4.2 Variation of interphase debonding shear strength, τ_d , and frictional shear stress, τ_s , with test temperature.

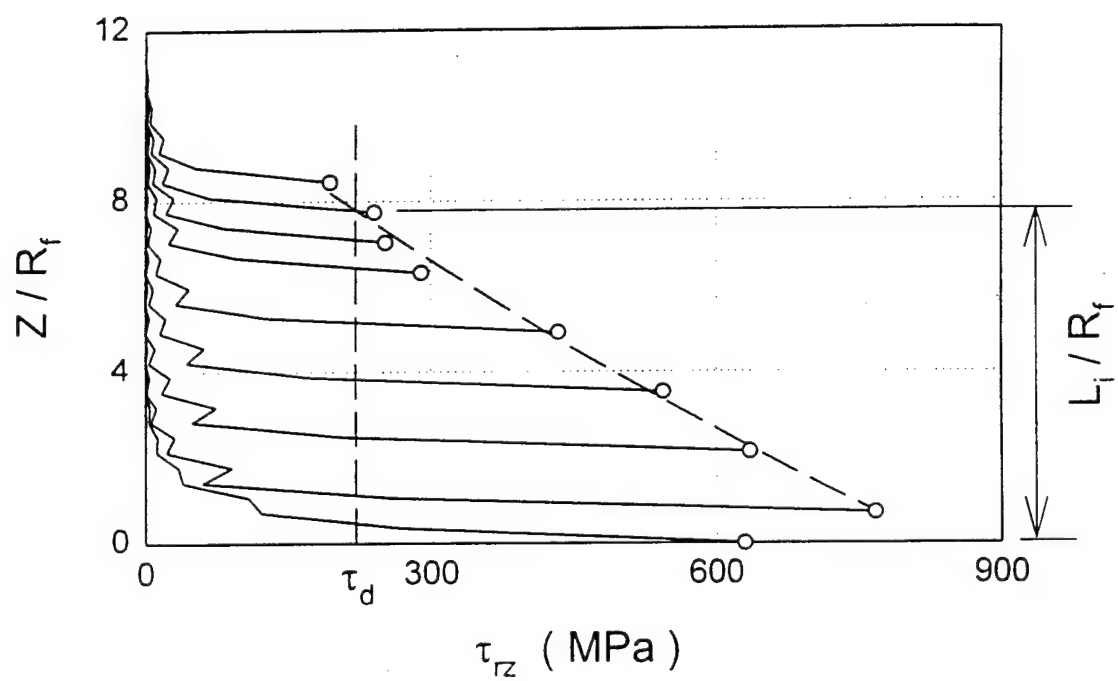


Fig. 4.3 Procedures for establishing the initial debonding length, L_i , along a bridging fiber through incremental debonding and force equilibrium considerations.

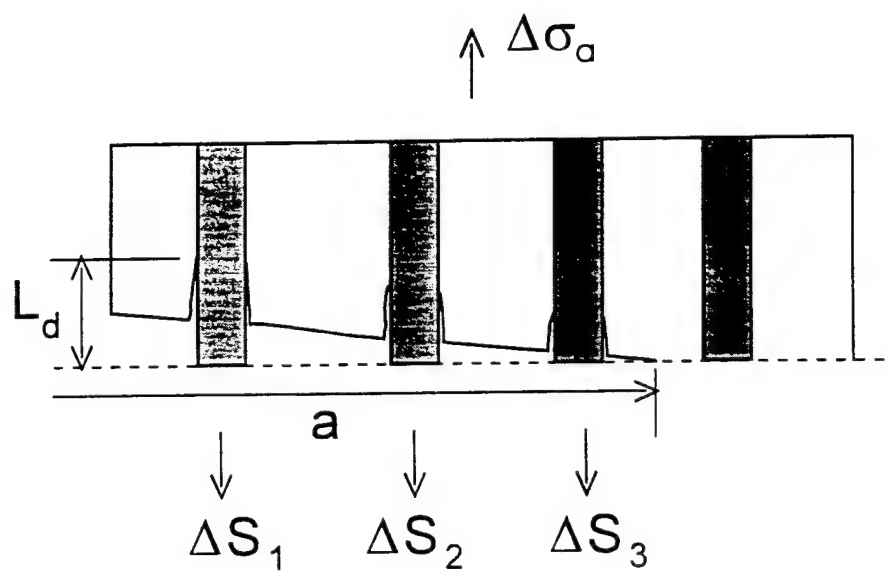


Fig. 4.4 Schematic of a crack bridging scenario in a unidirectional MMC.

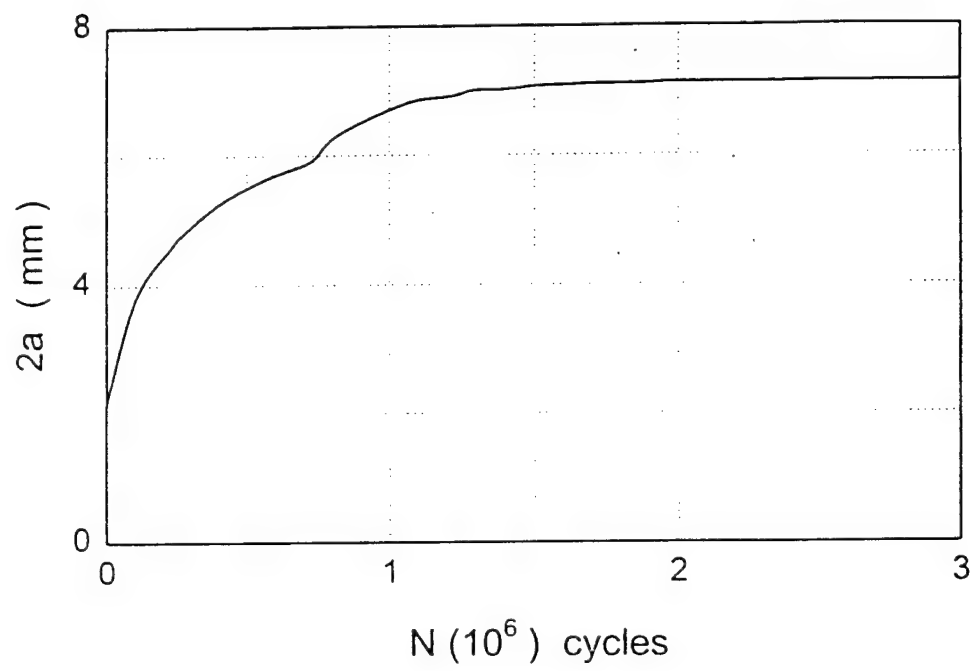


Fig. 4.5 Growth behavior of a fiber-bridged crack in a SCS-6/Timetal-21S composite at 25 °C.

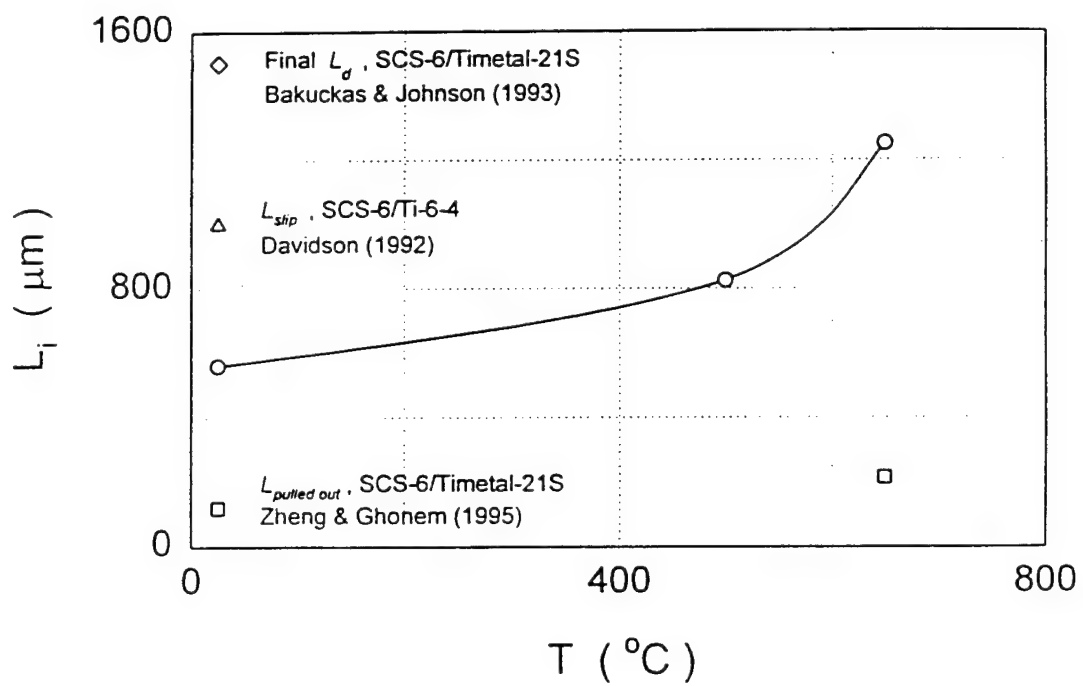


Fig. 4.6

Influence of test temperature on initial debonding length of a SCS-6/Timetal-21S composite subjected to $\Delta\sigma = 270$ MPa, $R = 1$. Also shown are experimental measurements for several SiC/Ti MMCs.

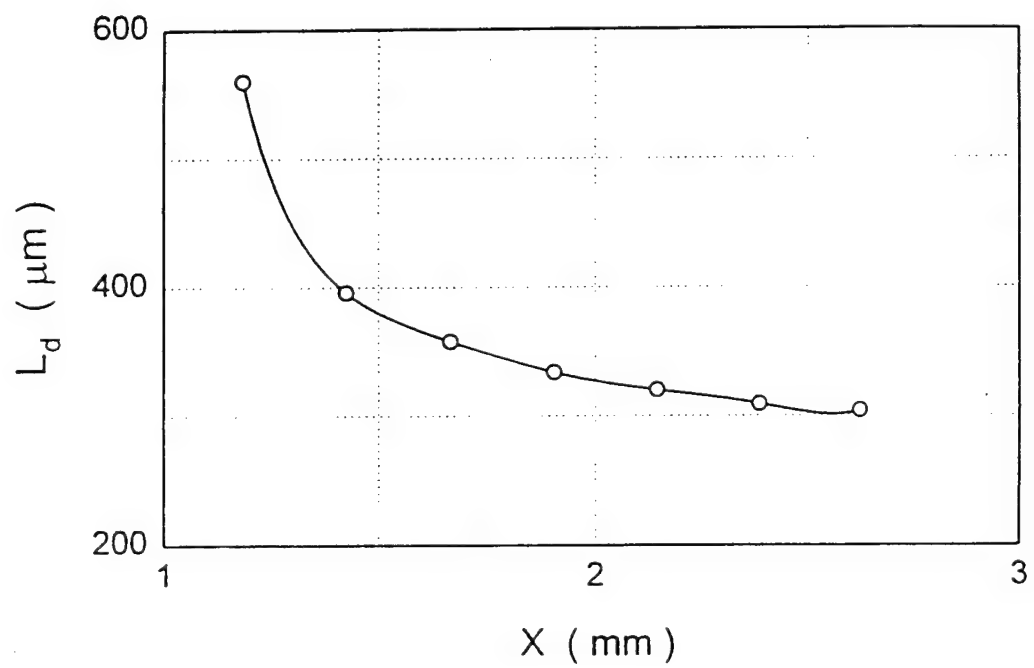


Fig. 4.7 Distribution of interface debonding lengths along a fiber-bridged matrix crack.

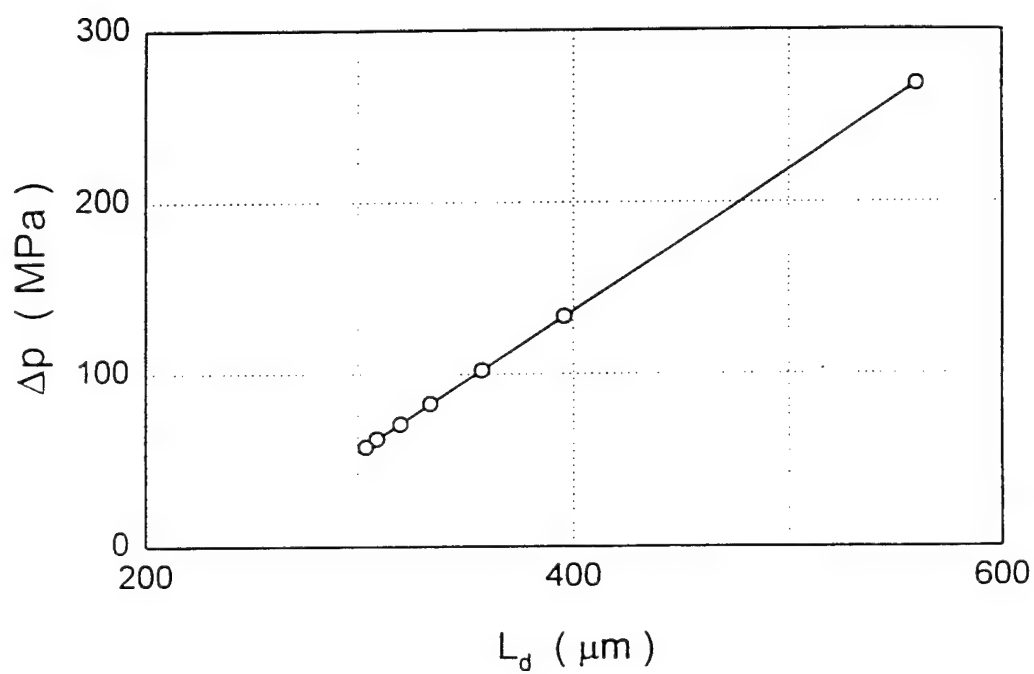


Fig. 4.8 Correlation between closure pressure, Δp , and interface debonding lengths, L_d , at 25 °C.

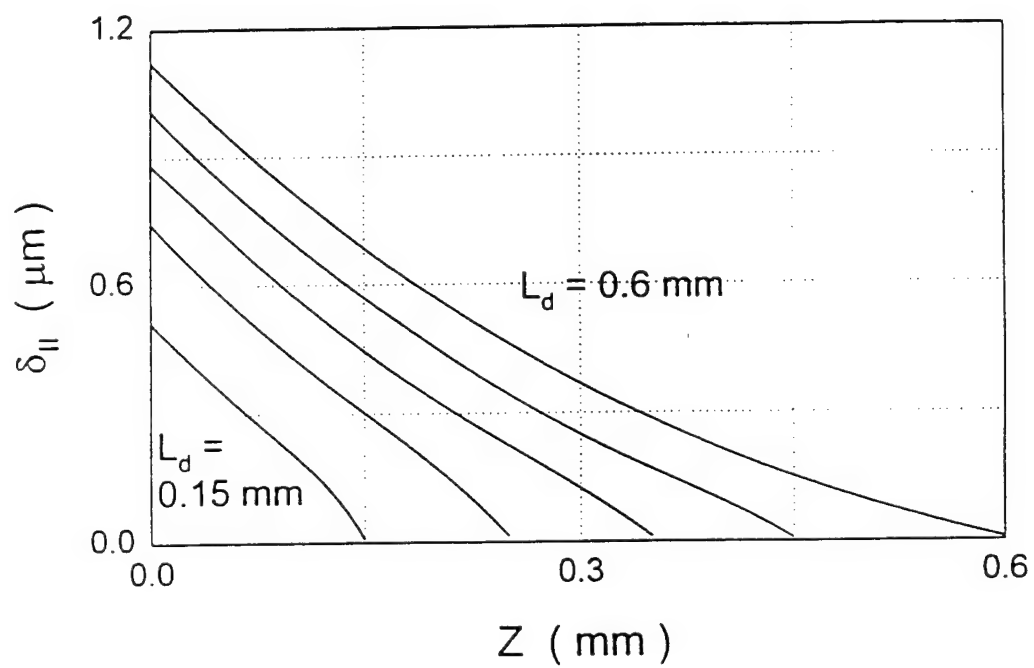


Fig. 4.9 Interface crack opening displacement profile for different debond crack lengths at 25 °C.

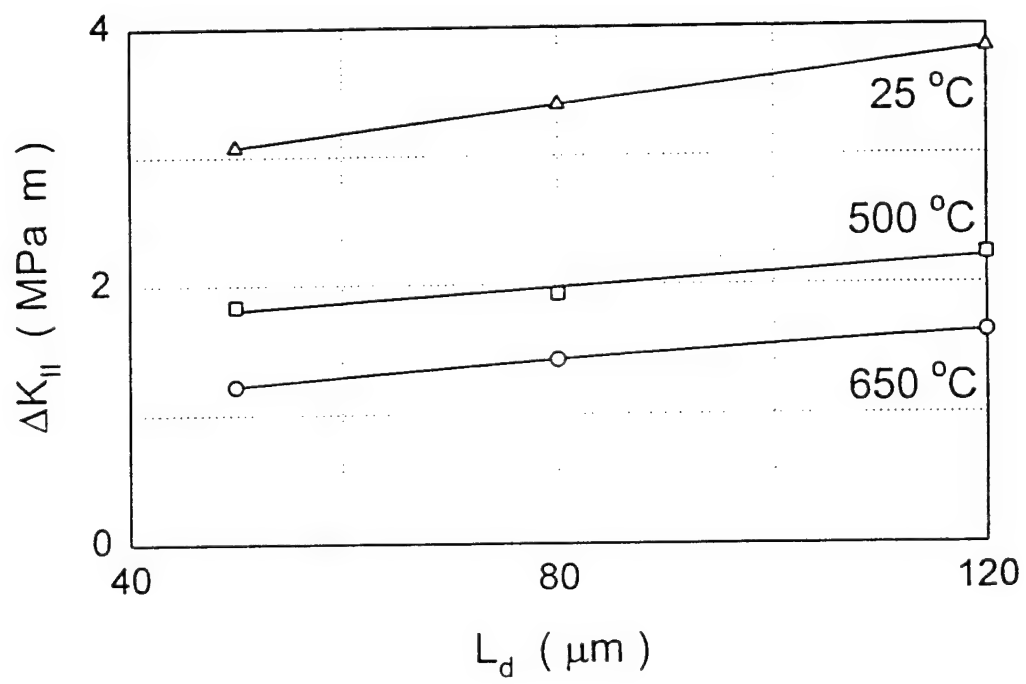


Fig. 4.10 Interface crack tip driving force for various debond crack length and temperature levels.

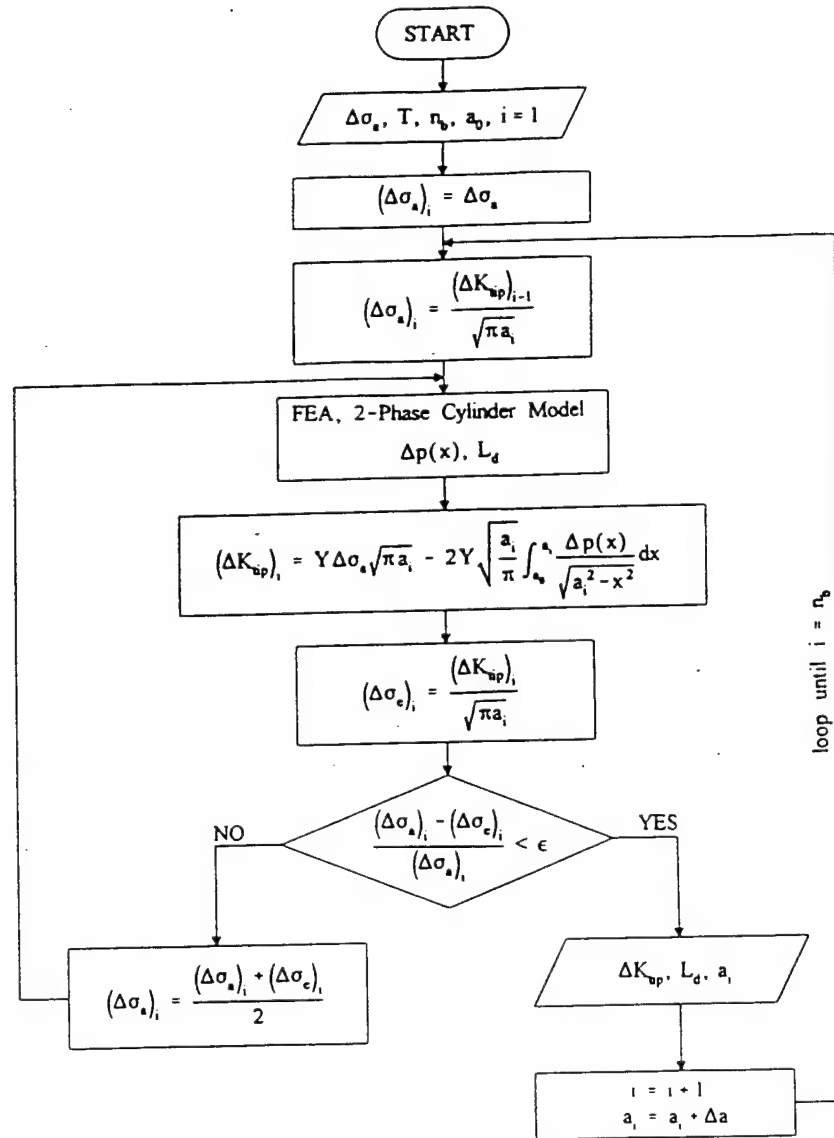


Fig. 4.A-1 Flow diagram for crack bridging model to establish debonding lengths and closure pressure profile along a fiber-bridged crack.

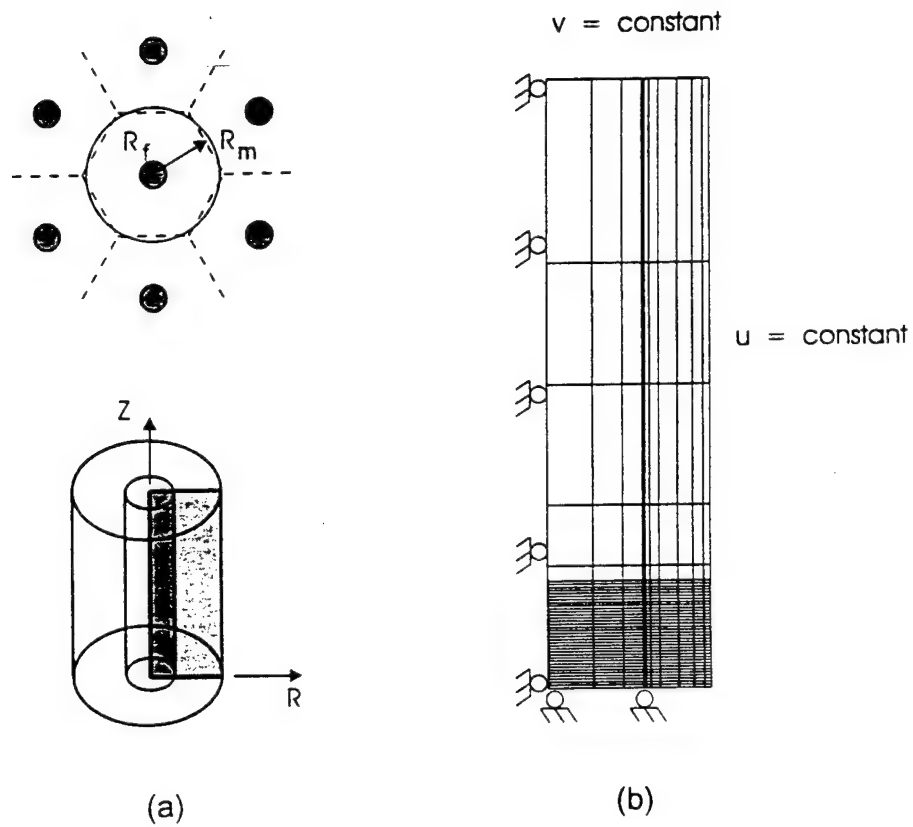


Fig. 4.A-2 (a) Unit cell model for fiber bridging. (b) Finite element mesh and boundary conditions for unit cell model of fiber bridging.

CHAPTER 5. Evolution of Bridging Fiber Stress in Titanium Metal Matrix Composites at Elevated Temperature⁵

Abstract

This paper deals with the determination of the stress evolution in bridging fibers during the fatigue crack growth in SM1240/Timetal-21S composite using the finite element method. Several parameters affecting this evolution were considered: namely, the process-induced residual stress, the creep characteristics of the matrix layer surrounding the fiber, the test temperature and the loading frequency. In support of these calculations, a series of elevated temperature fatigue crack growth tests was conducted in order to identify the crack growth behavior of the composite when subjected to different temperatures at both high and low loading frequencies. Results of this numerical/experimental work were then utilized in conjunction with a postulated fiber fracture criterion based on the notion that a competition exists between the increase in the axial fiber stress and the continuous degradation of the

⁵ Published as: Tamin, M. N. and Ghonem, H., "Evolution of Bridging Fiber Stress in Titanium Metal Matrix Composites at Elevated Temperature," *Advances in Fatigue Lifetime Predictive Techniques: 3rd Volume*, ASTM STP 1292, M. R. Mitchell and R. W. Landgraf, Eds., American Society for Testing and Materials, 1996, pp. 24-38.

fiber strength due to cyclic wear induced by the interface frictional shear stress. The conclusions of this study show that the axial stress in the bridging fibers increases with the increase in temperature and with the decrease in both the loading frequency and the matrix grain size. A combination of high temperature, low frequency and small matrix grain size would enhance creep deformation of the matrix, thus leading to an increase in the rate of the load transfer from the matrix to the bridging fibers. Furthermore, the presence of a compressive residual stress state in the bridging fibers retards the time-dependent increase of their axial stress. The fatigue strength of the bridging fibers was estimated to range from 720 MPa to 870 MPa within the temperature range of 500 °C to 650 °C. This strength was found to depend on both the temperature and the loading frequency.

5.1 Introduction

Previous studies on several unidirectional fiber-reinforced metal matrix composites (MMCs) including SCS-6/Ti-6Al-4V, SCS-6/Ti-15V-3Al-3Cr-3Sn, SCS-6/Ti-24Al-11Nb and SCS-6/25Al-10Nb-3Cr-1Mo indicated that fiber bridging is an operative damage mechanism under loading conditions of practical interest [Davi92, Tele93, Baku93, Jeng92, Sens90, Bowe91, Ibbo92, Brin92]. Fiber bridging occurs when the fiber strength is sufficiently high that a fatigue crack extends through the matrix leaving unbroken fibers in the crack wake [Evan89, Mars85, Cox92]. Bridging fibers can improve the fatigue crack growth properties by carrying part of the applied load, thus shielding the crack tip driving

force. Silicon carbide (SiC) fibers used as reinforcement in these composites have several carbon-rich coatings to accommodate fiber/matrix sliding and debonding [Lerc90, Peti88]. Cyclic loading the composites with SiC fibers causes debonding to occur between the carbon-rich coating and the SiC part of the fiber while the existence of carbon-rich region permits slippage to occur within the coating [Zhen94a]. During fiber bridging, the crack tip driving force is modified by the presence of crack tip shielding force as the result of load transfer from the matrix to the fibers. Thermal residual stresses arising from the mismatch of the coefficients of thermal expansion (CTEs) of the composite constituents during initial cool down may influence the load transfer characteristics by altering the fiber/matrix interfacial strength. The combination of chemical bonding and thermally induced clamping results in high interfacial shear strength especially at low temperature. The transfer of load is further modified by various inelastic processes occurring at or in the vicinity of fiber/matrix interface such as matrix plasticity, interfacial debonding and frictional sliding. The stress experienced by a bridging fiber is a function of applied load, crack length, number of bridging fibers, the load partition between uncracked and cracked regions of the composite as well as the frictional shear stress present in the fiber/matrix interface region. The fiber surface frictional-related damage could result in a severe deterioration of the fiber strength and thus decrease its ability to carry the evolving load. The objective of this work is to determine the evolution characteristics of the stress in the bridging fibers as influenced by temperature, loading frequency, residual stress state and material variables. A link will then be established between the fiber bridging damage mechanisms and the fiber stress state for the purpose of determining the influence of the aforementioned parameters on the bridging

fiber strength.

In the next section, the composite material used and the experimental procedures employed in fatigue crack growth tests are briefly outlined. This will be followed by a description of the resulting crack growth characteristics. The stress evolution of the bridging fiber will be calculated using the finite element method and the results will be applied in a proposed fiber fracture criterion.

5.2 Material and Experimental Procedures

Fatigue crack growth tests were conducted on SM1240/Timetal-21S composite specimens. The chemical composition of the metastable β titanium alloy, Timetal-21S is (in wt%): 0.1 Fe, 16.0 Mo, 3.06 Al, 2.9 Nb, 0.2 Si, 0.22 C, 0.12 O, 0.005 N with the balance being Ti. The SM1240 fiber with a diameter of 100 μm consists of chemically vapor deposited SiC on a 10- μm tungsten monofilament. A dual coating of carbon and titanium diboride, each layer having a thickness of 1 μm , is deposited on the surface. The consolidated, eight-ply, unidirectional composite, ($[0^\circ]_{(8)}$), has a nominal fiber volume fraction of 35%.

Center-hole rectangular specimens measuring 75 mm X 4 mm, with notches cut at opposite horizontal sides of the 1.577 mm diameter hole, were used in fatigue crack growth tests. The tests were carried out at room temperature as well as 500 °C and 650 °C. The room temperature tests established the baseline crack growth behavior. The 500 °C, on the

other hand, is the expected service temperature while the 650 °C represents the near upper limit use of the matrix material. All tests were carried out under a constant applied stress range of 270 ± 5 MPa with the load ratio, R, of 0.1. The two loading frequencies considered in this study were 10 Hz and 0.1 Hz. The selection of these frequencies is based on earlier work on Timetal-21S fiberless laminates which showed that frequencies higher than 10 Hz produced insignificant oxidation damage effect at temperatures below 650 °C, while those lower than 10 Hz showed effects related to viscoplastic deformation and oxidation at temperatures up to 650°C [Ghon93].

Fig. 5.1 shows a polished and chemically etched cross section of the as-fabricated composite. The fibers are aligned in a hexagonal array with an average center-to-center distance of 150 μm . The microstructure of the heat treated matrix alloy consists of distinctive β grains with an average size of 80 μm containing Widmanstatten acicular α phase and a continuous grain boundary α material with a thickness of about 0.8 μm . The micrograph also reveals a distribution of small equiaxed grains immediately surrounding each fiber with an average grain diameter of 15 μm , see Fig. 5.1(b). This fine grain structure could have been the result of recrystallization during fabrication of the composite [Zheng95]. In high temperature loadings, this zone with small grain size around the fibers will experience a creep deformation with a rate higher than that of the larger grain base matrix material. The effect of enhancement of creep deformation due to the existence of the duplex microstructure on the efficiency of load transfer to the fiber at elevated temperature loading is considered in this study.

5.3 The Crack Growth Process

In all the tests, the fatigue fracture process was seen to advance along a single dominant crack perpendicular to both the 0° fiber orientation and the direction of the applied load. The growth of the single crack was found to follow a trend in which the crack growth rate decreases continuously with increasing applied stress intensity factor (or crack length). The work in Ref [Zhen95] has associated this decrease in the crack growth rate with an increase in the number of fibers bridging the crack wake. The end of this stage is marked by the attainment of the minimum crack growth rate pertaining to the particular test condition. The first decelerated growth stage is followed by a transition to a stage which consists of repeated events of crack growth acceleration and retardation leading ultimately to crack instability and final failure of the test specimen. The crack growth rate versus the applied stress intensity factor curves limited to the first accelerated and decelerated stages in each test are shown in Fig. 5.2.

The $500^\circ\text{C}/10\text{ Hz}$ test was repeated twice to establish the reproducibility of the observed behavior. Two additional $500^\circ\text{C}/10\text{ Hz}$ tests were interrupted: one while in the initial crack growth deceleration stage and the other while in the following crack growth acceleration stage. A typical crack growth curve for this load case is shown in Fig. 5.2. The specimens were ground to the first layer of fibers and examined using optical microscopy to identify fractured fibers and the location of the fracture sites. Results of this work showed that all bridging fibers are intact while in the bridging stage. During the accelerated growth stage, however, several fibers at locations farthest away from the crack tip were broken along

planes not coinciding with the matrix crack plane. These observations indicate that the crack growth transition from decelerated to accelerated growth is associated with the breakage of bridging fibers. In this, the fibers located near the crack mouth are the ones that have experienced the largest number of fatigue cycles, thus the greatest frictional surface wear which in turn may result in extensive fiber strength degradation [Chan93]. As the bridged crack propagates, a competition is set between the increase in the axial stress at a critical fiber cross-section and the continuous decrease of the fiber strength. The failure of any of the bridging fibers would result in a decrease of the crack tip shielding force thus triggering a condition of crack growth acceleration. As will be discussed in the following section, the frictional shear stress, the component responsible for the surface wear damage of bridging fibers, is uniformly distributed along the fiber/matrix interface region. Emphasis will then be placed on estimating the stress evolution in the bridging fibers at a plane coinciding with the tip of the debonded interface since at this position bridging fibers experience the largest stress gradient due to the presence of large stresses at the crack tip.

5.4 Stress Distribution in Bridging Fibers

The stress distribution in the constituents of the composite and the evolution of fiber stress in the bridging fibers are predicted using the finite element method. Based on the fiber arrangement in this composite (see Fig. 5.1(a)), the fiber distribution is idealized as a hexagonal array architecture. A unit cell is then modelled as two concentric cylinders of a

fiber with radius, r_f and a matrix phase with an outer radius of $r_m = r_f / \sqrt{v_f}$, where $v_f = 0.35$ is the fiber volume fraction of the composite. A section of this axisymmetric cylinder is discretized into finite elements with the mesh shown in Fig. 5.3. The SiC fiber, SM1240 is assumed to behave elastically for all loading conditions with elastic modulus, $E_f = 400$ GPa, Poisson ratio, $\nu = 0.22$, tensile strength, $\sigma_u = 3750$ MPa and temperature dependent coefficient of thermal expansion (CTE) [Peti88, SIGMA]. (See Fig. 5.4). The elastic modulus, CTE and yield limit of the Timetal-21S matrix alloy were also considered to be temperature-dependent [Ghon93], as shown in Fig. 5.4. The creep properties of the matrix alloy are based on limited experimental data [Khob94, Mart92], and the creep behavior is represented by the Bailey-Norton's equation in the transient and the steady state stages of creep deformation [Tami94a]. The effect of duplex microstructure of the matrix phase is approximated through the assumption that the strain rate varies inversely proportional to the square of the grain diameter for self-diffusion creep [Reed64].

The loading sequence of the present simulation includes cool down from consolidation temperature to room temperature at a rate of 0.1 °C/sec, followed by reheating to the test temperature and the application of cyclic loading. The fiber/matrix interface is assumed to be perfectly bonded throughout cool down from fabrication to room temperature and subsequent reheating to the test temperature. At the test temperature, the matrix crack and fiber/matrix debonding are introduced simultaneously. The outer surface of the matrix is maintained vertical in order to preserve the displacement compatibility of the unit cell with the surrounding composite. Schematic diagram of the model is illustrated in Fig. 5.5 defining the length of the debonded interface, L_d and the distance, z along the fiber measured

from the plane coinciding with the matrix crack plane. These notations will be used in subsequent figures. Frictional effects are assumed to act along the fiber/matrix debonded length in the presence of compressive radial stress. The debonded length and the coefficient of friction required for use with the Coulomb law are selected so that the resulting crack opening displacement (COD) at a particular crack length matches that experimentally obtained [Zhen94a]. This value of COD is assumed not to vary throughout the duration of the loading cycles. This assumption corresponds to the steady state stage of the bridged crack growth where the debonded length is assumed to be stable [Su95].

Table 5.1 summarizes the test cases considered in this study. The variables being investigated are temperature, loading frequency, residual stress state and the grain size of the fiber-surrounding matrix material. When the bridged crack reaches a length at which deceleration/acceleration crack growth transition occurs, the axial stress in the bridging fiber closest to the crack mouth is believed to have reached a maximum value. The finite element results show that the maximum axial stress in the bridging fiber is at the section coinciding with the matrix crack plane as illustrated in Fig. 5.6. However, fractographic analysis of SM1240/Timetal-21S composite specimens subjected to isothermal fatigue loadings showed that bridging fibers fractured at planes located above and below the matrix crack plane, as illustrated in Fig. 5.7. Studies on other MMCs such as SCS-6/Ti-6-4 and SCS-6/Ti-15-3-3 also reported a similar fracture feature of bridging fibers [Davi92, Jeng93]. Furthermore, work by Thouless et al. [Thou89] has suggested that the fracture plane of bridging fibers is at a distance from the matrix crack plane and the location depends on the magnitude of the frictional shear stress along the fiber/matrix interface.

Typical distributions of radial and shear stress components along the fiber/matrix interface are illustrated in Figs. 5.8 and 5.9, respectively. It is noted that only small variation of frictional shear stress occurred along the slip length of the fiber/matrix interface, with an average value of 3.5 MPa. Consequently, it can be assumed that degradation of the fiber strength resulting from the frictional wear of the surface of the fiber is uniform, and the location of most probable failure site is determined from statistical consideration. In the crack tip region of the debonding length, the shear stress gradient is the highest due to the transition from debonded region to fully bonded region along the fiber/matrix interface. In addition, the evolution of the bridging fiber axial stress is most pronounced at cross sections in the vicinity of the Mode II crack tip because the residual stress state is less affected by the matrix crack and the debonding interface. Consequently, the evolution of axial stress at a bridging fiber plane coinciding with the tip of the fiber/matrix interface is addressed in this study.

5.5 Stress Evolution in Bridging Fibers

The evolution of the axial bridging fiber stress at the cross-section coinciding with the tip of the fiber/matrix debonded region during fatigue loading for test cases listed in Table 5.1 is shown in Fig. 5.10(a) and 5.10(b), for loading frequencies of 0.1 Hz and 10 Hz, respectively. As the loading cycles proceed, the matrix undergoes creep deformation and subsequent stress relaxation resulting in a load transfer to the fiber. A higher level of axial

fiber stress is predicted for a composite in which the fabrication-related compressive residual stress in the composite is not considered. Similarly, the fiber stress was found to increase when the layer of the matrix surrounding the fiber was assumed to consist of grain size smaller than that in the remaining of the matrix material. The presence of fine grains in the direct vicinity of the fiber enhances the stress relaxation of the matrix phase through creep deformation, thus, increases the load being transferred to the bridging fiber.

Furthermore, comparison of the stress evolution curves for the 650 °C and 500 °C indicates that the level of bridging fiber stress reached after the application of a certain number of load cycles is lower at lower temperature. This could be attributed to the rapid transfer of load from the matrix to the bridging fiber at higher temperature level. For the same temperature, the material experienced the higher portion of the applied stress for a longer duration of time at a lower frequency, thus greater contribution to matrix creep deformation resulting in higher level of bridging fiber stress. This contribution is also apparent in the higher slope of the evolution curve at lower frequency, which reflected higher rate of load transfer to the bridging fiber due to stress relaxation of the matrix phase. The evolution of the fiber stress during isothermal fatigue is therefore dictated by the time-dependent deformation of the matrix which is significant at lower frequency.

TABLE 5.1 - Test parameters for the cases used in the finite element calculations

Test Case	Temp (°C)	Frequency (Hz)	d^{++}
1A	500	10	1
1B	500	0.1	1
1C ⁺	500	10	1
1D ⁺	500	0.1	1
1E	500	10	0.3
1F	500	0.1	0.3
2A	650	10	1
2B	650	0.1	1
2C ⁺	650	10	1
2D ⁺	650	0.1	1
2E	650	10	0.3
2F	650	0.1	0.3

⁺A case in which the process-induced residual stresses are not considered in the FE calculations.
⁺⁺ $d = d_1/d_2$ (where d_1 is grain size of the matrix layer in the immediate vicinity of the fiber and d_2 is the grain size of the basic matrix material)

5.6 Fatigue Strength of Bridging Fibers

As mentioned above, the transition from decelerated to accelerated crack growth is a result of the breakage of bridging fibers located near the crack mouth. The fracture of these fibers is assumed to occur when the evolving fiber stress level reached the value of the continuously decreasing fiber residual strength. This concept forms the basis for the fracture criterion of bridging fibers at elevated temperature [Tami94b]. The fatigue strength, S_f , is determined by locating along the fiber stress evolution curve, the stress level corresponding to the cycle number, or the equivalent time, at which the first transition to accelerated crack growth occurred, as indicated in Fig 5.10(a) and (b) for 0.1 Hz and 10 Hz test cases, respectively. The resulting fatigue strength, S_f , of the bridging fibers ranges from 720 MPa to 870 MPa for the two temperature levels considered. It is further noted that the fatigue strength of the bridging fiber is both time- and cycle-dependent. The fiber strength at the test condition of 650 °C, 10 Hz, for example, is determined as 760 MPa. As seen from Fig. 5.10(b), assuming that this strength is unique for the particular bridging fiber, it is then apparent that for a matrix with a uniform grain size, the presence of residual stresses due to consolidation could prolong the fatigue life of the bridging fibers. On the other hand, the absence of residual stresses would decrease the fiber life.

The influence of elevated temperatures and loading frequencies on the bridging fiber strength is summarized in Fig. 5.11. For the same temperature level, the bridging fiber strength increases as the frequency decreases. The decrease in frequency and the associated increase in the matrix creep rate permit the fiber stress to evolve to a higher level before the

fiber surface wear generated by cyclic frictional sliding causes fiber failure. This type of competition between the fiber stress evolution and the fiber strength degradation due to frictional surface effects could also be used to interpret the observation that the number of loading cycles, and thus the fiber strength, decreases as the frequency increases, as indicated in Fig. 5.11. Experimental observation indicated that the number of fatigue cycles at the transition point for loading frequency of 10 Hz is about two order of magnitude higher than that for the low frequency of 0.1 Hz. At any frequency, the strength of the bridging fiber increases with increasing temperature level. This is due to the fact that the frictional shear stress which represents the degree of surface wear of the fiber is lower at higher temperature level. The temperature dependency of interfacial shear stress for several titanium MMC is reported elsewhere [Eldr94, Osbo94]. Based on the evolution characteristics of the bridging fiber stress and its postulated strength degradation during the fiber bridging process, it is noted that the evolution of the bridging fiber stress is time-dependent in nature while the bridging fiber strength is primarily cycle dependent.

5.7 Conclusions

An attempt was made to determine the evolution of stress in bridging fibers during the fatigue crack growth in SM1240/Timetal-21S composite using the finite element method. Several parameters affecting this evolution were considered; namely, the presence of the process-induced residual stress, the creep behavior of the matrix layer surrounding the fiber,

the test temperature and the loading frequency. In support of these calculations, a series of elevated temperature fatigue crack growth tests was conducted in order to identify the crack growth behavior of the composite when subjected to different temperatures at both high and low loading frequencies. Results of this numerical/experimental work were then utilized in conjunction with a postulated bridging fiber fracture criterion based on the notion that a competition exists between the increase in the axial fiber stress and the continuous degradation of the fiber strength due to cyclic wear induced by the interface frictional shear stress. The conclusions of this study are summarized as follows:

1. The stress in the bridging fibers increases with increasing temperature level and with the decrease of both the loading frequency and the fiber-surrounding matrix grain size. The rate of increase in the stress is proportional to the temperature but inversely proportional to the loading frequency and the matrix grain size. A combination of high temperature, low frequency and small matrix grain size enhances creep deformation of the matrix, thus leading to an increase in the load being transferred to the bridging fiber. The evolution of the bridging fiber stress basically is time-dependent.
2. The fiber compressive residual stress state induced during consolidation of the composite retards the time-dependent increase of the axial stress in the bridging fiber. This residual stress state decreases with increasing temperature level and number of fatigue cycles.

3. The fatigue strength of bridging fibers ranges from 720 MPa to 870 MPa within the temperature range of 500 °C to 650° C and the strength depends on both the temperature and loading frequency.

5.8 References

- [Davi92] Davidson, D. L., "The Micromechanics of Fatigue Crack Growth at 25 C in Ti-6Al-4V Reinforced with SCS-6 Fibers", Metallurgical Transactions A, Vol. 23A, March 1992, pp. 865-879.
- [Baku93] Bakuckas, J. G. and Johnson, W. S., "Application of Fiber Bridging Model in Fatigue Crack Growth in Unidirectional Titanium Matrix Composites". Journal of Composite Technology & Research, Vol. 15, No. 3, Fall 1993, pp. 242-255.
- [Bowe91] Bowen, P., Ibbotson, A. R. and Beevers, C. J., "Characterization of Crack Growth in Continuous Fiber Reinforced Titanium Based Composites Under Cyclic Loading", in Fatigue of Advanced Materials, R. O. Ritchie, Dauskardt, R. H. and Cox, B. N., eds., Materials and Component Engineering Publications Ltd., P. O. Box 1550, Edgbaston, Birmingham B15 2JZ, England, 1991, pp. 379-393.

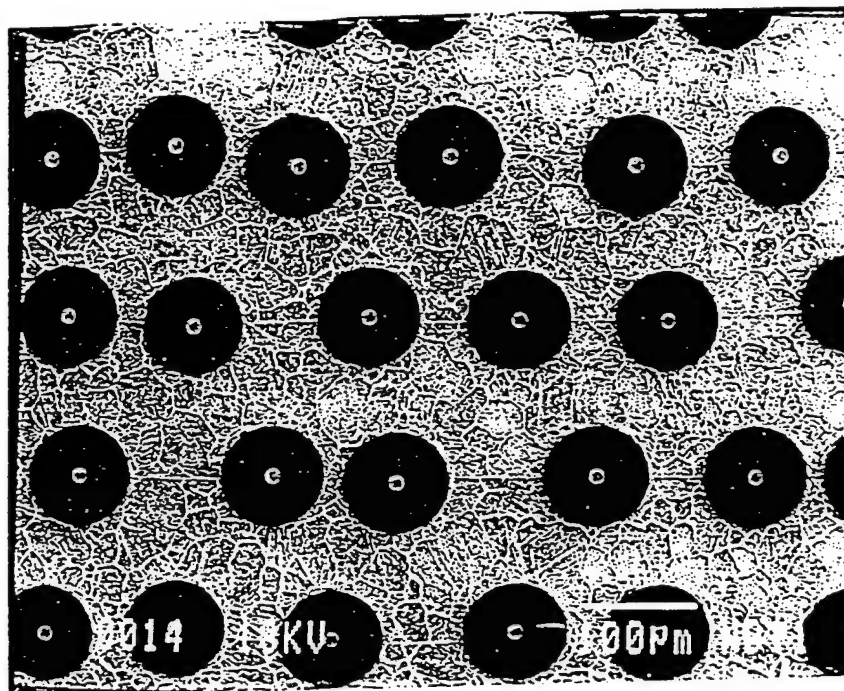
- [Brin92] Brindley, P. K., Draper, S. L., Eldridge, J. I., Nathal, M. V. and Arnold, S. M. "The Effect of Temperature on the Deformation and Fracture of SiC/Ti-24Al-11Nb". Metallurgical Transactions. Vol. 23A. 1992. pp. 2527-2540.
- [Chan93] Chan, K. S., "Effects of Interface Degradation on Fiber Bridging of Composite Fatigue Cracks". Acta Metall. Mater.. Vol. 41. No. 3. 1993. pp. 761-768.
- [Cox92] Cox, B. N. and Lo, C. S., "Load Ratio, Notch, and Scale Effects for Bridged Cracks in Fibrous Composites", Acta Metall. Mater.. Vol. 40. No. 1. 1992. pp. 69-80.
- [Eldr94] Eldridge, J. I. and Ebihara, B. T., "Fiber Push-out Testing Apparatus for Elevated Temperatures". Journal of Materials Research. Vol. 9. No. 4. April 1994. pp. 1035-1042.
- [Evan89] Evans, A. G. and He, M. Y., "Interface Debonding and Fiber Cracking in Brittle Matrix Composites". Journal of the American Ceramic Society, Vol. 72[12]. 1989. pp. 2300-2303.

- [Ghon93] Ghonem, H., Wen, Y., Zheng, D., Thompson, M. and Linsey, G., "Effects of Temperature and Frequency on Fatigue Crack Growth in Ti- β 21S Monolithic Laminate". Materials Science and Engineering, Vol. 161, 1993, pp. 45-53.
- [Ibbo92] Ibbotson, A. R., Bowen, P. and Beevers, C. J., "Cyclic Fatigue Resistance of Fiber Reinforced Titanium Metal Matrix Composites at Ambient and Elevated Temperature". 7th Titanium Conference, San Diego, July, 1992.
- [Jeng92] Jeng, S. M., Allasoeur, P. and Yang, J. -M., "Fracture Mechanisms of Fiber-reinforced Titanium Alloy Matrix Composites. V: Fatigue Crack Propagation". Materials Science and Engineering", A154, 1992, pp. 11-19.
- [Jeng93] Jeng, S. M., Nguyen, T. -H. B., Dana, O. and Yang, J. M., "Fatigue Cracking of Fiber Reinforced Titanium Matrix Composites". Journal of Composite Technology & Research, Vol. 15, No. 3, Fall 1993, pp. 217-224.
- [Khob91] Khobaib, M. and Ashbaugh, N., University of Dayton Research Institute, Dayton, OH, October 1991, Unpublished work.
- [Lerc90] Lerch, B. A., Hull, D. R. and Leonhardt, T. A., "Microstructure of a SiC/Ti-15-3 Composites". Composites, Vol. 21, No. 3, May 1990, pp. 216-224.

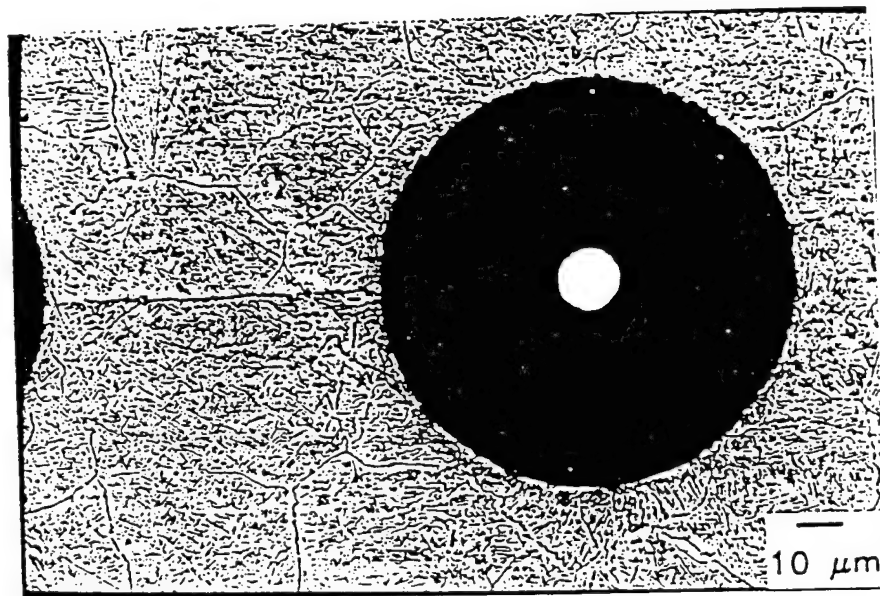
- [Mars85] Marshall, D. B., Cox, B. N. and Evans, A. G., "The Mechanics of Matrix Cracking in Brittle-Matrix Fiber Composites", Acta Metallurgica, Vol. 33, No. 11, 1985, pp. 2013-2021.
- [Mart92] Martin, P. L., Bingel, W. H. and Mahoney, M. W., "SiC-Reinforced β -21S Creep Properties", in Workshop Proceedings on Titanium Matrix Components, P. R. Smith and W. C. Revelos, eds., April 1992, WL-TR-92-4035, pp. 277-291.
- [Osbo94] Osborne, D. and Ghonem, H., "Determination of Frictional Shear Stress of SM1240/ Timetal-21S at Elevated Temperature", Internal Report, University of Rhode Island, 1994.
- [Peti88] Petitcorp, Y. L., Lahaye, M., Pailler, R. and Naslain, R., "Modern Boron and SiC CVD Filaments: A Comparative Study", Composites Science and Technology, 32, 1988, pp. 31-55.
- [Reed64] Reed-Hill, E.E., Physical Metallurgy Principles, Van Nostrand, New York and London, 1964.

- [Sens90] Sensmeier, M. D. and Wright, P. K.. "The Effect of Fiber Bridging on Fatigue Crack Growth in Titanium Matrix Composites". in Fundamental Relationships Between Microstructure & Mechanical Properties of Metal-Matrix Composites, P. K. Liaw and M. N. Gungor, eds.. The Minerals, Metals & Materials Society, 1990, pp. 441-457.
- [SIGMA] SIGMA Monofilament Products, Information Sheets, BP Metal Composites Limited, RAE Road, Farnborough, Hampshire GU14 6XE, England.
- [Su95] Su, Z. and Ghonem, H.. "Fatigue Crack Tip Shielding Effects in Metal Matrix Composites". Mechanics of materials Laboratory, University of Rhode Island, Kingston, RI. Report: MML-95-2, 1995.
- [Tami94a] Tamin, M.N., Zheng, D. and Ghonem, H.. "Time-Dependent Behavior of Continuous-Fiber-Reinforced Metal Matrix Composites: Modeling and Applications". Journal of Composites Technology & Research, Vol. 16, No. 4, October 1994, pp. 314-322.
- [Tami94b] Tamin, M.N. and Ghonem, H.. "A Fracture Criterion for Bridging Fibers in Titanium Metal Matrix Composites at Elevated Temperature", Symposium on Durability of Composite Materials, R.C. Wetherhold (ed.), ASME Winter Annual Meeting, Chicago, IL, Nov. 6-11, 1994, MD-Vol. 51, pp. 51-58.

- [Tele93] Telesman, J., Ghosn, L. J. and Kantzos, P., "Methodology for Prediction of Fiber Bridging Effects in Composites". Journal of Composites Technology & Research, Vol. 15, No. 3, Fall 1993, pp. 234-241.
- [Thou89] Thouless, M. D., Sbaizero, O., Sigl, L. S. and Evans, A. G., "Effect of Interface Mechanical Properties on Pullout in a SiC-Fiber-Reinforced Lithium Aluminum Silicate Glass Ceramic". Journal of the American Ceramic Society, 72[4], 1989, pp. 525-532.
- [Zhen94a] Zheng, D. and Ghonem, H., "High Temperature/High Frequency Fatigue Crack Growth Damage Mechanisms in Titanium Metal Matrix Composites". Symposium on Life Prediction Methodology for Titanium Matrix Composites, Crystal Sands Resort, Hilton Head Island, South Carolina, March 22-24, 1994.
- [Zhen95] Zheng, D. and Ghonem, H., "Fatigue Crack Growth in Titanium Metal Matrix Composites". Metallurgical Transaction A, Vol. 26A, No.9, 1995, pp. 2469-2478.



(a)



(b)

Fig. 5.1 A Polished and etched cross section of the as-received SM1240/Timetal-21S composite showing (a) the distribution of fibers, and (b) the region of fine matrix grains around the fiber.

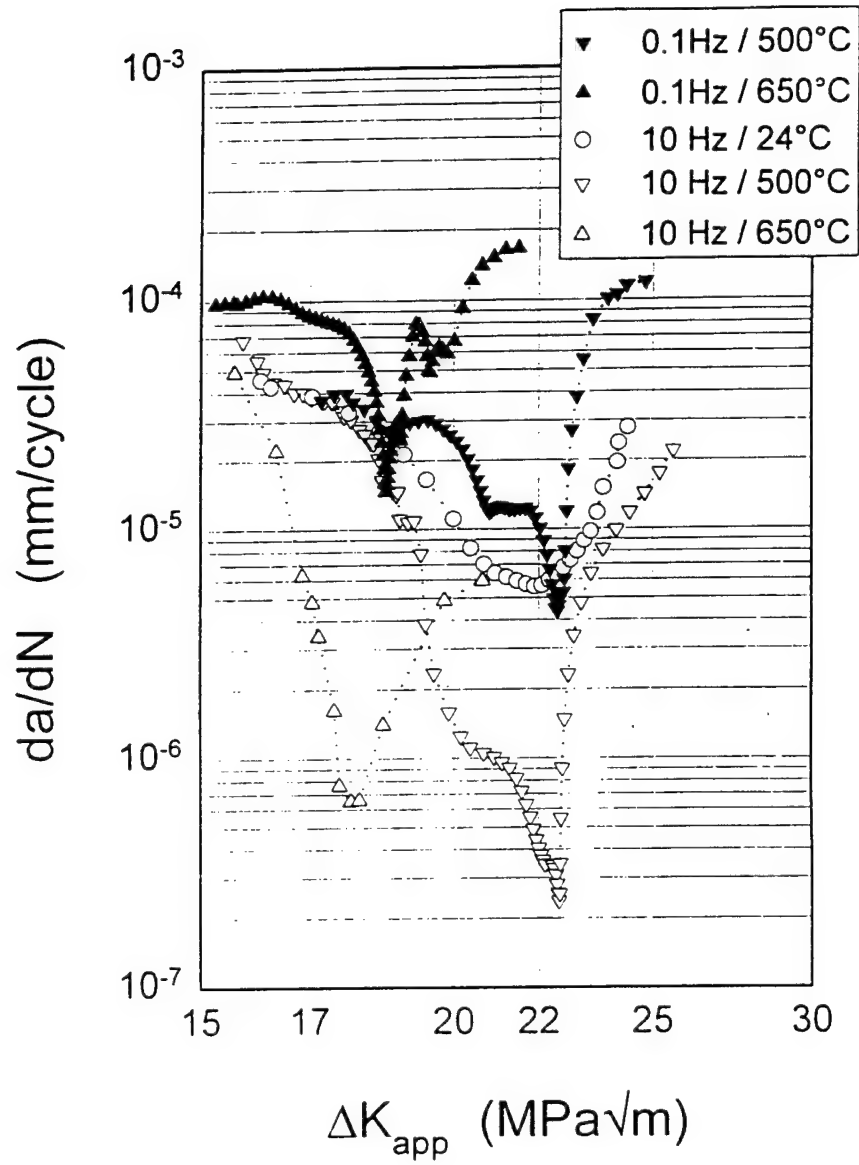


Fig. 5.2 Fatigue crack growth rate, da/dN , versus the applied stress intensity factor, ΔK_{app} , during the initial crack growth deceleration and acceleration stages.

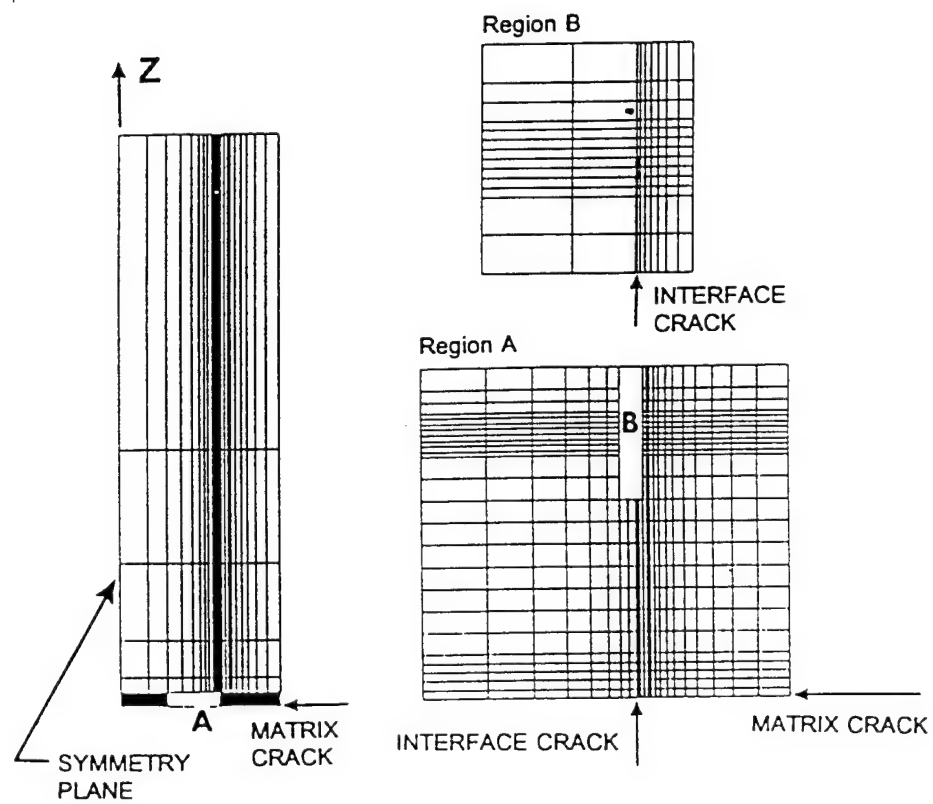


Fig. 5.3 Finite element mesh employed in modelling the response of bridging fiber under cyclic loading.

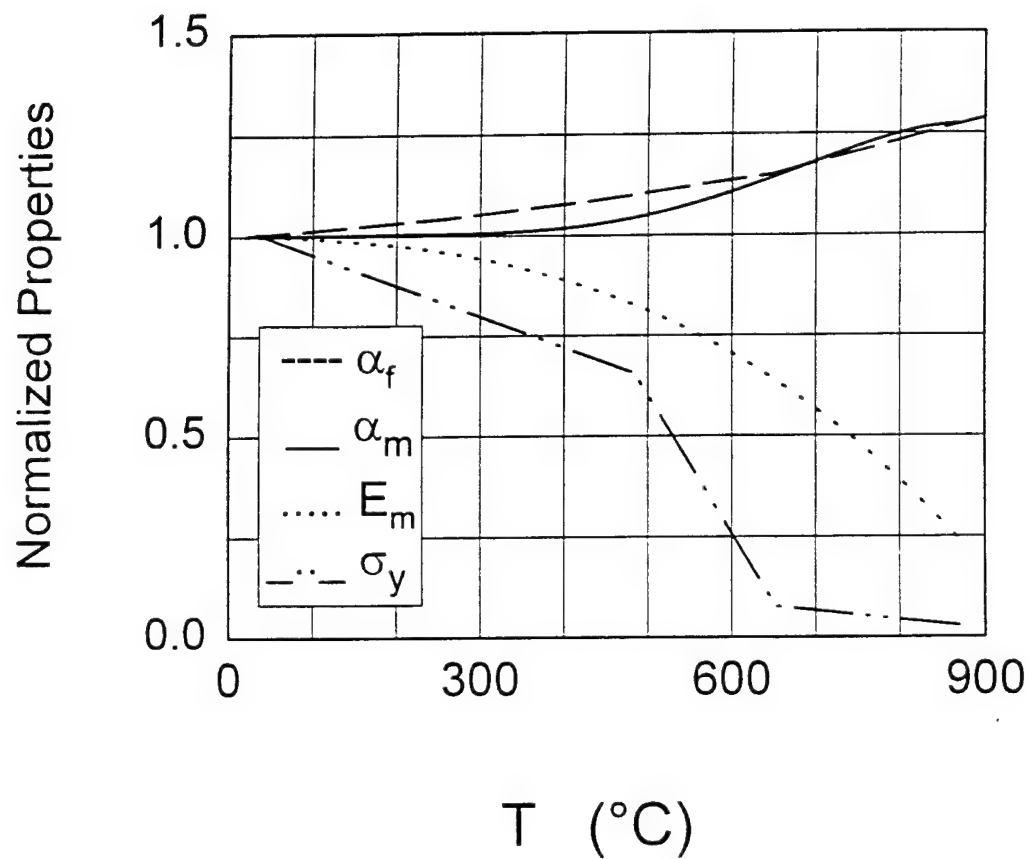


Fig. 5.4 Young's modulus, E , yield strength, σ_y , and coefficient of thermal expansion, α_m , for Timetal-21S matrix alloy, and coefficient of thermal expansion, α_f for SM1240 fiber. The properties are normalized by their respective values at 24 °C : $E_{RT} = 94$ GPa, $\sigma_{Y,RT} = 1040$ MPa, $\alpha_{m,RT} = 8.41 \times 10^{-6} / ^\circ\text{C}$, and $\alpha_{f,RT} = 4.72 \times 10^{-6} / ^\circ\text{C}$.

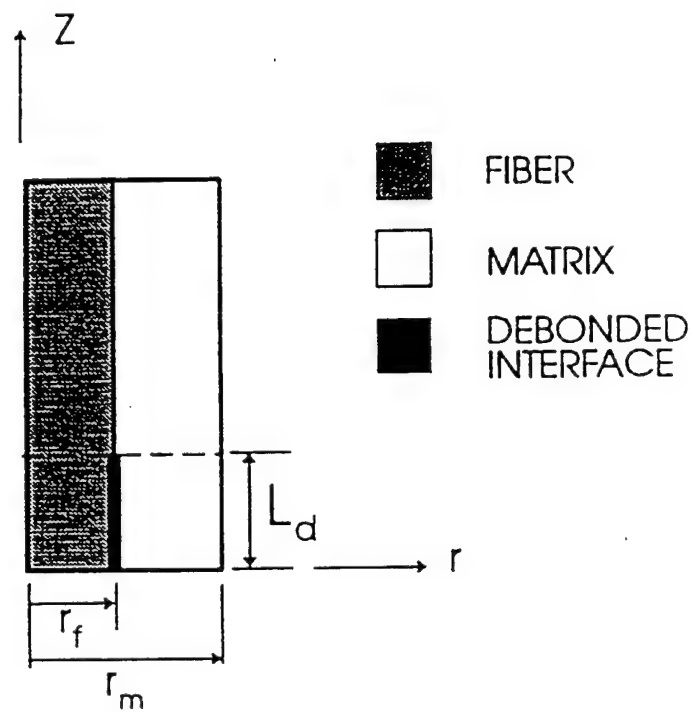


Fig. 5.5 Cross section of the axisymmetric model showing the debonded length, L_d , radius of fiber, r_f and radius of matrix cylinder, r_m . z and r are the axial and radial coordinate axes, respectively.

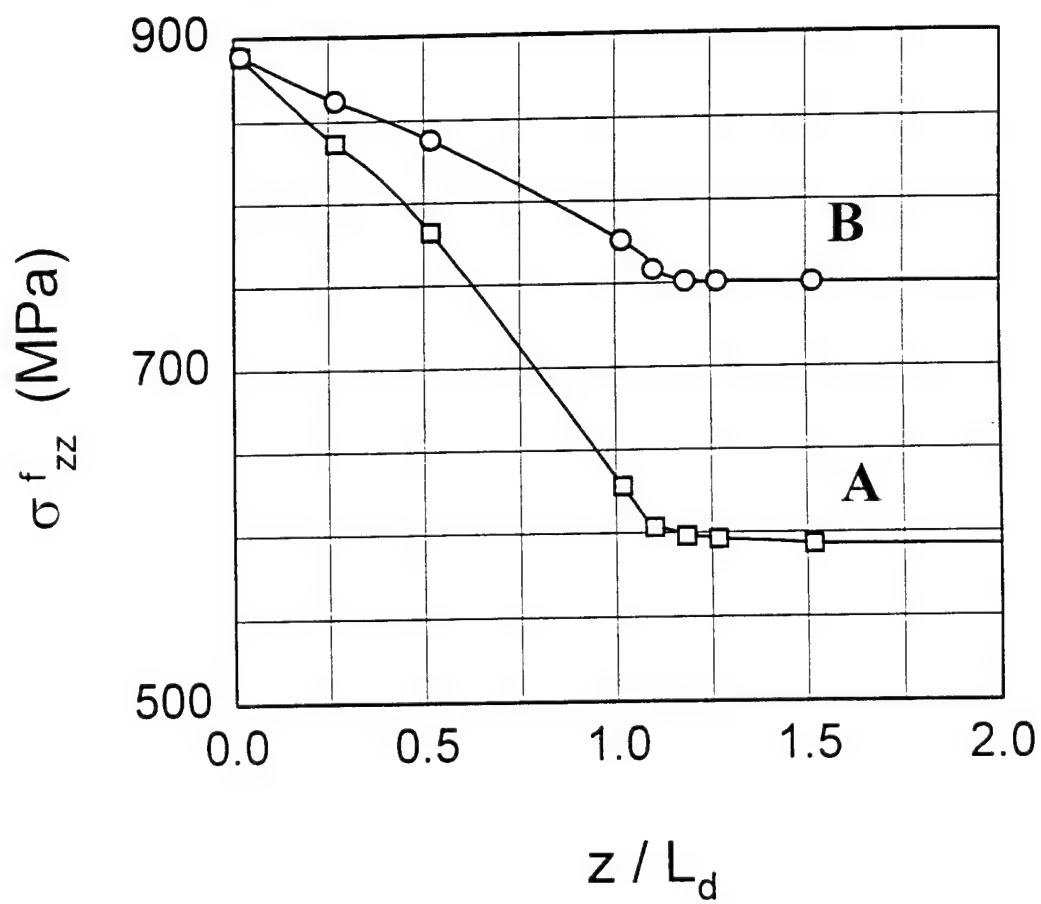


Fig. 5.6

Variation of axial stress along the bridging fiber at different loading cycles. Curve A represents the stress variation after 1 load cycle while curve B is the variation at the end of 500 load cycles. The debonded length, $L_d = 1200 \mu\text{m}$.

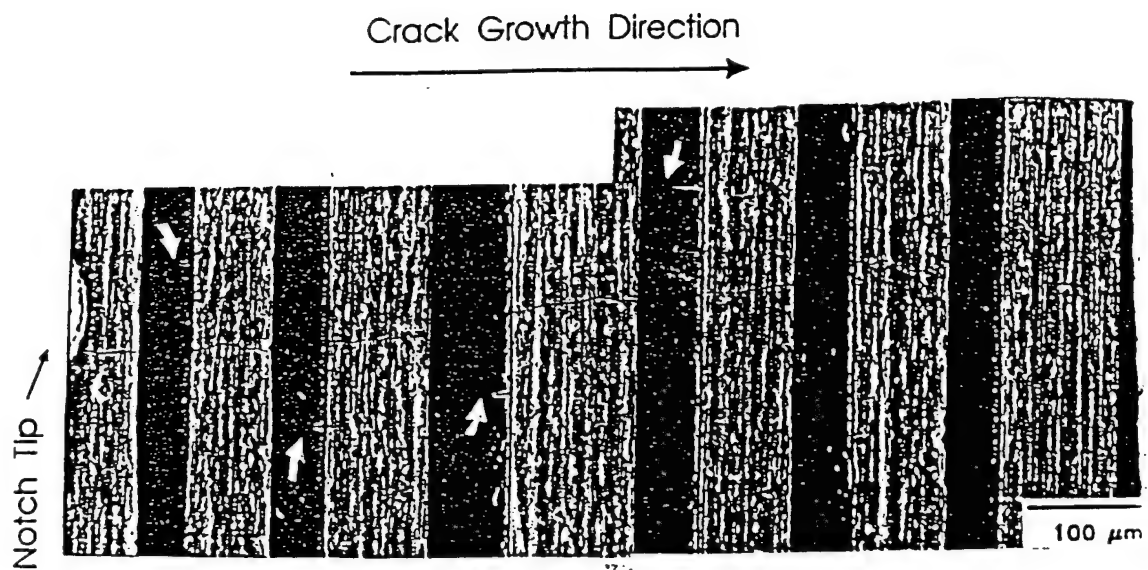


Fig. 5.7 Fracture sites of bridging fibers for test condition 2B, (see Table 5.1), marked with white arrows, above and below the matrix crack plane. The dark areas are the fiber phase.

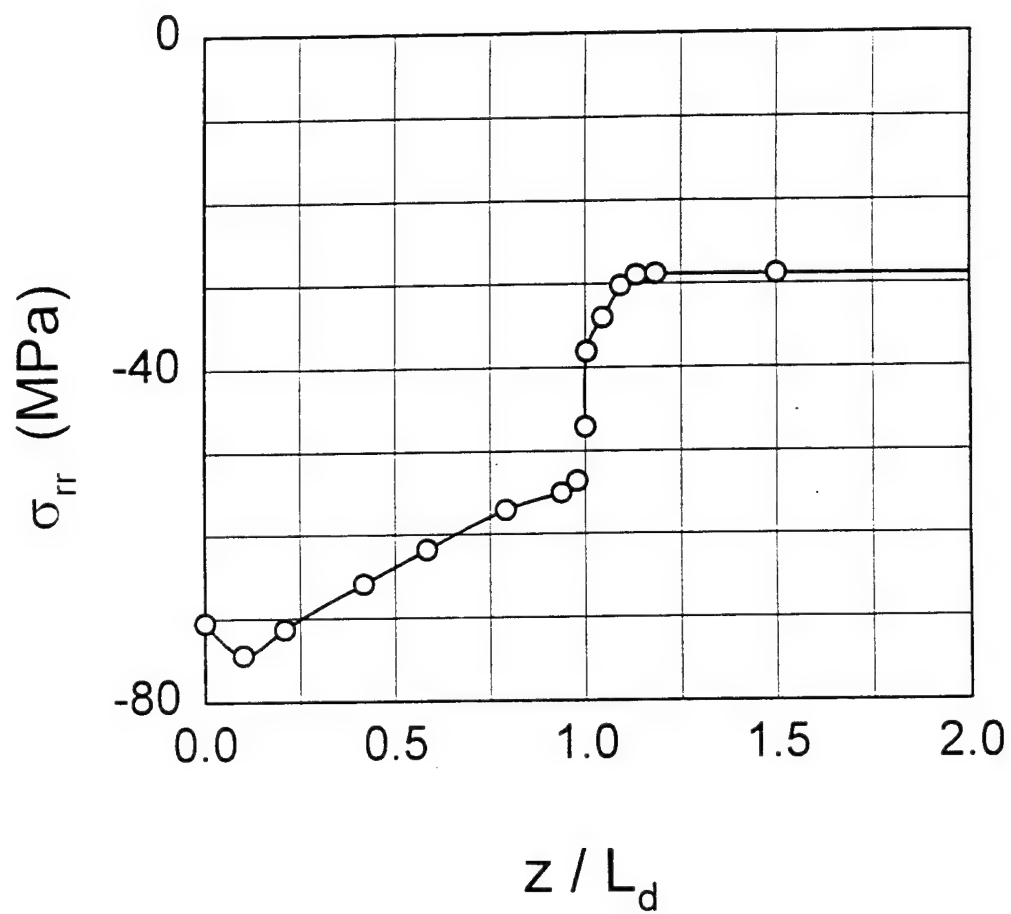


Fig. 5.8

Variation of radial stress along the fiber/matrix interface at the peak of the first applied load cycle. The temperature is 650 °C and the debonded length, $L_d = 1200 \mu\text{m}$.

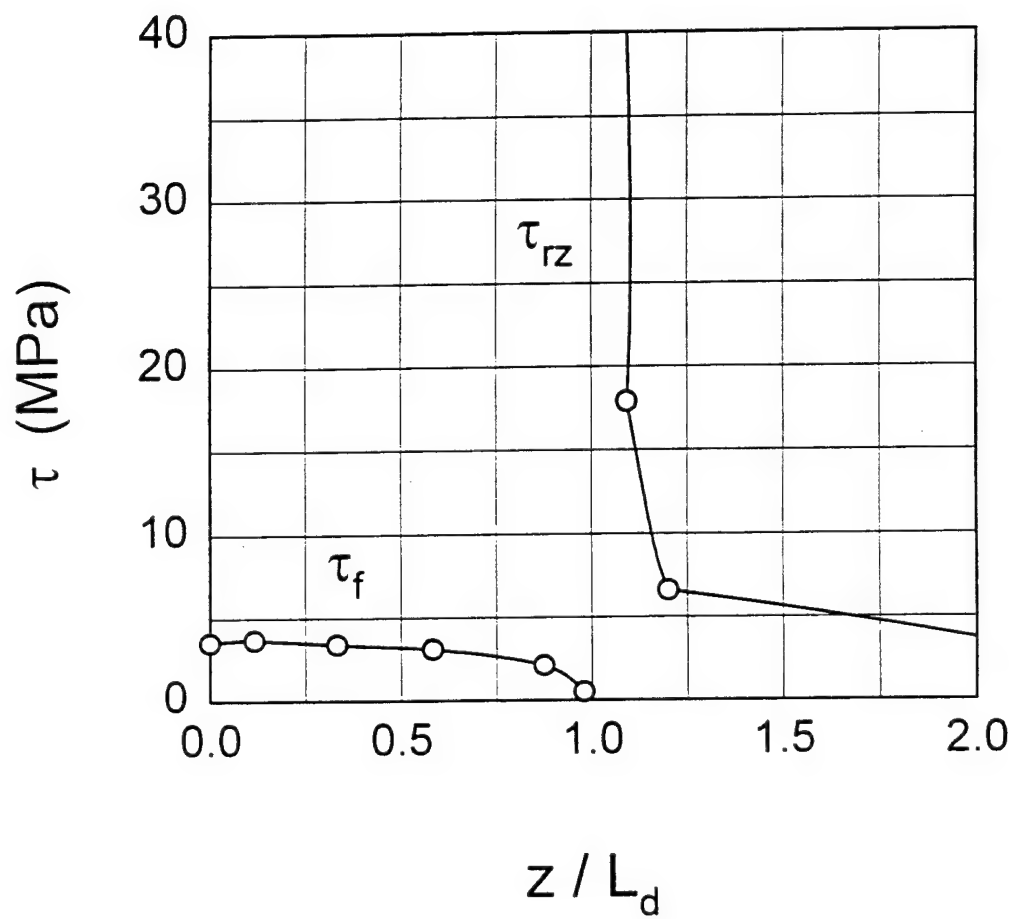
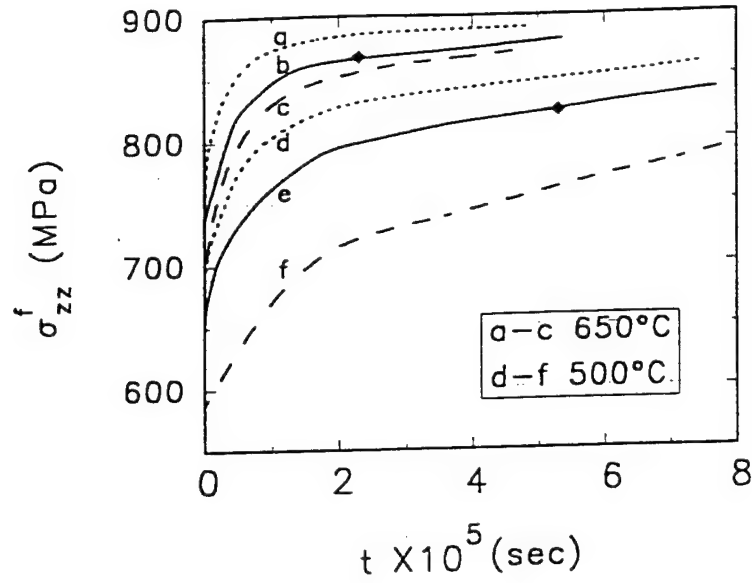
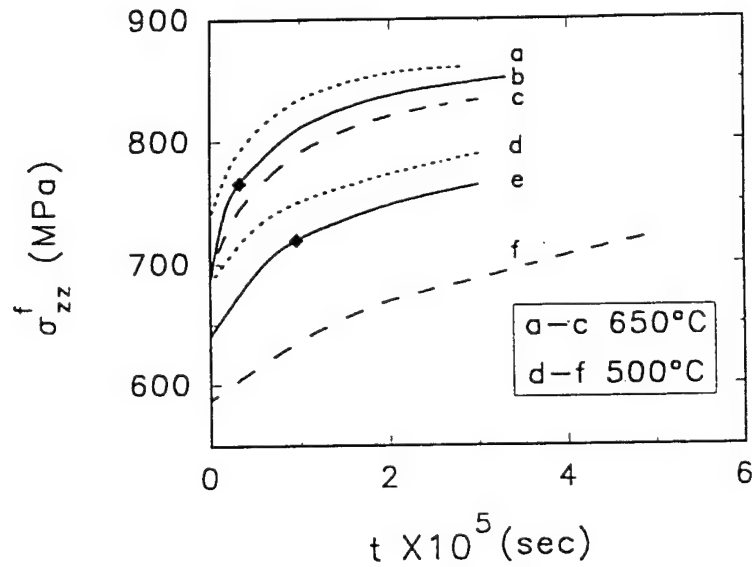


Fig. 5.9

Variation of shear stress along the fiber/matrix interface. The frictional shear stress, τ_f , acts along the slip length, $L_s = 950 \mu\text{m}$, with the coefficient of friction, $\nu = 0.05$ at test temperature 650°C . The debonded length, $L_d = 1200 \mu\text{m}$.



(a)



(b)

Fig. 5.10

Evolution of axial stress in the bridging fiber at the loading frequencies of (A) 0.1 Hz and (B) 10 Hz. - - - - without process induced residual stress and with uniform large matrix grain size. ——— with residual stress and duplex microstructure of the matrix phase. — — — — with residual stress and uniform large matrix grain size. The filled diamond symbols on curves b and e represent the fatigue strength, S_f of the bridging fibers.

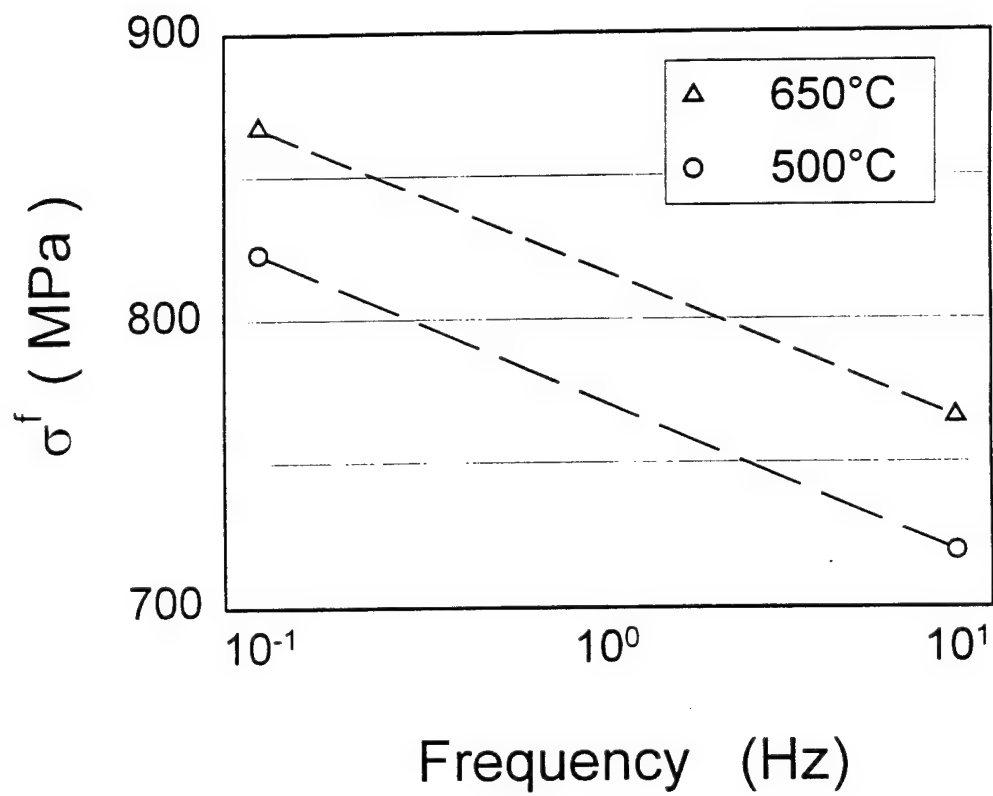


Fig. 5.11 The influence of temperature and loading frequency on the fatigue strength of bridging fiber in SM1240/Timetal-21S composite.

CHAPTER 6. Fibers Damage Mechanisms in Titanium Metal Matrix Composites ⁶

Abstract

This work examines the fatigue damage mechanisms of SiC fibers at different temperatures. For this purpose, a series of monotonic tension, residual fatigue strength and fatigue life tests on SCS-6 fibers were performed at ambient temperature, 500 and 650 °C. The surface of fatigued fibers were examined for damage features such as distribution of cracks and spalling of the carbon-rich coating. The results show that both static and fatigue strength of SCS-6 fibers are unaffected by test temperature of 650 °C or below. In addition, the onset of fiber fracture is instantaneous. Temperature influenced the fracture process of these fibers through the density of cracks in the outermost carbon-rich coating layer. A higher mean crack density was observed on surface of fibers fatigued at 650 °C than those fibers tested at 500 °C. The composite damage, in terms of crack distribution along the embedded fibers, was examined using finite element analysis. In support of these calculations, SCS-6/Timetal-21S composite specimens were fatigued to the same number of

⁶ Based on: M. N. Tamin and H. Ghonem, "Fibers Damage Mechanisms in Titanium Metal Matrix Composites," *Fatigue and Fracture of Engineering Materials and Structures*, submitted for publication, April 1997.

cycles as employed in the fiber residual strength test at the respective temperature. One surface of each fatigued composite specimen was ground and polished to the first layer of fibers to examine microcrack initiation sites in the interphase region along the fiber. Results show that the mechanism of crack initiation in the coating/interphase region of a SCS-6/Timetal-21S composite and in the carbon-rich coating of a SCS-6 fiber specimen are similar. In addition, the interphase zone does not influence the strength of reinforcing fibers in the temperature range of up to 650 °C.

6.1 Introduction

The stress evolution in a bridging fiber during the crack growth bridging is a direct result of load transfer from the deforming matrix phase. The rate of the stress build-up in the fiber is a function of loading parameters such as stress range and temperature and material variables including matrix grain size, fiber volume fraction and process-induced residual stress [Tami96]. The application of cyclic loading, simultaneously, results in fatigue strength degradation of the fiber. Fracture of a bridging fiber is likely to occur in the debonded fiber/matrix interface region along the fiber where extensive frictional wear of the fiber has occurred [Thou89, Davi92, Jeng93]. Since a bridging fiber provides traction which acts to close the matrix crack surfaces, the growth of the crack is retarded. Upon breakage of the fiber, the load carried by this fiber is redistributed to the surrounding fiber which leads to an increase in the crack-tip driving force and accelerate the propagation of the crack.

The fracture process of a fiber, generally, begins with initiation of microcracks in the interphase region and/or fiber coating materials. The interphase region in a SiC/Ti MMC, which form during consolidation of the composite is a brittle layer consisting of titanium carbide and silicides, mainly TiC and Ti_5Si_3 . Elemental analysis of the reaction region in a SCS-6/Ti-6Al-4V composite showed that the interphase zone consists of TiC and a titanium silicide, Ti_5Si_3 and/or Ti_3SiC_2 [Lanc88]. This zone is a highly stressed region due to mismatches in the coefficient of thermal expansion of the adjacent fiber and matrix phase. In addition, the interphase becomes more critical during loading of the composite because of the load transfer between the fiber and the matrix across the zone. The presence of the interphase zone, however, does not in itself contribute to the degradation of the uniaxial properties of the reinforcing fiber. The strength of SiC SCS-6 fibers was found unaffected by the deposition of a titanium coating and annealed for as long as 8 hours at 850 °C [LePe88]. In a separate study, the fibers extracted from a SiC/Ti-24-11 composite by etching away the matrix also displayed a negligible strength degradation [Brin90]. The high tensile residual stress components in the interphase region coupled with a lower strength carbon-rich coating layer of the fiber facilitate the initiation of radial cracks along the interface. While the interface crack initiation depends on the fracture strain or strength of the interphase layer, the propagation of these cracks, either into the matrix phase or the fiber, depends on the toughness of the respective region. In the event that the fiber does not fracture, these cracks could also extend along the fiber/matrix interface.

Multiple cracks growing parallel to each other have been observed in SiC/Ti MMCs subjected to a maximum stress as low as 17 % of the static notched strength of the composite

[Naik91, Baku92, Harm89, Hill90]. These matrix cracks lead to stiffness and strength degradation of the composite even without fracture of the reinforcing fibers. Since the crack density in the composite is governed by the externally applied load, similar crack density and its dependencies on applied stresses and temperatures is expected to occur on isolated fibers subjected to identical loading conditions. On the basis of this assumption, the objective of this work is to examine the mechanism by which fracture of a bridging fiber in a SiC/Ti MMC occurs through the formation of cracks in the carbon-rich coating layer of isolated SiC fibers. In this respect, the strength characteristics and surface crack features of SiC fibers are investigated through a series of residual fatigue strength and fatigue-life tests performed on SCS-6 fibers at ambient temperature, 500 and 650 °C. While these tests provide the strength and strength degradation characteristics of SCS-6 fibers, the monotonic tension tests are conducted at these temperatures for baseline strength properties. Tests on SiC/Ti MMC specimens are carried out to establish the correlation between the density of cracks observed in the interphase region along a fiber and the circular surface crack density on isolated fiber. The results will be utilized in interpreting the observed variations in composite strengths tested at different temperatures.

The fiber-mat specimen and composite material used in this study are introduced in the next section. Experimental procedures for monotonic tension, fatigue-life and residual fatigue tests at elevated temperature are described in this section. This is followed by a description of composite fatigue tests and their results with emphasis placed on the observed circular cracks spacing along the fatigued fiber. A simple model based on linear elastic fracture mechanics is utilized to support the formation of multiple cracks prior to fiber

fracture. The strength and residual strength characteristics of the fiber are also described in this section. The fourth section of the paper deals with a numerical procedures aiming at determining the evolution characteristics of stresses in a critical fiber during bridging fatigue crack growth in the composite. The fracture of a bridging fiber is then postulated through a stress-based fracture criterion. The correlation between circular surface crack density on isolated fiber and the distribution of microcrack initiation sites along the fiber/matrix interface in the composite is also discussed.

6.2 Materials and Experimental Procedures

The material used in this study is a unidirectional SCS-6/Timetal-21S composite with a fiber volume fraction, $v_f = 0.35$. The 140- μm diameter SCS-6 fiber consists of a carbon core, an inner coating, three SiC layers which exhibit different contrasts and an outermost carbon-rich coating with a typical cross-section as shown in Fig. 6.1. The SCS-6 fiber has a thick carbon-rich coating (3-4 μm) in which the silicon content exhibits maxima at the outer surface and 1.5 μm from the surface. The coating, which is made of a sequence of low shear strength pyrocarbon sublayers alternating with strong SiC + C sublayers, consists of 65 % carbon and 35 % SiC [LePe88]. The structural and chemical aspects of each layer have been characterized in a microstructural study using various techniques of electron microscopy [Ning91]. The chemical composition of several fibers have also been established in a comparative study on boron and SiC filaments [LePe88]. The outermost carbaceous

layer consisting of a carbon matrix with SiC particles embedded in it apparently doubles the strength of the uncoated SCS fiber [McEl87]. This thick soft layer would not be totally consumed by the coating-matrix reaction when the fibers are embedded within the metal matrix at elevated temperatures. In addition, the cracks that occur in the reaction zone, under loading, cannot act as stress raiser at the SiC deposit surface. The pyrolytic carbon in the SCS-6 coating exhibits anisotropic properties similar to that of a graphite crystallite with the principal c-axis perpendicular to the fiber surface. The properties of massive pyrolytic carbon deposit have been estimated by Li and Wisnom [Li96] based on properties of graphite crystal [Bokr69] and some deposited pyrolytic graphite [Gebh65, Bokr66].

Tests on SiC fibers are performed using SCS-6 fiber-mat specimens. The as-received fibers, which are weaved by molybdenum wires, were cut to a length of 50 mm. A water-based polymeric binder is applied to both ends of each fiber-mat specimen to form a tab and help maintain the regular fiber spacing. Each fiber-mat specimen, which consists of between 35 to 40 fibers, is aligned and held by a flat hydraulic-actuated grips in a closed-loop servohydraulic testing machine. The baseline tension tests are conducted under load control at a loading rate of 10 MPa/sec. Heating of the specimen is provided by a quartz-lamp heating unit and the specimen is soaked at the test temperature for a duration of 30 minutes prior to loading. In a residual strength test, a fiber-mat specimen is subjected to fatigue loading for a specified number of cycles without breaking any fiber. The specimen is then pulled to fracture at a loading rate of 10 MPa/sec. The load at fracture indicates the residual strength of the fatigued fiber-mat specimen. In a fatigue-life test, the specimen is cycled at a loading frequency of 10 Hz until fracture. The loading conditions employed for all tests

are summarized in Table 2. The loading of the fiber below 2000 MPa is of practical interest while a higher load of 2500 MPa is employed to build the concept for visualizing the damage mechanism of the fiber. At the end of the fatigue tests, the fractured fibers were examined under a scanning electron microscope for surface cracks and measurements of crack spacings were taken from the gage length portion of the specimen.

Composite fatigue tests were performed on 6.5 X 1.5 X 75-mm length unnotched composite specimens at 500 and 650 °C with a loading frequency of 10 Hz. The applied load range was selected to generate a fiber stress level similar to that experienced by the isolated fibers during the corresponding fiber test. In addition, the specimens were fatigued to the same number of cycles as employed in the fiber test. At the end of the test, one surface of each specimen was grounded to the first layer of fibers and polished. The surface was examined using SEM for the spacing of crack initiation sites along the fiber/matrix interphase.

6.3 Results

Fatigue tests performed on SCS-6 fiber-mat specimen yield information on the strength properties of the fibers as influenced by applied stress and test temperature, and the distribution of circular cracks formed throughout the duration of the test. The response of the fiber under static and fatigue loading is discussed in the next section. The following section discusses several features of surface cracks observed on the fiber.

6.3.1 Fiber Residual Strength

As shown in Fig. 6.2, the baseline tensile property of SCS-6 fibers indicates a mean tensile strength of 3.05 GPa with a standard deviation of 0.6 GPa. The strength is comparable to the fracture strength of SiC material, reported as 2.94 GPa for a 100 μ m-diameter fiber [Ochi79]. The mechanical strength of a ceramic fiber is also influenced by the gage length of the fiber specimen used. From fracture mechanics viewpoint, a longer gage length provides a greater volume of material, thus, contains a larger number of inherent defects. These defects, in the form of voids and microcracks, would propagate during fatigue loading of the fiber. In addition, within the test temperature range of 650 °C and below, the intrinsic strength of a SiC fiber is independent of temperature. This is expected as only slight increase in strength (~10 %) was observed in the SCS-2 and SCS-6 fibers after an annealing treatment at 850 °C for duration of 100 hours [LePe88]. Furthermore, the SCS-6 fiber deforms elastically with no measurable creep deformation up to 800 °C while in the temperature range of 800 to 1400 °C, the fiber exhibits anelastic creep behavior [DiCa86, Beal90, Cart84]. At higher temperature above 1400 °C, segregation of the free carbon film present at the SiC grain boundaries to the grain junctions occurs [Ning92].

The residual fatigue strength of SCS-6 fibers plotted as function of number of load cycles at various maximum applied stress is illustrated in Fig. 6.3. These data correspond to tests performed at 500 and 650 °C for various applied stress ranges as listed in Table 6.2. Although the core/fiber reaction kinetic study of SiC (SM1240) fiber suggested that prolonged thermal exposure would degrade the tensile strength of the fiber (e.g. 100 hours

at 900 °C). the low temperature range used in this study eliminates such possibility. This is noted in Fig. 6.2 and Fig. 6.3 where the tensile and fatigue response of SiC SCS-6 fiber is insensitive to temperature of 650 °C and below. The characteristic of each residual life curve suggests that the fiber retains its strength throughout the duration of applied load cycles until fracture occurs. This sudden fracture behavior is typical of a ceramic fiber. For small applied load range ($\Delta\sigma = 100$ MPa), however, the transition period for strength degradation prior to fracture becomes more apparent.

Data points along the abscissa of residual-life plot (Fig. 6.3) provides information on the fatigue life of SCS-6 fibers. These data are presented in the form of fatigue strength versus cycle to fracture, S-N plot as shown in Fig. 6.4. The fibers display an "endurance" limit of 1.3 GPa, below which the fatigue lives of these fibers exceeds 10^6 load cycles. The fatigue fracture of the ceramic SCS-6 fiber, when subjected to maximum stress level above 1.3 GPa, was observed to occur instantaneously. Therefore the fatigue process of the fiber is viewed, in this study, to consist of initiation of microcracks in the outermost carbon-rich coating layer. The low fracture strength of the coating layer (20.7 MPa for amorphous carbon) compared to the SiC-body of the fiber (2.94 GPa) allows for multiple cracks to form in the layer prior to notching the SiC-body of the fiber.

Although the strength of isolated SCS-6 fibers is insensitive to temperature of 650 °C and below, the strength of Ti-alloy reinforced with these fibers is known to vary within this temperature range. The variation in the composite strengths with temperature is interpreted through the fracture process of the reinforcing fiber. In this respect, the formation of circular cracks on the surface of fatigued fibers and the initiation of microcracks in the

interphase region of a SCS-6/Timetal-21S composite are examined.

6.3.2 Fiber Cracks

During tensile loading of a SCS-6 fiber, the carbon-rich fiber coating is expected to fail first because the fracture strain of the coating at room temperature ($\epsilon_c = 0.227\%$) is smaller than that of the SiC-body of the fiber ($\epsilon_b = 0.667\%$), as estimated from elastic calculations. In the presence of a notch, the fracture strain of the SiC-body of the fiber and its coating for a given load condition could be determined from simple fracture mechanics model, as outlined in the appendix (Section 6.7). Calculation of strain in the SiC-body of the fiber, employing material properties as quoted in the appendix in eq. (6.4), indicates that the notch reduces the strain to fracture the fiber by 43 %. Since the corresponding strain in the SiC-body of the fiber when the coating fractures is lower than that required to fracture the body in the presence of a coating crack, multiple cracks could form in the coating before the fiber fracture event. The strain distribution along the fiber coating in the vicinity of a circular crack subjected to a monotonic loading is examined using the finite element analysis to estimate the minimum spacing between the cracks. In the simulation, the SiC elastic properties is assumed to be independent of temperature while the carbon coating assumes the properties of amorphous carbon [Bues92]. These properties are listed in Table 6.1. The minimum spacing of the coating crack is inferred from this strain distribution as illustrated in Fig 6.5(a). A new crack is likely to initiate at a distance along the fiber where the strain

gradient due to the existing crack diminishes. Since only slight variation in the properties of amorphous carbon over the temperature range of 24 to 650 °C is observed (see Table 6.1), the resulting minimum crack spacings predicted for temperatures within this range are practically identical at 0.023 mm. The model is also capable of predicting the minimum coating crack spacing along a SiC fiber subjected to fatigue loading, however, the required strength-life characteristics of amorphous carbon is unavailable.

The surfaces of fatigued SCS-6 fibers are examined for multiple circular cracks which are initiated during cyclic loading of the fiber-mat specimen. A typical morphology of circular cracks in the gage length section of a fiber-mat specimen fatigued at 650 °C is shown in Fig. 6.6. These fibers have accumulated $24.8 (10^6)$ cycles at an applied load of 1500 MPa. The distribution of 785 measurements of spacings between adjacent cracks on these fibers is shown in Fig. 6.7(a). The data shows that 78 % of the measured crack spacings fall under 40 μm . These portion of the data are reanalyzed, as illustrated in Fig. 6.7(b), assuming a Weibull distribution function which yield a mean distance between adjacent cracks along the fiber of 7.5 μm . The crack density is then defined as the inverse of the mean crack spacing. Similar statistical features of the crack distribution on fatigued fibers for test cases listed in Table 2 are observed. The variation of circular crack density as functions of maximum applied stress and test temperature at fracture of the fibers is summarized in Fig. 6.8. In a fatigue cycle with applied load which is not sufficient to cause immediate fiber fracture but high enough to exceed the fracture strain of the fiber coating layer, multiple cracks will form along the fiber. In this case, a small load would result in higher crack density in the coating due to greater number of accumulated load cycles to

fracture, as illustrated in Fig. 6.8. The results show that the crack density at fracture is higher for fibers tested at 650 °C compared to that fatigued at 500 °C. This temperature effect could have come through temperature variations in the properties of the coating. The carbon-rich coating of SCS-6 fiber is assumed, in this study, to have the properties of amorphous carbon in which the elastic modulus increases with increasing temperature [Bues92]. Therefore, the fracture strain of the coating will decrease with increasing temperature as predicted from elastic consideration which leads to a higher number of cracks to form at higher temperature. Since the strength degradation of SCS-6 fibers does not occur below 650 °C, this result suggests that the density of cracks in the carbon-rich coating of SCS-6 fiber is not the source of fiber strength degradation. This is further supported by the observation that the severe spalling of the carbon layer due to abrasion by Mo-weave, as illustrated in Fig. 6.9, does not cause fracture of the fiber in this region.

The crack initiation sites in a SCS-6/Timetal-21S composite along the fiber/matrix interphase region are identified and examined. The applied loading are such that the fibers in this composite experienced the same loading conditions and accumulated load cycles as those applied to isolated fiber-mat specimen in the residual strength test of the fiber. Acoustic emission (AE) monitoring of the damage evolution in the composite throughout the duration of fatigue testing did not indicate any event of fiber fracture. The fracture event of a SiC fiber is associated with acoustic emission of a high amplitude signal (≥ 90 dB) with a narrow pulse width (rise time ≤ 35 μ sec). The collected AE signal from the composite fatigue tests showed that only moderate amplitude signal (between 40-65 dB) were triggered, as shown in Fig. 6.10(a) for 650 °C. A representative AE data collected over a period of 10

seconds is illustrated in Fig. 6.10(b) in terms of the energy count. The three distinct bands of energy counts correspond to other damage mechanisms such as matrix cracking and debonding along fiber/matrix interface [Luo95, Baku94]. The longitudinal cross section of the fatigued composite specimen at the first layer of fiber shows that all the fibers are intact with extensive matrix cracking, see Fig. 6.11. These cracks are intergranular cracks which have initiated in the interphase region along a fiber. Since the carbon-rich layer acts as a stress diffuser, the crack propagates either along the grain boundaries into the matrix or along the fiber/matrix interphase region. The matrix grain boundaries which meet the interphase region, therefore, are susceptible to become the initiation sites for the cracks. The spacing between adjacent cracks which have initiated from the interphase region are measured. The data indicated that 75 % of the total of 715 measurements fall within 200- μm distance for specimen fatigued at 500 °C while 84 % of 780 measurements fall within a 100- μm distance for specimen tested at 650 °C. The statistical distribution of these measurements, as illustrated in Fig. 6.12, yield a mean spacing between adjacent crack initiation sites of 60 and 40 μm for test at 500 and 650 °C, respectively.

Since the distribution of crack initiation sites in the interphase region along the fiber in a SCS-6/Timetal-21S composite and the spacing of circular cracks on isolated SCS-6 fibers display identical trends, the densities of the mean spacings in each case are related. This correlation, shown in Fig. 6.13, can be described mathematically as an exponential function.

6.4 Bridging Fiber Damage Mechanism

Results obtained from the experimental program are utilized in this section to formulate a model to predict the failure of a bridging fiber traversing a fatigue propagating crack. The simultaneous build-up of stresses in a bridging fiber and the degradation of the fiber strength during bridging fatigue crack growth forms the basis for the fiber fracture criterion proposed in this study. The criterion is schematically illustrated in Fig. 6.14(a).

The process of fiber fracture during bridging fatigue crack growth of a SCS-6/Timetal-21S composite, based on the strength of fiber material, can be visualized as follows. The evolution of fiber stress in the critical section along the fiber is represented by curve 0-a in Fig. 6.14(b), while curves b-c, b-d, and b-e are the residual life plot for different fiber stress. After accumulating N_1 load cycles, the load transfer from the matrix resulted in fiber stress σ_1 . The corresponding residual strength of the bridging fiber is represented by the line S_1-m_1 , where S_1 is located on curve b-e. Since the residual strength, $S_R (= S_1 - \sigma_1)$ is larger than zero, the fiber will not fracture at cycle N_1 . Subsequent application of load cycles will result in an increase in the fiber stress to σ_2 with a corresponding decrease in fiber strength as indicated by line S_2-m_2 , where S_2 lies on curve b-d. At fracture of the bridging fiber, the fiber stress σ_3 reached the fatigue strength of the fiber at S_3 .

The evolution characteristics of bridging fiber stress in a SCS-6/Timetal-21S composite is examined using finite element method. The stress build-up in the fiber is dependent on the rate of load transfer from the matrix to the fiber. An accurate modeling of the response of the matrix phase due to fatigue loading at elevated temperature, therefore,

is essential in predicting the rate of load transfer to the fiber. In this respect, the constitutive behavior of Timetal-21S matrix material is described using a unified Bodner-Partom inelastic strain model [Bodn75, Neu95]. The SCS-6 fiber is assumed to be elastic in the temperature range examined in this study.

Crack bridging in a SiC/Ti MMC is always accompanied by fiber/matrix interface debonding along a bridging fiber [Davi92, Sens90, Bowe91, Tele93, Zhen95, Tami95]. The fracture of this fiber, from strength of material viewpoint, would occur across a critical plane along the fiber. The location of this fiber is selected, in this study, based on a unit cell configuration consisting of a fiber embedded in the matrix phase under crack bridging condition, see Fig. 6.15(a). Although the maximum load in the fiber occurs at section a-a based on equilibrium of forces on the cylinder model, the critical plane is identified as section b-b which coincide with the tip of the debond crack, as illustrated in Fig. 6.15(b). The material points in the fiber along this section would experience the highest rate of load transfer due to extensive deformation of the adjacent matrix phase. In addition, the plane is also subjected to stress localization due to sudden transition from debonded interface to bonded region ahead of the debond crack tip. The radial section of the axisymmetric model is then discretized into finite elements with the mesh and boundary condition as illustrated in Fig 6.15(b). The loading conditions of applied stress range, $\Delta\sigma = 280$ MPa, load ratio, $R = 0.1$ and loading frequencies of 0.1 and 10 Hz are applied to the composite. The results of the simulation is illustrated in Fig. 6.16 for the test temperature of 500 and 650 °C. The trends of the stress build-up curves are governed by viscoplastic deformation of the matrix phase particularly in the vicinity of the fiber/matrix interface where the process-induced

residual stresses are high. During fatigue loading, a lower frequency (0.1 Hz), for the same temperature level, would exposed the composite to higher stresses for a longer duration of time than that due to a higher frequency (10 Hz) loading. The rate of load transfer to the fiber is faster at higher temperature as reflected by the higher slope of the build-up curve for test conducted at 650 °C than at 500° C. The combination of high temperature and low loading frequency, therefore, facilitate the load transfer process from the matrix to the bridging fiber through viscoplastic deformation of the matrix phase. However, the compressive residual stresses in the fiber affect the time-dependent load transfer process by retarding the increase of axial stress component in the fiber.

The transition from initial bridging crack growth deceleration to acceleration stage is assumed, in this study, to be associated with the fracture of critical bridging fibers located farthest away from the bridged matrix crack tip. An accurate determination of the accumulated number of load cycles at the transition point for bridging crack growth of a SCS-6/Timetal-21S composite, based on available experimental data, is not feasible. The response of a SM1240/Timetal-21S composite to identical loading condition as employed in this study showed that the SM1240 bridging fibers accumulated 53.0 (10^3) and 22.9 (10^3) cycles at loading frequency of 0.1 Hz for 500 and 650 °C, respectively [Tami94]. Based on these results, the build-up axial stress in SCS-6 bridging fibers, as illustrated in Fig. 6.16, would not reach saturation prior to a fiber fracture event. This implies that the insitu fiber strength is not being exploited. It is also noted that the cylinder model, employed in the simulation, would predict a saturation stress level corresponding to the balance of external forces acting on the cylinder. Once the stress at a fiber section reached saturation, stress

evolution would continue on adjacent section along the fiber for the remaining load cycles. Larger volume of the fiber would reached the saturation stress level with continued loading until fracture occurs.

6.5 Conclusions

The damage mechanism of a bridging fiber is examined through a series of tests on isolated SCS-6 fibers and the corresponding SCS-6/Timetal-21S composite. The strength characteristics and features of surface cracks on fatigued fibers are examined. The crack density is correlated with the distribution of crack initiation sites in the interphase region of the composite. Major conclusions of the study can be summarized as follows:

1. The residual fatigue strength of SCS-6 fibers is insensitive to test temperature of 650 °C and below. The temperature, however, results in a rapid initiation of cracks in the outermost coating layer of the fiber at higher temperature and lower applied fiber stress.
2. The surface cracks on fatigued isolated fibers have been correlated with the initiation sites of microcracks in the interphase region/fiber coating layer of the composite. The variation of composite strength at different temperatures is explained through the initiation and propagation of these microcracks in the fracture process of the fiber.

3. During the initial crack bridging stage of fatigue crack growth, the fracture of a bridging fiber is predicted when the evolving fiber stress reaches the deteriorating strength of the fiber. The combination of high temperature and low loading frequency results in a faster rate of load transfer per cycle to the bridging fiber.

6.6 References

- [Baku92] Bakuckas, J. G. Jr., Johnson, W. S. And Bigelow, C. A., "Fatigue Damage in Cross-Ply Titanium Metal Matrix Composites Containing Center Holes." NASA TM 104197, February 1992.
- [Baku94] Bakuckas, J. G. Jr., Prosser, W. H. And Johnson, W. S., "Monitoring Damage Growth in Titanium Matrix Composites Using Acoustic Emission." Journal of Composite Materials, Vol. 28, No. 4, 1994, pp. 305-328.
- [Beal90] Beale, J., Curzio, E. L. And Sternstein, S. S., "High Temperature Deformation Studies on CVD Silicon Carbide Fibers." Proceedings of the 35th International SAMPE Symposium, 1990, pp. 1193-1204.
- [Bodn75] Bodner, S. R. And Partom, Y., "Constitutive Equations for Elastic Viscoplastic Strain Hardening Materials." Journal of Applied Mechanics, ASME, Vol. 42, 1975, pp. 385-389.
- [Bokr69] Bokros, J. C., "Deposition, Structure and Properties of Pyrolytic Carbon". Chemistry and Physics of Carbon, Vol. 5, P. L. Walker, ed., 1969, pp. 1-119.

- [Bokr66] Bokros, J. C. and Price, R. J., "Deformation and Fracture of Pyrolytic Carbons Deposited in a Fluidized Bed", Carbon, Vol. 3, 1966, pp. 503-519.
- [Bowe91] Bowen, P., Ibbotson, A. R. And Beevers, C. J., "Characterization of Crack Growth in Continuous Fiber Reinforced Titanium Based Composites Under Cyclic Loading," Fatigue of Advanced Materials, R. O. Ritchie, R. H. Dauskardt and B. N. Cox, ds., Materials and Component Engineering Publications Ltd., PO Box 1550, Edgbaston, Birmingham B15 2JZ, UK, 1991, pp. 379-393.
- [Brin92] Brindley, P. K., Draper, S. L., Eldridge, J. I., Nathal, M. V. And Arnold, S. M., "The Effect of Temperature on the Deformation and Fracture of SiC/Ti-24Al-11Nb," Metallurgical Transactions, Vol. 23A, 1992, pp. 2527-2540.
- [Bues92] Buesking, K. W., Young, J. L. And Reynolds, G. H., "Status of Advanced Filament Development for Titanium Alloy and Titanium Intermetallic Matrix Composites, Part 2. Computed Residual Stresses in Gamma TiAl/Advanced Filament Composites," in Workshop Proceedings on Titanium Matrix Components, P. R. Smith and W. C. Revelos, Eds., April 1992, WL-TR-92-4035, pp. 42-64.

- [Cart84] Carter, C. H. Jr. and Davis, R. F., "Kinetics and Mechanisms of High Temperature Creep in Silicon Carbide: II. Chemically Vapor Deposited." Journal of the American Ceramic Society, Vol. 67, No. 11, 1984, pp. 732-740.
- [Davi92] Davidson, D. L., "The Micromechanics of Fatigue Crack Growth at 25 C in Ti-6Al-4V Reinforced with SCS-6 Fibers." Metallurgical Transaction A, Vol. 23A, Mar 1992, pp. 865-879.
- [DiCa86] DiCarlo, J. A., "Creep of Chemically Vapor Deposited SiC Fibers." Journal of Materials Science, Vol. 21, 1986, pp. 217-224.
- [Gebh65] Gebhardt, J. J. and Berry, J. M., "Mechanical Properties of Pyrolytic Graphite", AIAA Journal, Vol. 3, 1965, pp. 302-308.
- [Harm89] Harmon, D. M. And Saff, C. R., "Damage Initiation and Growth in Fiber Reinforced Metal Matrix Composites." Metal Matrix Composites: Testing, Analysis and Failure, ASTM STP 1032, W. S. Johnson, Ed., American Society for Testing and Materials, Philadelphia, PA, 1989, pp. 237-250.
- [Hill90] Hillberry, B. M. And Johnson, W. S., "Matrix Fatigue Crack Development in a Notched Continuous Fiber SCS-6/Ti-15-3 Composite." Symposium on

Microcracking Induced Damage in Composites. ASME Winter Annual Meeting, Dallas, TX, 26-28 November 1990, pp. 121-127.

- [Jeng93] Jeng, S. M., Nguyen, T. H. B., Dana, O. And Yang, J. M.. "Fatigue Cracking of Fiber Reinforced Titanium Matrix Composites." Journal of Composites Technology and Research, Vol. 15, No. 3, Fall 1993, pp. 217-224.
- [Lanc88] Lancin, M., Thibault-Desseaux, J. And Bour, J- S., J. Microsc. Spectrosc. Electron, Vol. 13, 1988, pp. 503.
- [Li96] Li, D. S. And Wisnom, M. R., "Micromechanical Modeling of SCS-6 Fibre Reinforced Ti-6Al-4V under Transverse Tension - Effect of Fiber Coating." Journal of Composite Materials, Vol. 30, No. 5, 1996, pp. 561-588.
- [Luo95] Luo, J-J., Wooh, S-C. And Daniel, I. M., "Acoustic Emission Study of Failure Mechanisms in Ceramic Matrix Composite under Longitudinal Tensile Loading," Journal of Composite Materials, Vol. 29, No. 15, 1995, pp. 1946-1961.
- [McEl87] McElman, J. A., in Engineering Materials Handbook: Composites, ASM International, Vol. 1, 1987, pp. 858-866.

- [Naik91] Naik, R. A. And Johnson, W. S., "Observations of Fatigue Crack Initiation and Damage Growth in Notched Titanium Matrix Composites." Third Symposium on Composite Materials: Fatigue and Fracture, ASTM STP 1110, T. K. O'Brien, Ed., American Society for Testing and Materials, Philadelphia, PA, 1991, pp. 753-771.
- [Neu95] Neu, R. W. And Bodner, S. R., "Determination of Material Constants of Timetal-21S for a Constitutive Model," Contributive Research and Development, Vol. 6, Prepared for Wright-Patterson AFB, Ohio, Sept 1995.
- [Ning92] Ning, X. J., Pirouz, P. and Bhatt, R., "The Effect of High Temperature Annealing on the Microstructure of SCS-6 SiC Fiber." Material Research Society Symposium Proceedings, Vol. 250, 1992, pp. 187-192.
- [Ning91] Ning, X. J. and Pirouz, P., "The Microstructure of SCS-6 Fiber", J. Mater. Res., Vol 6, No. 10, Oct. 1991, pp. 2234-2248.
- [Ochi79] Ochiai, S. And Murakami, Y., "Tensile Strength of Composites with Brittle Reaction Zones at Interfaces," Journal of Materials Science, Vol. 14, 1979, pp. 831-840.

- [LePe88] Le Petitcorps, Y., Lahaye, M., Pailler, R. and Naslain, R., "Modern Boron and SiC CVD Filaments: A Comparative Study", Composites Science and Technology, Vol. 32, 1988, pp. 31-55.
- [Sens90] Sensmier, M. D. And Wright, P. K., "The Effect of Fiber Bridging on Fatigue Crack Growth in Titanium Matrix Composites." in Fundamental Relationships Between Microstructure and Mechanical Properties of Metal-Matrix Composites, P. K. Liaw and M. N. Gungor, Eds., The Minerals, Metals & Materials Society, Warrendale, PA, 1990, pp. 441-457.
- [Tada73] Tada, H., Paris, P. And Irwin, G., The Stress Analysis of Cracks Handbook, Del Research Corporation, Hellertown, Pennsylvania, 1973, pp. 27.1.
- [Tami94] Tamin, M. N. And Ghonem, H., "A Fracture Criterion For Bridging Fibers in Titanium Metal Matrix Composites at Elevated Temperature." in Durability of Composite Materials, R. C. Wetherhold, ed., The American Society of Mechanical Engineers, New York, NY, MD-Vol. 51, 1994, pp. 51-58.
- [Tami96] Tamin, M. N. And Ghonem, H., "Evolution of Bridging Fiber Stress in Titanium Metal Matrix Composites at Elevated Temperature," Advances in Fatigue Lifetime Predictive Techniques: 3 rd Volume, ASTM STP 1292, M.

R. Mitchell and R. W. Landgraf, Eds., American Society for Testing and Materials. 1996, pp. 24-38.

- [Tami95] Tamin, M. N., Osborne, D. And Ghonem, H., "Influence of Interfacial Properties on Fiber Debonding in Titanium Metal Matrix Composites." Fatigue and Fracture at elevated Temperature, A. Nagar and S. Mall, eds., The American Society of Mechanical Engineers, New York, NY, AD-Vol. 50, 1995, pp. 121-134.
- [Tele93] Telesman, J., Ghosn, L. J. And Kantzos, P., "Methodology for Prediction of Fiber Bridging Effects in Composites," Journal of Composites Technology and Research, Vol. 15, No. 3, Fall 1993, pp. 234-241.
- [Thou89] Thouless, M. D., Sbaizero, O., Sigl, L. S. and Evans, A. G., "Effect of Interface Mechanical Properties on Pullout in a SiC-Fiber-Reinforced Lithium Aluminum Silicate Glass Ceramic." Journal of The American Ceramic Society, Vol. 72, No. 4, 1989, pp. 525-532.
- [Zhen95] Zheng, D. And Ghonem, H., "Fatigue Crack Growth of SM1240/Timetal-21S Metal Matrix Composite at Elevated Temperature." Metallurgical and Material Transaction A, Vol. 126A, 1995, pp. 2469-2478.

Table 6.1 Properties of amorphous carbon and SiC SCS-6 fiber

Amorphous Carbon				
T (°C)	E (GPa)	ν	$\alpha(10^{-6}) / ^\circ\text{C}$	σ_{fract} (MPa)
24	9.10	0.11	0 (Ref)	20.7
260	9.24	0.11	2.500	20.7
538	9.38	0.12	2.899	20.7
816	9.72	0.13	3.333	20.7
1094	10.06	0.13	3.542	20.7
1204	10.34	0.13	3.653	20.7

SiC SCS-6 Fiber
E = 441 GPa
$\nu = 0.25$
$\sigma_{\text{fract}} = 2.94 \text{ GPa}$

Table 6.2 Test matrix for fatigue testing of SCS-6 fibers

Test No.	σ_{\max} (MPa)	N (10^3) cycle	S _{Res} (GPa)
1	1000 / 500 °C	515	2.39
2	1000	875	2.05
3	1000	4648	1.75
4	1000	7000	1.82
5	1500	3.29	2.35
6	1500	10.78	2.30
7	1500	41.12	2.50
8	1500	146.6	2.1
9	1500	410.7	Fractured
10	1500	534.7	Fractured
11	2000	40.87	2.54
12	2000	105.93	Fractured
13	2000	161.57	Fractured
14	2500	15.13	Fractured
15	1500 / 650 °C	247.55	2.04
16	1800	30.03	2.2
17	1800	29.5	Fractured
18	1800	93.52	Fractured
19	1800	178.1	Fractured
20	2500	11.64	Fractured

6.7 Appendix

The fracture strain of the fiber can be determined from fracture mechanics analysis by treating the fiber as a rod with a circumferential crack. A schematic of the fiber as a two-phase cylinder of a SiC-body coated with carbon layer is illustrated in Fig. 6.A-1. The SiC-body has a diameter of $2a$ and the outside diameter of the fiber is $2b$. The coating thickness $c = (b-a)$. The fracture toughness is given by [Tada73]

$$K = \sigma_{\text{net}} \sqrt{\pi c} F(a/b) \quad (6.1)$$

where σ_{net} is the fiber stress at $z = 0$, and the geometry factor, $F(a/b)$ is given by

$$F(a/b) = \frac{1}{2} \sqrt{a/b} \left[1 + \frac{1}{2}(a/b) + \frac{3}{8}(a/b)^2 - 0.363(a/b)^3 + 0.731(a/b)^4 \right] \quad (6.2)$$

The critical strain energy rate for the fiber for plane stress condition is [Tada73]

$$G_c = \frac{K^2}{E_b} \quad (6.3)$$

where E_b is the Young's modulus of the SiC-body of the fiber. At fracture, the toughness of

the fiber reaches its critical value, K^* . The fiber strain at fracture of the SiC-body in the presence of the crack in the coating, ϵ_f^* , is determined as

$$\epsilon_f^* = \frac{1}{F(a/b)} \sqrt{\frac{G_c^*}{E_b \pi c}} \quad (6.4)$$

For SiC SCS-6 fiber, $(a/b) = 0.9718$, $c = 2.0 \mu\text{m}$, $G_c^* = 45.9 \text{ Jm}^{-2}$ and $E_b = 441 \text{ GPa}$.

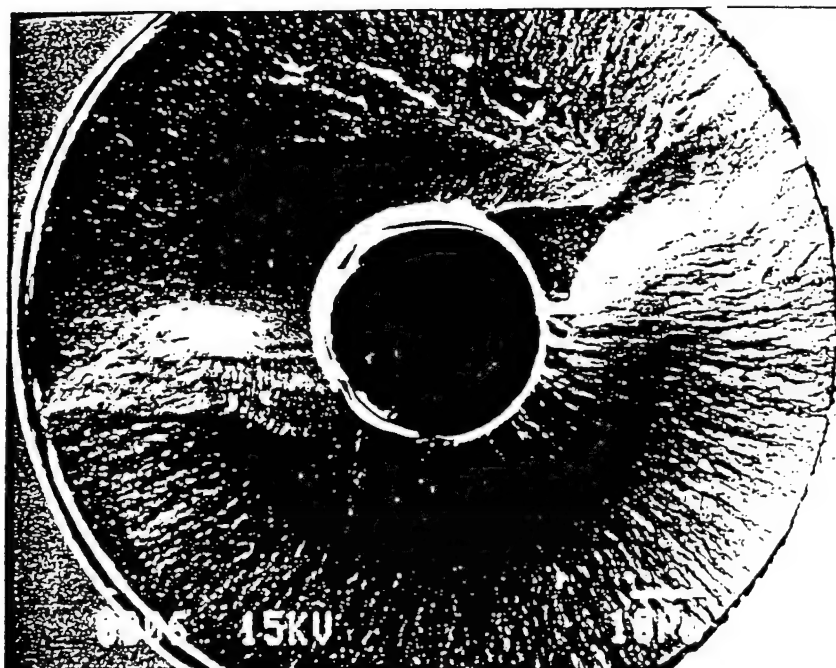


Fig. 6.1 Surface morphology of a SiC SCS-6 fiber.

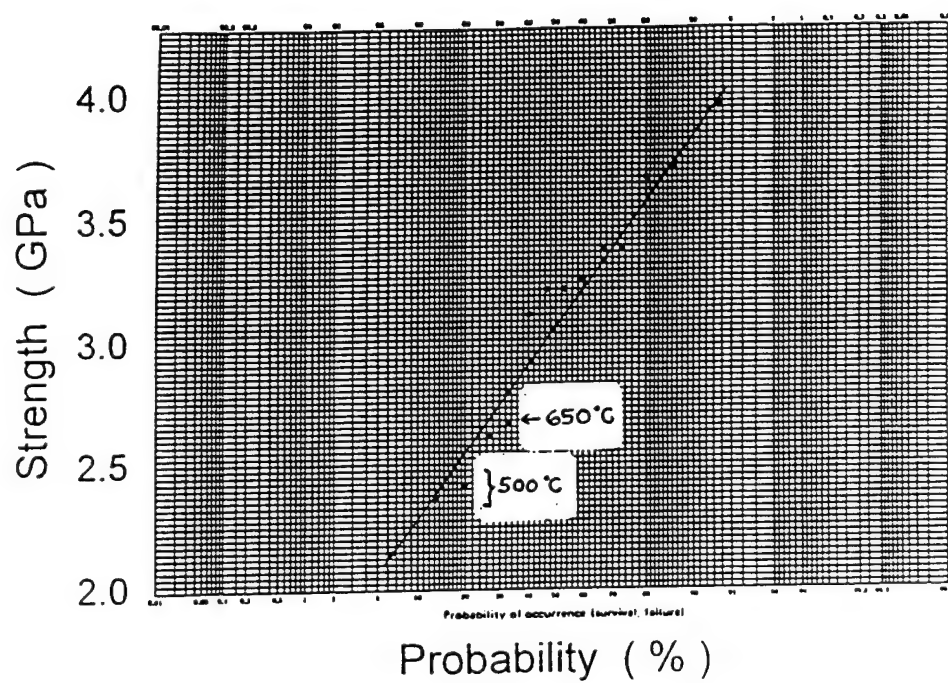


Fig. 6.2 Weibul distribution of tensile strengths of SCS-6 fibers.

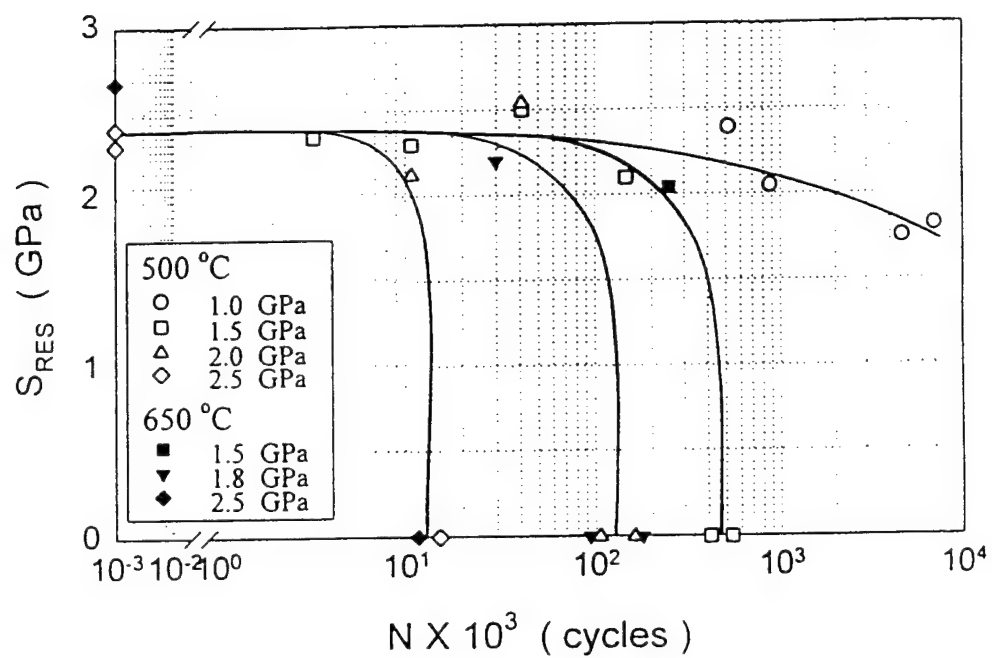


Fig. 6.3 Residual fatigue strength of SCS-6 fibers at 500 and 650 °C for various maximum applied stress (stress ratio, $R = 0.1$).

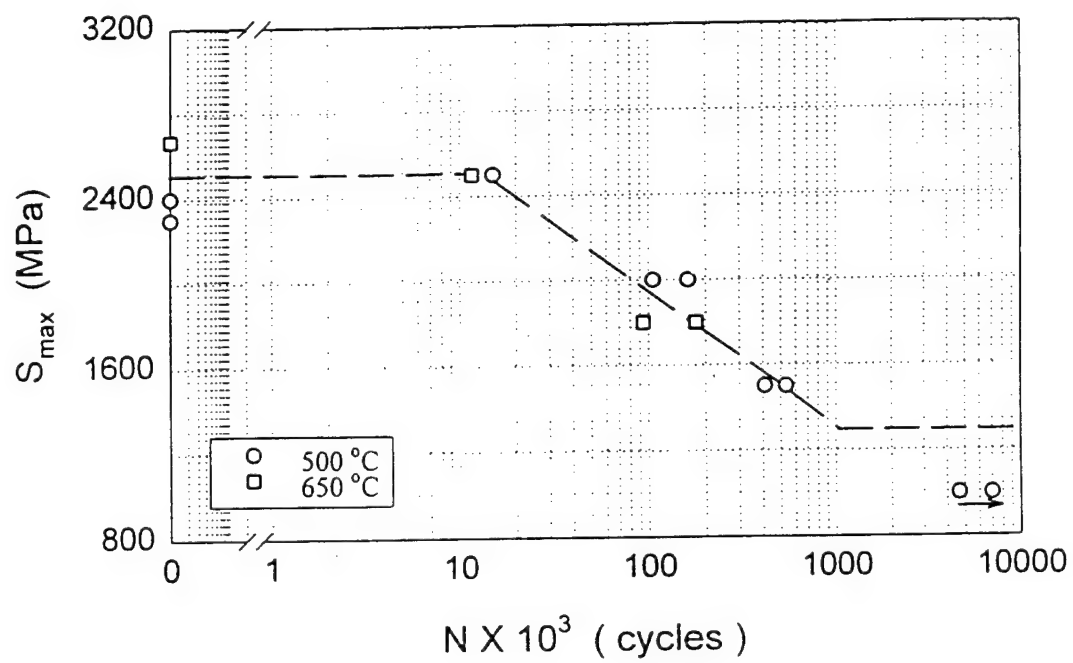


Fig. 6.4 Fatigue strength-life (S-N) curve for SCS-6 fibers.

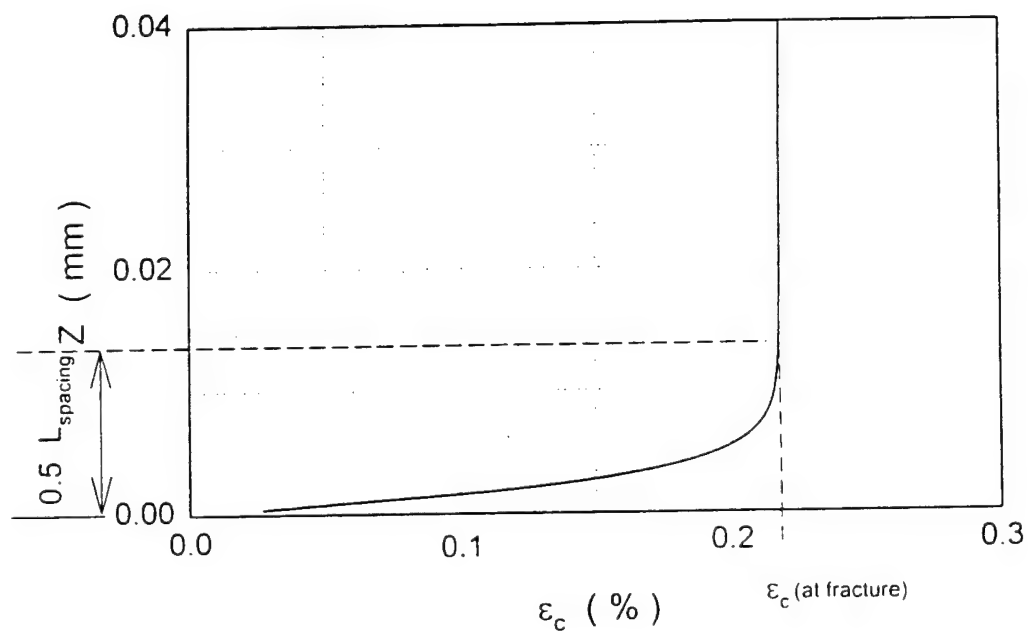
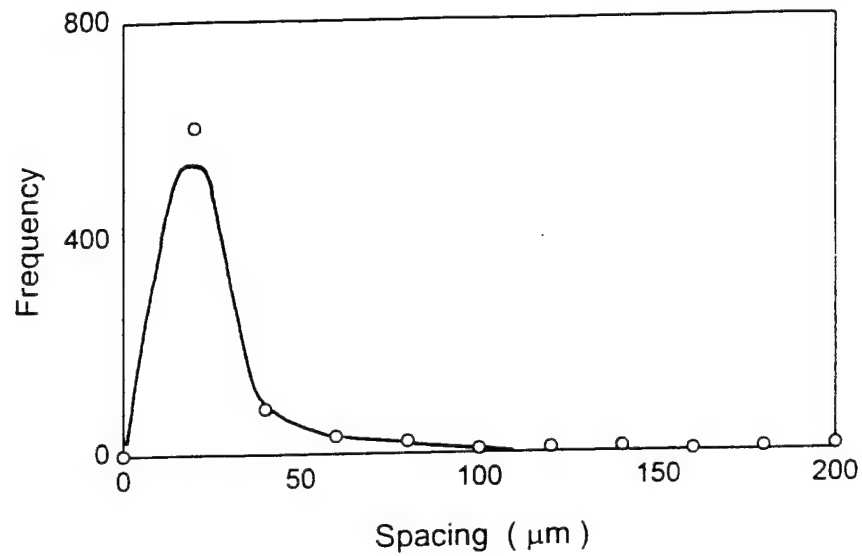


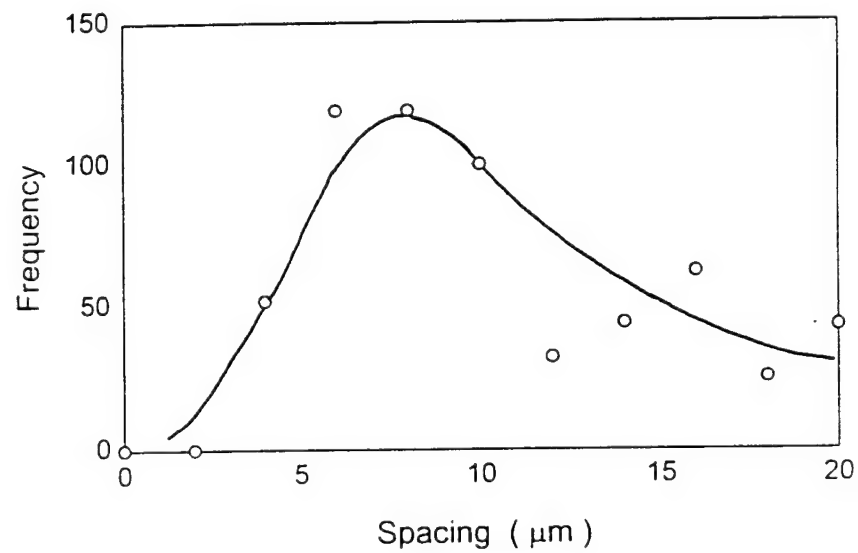
Fig. 6.5 Determination of minimum crack spacing based on the distribution of axial strain in the vicinity of the crack along a SiC fiber at fracture of the coating.



Fig. 6.6 Typical surface morphology of SCS-6 fibers fatigued at 650 °C showing distribution of circular coating cracks.



(a)



(b)

Fig. 6.7 (a) Statistical distribution of 785 measurements of spacing between adjacent cracks along SCS-6 fibers fatigued at 650 °C for 24.8 (10^6) cycles, $\sigma_{\max} = 1500$ MPa, $R = 0.1$. (b) Statistical distribution of 78 % of the measurements which fall within a 40- μm spacing.

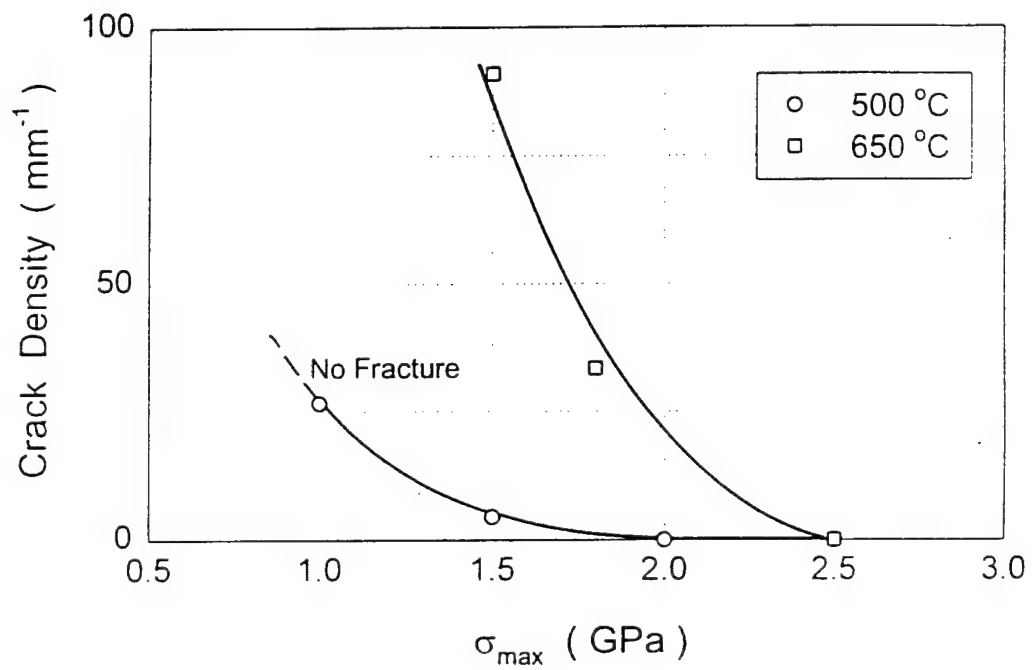


Fig. 6.8 Variation of surface cracks density on fatigued fibers at fracture with maximum applied stress and temperature.

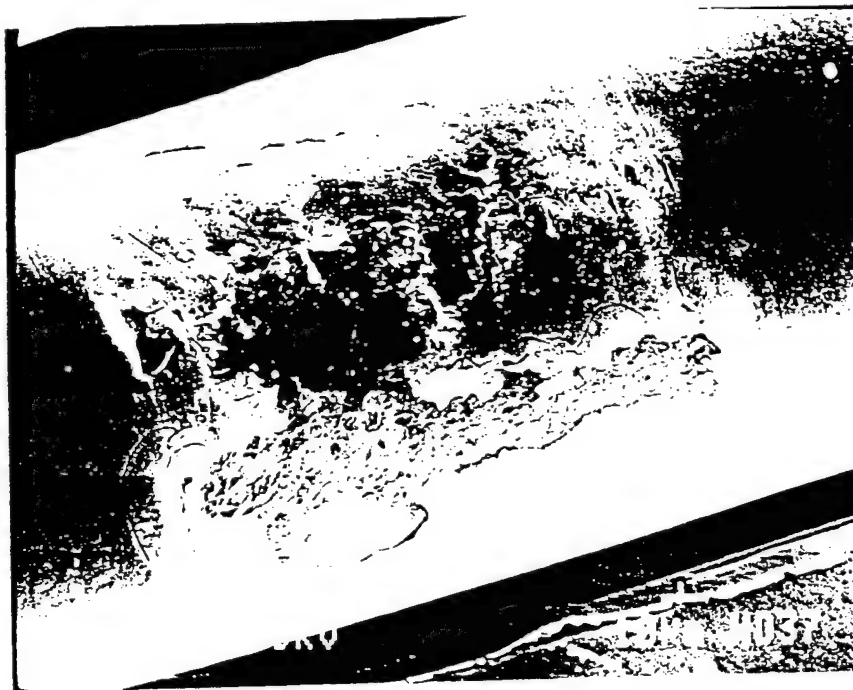
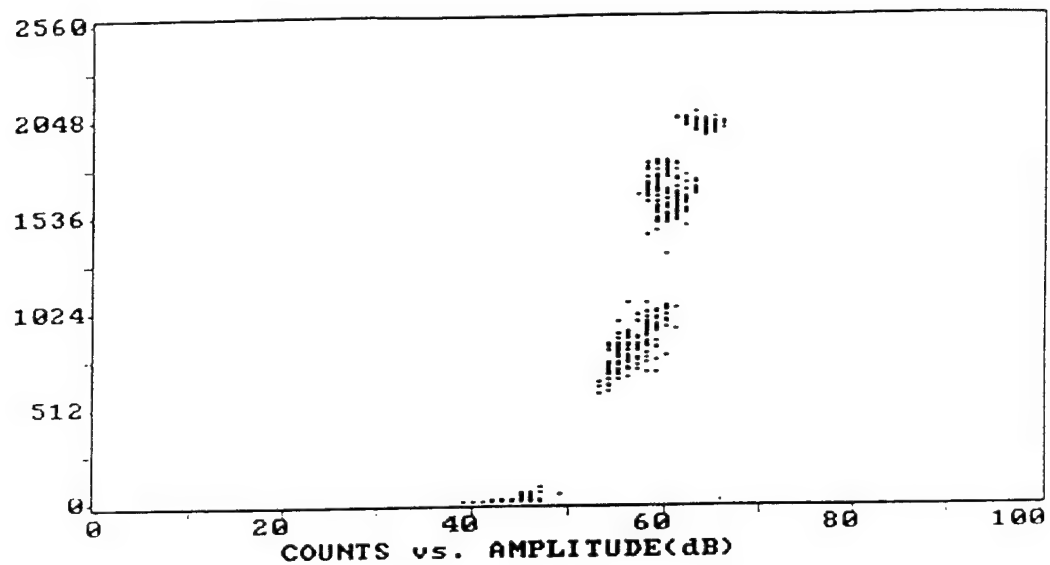
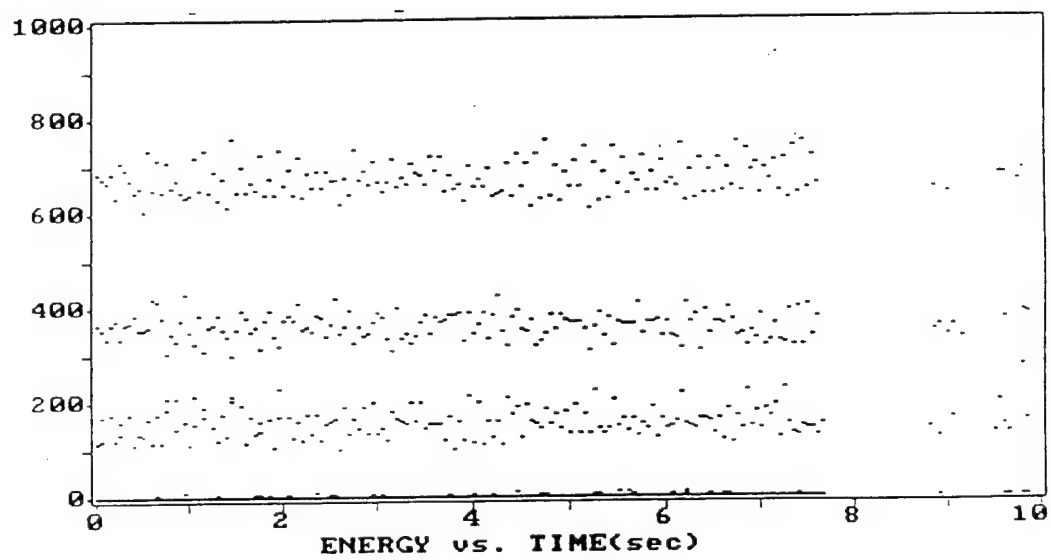


Fig. 6.9 Spalling of the carbon-rich coating layer from SCS-6 fiber due to abrasion by the molybdenum weave during fatigue test at 650 °C.



(a)



(b)

Fig. 6.10 Acoustic emission signal in terms of: (a) amplitude and (b) energy count from a fatigue test on SCS-6/Timetal-21S composite at 650 °C during a representative period of 10 seconds.

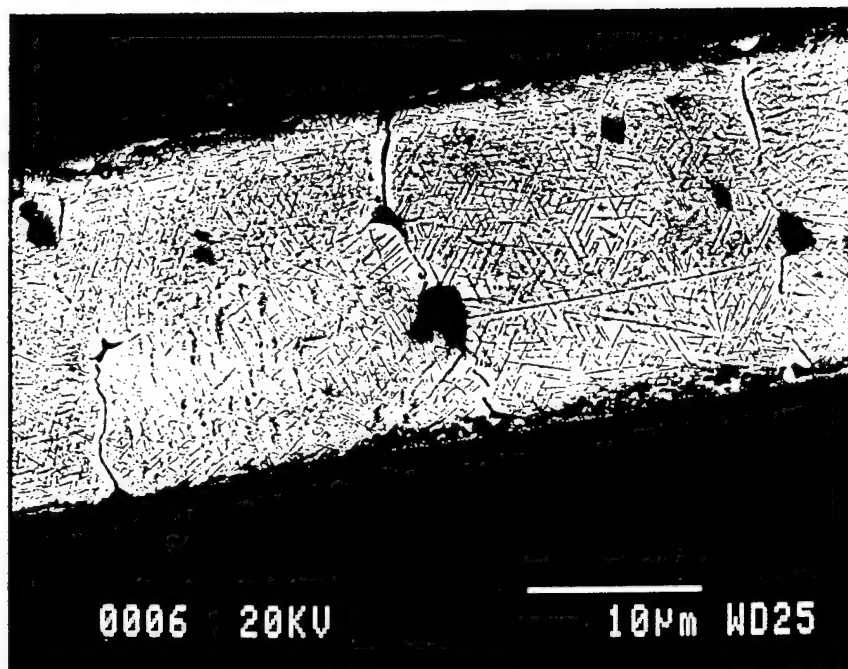


Fig. 6.11 Matrix cracking in a fatigued SCS-6/Timetal-21S composite at 650 °C. The dark area is the fiber phase.

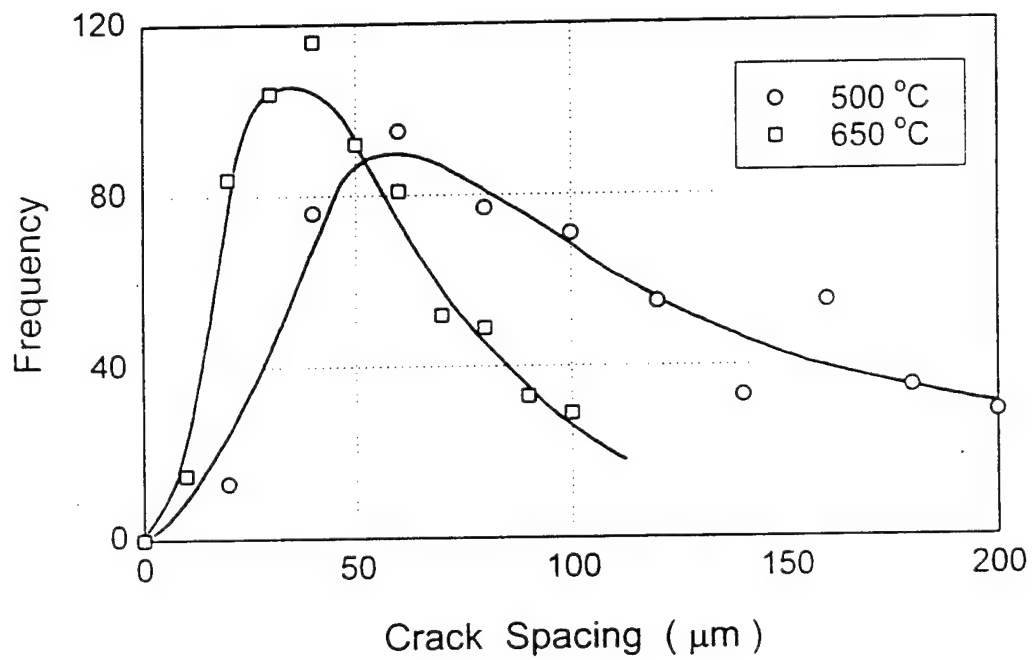


Fig. 6.12 Statistical distribution of measurements of spacing between adjacent crack initiation sites in a fatigued SCS-6/Timetal-21S composite at 500 and 650 °C.

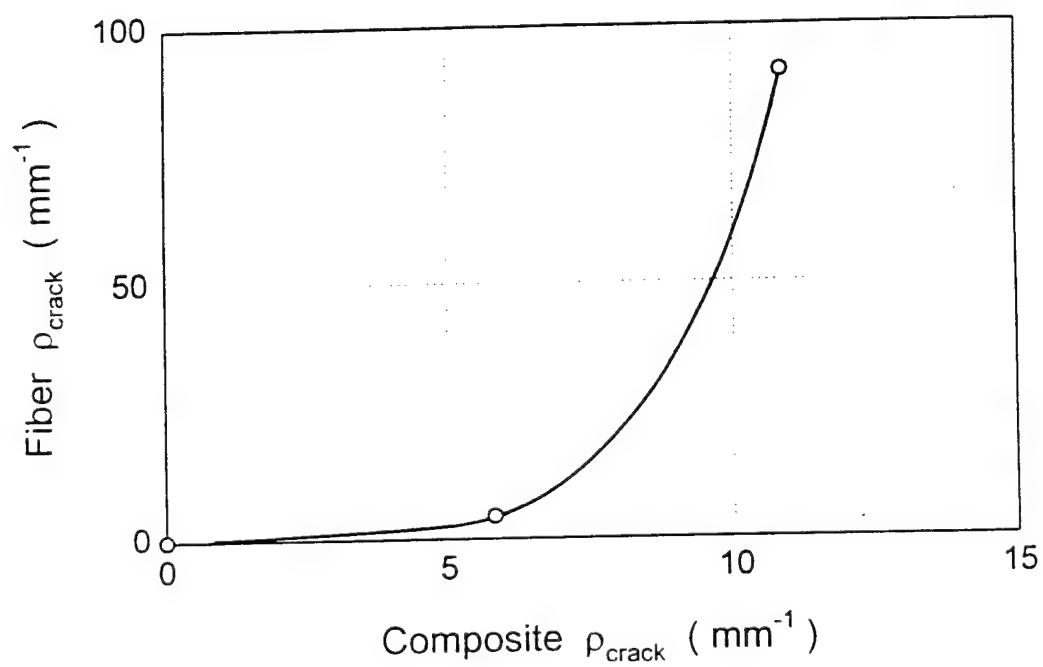


Fig. 6.13 Correlation between density of cracks on isolated SCS-6 fiber with density of crack initiation sites along the interphase in a SCS-6/Timetal-21S composite.

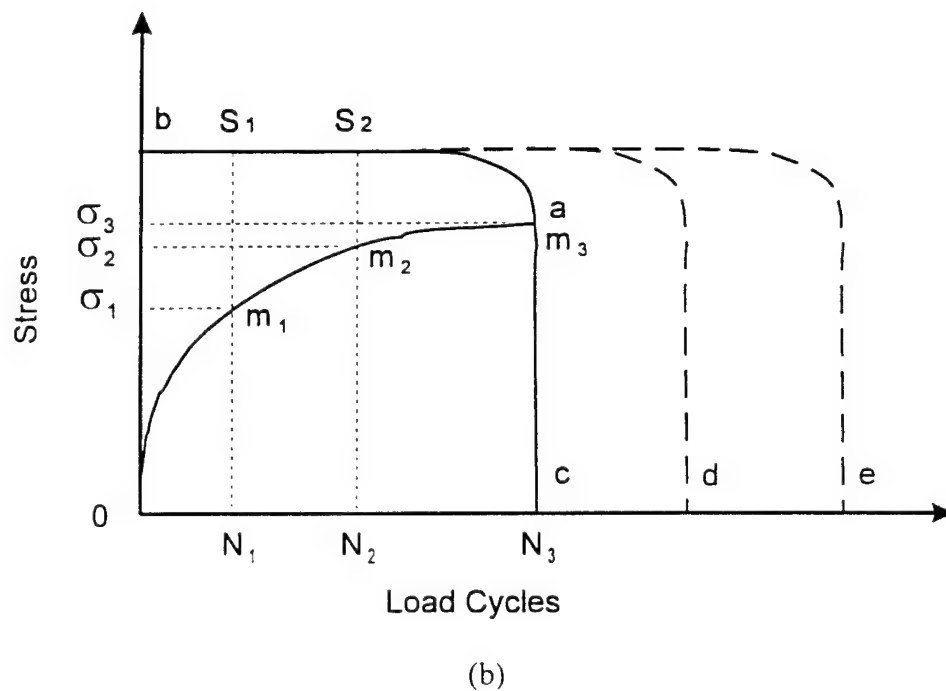
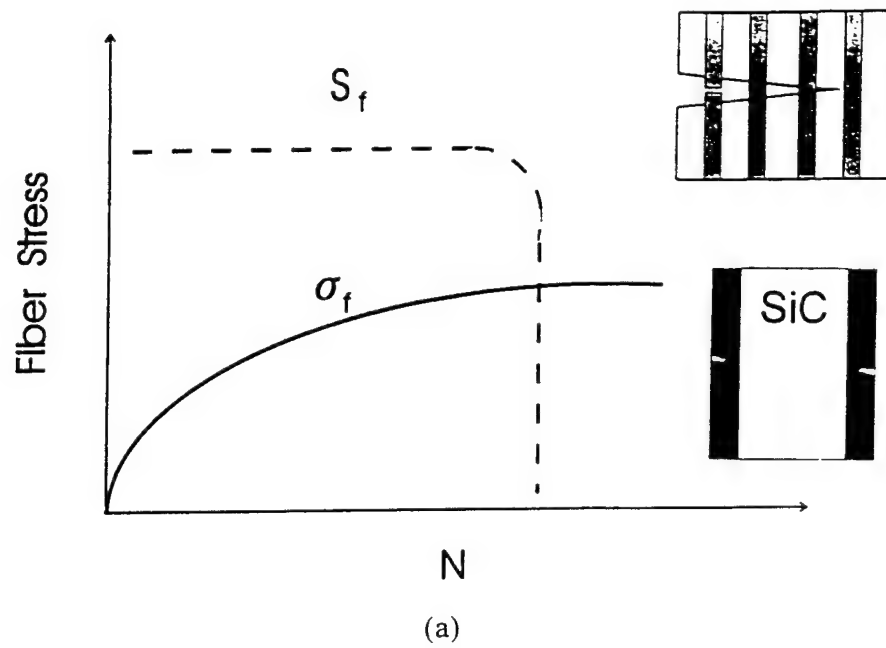


Fig. 6.14 (a) Concept for bridging fiber fracture criterion. (b) Illustration of the fracture process for a bridging fiber.

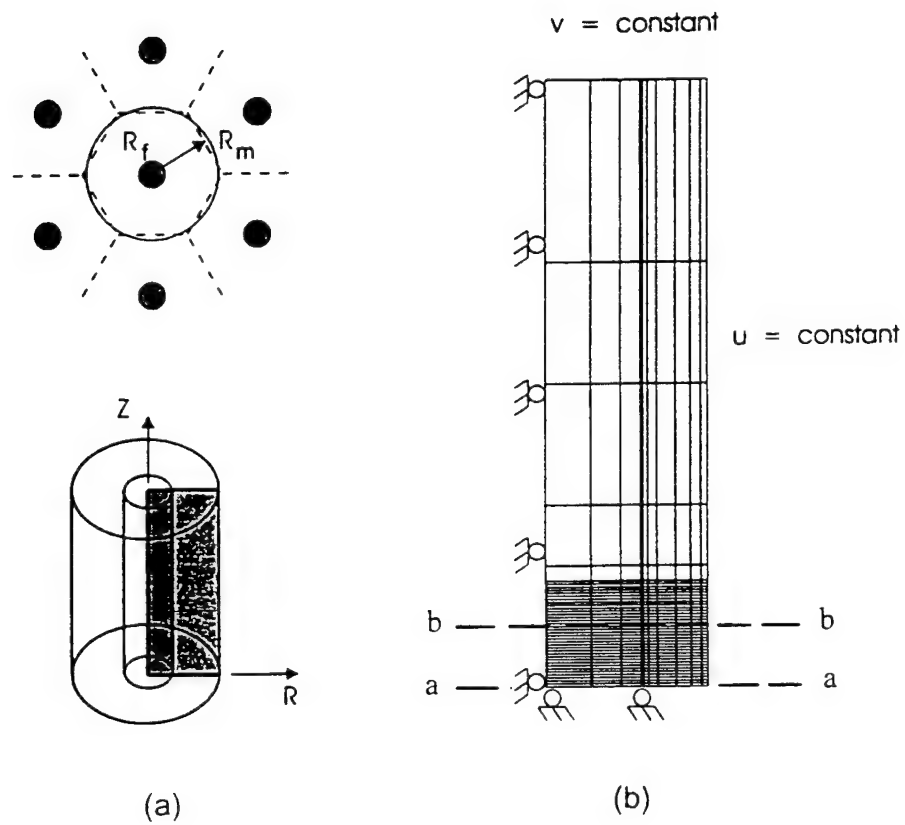


Fig. 6.15 (a) unit cell model for crack bridging condition. (b) Finite element mesh and boundary conditions of a radial section of the model.

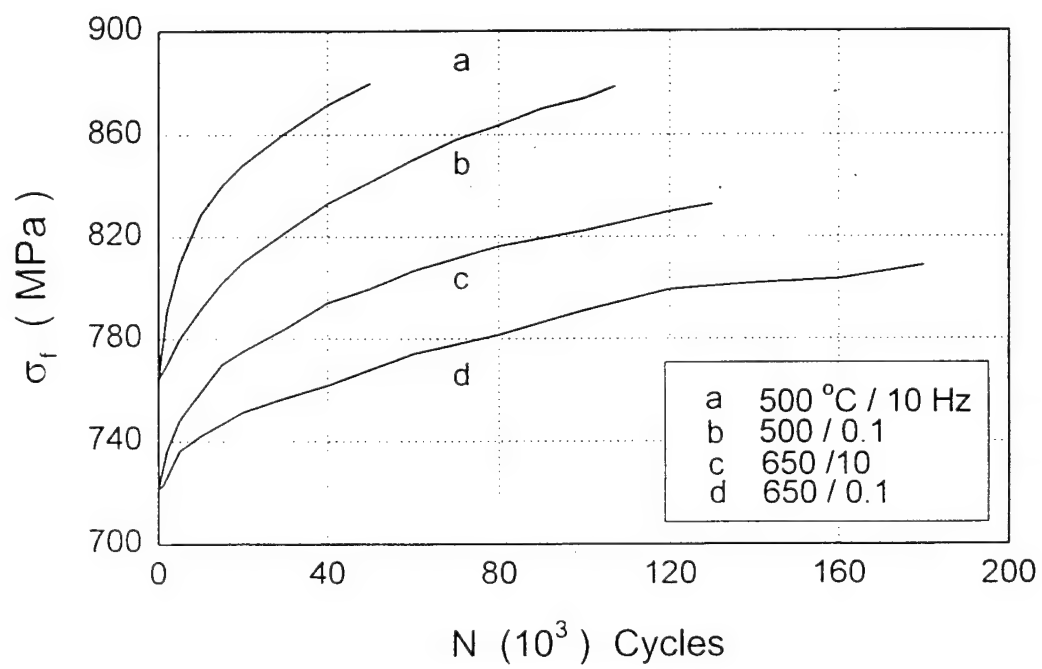


Fig. 6.16 Evolution of bridging fiber stresses at various loading conditions.

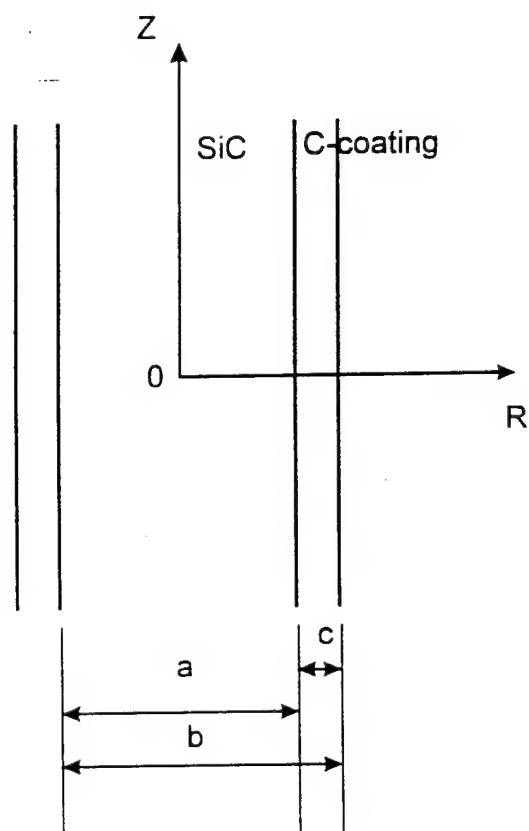


Fig. 6.A-1 A two phase cylinder model of a SiC SCS-6 fiber

APPENDIX A Introduction to the Study

A.1 Damage Mechanisms in Metal Matrix Composites

Advanced aerospace applications such as gas turbine engines, airframes for hypersonic aircraft, advanced energy conversion systems and propulsion systems present an ever increasing demand for higher performance materials [Step90]. These materials must be able to withstand high temperatures and high operating loads while maintaining dimensional stability and mechanical strength and toughness. Such requirements for lightweight materials with exceptional elevated temperature performance, oftentimes, could not be derived from properties of existing monolithic materials. Consequently, composite materials are being developed in which two or more dissimilar basic materials with vastly different mechanical and physical properties are combined to yield a material with properties superior than each of their constituents [Smit84]. Various types of metallic and ceramic-matrix fiber-reinforced composites have been proposed as candidate materials for such structural and machine applications because they possess unique combinations of several attractive properties such as high specific stiffness, high specific strength, excellent corrosion resistance and good thermal stability.

Titanium alloy matrices reinforced with ceramic fibers are of specific interest for aerospace applications because they offer significant improvements in specific strength and stiffness over their monolithic counterparts [Rona89]. Titanium-based metal matrix composites, MMCs, reinforced with SiC fibers are fabricated at high temperature in excess of 900 °C [Yang91, Sohi91]. During cool down from this strain-free temperature to room temperature, residual stresses are induced in both the metal matrix and the ceramic reinforcing phase resulting from the mismatch in the coefficient of thermal expansions among the constituent phases. These residual stresses can be detrimental as in the case of SCS-6/Ti-24Al-11Nb (at.%) where the matrix yielded during cool down below 500 °C [Saig92]. The residual hoop stresses have been observed to generate radial cracks at the fiber-matrix interface during cool down of SCS-6/Ti-24Al-11Nb [Brin92] and SCS-6/Ti-15V-3Al-3Cr-3Sn composites [MacK90]. Multiple circumferential cracks caused by the thermal expansion mismatch were observed in the matrix at the fiber-matrix interfacial region in SCS-6/Ti-24Al-10Nb-3Cr-1Mo due to cool down from 927 °C [Sohi91]. On the other hand, the compressive radial residual stress component at the interface acts to clamp the matrix around the fiber, thus influence the load transfer process. In some composite systems such as SCS-6/Ti-15V-3Al-3Cr-3Sn, where the fiber-matrix chemical bonding is weak, this stress component provides the frictional force which is a critical mean of achieving the load transfer. The axial component of the residual stress superimposes directly on the applied stress. In addition, the axial residual stress has a definite influences on debonding and fiber bridging processes [Hsue91, Kera91, Davi92, Mars88, Sigl89]. An investigation on the residual stress distribution and its evolution in a composite system is

therefore important in understanding its role in the load transfer efficiency within the composite, as well as its influence on the damage mode and damage location in relation to the composite constituents. These aspects are important in the process development and the structural design of composite systems.

In a unidirectional MMC, the fiber reinforcement is designed as the load carrying member while the matrix phase served to hold the fiber and transfer the load from the matrix to the fiber. Since titanium alloy matrices such as Ti-6Al-4V, Ti-24Al-11Nb and Timetal-21S, may exhibit combination of elastic-plastic-creep behavior depending on the applied load conditions, the response of MMCs with these matrices under cyclic thermal and mechanical loadings could be highly nonlinear [Neu93, Pern94, Ghon93]. On the other hand, the SiC fiber reinforcements are found to deform elastically with no measurable creep deformation up to temperatures of 800 °C (DiCarlo, 1986; Carter and Davis, 1984). The interphase region, in the vicinity of the fiber/matrix interface, is often the product of processing conditions involved in composite manufacture. Hence, the properties of this region depend directly upon the chemical, mechanical and thermodynamical nature of the bonding process between the matrix and the fiber materials. The interfacial characteristics, such as the frictional shear stress, τ_c , and debond strength, τ_d are also found to be influenced by elevated temperatures and durations of thermal exposure [Eldr94]. The different response of each composite constituents when subjected to mechanical and thermal loadings pose a challenging task to predict the response of the composite from the knowledge of their constituent behavior.

Several metallurgical processes employed to fabricate continuous fiber-reinforced MMC include casting process, plasma spray bonding and diffusion bonding. These fabrication methods are favorable for titanium alloys which can be superplastically formed and rolled into foils for MMC panels. Casting process involves passing continuous reinforcing fibers through a pot of molten metal or introducing the molten metal into, around and through bundles of fibers by vacuum, gravity pouring or pressure casting [Davi70]. In plasma spray bonding, a layer of fibers is laid on a rotating mandrel and the matrix is deposited on the fibers by plasma spraying. A second layer of fibers is then put on and the operation is repeated until the desired number of layers are completed. The final layup is then consolidated by hot pressing. Diffusion bonding consists is achieved by the simultaneous application of heat and pressure through hot isostatic pressing or vacuum hot pressing to alternating layers of metal foils and the reinforcing fibers [Gege85].

The extreme reactivity of titanium matrices with the ceramic reinforcing fibers during fabrication at elevated temperature, however, causes degradation of mechanical properties of the composite materials [What85]. This problem has been minimized through the development of BORSIC, SIGMA and SCS fibers with coating layers which limits the rate of reaction between the fiber and the titanium matrix. The different processing methods to fabricate MMCs also leads to the formation of microdefects such as voids and cracks which are likely to propagate under cyclic loading. The degradation of thermally cycled MMCs has been primarily attributed to the formation of reaction products at the fiber/matrix interface leading to stress-strain amplification at the interface [Kyno89]. As a result, the fiber/matrix interphase region is the weakest and most highly stresses region in a MMC, thus, become a

prime source of fatigue cracking. The growth behavior of these cracks leading to the catastrophic fracture of the composite, therefore, becomes a critical factor in determining the residual strength of a composite system.

The development of these composites requires a fundamental understanding of the mechanical interactions between the fiber and the matrix phases as they exist in a composite system, their complex interfacial phenomena, as well as damage modes and damage evolution in the composite under complex loading conditions. Their potential success as an engineered advanced material intended for designs involving load reversal at elevated temperature lies in the understanding of their fatigue damage tolerance characteristics which recognizes the propagation of fatigue cracks as a critical damage mode.

This section presents an overview of physical and mathematical aspects of fatigue crack growth mechanisms in titanium metal matrix composites reinforced with silicon carbide fibers. The following section focuses on the response of the crack growth rate to different loading conditions particularly test temperature and frequency of the loading cycle. The characteristics of various parameters associated with the fatigue crack bridging phenomenon, namely: the crack opening displacement, the bridging fiber stress, the fiber matrix frictional shear stress and the debonding length along a bridging fiber, are discussed on the basis of available experimental results in current literatures. The next section defines the conditions at which the crack bridging/acceleration transition occurs. This transition is described in terms of the load transfer process leading to fracture of bridging fibers located in the wake of the crack tip. The last section of the chapter reviewed various different analytical models which have been developed to identify the crack tip driving force

under the condition of crack bridging. While an attempt is made to avoid exhaustive mathematical derivations, emphasis is placed on the general structure of these models and their key parameters.

A.2 Bridging Fatigue Crack Growth Process

The growth behavior of a single dominant fatigue crack propagating perpendicular to the fiber orientation and the direction of applied loading in a unidirectional MMC have been investigated in several studies (eg. [Sens90, Davi89, McCa87, McMe90, Soum86]). The propagation of this crack is governed by properties of the fiber, matrix and fiber/matrix interface. In composites with strong interfaces and weak fibers such as the B_4C -B/Ti-6Al-4V composite, the crack growth is dominated by fiber and matrix fracture. On the contrary, SiC/Ti metal matrix composites characterized by weak interfaces and strong fibers are susceptible to crack branching at the fiber/matrix interface. This process allows the crack to propagate through the matrix leaving intact fibers in the crack wake, thus, bridging the fatigue crack. The crack bridging process leads to substantial increase in toughness of the composite. This is achieved because the high strength bridging fibers reduce the crack tip stress intensity amplitude (relative to an unbridged crack) and thus reduce the rate of matrix cracking by carrying part of the applied load [Sens90, Kant91, Wall93, Bowe91, Cox91, Davi92, Ghos92]. The growth mechanism under this condition involves a process in which the increase in the matrix crack length is accompanied by an increase in the number of

fibers bridging the crack. This process would continue up to a steady state condition produced by the balance between creating more bridging fibers as the crack length increases and the fracture of these fibers as more stress is transferred to them by the cracked matrix. The following event of crack growth arrest or acceleration, which is associated with the fracture of one or several bridging fibers, particularly those fibers farthest away from the crack tip, depends on the nature of this balance. The crack bridging phenomenon, as described above, was observed in several SiC/Ti MMCs including SCS-6/Ti-6Al-4V, SCS-6/Ti-15V-3Al-3Cr-3Sn, SCS-6/Ti-24Al-11Nb, SCS-6/24Al-10Nb-3Cr-1Mo, SM1240/Timetal-21S and SCS-6/Timetal-21S composites subjected to loading conditions of practical interest [Davi92, Tele93, Baku93, Jeng92, Sens90, Bowe91, Ibbo92, Brin92, Zhen95a].

Basic characteristics of bridged cracks in Ti-MMCs have been studied by a number of authors. Davidson [Davi92] measured the crack growth rate in a SCS-6/Ti-6Al-4V composite ($[0^\circ]_t, V_f = 42\%$) using center notched specimens subjected to stress ratio of 0.1. For an applied load range, $\Delta\sigma_a$, varying from 118 - 175 MPa, the crack growth rates ranged from 10^{-10} to 10^{-7} m/cycle. Growth rate acceleration or deceleration with increasing crack length depended on the stress level. At low applied stresses, however, the crack arrested. In addition, the growth rates were relatively insensitive to the number of bridging fibers in the crack wake. Fiber/matrix interface debonding reached up to 1 mm from the crack plane and occurred at several locations including between fiber and coating, within the coating layers and between coating and matrix. Cotterill and Bowen [Cott93] have also observed the arrest of bridging cracks in a SCS-6/Ti-15-3 composite tested at room temperature with

stress ratios $R = 0.1$ and 0.5 . The fatigue crack growth rates were slower at $R = 0.1$, and the crack length at arrest is lower than that at $R = 0.5$. Although the fatigue crack growth rates were initially similar, fiber breakage occurred more readily at a higher load ratio resulting in a faster growth rate and shorter life. In the fatigue crack growth study of SCS-6/Ti-6Al-4V composite, Bowen et al. [Bowe91a] observed that increasing $\Delta\sigma_a$ from 100 to 125 MPa, for the same stress ratios (0.1 or 0.5), or increasing the stress ratio for the same $\Delta\sigma_a$, has a minimal effect on the crack growth rate. However, for $R=0.1$, the onset of catastrophic failure is promoted at smaller crack lengths, similar to that of SCS-6/Ti-15-3 composite [Zhen95b, Cott93]. Fatigue crack growth in a SM1240/Timetal-21S $[0]_6$ composite subjected to loading conditions of $\Delta\sigma_a = 270$ MPa, $R=0.1$ and frequency = 10 Hz, however, did not show crack arrest [Zhen95b]. Larsen et al. [Lars95] in their work on a SCS-6/Timetal-21S $[0]_4$ composite ($\Delta\sigma_a$ varied from 270 to 668 MPa and $R=0.1$) observed that crack bridging was significant for stress ranges up to 300 MPa, while the extent of bridging was limited or nonexistent at the higher stresses.

Limited work on the fatigue crack growth behavior of MMCs has been carried out at elevated temperatures. The observed crack growth rate from these data, however, appear to differ. Cotterill and Bowen [Cott93] measured the crack growth rate of a SCS-6/Ti-15-3 composite using single edge notched, SEN, specimen in three-point bending tests. Comparison of the 25 and 500 °C tests (initial $\Delta K = 16$ MPa \sqrt{m} with $\Delta\sigma_a$ of 13 MPa, $R = 0.5$, and a frequency of 10 Hz) showed that the crack growth rate is higher at higher temperatures as shown in Fig. A.1. In addition, at 500 °C, the initial deceleration of crack growth is interrupted by discrete events of fiber failure which lead to instantaneous rise in

the crack growth rate. The fatigue response of a single edge notch specimen made of a SiC/Ti-6Al-4V composite exhibits a similar trend of higher crack growth rate at 550 °C (0.5 Hz) when compared to that obtained at ambient temperature [Ibbo92]. Barney et al. [Barn93] performed a study on the fatigue performance of the same composite by three point bending tests. The tests were carried out at a frequency of 10Hz, $\Delta K_a = 12 \text{ MPa}\sqrt{\text{m}}$, $R = 0.5$ and at room temperature as well as at 500 °C. At room temperature, the crack growth rate, da/dN , was found to decrease as the crack length increases until the crack arrested thus indicating that significant fiber bridging occurred. At 500 °C, while the growth rate was higher than that at room temperature, it increased rapidly with the increase in the crack length due to the presence of limited, if any, crack bridging. Measurements of fatigue crack growth of a SM1240/Timetal-21S composite using center-notched specimens were carried out by Zheng and Ghonem [Zhen95b]. The tests were performed at room temperature, 500 and 650 °C for loading frequencies of 10, 0.1 and 0.02 Hz with $\Delta\sigma_a = 273 \text{ MPa}$ and $R = 0.1$. The common feature of the growth rate curves, shown in Fig. A.2, is the presence of an initial crack bridging stage followed by repeated events of crack growth acceleration and retardation (see also [Cott93, Bowe91b]). Focusing on the initial crack bridging stage, one observes that, opposite to results of Ibbotson et al. [Ibbo92] and Cotterill and Bowen [Cott93], the crack growth rate, for the same loading frequency, decreases as the temperature increases. Furthermore, the slope of the crack growth rate curve which is a measure of the build up of the crack tip shielding force, is lowest in the room temperature test and highest in the 650 °C test. This suggests that, for the same crack length, the crack tip shielding force increases as temperature increases.

The observed differences in the effect of elevated temperature on the bridging fatigue crack growth rate of several MMC systems discussed above could be explained in terms of the balance between the response of different matrix materials to temperature and the degree of debonding along the fiber/matrix interface. The mechanical response of the titanium alloys Ti-15V-3Al-3Cr-3Sn, Ti-6Al-4V and Timetal-21S at elevated temperatures vary to a great extent in modifying the stress and strain states in these composites. The different variation in chemical composition of the interphase zone in each composite results in different interphase characteristics including interphase shear strength, surface roughness of the debonded interface and debonding length. Consequently, these differences are expected to produce different crack growth rate responses. The effect of cyclic bending induced by the three-point bend test [Cott93] and the SEN specimen geometry [Ibbo92] attenuates the fracture of bridging fiber in the crack wake resulting in higher crack growth rates. Such effect, however, is absent in the fatigue loading of a center crack specimen [Zhen95a].

The different fracture processes encountered in each of the crack growth stages, namely: bridging, transition and acceleration, are evident in the appearance of the fracture surface features. The micrograph shown in Fig. A.3, for the 500°C test of a SM1240/Timetal-21S composite, displays two different fracture zones, the first for the crack bridging stage and the second for the repeated crack growth acceleration/retardation stage. The first zone has excessive fiber core damage which may have resulted from the application of a large number of fatigue cycles and prolonged thermal exposure. The pulled-out fibers in this zone are relatively short. In examining the interfacial region of bridging fibers in the composite mentioned above, Marshall et al. [Mars91] and Zheng and Ghonem [Zhen95a]

observed that debonding always occurred within the carbon coating layer or between the carbon and the TiB_2 layers at any test temperature. Fig. A.4 is an example of a debonded carbon layer at a plane located immediately under the fracture surface of a room temperature test. The second zone in Fig. A.3 shows no fiber core damage and displays longer fiber pull-out length. An example of the unstable fracture zone is Fig. A.5 which shows a high degree of matrix deformation surrounding the pulled-out fibers.

The effect of prior thermal exposure on the fatigue crack growth behavior of a SM1240/Timetal-21S and $\text{B}_4\text{C-B/Ti-6Al-4V}$ composites was examined by Zheng and Ghonem [Zhen95b] and Chan and Davidson [Chan90], respectively. In the former study, the crack growth rates for both as-received and specimen aged for 42 hours at 650 °C are measured at room temperature, see Fig. A.6. Although both samples display identical crack growth rate, the duration of crack bridging is prolonged for the aged sample. This result indicates a delay in the fracture of bridging fibers which triggers the transition from deceleration to acceleration crack growth rate. This delay is explained as follows. In addition to the expected change of microstructural properties of the matrix, or degradation of the interphase due to thermal exposure, thermal aging of a metal matrix composite, particularly at a temperature as high as 650 °C, could result in decreasing the compressive residual stress acting in the fiber. A separate study on SCS-6/Timetal-21S showed that the decrease in the mean stress for a particular applied stress range, while does not influence the growth rate in the crack bridging stage, causes a delay in reaching a condition of crack growth rate acceleration [Ghon96]. The effect of aging on a $\text{B}_4\text{C-B/Ti-6Al-4V}$ composite was investigated using single edge notched (SEN) specimen [Chan90]. In as-received specimen,

the crack grows in Mode I, while in a thermally exposed (7 days at 500 °C) specimen, crack growth occurred both across the fiber and along fiber/matrix interfaces. Thermal exposure was found to increase the amount of crack growth in the interface. Interface debonding occurred while the main crack is relatively far from the interface (typically 80 to 100 μm at $\Delta K = 32 \text{ MPa}\sqrt{\text{m}}$). In the as-received specimen, on the other hand, a crack as close as 20 μm at $\Delta K = 22 \text{ MPa}\sqrt{\text{m}}$ to the interface did not cause debonding. This reflects a higher interface strength in the latter case. Chan [Chan93] also proposed that the lowering of the interphase shear strength value due to thermal exposure would favor extensive interface cracking and crack bridging mechanisms over fracture of fibers, provided that such thermal exposure does not degrade the fiber strength. Although different shear strength levels of the interphase region could be obtained through different processing methods, aging studies on a SCS-6/Timetal-21S composite for duration up to 200 hours at 650 °C, however, showed no degradation of interphase strength due to thermal exposure in vacuum condition [Osbo95].

A.3 Factors Influencing Crack Bridging Process

Efforts have been made to identify the different factors influencing the crack bridging process with the aim of determining the crack tip driving force. These efforts have largely followed models which employ concepts of linear fracture mechanics coupled with micromechanical interpretation of balance of forces acting on the debonded region of

bridging fibers [McCa87, McMe90, Davi92, Tele93, Mars95, Ghos92, Wall93, Chia93]. While the majority of these models may not be directly applicable to fatigue crack growth in composites with ductile matrices, they do, however, identify the crack opening displacement range, Δu , the fiber bridging stress range, Δp , the fiber/matrix frictional shear stress, τ_c , and the interface debonding length, L_d , as being critical governing parameters for the fatigue crack bridging process. Attempts have been made to study each of these parameters and their form of correlations with mechanical and material properties of the composite. This section will describe these attempts and their results.

A.3.1 Crack Opening Displacement

The experience gained from studying the fracture processes of high strength monolithic materials shows that the crack opening displacement, COD, particularly near the crack tip region, is a measure of the crack tip driving force. In addition, COD has the advantage, in spite of its expected small magnitude in bridging cracks, of being a measurable parameter. This provides the possibility of establishing an experimentally based methodology to analyze the crack bridging phenomenon. A number of studies have been carried out in this regard. For example, Davidson [Davi92], in his study of fatigue cracks in SCS-6/Ti-6Al-4V and SCS-6/Ti-14Al-21Nb composites considered that a residual crack opening displacement (CODr) is caused by the relieve of axial residual stresses due to the occurrence of sliding between the matrix and the bridging fiber. Using a stereo-imaging technique, the CODr was

measured as a function of the crack length and the applied stress and a conclusion was made that the CODr could be used to compute the slip distance along the corresponding bridging fiber. Crack opening displacements due to the applied load were also measured and were shown to be a function of the square root of the distance behind the crack tip [Davi92]. Telesman et al. [Tele88] used a loading stage mounted inside a scanning electron microscope chamber to measure the Δu profiles of cracks propagating in a SCS-6/Ti-24Al-11Nb composite and used the results to compare with those obtained using different analytical methods. John et al. [John93], using a SCS-6/Timetal-21S composite at room temperature, measured the COD along a fatigue crack using an IDG system and, similar to the work of Davidson [Davi92], measured the CODr values for the same crack length using a scanning electron microscope. A procedure was then developed to generate the absolute COD profiles along the crack length at different stress levels. Zheng and Ghonem [Zhen95b] measured, also using an IDG system, the COD at positions along different bridged crack lengths in a SM11240/Timetal21S composite tested in air environment at three different temperatures: 24, 500 and 650°C. Their data, which were not resolved into residual and absolute components, are plotted in Fig. A.7. They show that for this particular composite system, $\Delta u(x)$ increases with temperature. Since the axial residual stress is inversely proportional with temperature, the difference in the absolute COD values at these temperatures would be higher than that shown in the previous figure. The increase in COD with temperature is possibly due the change in the debonding strength, τ_d , of the fiber/matrix interface with temperature (see [Osbo95]). This, in turn permits, for the same crack length, a larger fiber/matrix relative displacement as temperature increases. Furthermore, in the work of Zheng and Ghonem

[Zhen95b], by selecting the value of COD at a unit distance from the crack tip to represent the crack tip opening displacement, Δu_T , the relationship between Δu_T and da/dN , for the different test temperatures mentioned above is plotted in Fig. A.8. As Δu_T was observed to increase with the increase in the crack growth rate, the authors concluded that, unlike ΔK_{app} , the crack tip opening displacement is a measure of the crack tip driving force in MMC's. The need of COD measurements to assess the crack growth process produces a set of problems one of which is the difficulty in measuring a displacement in the range of a few microns. In addition, the variations in residual stresses due to non-uniformity of fiber spacing in composites produce significant errors in COD measurements.

A.3.2 Bridging Fiber Stress

The second important parameter in the crack bridging process is the bridging fiber discrete stress, ΔS . The significance of this parameter comes from the fact that theoretical models developed to calculate the effective crack tip driving force, as will be seen later, base their derivations on the idea that the effect of bridging fibers on the crack tip stress intensity factor can be computed by treating the loads carried by these fibers as a pressure applied along the crack wake. The direction of this pressure is opposite to that of the applied stress. The pressure concept averages the fiber loads on individual fibers resulting, therefore, in a distribution whose discrete values, Δp , at locations of individual fibers is calculated by multiplying the fiber traction by the fiber volume fraction. The key to use these models is,

therefore, knowing the continuous function describing the fiber pressure distribution along the bridged crack length. Davidson [Davi92] assumed, on the basis of experimental observations related to COD and slip length along bridging fibers, that the fiber pressure is constant. Using this simplifying assumption, the fiber stresses in the Ti-6Al-4V matrix composite were calculated; their values were found to be in the range of 1.1 to 4 GPa and approximately independent of the distance from the crack tip. John et al. [John93], employing the weight function method, calculated the bridging fiber stress distribution, Δp , by correlating predicted and measured crack opening displacements. Their work showed that the bridging fiber stress distribution at the maximum applied fatigue stress is not uniform, but increases rapidly from a low value at the crack tip to a near constant away from the crack tip. Chiang et al. [Chia93] applied a modified shear-lag model and showed that Δp attains a finite value at the crack tip. Zheng and Ghonem [Zhen95b], using experimentally measured COD values, employed a linear elastic fracture mechanics based relationship to calculate the fiber pressure distribution as function of crack length and temperature. Results for three temperatures 24, 500 and 650°C are shown in Fig. A.9. A feature of these distributions is the presence in all test cases of a minimum finite value of Δp at the crack tip. Also, the average value of Δp increases proportionally to the increase in both temperature and the crack length. Furthermore, for the same test temperature, the difference between the maximum and minimum bridging fiber pressure for a particular crack length decreases as the crack length increases. This tendency of Δp to approach a uniform level is also influenced by the temperature as can be seen in Fig. A.9. The maximum value of ΔS_f is reached at the end of the crack bridging stage and acts on the first bridging fiber located at the crack mouth. These

values for the three temperatures are 776 MPa (24°C), 873 MPa (500°C) and 877 MPa (650°C). Fig. A.10 shows the evolution of ΔS_f calculated at the crack mouth as a function of the crack length and at different temperatures. ΔS_f seems to converge to an upper limit of about 900 MPa. Since these crack-mouth bridging fibers are most likely to be the first to fracture at the end of the crack bridging stage, the 900 MPa. would represent the fracture strength of the Sigma fibers. This value is much lower than the monotonic tensile strength of this type of fiber which is estimated as 3000 MPa level [Peti88]. This discrepancy could be explained by assuming that the fatigue fracture strength of a SiC fibers is lower than its monotonic fracture strength. Furthermore, it was speculated that fibers break at distances farthest from the crack tip because of the increased volume of fiber exposed to stress rather than increased stress on fiber [Davi92].

A.3.3 Fiber/Matrix Frictional Shear Stress

The frictional shear stress, τ_s , has been the parameter most studied due to the recognition that the mechanics of the fiber/matrix interface region is critical for the understanding of the composite behavior [Baku93, Ghos92, Chan93, Thou89]. Different methods of measurement have been applied to determine the magnitude of τ_s . The most common of these is the use of fiber push-out/pull-out tests which measure τ_s in terms of the stress required to cause fiber/matrix slippage in thin-slice specimens of the composite under investigation [Mars91, Osbo95, Mars87, Eldr94, Wats92]. These methods however view τ_s

as being a single material constant. This view has been utilized in variety of bridging models to predict the crack tip driving force, the debonding length and the crack opening displacement. The existence of a gap between the results of these models and corresponding experimental data has focused the attention on examining the characteristics of τ_i and the validity of extending its single value as measured from pre-fatigued specimens to conditions under which fiber/matrix interfacial damage accumulates [Davi92, Tele93, Baku93]. Recent work in this area has shown that repeated sliding on a fiber/matrix interface may lead to deterioration of that interface either by fracture of fiber coatings [Kant92, Warr92], wear of asperities or plastic relaxation of the friction stress on the interface [Maki92]. Indeed, available fiber push-out/pull-out tests have revealed reduced interface frictional stress in metal-, intermetallic and ceramic composites after a few loading/unloading cycles. However, push-out tests performed on fatigued composite specimens have shown either further decrease or limited increase in the value of τ_i when compared with that obtained from as-received specimens. Furthermore, the variation in debonding mechanisms along the interface as discussed by Bakuckas and Johnson [Baku93] indicates that the value of τ_i is apparently a function of the location along the debonding length and crack length. These results led several authors to suggest that τ_i is not a material constant but should rather be viewed as a variable which depends on loading conditions (applied stress level, temperature and frequency), debonding mechanisms, viscoplastic deformation of surrounding matrix and environmental attack of the fiber/matrix interface region [Baku93, Zhen95b, Chan93]. Eldridge [Eldr92] measured the frictional shear stress in titanium matrix composites at different high temperatures in vacuum controlled environment. His work showed that the

increase in temperature causes a decrease in the value of τ_s . In contrast, pull-out tests by Marshall et al. [Mars85] and push-out tests by Clyne and Withers [Clyn93] both applied to SM1240/Timetal-21S, at room temperature, have showed that high temperature aging prior to testing leads to an increase in the as-received τ_s . These results imply that τ_s is a condition-sensitive parameter. Here, again, similar to the COD measurements, τ_s , while essential to the understanding of the crack bridging mechanism, has a magnitude ranging from 0.9 to 360 MPa [Baku93, Osbo95, Warr92, Yang90]. This large variation in the values of τ_s is due to many factors including differences in test methods; pull-out versus push-out as well as test specimen size; test environment, air versus vacuum and composite fabrication processes. Furthermore, measured values of τ_s using fiber pull-out or push-out methods, does not account for the degradation of the frictional shear stress due to time or number of loading cycles. In the absence of accurate values of τ_s it would be difficult to close the gap between experimental observations and results of crack growth analytical models.

A.3.4 Fiber/Matrix Interface Crack Length

The crack tip shielding associated with crack bridging phenomenon is the outcome of two successive damage events. In the first event, relative displacement between the fiber and the matrix due to the crack opening displacement results in a continuum shear stress distribution, τ , along the interface. This, in turn, initiates interfacial debonding with an initial crack length which depends on the stresses acting along the interface and the properties of

the interphase region. In the second event, the balance of axial forces along this bridging fiber requires that the fiber traction at the plane coinciding with the matrix crack surface exceeds its far-field value. Once the initial debonding length has been established for a bridging fiber, progressive debonding of this interface is governed by a Mode II crack propagating between two materials with different elastic constants. An important parameter in this case is the critical stress intensity factor (or the critical strain energy release rate) of the interphase [Chan89, Hutc87, Suo90]. The distribution of the debonding length along a bridging crack is such that the maximum length occurs at the crack mouth while the minimum near the crack tip. Results of shear lag models show that an increase in debonding length leads to a higher fiber stress. The occurrence of fiber/matrix debonding and sliding, therefore, results in bridging traction as well as a pullout resistance to crack opening [Thou88]. The fiber/matrix interface debonding accommodates the crack opening displacement, thus contributing the toughening effect which is provided by the dissipation of energy associated with the debonding process.

Marshall et al. [Mars91] examined the surface of pulled out fibers in a SM1240/Timetal-21S composite and concluded that sliding occurs between carbon and TiB_2 fiber coating layers in both as-fabricated and heat treated specimens. Similar results were reported by Zheng and Ghonem [Zhen95a]. On the other hand, in a SCS-6/Ti-6-4 composite, cyclic loading causes debonding to occur between the carbon-rich coating and the SiC part of the fiber, as well as between the different layers of the carbon coating [Davi92]. Yang et al. [Yang91] and Eldridge and Ebihara [Eldr94] in separate studies, reached a similar conclusion regarding the locations of interfacial debonding in a SCS-6/Ti-15-3 composite.

They observed that debonding occurs at locations between the fiber and its multiple carbon coatings, within the carbon layers, and occasionally between the coating and the reaction zone. SEM observation of fiber surface of a SCS-6/Ti-24-11 composite showed, however, that interface debonding always occurs between the carbon coating and the reaction zone of the composite [Eldr94]. From these studies it is apparent that, for the same temperature level, interfacial debonding in SiC/Ti-MMCs could occur at different locations across the fiber/interphase/matrix region. This dictates the frictional coefficient of the mating debonded interfaces. In addition, the interphase shear strength is influenced by the growth kinetics and thermal aging characteristics of the interphase, as described in the previous section. While direct measurements of τ_s are difficult to obtain, compared values of τ_s could be extracted from results of fiber pull-out or push-out tests of composite samples.

A recent analysis of fatigue crack growth in a SCS-6/Ti-6Al-4V composite employing an elastic bridging model [Nguy94] concluded that the interface debonding length, rather than the interface shear stress, is the defining variable for modeling the bridging fatigue crack growth in MMCs. Modeling of interface debonding could be achieved using classical fracture mechanics concepts [Hutc90]. Other approaches are based on the balance between the interfacial shear stress and the shear strength of the interphase [Aves73, Lee92, Cho92]. The basic requirement to establish this balance is the knowledge of the internal stress states acting along the fiber/matrix interface and the shear strength of the interphase region.

The length of the fiber/matrix debonding interface along the bridged matrix crack has been studied by several authors [Davi92, Baku93, Zhen95a, Hutc90, Cox91]. The slip

length, which include the entire interface damage process zone in a SCS-6/Ti-6-4 composite, measured from the crack plane, was reported to reach up to 1 mm [Davi92]. Bakuckas and Johnson [Baku93] estimated that the debonded length in a SCS-6/Ti-15-3 composite at room temperature ranges from 1500 μm at the first intact fiber closest to the crack mouth to 100 μm at 1.2 mm away from this fiber (crack length, $a = 4.28$ mm). Zheng and Ghonem [Zhen95a] measured the fiber pulled-out length along fracture surfaces of SM1240/Timetal-21S composite specimens. This length, which was assumed to be proportional to the debonding length of the corresponding fiber, was found to be temperature dependent with an average ranging from 120 μm at 24 °C to 215 μm at 650 °C. These different results concerning the interface debonding length are compared in Fig. A.11.

Once the fiber/matrix interface of a bridging fiber is debonded, the growth of the resulting crack requires, as mentioned above, the knowledge of Mode II driving force of a crack propagating between two materials with different elastic constants. The significance of this knowledge lies in the fact that the increase in the interface debonding length during a particular number of fatigue loading cycles, results in an increase in the fiber stress which, in turn, influences the Mode I matrix crack growth rate. Using the oscillatory stress singularities for open tip interface cracks [Hut87, Rice88], Chan and Davidson [Chan89] developed a simple expression for the stress intensity factors ΔK_I and ΔK_{II} of an interface fatigue crack subjected to normal and shear loadings. The model relies on cyclic COD in both the normal and shear directions along the interface crack length. However, no work exists in current literature dealing with the fatigue propagation characteristics of interface cracks in Ti-MMC. This is possibly due to the fact that while the debonding length is an

important parameter in determining the fiber stress, no experimental technique is available yet to provide accurate measurements of its magnitude.

A.3.5 Bridging/Acceleration Fatigue Crack Growth Transition

The bridging fatigue crack growth in Ti-MMCs is characterized by a decrease in the growth rate with an increase of the applied stress intensity factor range, or crack length, indicating an initial fully crack bridging stage. This bridging fatigue crack growth stage could occupy larger than 30 percent of the fatigue life of the test specimens [Zhen95a]. The end of this crack growth retardation stage, corresponding to the attainment of the minimum crack growth rate, is followed either by a crack arrest or a transition to an accelerated crack growth process. In the latter case, this transition point in the crack growth rate curve was attributed to the breakage of bridging fibers, particularly those located near the crack mouth [Zhen95a, Cott93]. These fibers have experienced the largest number of fatigue cycles and have possibly suffered the severest damage in the form of cyclic wear induced by the fiber/matrix interfacial frictional shear stress [Chan93]. Meanwhile, during cyclic loading of the composite, particularly at elevated temperature, the time-dependent matrix deformation becomes more pronounced as the stresses in the matrix phase relax. This stress relaxation is accompanied, for equilibrium requirements, by the simultaneous build-up of stresses in the adjacent fiber through the load transfer process across the fiber-matrix bonded interface. These two damage events of stress build-up in a bridging fiber and continuous strength

degradation of the fiber, which occur simultaneously, interact and eventually results in breakage of bridging fibers at the transition stage of the fatigue crack growth. The failure of any of the bridging fibers would result in redistribution of stresses among unbroken bridging fibers resulting in a decrease of the crack tip shielding force, thus triggering a condition of crack growth acceleration.

A.4 Thesis Objectives

Thorough understanding of the fatigue crack growth process in a SiC/Ti metal matrix composite is vital to the development of the composite system for aerospace structural components with applications involving load reversal and elevated temperature environment. The contribution of fatigue crack bridging process in retarding the growth rate of a dominant crack in this composite, thus, improving the toughness of the composite system has been recognized. Dominant damage mechanisms responsible for the observed crack growth behavior and their link to the stress state in the composite has been examined. The objective of this thesis is to quantify the fiber/matrix interaction components which govern the fatigue crack growth in a unidirectional SiC/Ti MMC. These components include the residual stress evolution in the fiber and matrix phase, the debonding strength characteristics of the fiber/matrix interface, the initiation and propagation of the interface mode II crack, the evolution of fiber stress and the fracture behavior of the fiber phase. The significance of each of these components in relation to the overall crack bridging process

is illustrated in Fig. A.12. These components, when combined, would provide a quantitative tool to identify the fiber, matrix and interphase characteristics required for optimum composite damage resistance.

Chapter 1 describes a new four-phase concentric cylinder model (fiber/interphase region/matrix/equivalent composite media) capable of determining the internal stress states in the composite constituents. This micromechanical model incorporates elastic, plastic and creep response of a unidirectional metal matrix composite when subjected to thermal and mechanical loading conditions. The formulations of the governing equations for this model are presented in this chapter. The occurrence of matrix plasticity is treated using the deformation theory of plasticity in conjunction with the von Mises yield criterion. In the transient and steady-state stages of creep, the constraint-free creep deformation of the matrix phase and the effective composite media are calculated using the Bailey-Norton law with an Arrhenius-type expression for the time-dependent creep coefficient.

Chapter 2 examines, using the analytical model developed in Chapter 1, the influence of several parameters on the mechanical response of a SCS-6/Timetal 21S composite during post-fabrication cooling down and subsequent application of thermal load cycles. The parameters include thickness of the equivalent composite media for the cylinder model, types of fiber coating materials, thickness of the reaction zone, cooling rate from the consolidation temperature and kinetics of the creep process during thermal cyclic loading. The relaxation behavior of residual stresses in the matrix phase under thermal fatigue loading of the composite is investigated. Results of this parametric study are presented and discussed with respect to optimization of the composite properties.

Chapter 3 details a numerical approach which utilizes existing experimental results of fiber pushout tests carried out on a SCS-6/Timetal-21S composite to determine the fiber/matrix interphase shear strength. The tests, which were performed on thin-slice samples of the composite provided information on the load level at the onset of interface debonding as well as on frictional characteristics of the debonded interface. Finite element analysis is then performed, employing an axisymmetric cylinder model of the pushout fiber embedded in the matrix phase, to simulate a pushout test on the thin-slice specimen up to the debond load value. These calculations establish the interphase shear stress distribution along the pushout fiber at the onset of debonding. The interphase shear strength is defined as the peak of the stress localization along the pushout fiber where initial debonding occurs. The contribution of residual stress to the strength is quantified through this stress localization approach. The resulting debonding shear strength is presented as function of test temperature.

Chapter 4 highlights the significance of debonding process which is due to the fact that fracture energy made available by the externally applied load on a notched specimen is shared between Mode I matrix crack and Mode II fiber/matrix interface crack. An interdependent relationship thus governs growth behavior of these two cracks. An important step in quantifying this relationship is the understanding of the damage initiation and propagation in the interphase layer. The mechanics of fiber/matrix interface debonding is described, in this chapter, through a proposed stress-based criterion for debond crack initiation. The criterion is examined for a SiC/Ti MMC by establishing a distribution of debonding lengths along a fiber-bridged crack length. The procedures combine fracture

mechanics equations with the results of finite element calculations on a cylinder model of a bridging fiber embedded in the matrix phase. The calculated mode II interface crack opening displacement is used to determine the interface crack-tip driving force. The influence of test temperature on this driving force and the resulting interface crack lengths is examined and discussed in this chapter.

Chapter 5 examines the evolution characteristics of stresses in bridging fibers as influenced by test temperature, loading frequency, residual stresses and material variables. The fiber stress evolution is a result of load transfer from the matrix to the fiber which is occurring due to various inelastic processes such as matrix plasticity, progressive interface debonding and frictional sliding along bridging fibers. A link is established between the fiber-bridging damage mechanisms and the stress state in the fiber in order to determine the influence of these parameters on the strength of bridging fibers.

Chapter 6 focuses on the bridging fiber damage mechanisms which is associated with the observed transition behavior from crack growth rate retardation to acceleration stage of the fatigue crack bridging process. The fatigue failure process of the reinforcing fibers in a SiC/Ti MMC is described using a proposed bridging fiber fracture criterion. A series of tension, residual fatigue and fatigue-life tests were performed on SiC SCS-6 fibers at both ambient and elevated temperature (500 and 650 °C) to quantify the strength characteristics of the fibers. The evolution characteristics of stresses in bridging fibers during fatigue crack propagation in a SCS-6/Timetal-21S composite is examined using the finite element method. The results of these stress calculations are combined with the residual fatigue strength data, in the proposed fiber fracture criterion, to determine the

fatigue life of bridging fibers. This damage model could be used to predict the useful life of a SiC/Ti MMC component subjected to fatigue loading in which crack bridging an operative damage mode.

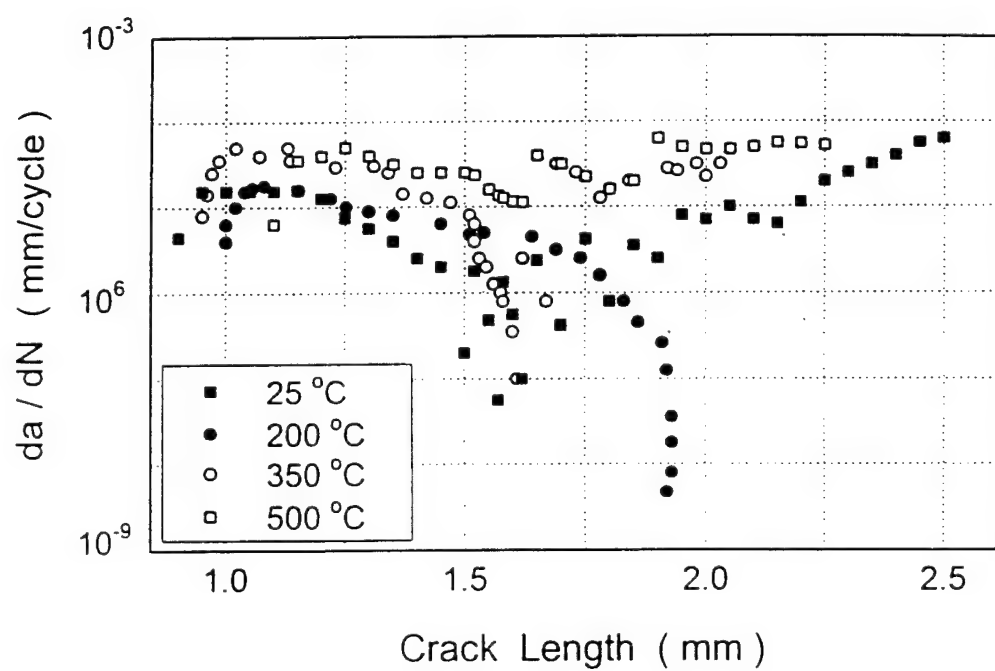


Fig. A.1 Fatigue crack growth rate of SCS-6/Ti-15-3 composite using SEN specimen in three-point bending tests, Cotterill and Bowen (1993).

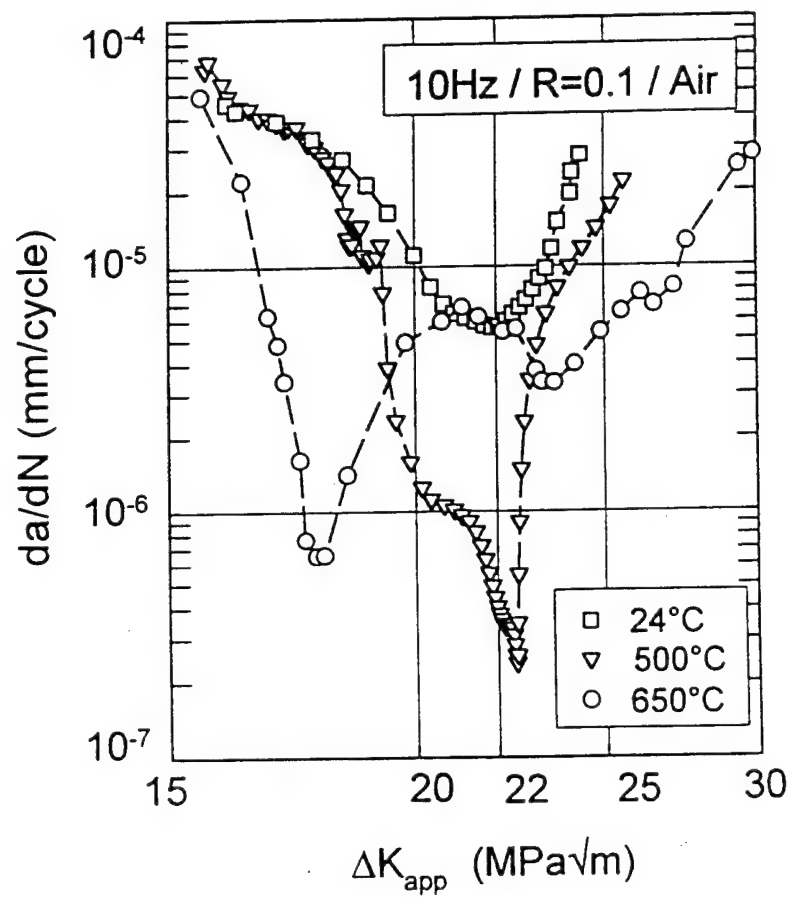


Fig. A.2 Fatigue crack growth of SM1240/Timetal-21S composite at room temperature, 500 and 650°C for loading frequencies of 10 Hz using center-notch specimens, Zheng and Ghonem (1995b)

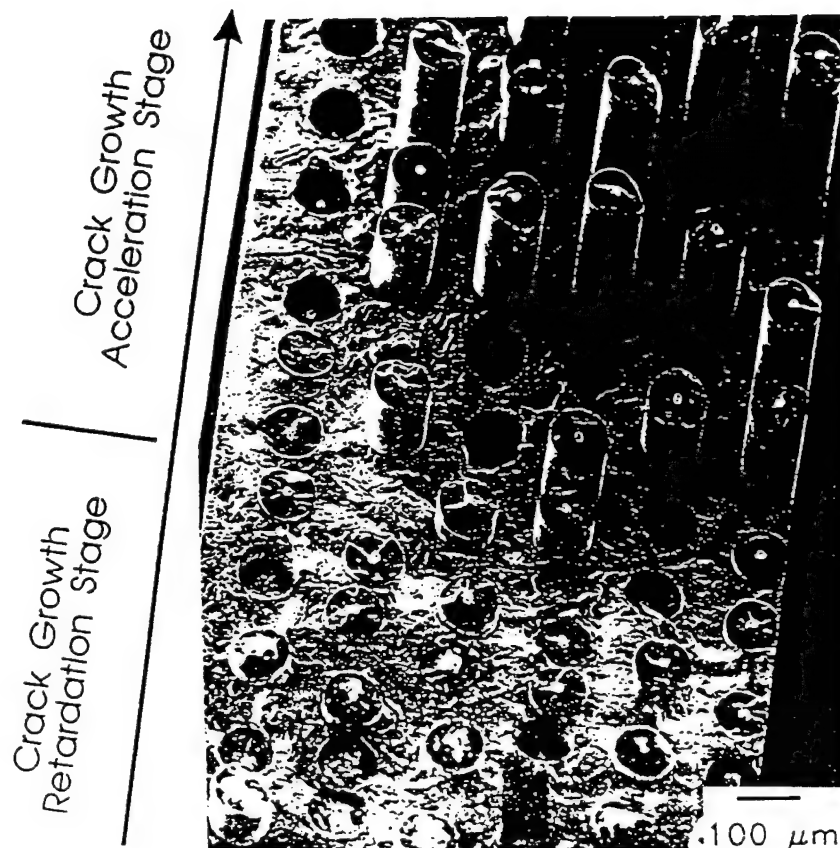


Fig. A.3 Micrograph of different fracture processes encountered in each of the crack growth stages, namely: bridging, transition and acceleration, Zheng and Ghonem (1995b)

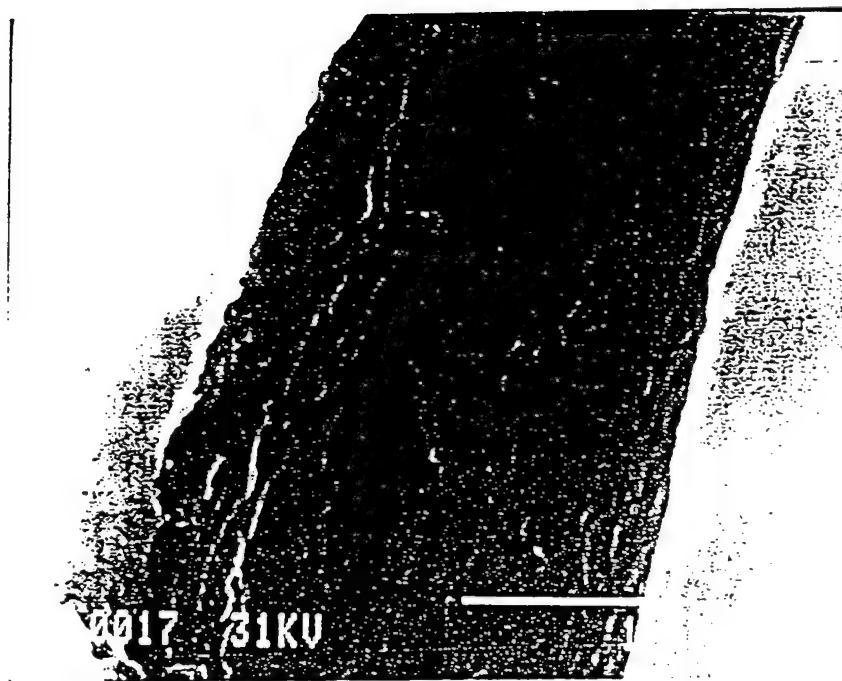


Fig. A.4 Example of a debonded carbon layer at a plane located immediately under the fracture surface of a room temperature test. Zheng and Ghonem (1995b)

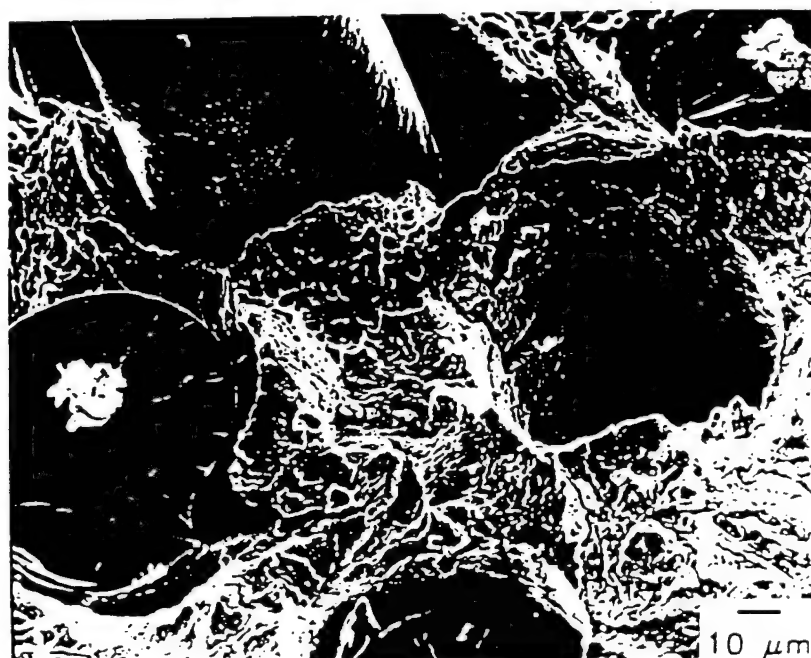


Fig. A.5 Example of an unstable fracture zone showing a high degree of matrix deformation surrounding the pulled-out fibers. Zheng and Ghonem (1995b)

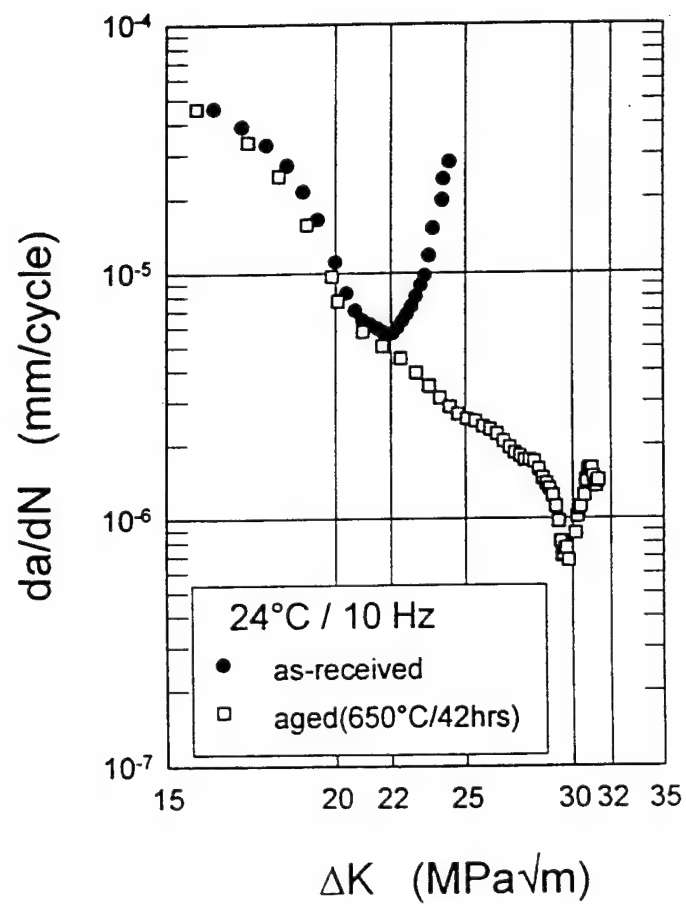


Fig. A.6 Room temperature crack growth rates for specimens in as-received condition and aged for 40 hours at 650 °C . Zheng and Ghonem (1995b)

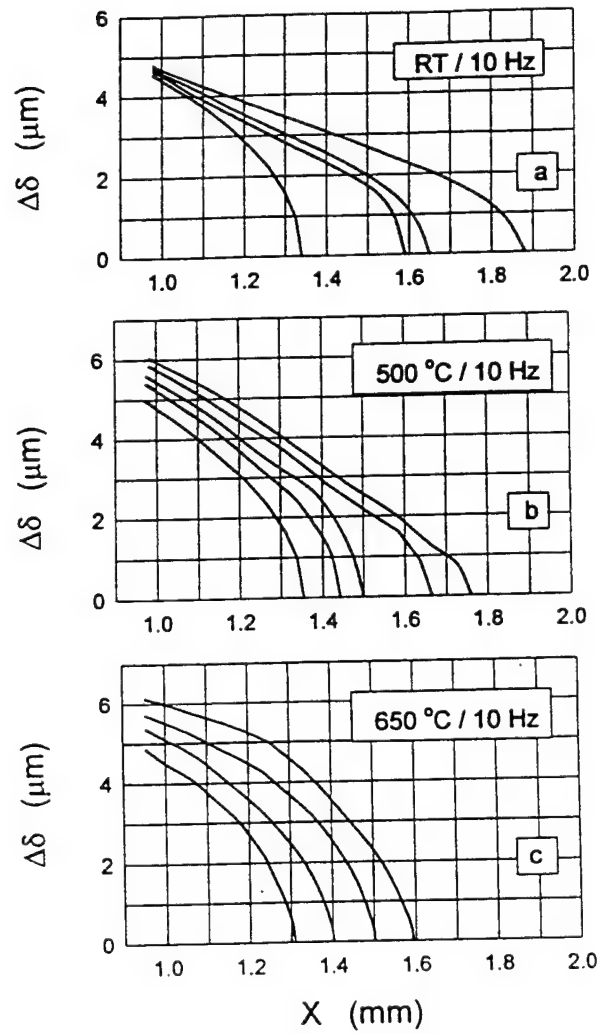


Fig. A.7 Crack opening displacement, COD, at positions along different bridged crack lengths in a SM1240/Timetal21S composite tested at three different temperatures: 24°C, 500°C and 650°C. Zheng and Ghonem (1995b)

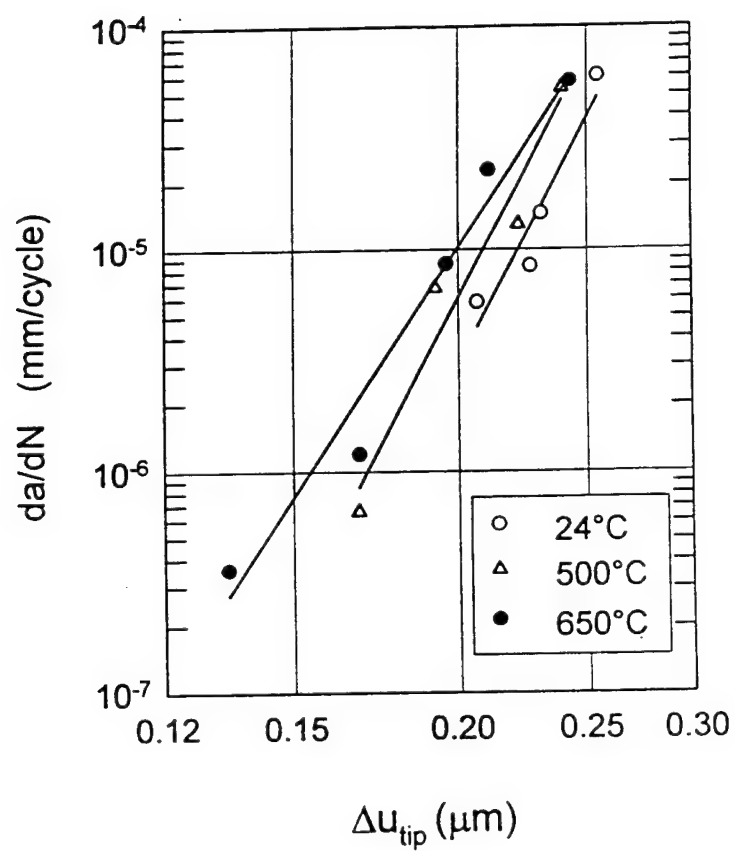
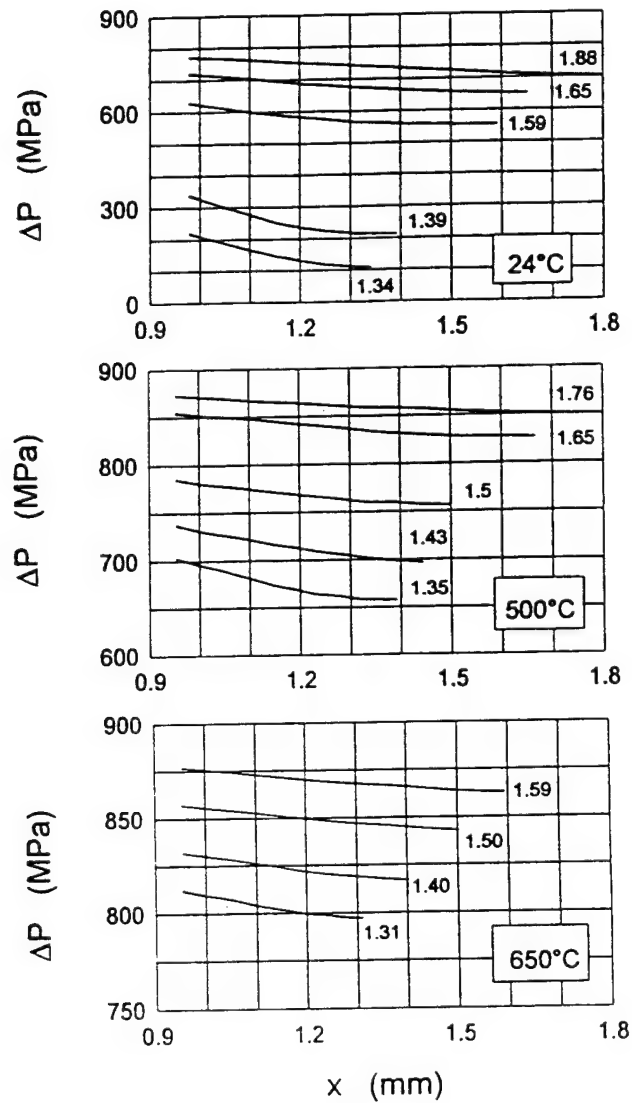


Fig. A.8 Relationship between Δu_T and a , for the different test temperatures, Zheng and Ghonem (1995b)



x is distance from center of hole (mm)

Fig. A.9 Fiber pressure distribution as function of crack length and temperature 24°C, 500°C and 650°C. Zheng and Ghonem (1995b)

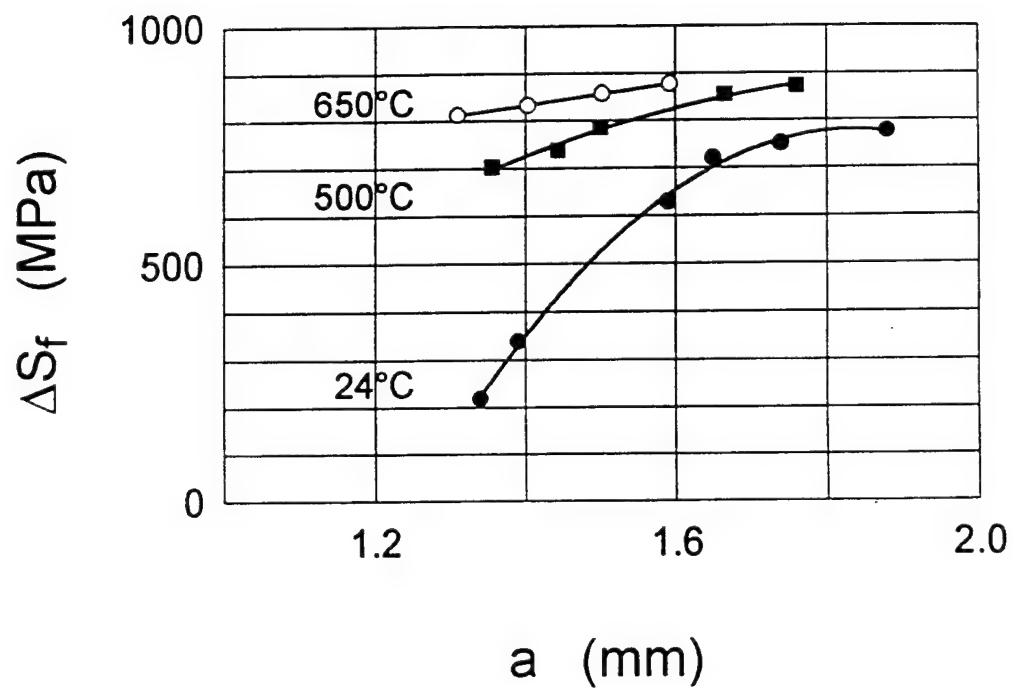


Fig. A.10 Evolution of ΔS_f calculated at the crack mouth as a function of the crack length and at different temperatures, Zheng and Ghonem (1995b).

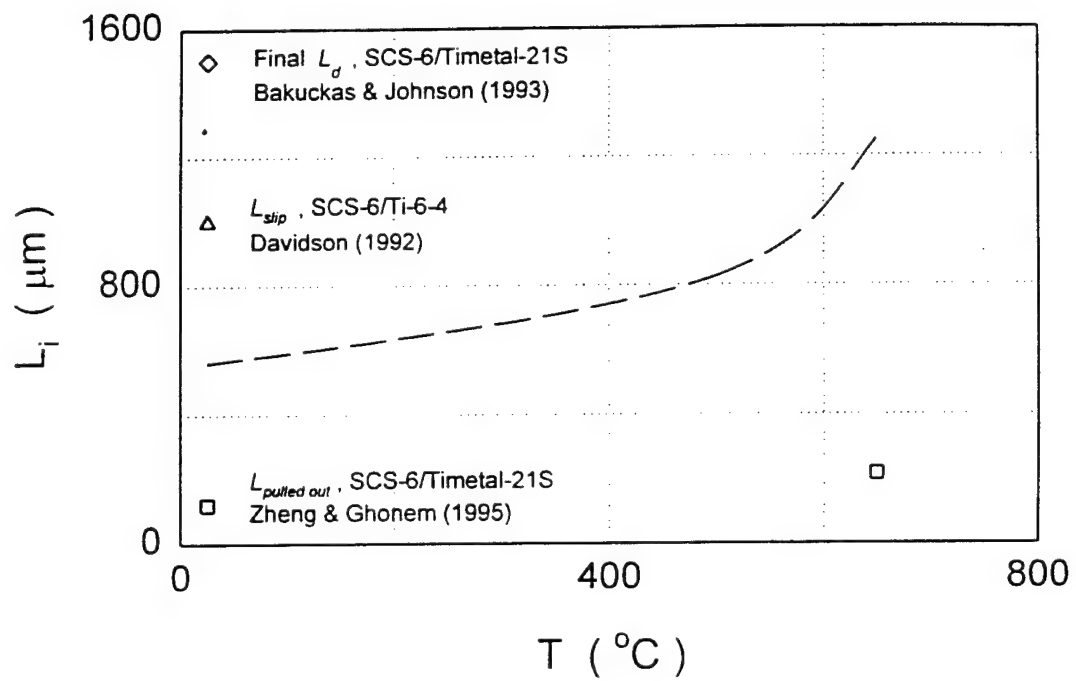


Fig. A.11 Fiber/matrix interface debonding lengths, slip lengths and pullout lengths at various temperatures. The line represents calculated trend of initial debonding lengths.

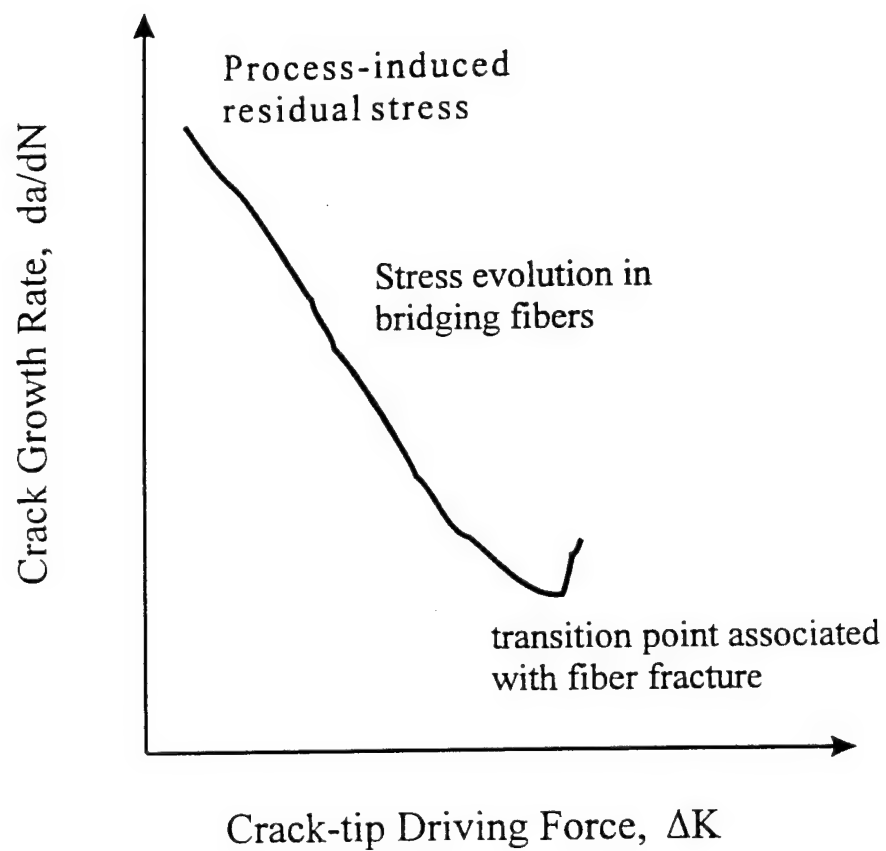


Fig. A.12 Damage components governing bridging fatigue crack growth process in a unidirectional SiC/Ti-MMC.

APPENDIX B Materials and Experimental Methods

This appendix describes the materials tested and experimental methods used in this program. The materials were selected from the newly developed advanced metallic matrix composites targeted for use in gas turbine engines. The experimental technique for testing isolated ceramic fibers at elevated temperature is developed. The procedures ensure that the data produced is representative of the physical response of the material studied with sufficiently low level of experimental error. Acoustic emission technique is employed to monitor the accumulation of damage during composite fatigue testing at elevated temperature.

B.1 Tensile and Fatigue Testing on Fibers

This section describes the fiber material used and the procedures relevant to monotonic tension and fatigue testing of SiC fibers at ambient and elevated temperatures.

B.1.1 Fiber Materials

The fibers used in this study, designated as SCS-6 fibers, are the SCS series of SiC fibers manufactured by Textron Specialty Materials, Textron Co., Inc., Lowell, MA. The SCS-6 fibers are produced by chemical vapor deposition (CVD) technique. The fiber consists of a 50 μm layer of SiC deposited on a 33 μm diameter carbon monofilament. The carbon core has a random aggregate of small (30-50 nm) turbostratic carbon block. An inner coating adjacent to the carbon filament is a layer of pyrolytic carbon. The SiC layer is then deposited on the inner coating. Along a radial distance away from the center of the fiber, the grain size becomes larger and the grains become increasingly aligned along the radial direction of the fiber. A multiple pass outermost carbon-rich coating consisting of a carbon matrix with SiC particles is deposited on the fiber. The nominal diameter of the SCS-6 fiber is 142 μm . The fibers are weaved with Mo-ribbon at every 5 mm interval along the fibers producing a fiber-mat panel of aligned, evenly-spaced fibers.

B.1.2 Specimen Preparation

A strip of woven fibers is separated from the fiber-mat panel by cutting the Mo-ribbon. A thin layer of polymeric binder is applied to the tab region of a fiber-mat specimen prior to cutting the fibers. The binder helps maintain the regular spacing of the fiber. Each fiber-mat specimen consists of between 35 to 40 fibers.

B.1.3 Tensile Testing procedures

Room temperature tensile tests on SCS-6 fiber-mat specimen are performed to established baseline data on strength properties of the fibers. The strength at elevated temperature are examined through tensile testing at 500 and 650 °C.

The fiber-mat specimen is held in an MTS 880 servo hydraulic testing machine using hydraulic-actuated high temperature grips. The test system is computer controlled with on-line data acquisition system. The applied hydraulic grip pressure is 4500 psi (31MPa).

Heating of the fiber-mat specimen for testing at 500 and 650 °C is achieved using a quartz-lamp heating unit. The unit consists of eight 1000-Watt quartz lamps enclosed in two aluminum boxes with quartz windows. The temperature of the specimen is raised manually using an Omega temperature controller. At the test temperature, the specimen was soaked for 30 minutes prior to the application of load.

The tension test was conducted in a load control mode at a loading rate corresponding to an applied stress of 10 MPa/sec until the specimen fractured. The load and cross head displacement readouts were recorded throughout the duration of the test.

Typical tension test data is plotted as shown in Fig. B.1. The slope of the load-displacement ϵ_0 is reflective of the elastic modulus of SiC fibers (~400 GPa). The load at fracture over the total area of fibers defines the tensile strength. The distribution of the strength values, as shown in a Weibull plot (Fig. B.2), yields a mean strength of 3.06 GPa with a standard deviation of 0.6 GPa.

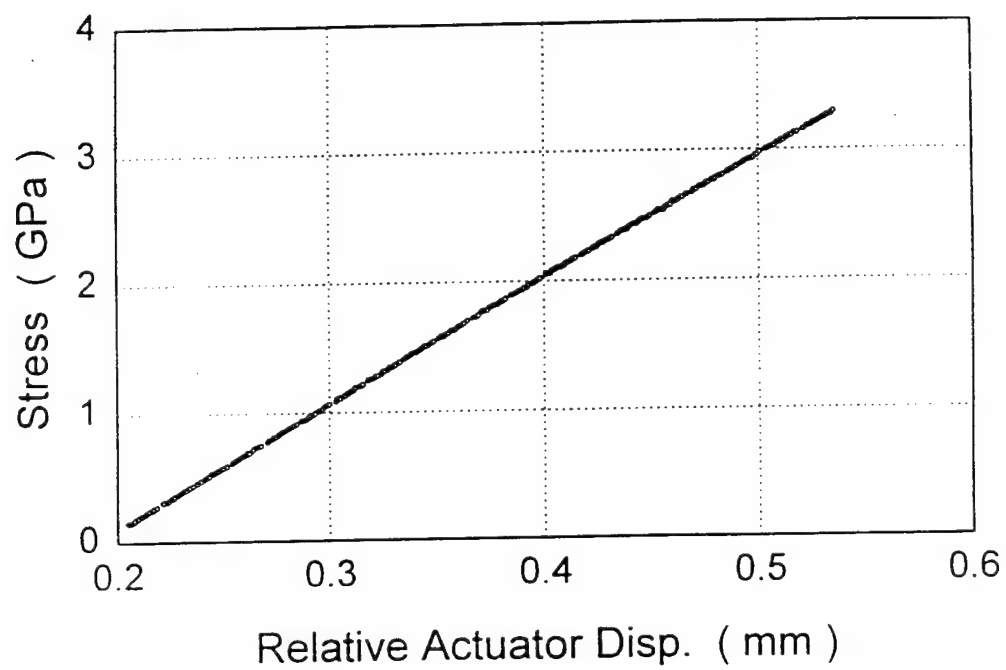


Fig. B.1 A typical tensile test result of SiC SCS-6 fiber-mat specimen.

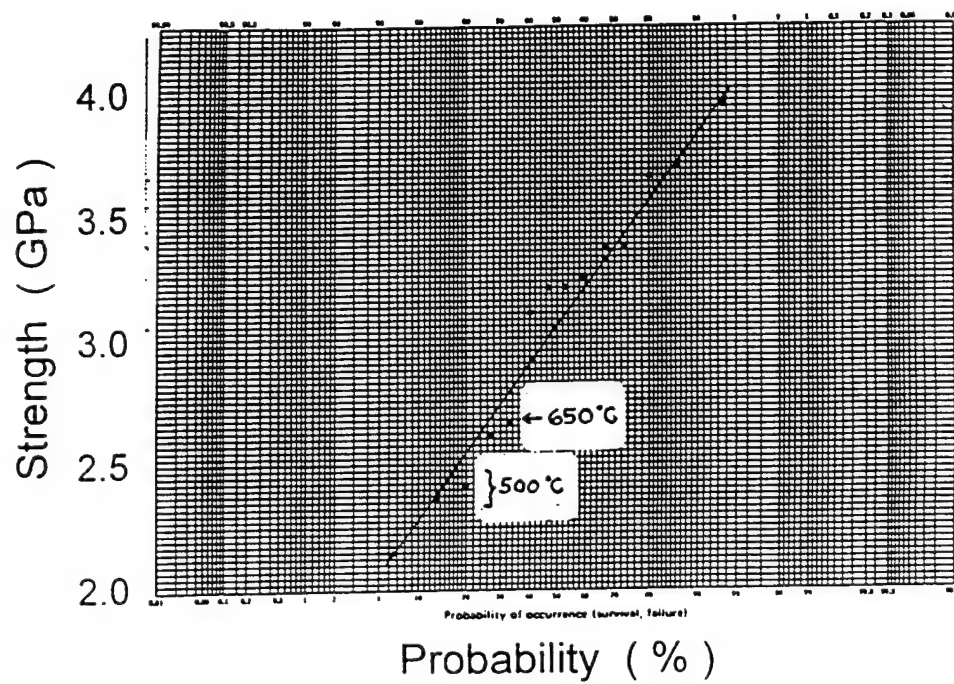


Fig. B.2 A Weibull distribution of tensile strengths of SiC SCS-6 fibers.

B.1.4 Fatigue Testing Procedures

The sample preparation, gripping and heating procedures for fatigue testing of SCS-6 fiber-mat specimen are identical as described in section B.1.2 and B.1.3. Prior to heating, however, a shakedown procedure is performed on the load train by applying a fatigue loading with a load amplitude of 30 % of the test amplitude at a loading frequency of 10 Hz for duration of 1000 cycles. This shakedown process would eliminate any backlash along the load train.

Two types of fatigue tests were conducted, namely, the residual strength test and the strength-life test. Both tests were run at a loading frequency of 10 Hz with a specified load amplitude and stress ratio of minimum to maximum, $R = 0.1$. In the residual strength test, the specimen is fatigued to a specified number of load cycles. The test is then stopped and the specimen examined to ensure that all the fibers are intact. The fatigued specimen is then pulled to fracture at a loading rate of 10 Mpa/sec. The load at fracture indicates the residual strength of the fatigued fibers. In the strength-life test, the fiber-mat specimen is fatigued until fractured.

B.2 Fatigue Testing on Metal Matrix Composites

This section describes the material used and the experimental procedures relevant to fatigue testing of metal matrix composites at ambient and elevated temperatures. The monitoring of progressive damage events such as microcrack initiation and propagation using acoustic emission technique is described in adequate detail.

B.2.1 Composite Materials

The material used in this study is a SCS-6/Timetal-21S metal matrix composite (MMC). The fiber reinforcement is a SiC SCS-6 fibers as described in Section B.1.1. The matrix phase of the composite, designated as Timetal-21S, is a metastable β titanium alloy with chemical composition as listed in Table B.1. The metastable β titanium alloy can be fabricated into the required thin-gage foil with relative ease and aged to high strength.

The SCS-6/Timetal-21S MMC was manufactured by Textron Specialty Materials, Textron Co., Inc., Lowell, MA. The six-ply unidirectional composite, $[0^\circ]_6$, was fabricated using Foil/Fiber/Foil layups technique employing pre-established critical processing parameters and consolidated by vacuum hot pressing. The composite plates have received a stabilization heat treatment (612 °C/8 hours) in a dynamic vacuum furnace. The resulting nominal fiber volume fraction is 0.35. A typical cross section of the composite is shown in Fig. B.3 indicating a staggered array distribution of fibers.

Table B.1 Chemical composition of titanium alloy Timetal-21S

Element	Fe	Mo	Al	Nb	Si	C	O	N	Ti
Comp. (Wt. %)	0.1	16.0	3.06	2.9	0.2	0.22	0.12	0.05	Bal.

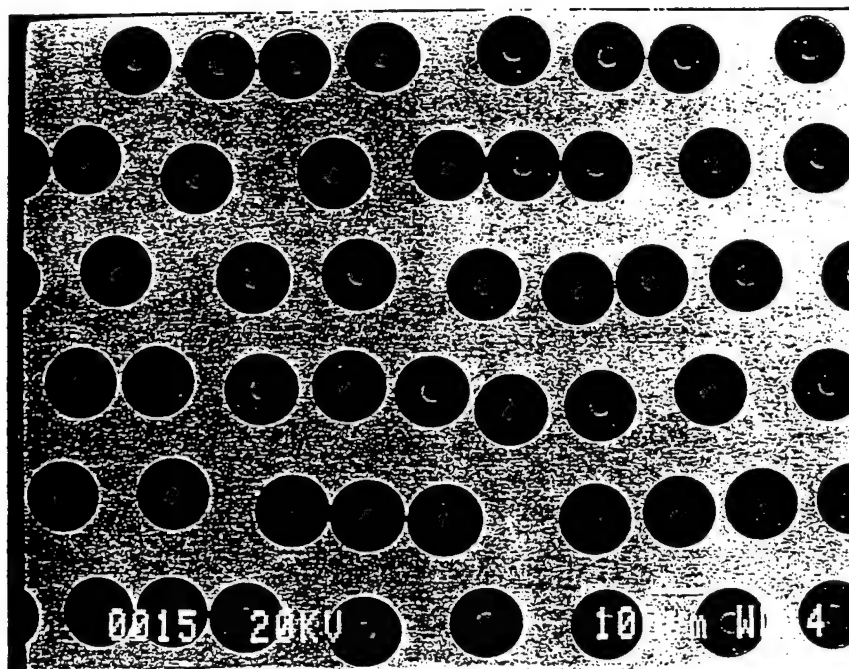


Fig. B.3

Cross-section of a SCS-6/Timetal-21S composite showing a staggered array distribution of fibers

B.2.2 Specimen Preparation

The specimen is cut from a composite panel with the axis of the fibers parallel to the long edges of the specimen. Each rectangular specimen measures 6.5 X 1.46 X 76 mm³. The surface of the specimen was ultrasonically cleaned with alcohol. A controlling K-type thermocouple was spot-welded on center region of a specimen surface. Additional thermocouples were welded on upper front and lower back of the gage length section of the specimen to monitor the temperature gradient across the section.

B.2.3 Fatigue Testing Procedures

The SCS-6/Timetal-21S composite specimen is attached to the load train of an MTS 880 testing machine using high temperature wedge-type gripping system. Concentric alignment of the specimen with the actuator is obtained by melting the metal pot of the actuator to relieve any twisting and bending due to misalignment.

The test temperatures of 500 and 650 °C were achieved by a split furnace with a manual temperature setpoint control. The specimen is soaked for 30 minutes at the test temperature prior to the application of load cycles. The applied load to the composite specimen is such that the fibers would experience the same load amplitude as employed in the fatigue test of isolated fibers (Section B.1.4). The load is estimated using the rule of mixture at each test temperature. The test was conducted at a loading frequency of 10 Hz

for the same number of cycles as the corresponding fiber test.

B.2.4 Acoustic Emission Monitoring

Acoustic emission (AE) system was used to monitor the different damage modes occurring during fatigue testing of an MMC. The system used in this study consists of a AEDSP-32/16 data acquisition board with MISTRAS-2001 software from Physical Acoustic Corporation (PAC), Princeton, NJ. The piezoelectric transducer is use with 1220A preamplifier unit for signal detection. The transducer flat face is coated with a layer of vacuum grease and taped to the load train of the testing machine outside the furnace.

Preliminary study on characteristics of AE signals associated with fracture of SCS-6 fibers was performed on signals collected from fatigue testing of isolated fibers. The results indicated that the fracture of SiC SCS-6 fibers could be identified by AE signals with the following characteristics:

Amplitude:	≥ 90 dB
Rise Time:	< 10 μ sec.
Energy Count:	≥ 80000

Based on these information, the system parameters selected for AE monitoring of composite fatigue testing as listed in Table B.2. These values are within the recommended range for

general-purpose testing of composites and non-metals.

Table B.2 System parameters used for AE damage monitoring in MMCs

Parameter	Value	Description
PDT	35 μ sec	Peak Definition Time (Rise Time) ensures correct identification of the signal peak for risetime measurement.
HDT	150 μ sec	Hit Definition Time ensures that each AE signal from the sample is reported as only one hit.
HLT	300 μ sec	Hit Lockout Time ensures that spurious measurements during the signal decay are avoided
Threshold (Fixed)	85 dB	AE signal 'hit' below threshold level will not be counted
Sampling Rate	4 MHZ	The rate at which the AEDSP board digitizes waveform on a per second basis.

The AE plots generated during fatigue test of a SCS-6/Timetal-21S MMC at 650 °C are shown in Fig. B.4. The AE signals has a maximum energy count of 800 and amplitude of 65 dB indicating that the signal emission is not due to fiber fracture. The three-band energy count data is related to microcrack initiation in the interphase region along the fiber and in the matrix phase of the composite and the propagation of these cracks into the matrix phase during fatigue loading.

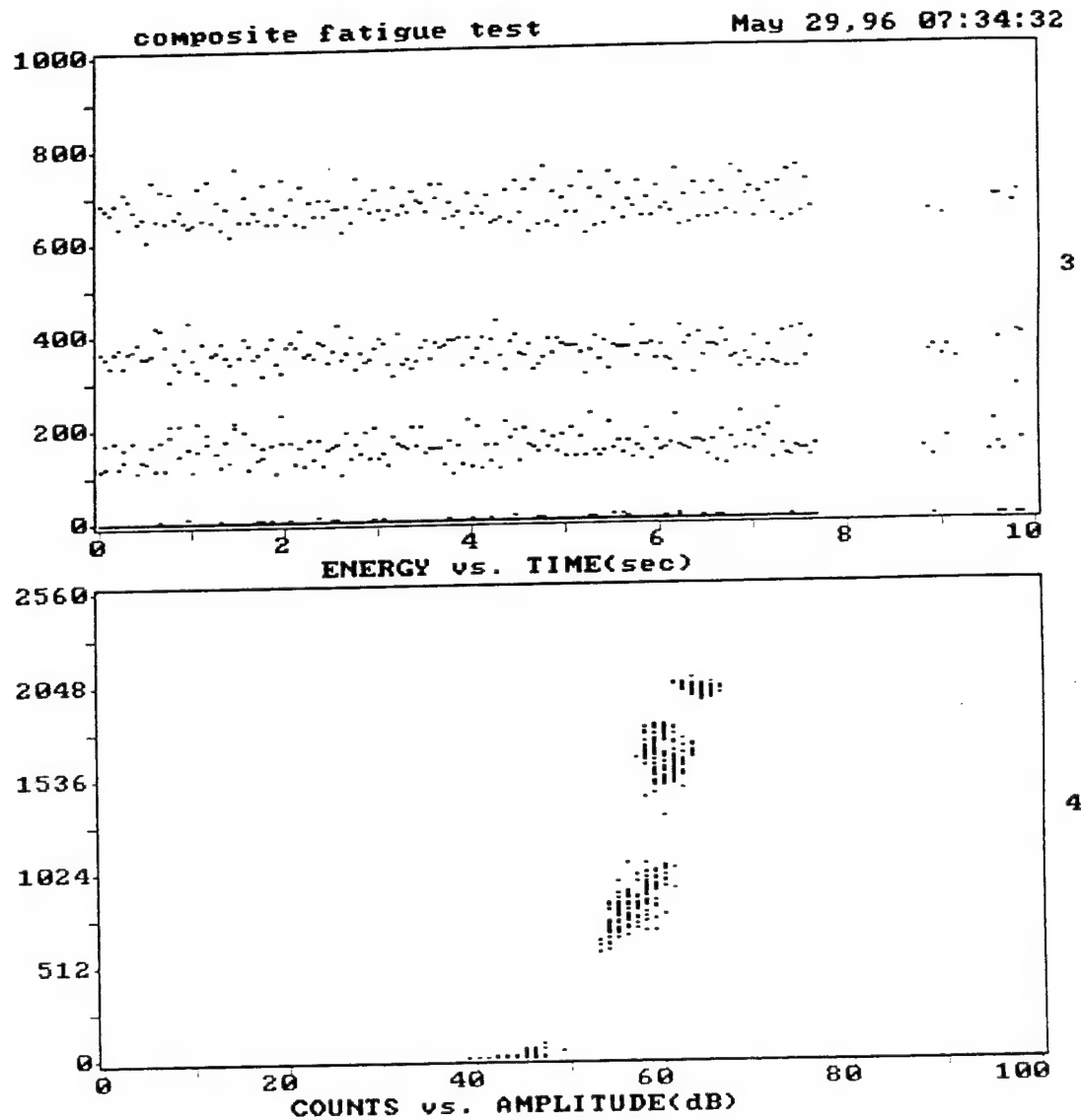


Fig. B.4 Acoustic emission (AE) data from a fatigue test on SCS-6/Timetal-21S composite specimen at 650 °C.

B.3 Scanning Electron Microscopy (SEM)

Scanning electron microscope examination of materials and fatigue features provides vital information for the determination of fracture mechanism responsible for the material behavior. This section describes some of the techniques used in the study.

B.3.1 Surface Cracks on Fiber Coatings

The surfaces of fatigued SCS-6 fibers were examined for fracture features such as surface cracks and spalling of the carbon-rich coating layer. Circular cracks were formed on the surface of the fibers during the test. Typical distribution of these cracks on fibers which have been fatigued at 650 °C is shown in Fig. B.5. The distance between adjacent cracks in the gage-length section of the fatigued fiber were measured. The statistical distribution of 784 crack spacing measurements is illustrated in Fig. B.6(a) illustrating a skewed distribution. About 77% of the measurements fall within a 20- μ m crack spacing. The density of the cracks was defined by the inverse of the mode crack spacing, which is determined as illustrated in Fig. B.6(b).

Another coating damage feature is the spalling of the carbon-rich layer, as shown in Fig. B.5. This type coating damage, however, did not cause fracture of the fiber at that location.

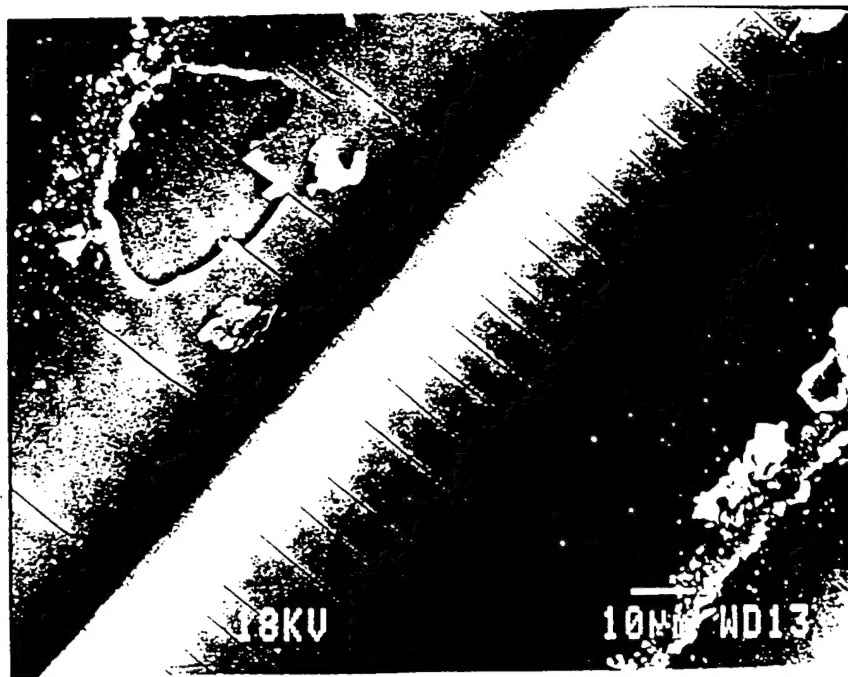


Fig. B.5 Distribution of surface cracks on fatigued SCS-6 fibers. The test was performed at 650 °C with a maximum load of 1500 MPa, $R = 0.1$. The accumulated load cycles is 247.6×10^3 .

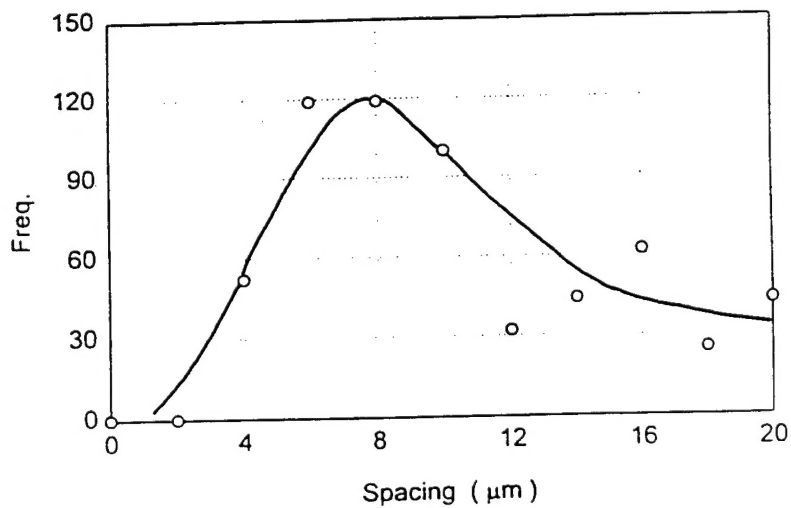
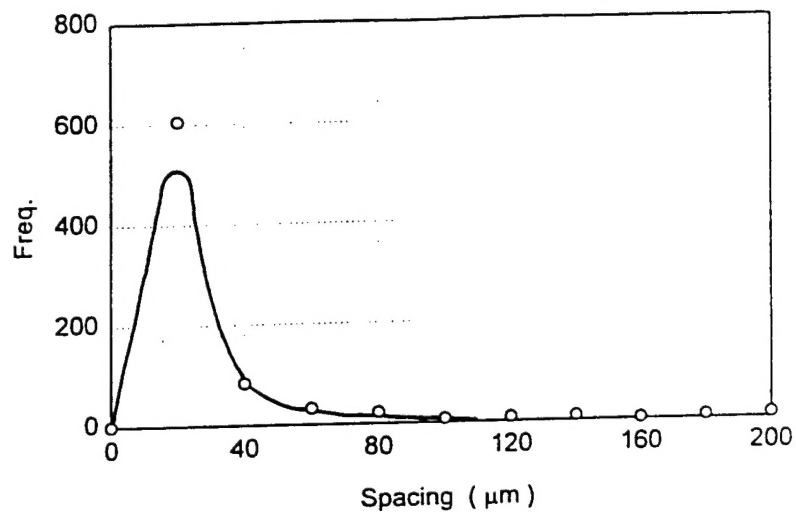


Fig. B.6 (a) Distribution of crack spacing measurements along SCS-6 fibers fatigued at 650 °C for a total of 247.6×10^3 cycles. Maximum applied stress is 1500 MPa, $R = 0.1$. (b) Statistical distribution of 77 % of the measurements which fall within a 20-μm range.

B.3.2 Microcrack Initiation Sites Along the Fibers

One surface of a fatigued MMC specimen was grounded to the first layer of fibers. The surface was then polished consecutively with SiC papers with grid # 400, 600, and 800, followed by final polishing with 9, 3 and 1- μm diamond suspension.

The microcrack initiation sites in the interphase zone along a fiber, within the gage-length section of the specimen, were identified. A typical distribution of the initiation sites is shown in Fig. B.7. The spacings between adjacent sites were determined and the statistical distribution of the spacings is shown in Fig. B.8 for both tests performed at 500 and 650 °C. The density of the crack initiation sites is defined by the inverse of the mode for the spacing measurements.

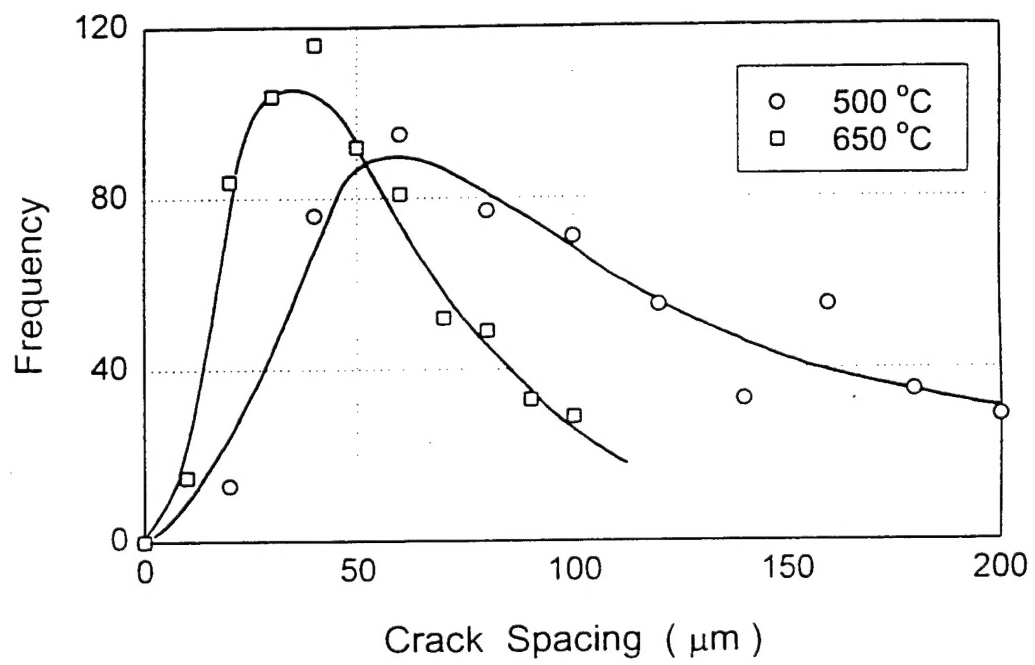


Fig. B.7 Statistical distribution of crack initiation sites along fibers in a composite fatigued at 500 and 650 °C.